The Mechanics of Strain-Induced Crystallization in Poly(ethylene terephthalate)

by

Patricia G. Llana

B.E. Mechanical Engineering, The Cooper Union for the Advancement of Science and Art, 1996

Submitted to the Department of Mechanical Engineering
in partial fulfillment of the requirements for the degree of

Master of Science in Mechanical Engineering

at the

MASSACHUSETTS INSTITUTE OF TECHNOLOGY

June 1998

Author .....
Mechanical Engineering
May 8, 1998

Certified by .....
Mary C. Boyce
Associate Professor of Mechanical Engineering
Thesis Supervisor

Accepted by .....
Ain A. Sonin
Chairman, Department Committee on Graduate Students
Department of Mechanical Engineering

The Mechanics of Strain-Induced Crystallization in Poly(ethylene terephthalate)

by

Patricia G. Llana

Submitted to the Department of Mechanical Engineering on May 8, 1998, in partial fulfillment of the requirements for the degree of Master of Science in Mechanical Engineering

Abstract

Poly(ethylene terephthalate) (PET) is a thermoplastic polymer found in numerous commercial applications. PET exhibits the capability of undergoing strain-induced crystallization during processing, the result of which is increased stiffness and hardness as well as better dimensional stability. An experimental study of the strain rate, strain state, and temperature dependencies of the stress-strain behavior of PET under large strain deformation was conducted over a wide range of strain rates ($-0.005/s$ - $02.0/s$) and temperatures ($25°C$ - $105°C$) and in both uniaxial and plane strain compression. The increase in crystallinity content with varying strain rate and temperature and for the two different states of strain that developed as a result of these deformation conditions was investigated using Differential Scanning Calorimetry (DSC). The nature and evolution of the crystallographic texture was studied using Wide Angle X-ray Diffraction (WAXD) measurements. The results of the mechanical tests, DSC and WAXD measurements indicated that strain-induced crystallization does not occur in uniaxial compression at temperatures below the glass transition, however, a shift in the cold crystallization exotherm was observed. Alternatively, in plane strain compression at these temperatures for the fastest strain rates, DSC measurements indicated an increase in crystallinity. At temperatures near the glass transition in uniaxial compression, DSC measurements indicated an increase in crystallinity, whereas WAXD measurements indicated only molecular orientation. In plane strain compression, however, both DSC and WAXD measurements indicated an increase in crystallinity. At temperatures above the glass transition temperature, both DSC and WAXD indicated an increase in crystallinity in both uniaxial and plane strain compression. It was found that the percent crystallinity increased with increasing strain rate and decreasing temperature and that the crystallographic texture that develops is dependent on the state of strain. A constitutive model that predicts the strain rate, strain state and temperature dependence of PET was developed that captures these dependencies very well.

Thesis Supervisor: Mary C. Boyce
Title: Associate Professor of Mechanical Engineering

Acknowledgments

I would first like to express my appreciation to Professor Boyce for her guidance and support over the past two years, for her boundless energy, for her commitment to the work and to her students, and for being a role model and mentor. I have learned so much from her and am graduating with a true admiration of her excellence and dedication.

The financial support of the National Science Foundation and Kodak are gratefully acknowledged. This work made used of the MRSEC Shared Facilities supported by the National Science Foundation under Award Number DMR-9400334.

I would like to thank my fellow Mechanics & Materials cellar dwellers for their friendship and companionship. I would like to thank Teresa and Yioula for all of our discussions ranging from careers to polymers to the regular girl talk (Teresa, congrats and best wishes to you and Rich), and Jorgen for helping me revive the Instron from its computer-caused coma, for all the helpful discussions on polymer testing and modeling, and for putting up with all the girl talk. I would also like to thank Brian Gally, whose help with the Instron I could not have done without, and for all the interesting discussions we had in the lab when we were supposed to be working. I would like to thank Vicky for her company on our late nights working on thesis. I would like to thank Prakash for being a great friend, and for always being here at night to talk to when I was working late. I would also like to thank the rest of the M&M group for their insight and friendship, particularly Ulf and Alexis for studying with me for those tough classes.

I would especially like to thank my friends outside the research group: Hector, Mark, Helen, and the missing Jerry and Mia. You have made my two years here the best they could have been. I will never forget the late nights out dancing and having fun, or the trips to the Cape - cramming into Mark's car, or the many meals that Mia so hospitably cooked for us that we ate sitting on milk crates in her kitchen. Hector, thanks for all the lunches we spent together, especially this year with Jerry and Mia gone, and for all the interesting discussions on Star Wars, The X-Files, South Park, and life in general; I know you'll find what you've been looking for when you go home, you deserve it. Mark, thanks for being the unofficial "mode of transport" for the group and for all of the interesting talks on jobs and relationships. Helen, I'm so glad we became better friends this past year and I know you'll have a blast in Paris. To the missing Jerry, thanks for keeping in touch all the way from Bath and for all of the interesting discussions we've had about relationships and family and jobs. Thanks for being my workout/aerobics partner and for being a true friend. And thank you Mia, whose life I live vicariously through. You do all the things that I would do if I weren't so conservative. You're a great friend and you inspire me to always have fun in everything that I'm doing. Your easygoing personality is one of the first that greeted me here at MIT and it has made all the difference.

I most especially thank Adrian, for being there for me the past 7+ years, for being so supportive and loving during times of panic and stress, for dinners cooked, dishes washed, groceries bought, and laundry done, for editing this thesis, for reminding me to relax and helping me to de-stress, and most importantly, for being my best friend.

This thesis is dedicated with all my love to my parents and my brother. You are all so important to me and are a large part of who I am. Thank you for all the love, support and encouragement, I know I would not be able to get very far without them.

Table of Contents

List of Figures

List of Tables

Chapter 1

Introduction

Poly(ethylene terephthalate) is a thermoplastic polymer found in numerous commercial applications including photographic films, milk containers, 2-liter beverage bottles, magnetic tapes, electrical cable wraps, and highly drawn fibers. It is typically processed in the solid state at temperatures in or above its glass transition temperature, T_g. The primary modes of processing PET are blow molding, vacuum forming, drawing, and biaxial stretching. As a result of these processes, the polymer takes either an oriented amorphous state or an oriented semi-crystalline state. PET thus exhibits the capability of undergoing crystallization during processing. This phenomenon is often termed strain-induced or stress-induced crystallization. The result of strain-induced crystallization is increased stiffness and hardness as well as better dimensional stability, also referred to as resistance to recovery.

There have been numerous investigations on the mechanical behavior of PET due to its wide range of applications. Its commercial success is mainly due to its ability to undergo strain-induced crystallization at various stretching rates, states, and temperatures. This strain-induced crystallization is also a primary reason for the inability to accurately predict its behavior during processing. The purpose of this thesis is to present recent research into the mechanics of strain-induced crystallization in PET.

In Chapter 2, experiments are presented which sample the mechanical behavior of PET under different states of large strain, over a wide range of strain rates, and over a wide range of temperatures spanning the glassy and the rubbery regimes. Differential Scanning Calorimetry (DSC) measurements are utilized to determine the crystallinity content as a

function of mechanical loading (strain state, strain rate, final strain, temperature). Wide Angle X-ray Diffraction (WAXD) is then used to determine the nature of this crystallinity and the evolution of texture with strain rate, final strain and deformation temperature.

Chapter 3 presents the constitutive model of the mechanical behavior for the finite deformation of PET above its glass transition temperature. The constitutive model captures the strain rate, strain state and temperature dependence of the material. The model utilizes a kinematic framework to model the two resistances observed in the mechanical behavior of PET. The model, with parameters reduced from uniaxial compression experimental data, is compared to experimental data of tests conducted in uniaxial compression and plane strain compression at temperatures above the glass transition temperature. The model is found to predict the experimental data reasonably well.

Chapter 4 summarizes the work presented in the thesis, highlighting the significance of the results obtained and suggesting the direction of future efforts in polymer deformation and processing problems.

Chapter 2

Experimental Work

2.1 Background

Over the years, investigators have studied PET in view of either understanding its crystallization behavior and/or its mechanical behavior [1]-[15]. The result of these works, only a few of which are mentioned here, have documented interesting and significant features of the deformation behavior of PET, such as the effects of temperature, strain rate, state of deformation, material anisotropy and heat transfer.

One of the earliest works on PET by Marshall and Thompson [1] consisted of the continuous-drawing of initially amorphous PET fibers at elevated temperatures. They examined the sensitivity of necking and the corresponding natural draw ratio (NDR)[1] to deformation draw speed ($5cm/s$ to $70cm/s$) and deformation temperature ($20°C$ to $80°C$). It was found that the NDR increases with increasing speed and decreasing temperature. The necking phenomenon during cold drawing was in part attributed to adiabatic heating. These tests were at relatively high rates and therefore complicated by the occurrence of adiabatic heating, as discovered by the author. There is greater heating at lower temperatures due to the higher stress levels required to deform the material and thus greater dissipation. Therefore the identification of the NDR is obscured due to the simultaneous occurrence of softening due to heating and hardening due to molecular orientation. An investigation by Arruda, Boyce and Jayachandran [2] discusses adiabatic heating and dissipation more thoroughly. The work of Marshall and Thompson was an important early

1. Marshall and Thompson define the NDR as the ratio of the specific length at the draw roll to the specific length at the feed roll, where the specific length is calculated by taking the inverse of the cross-sectional area multiplied by the density. This definition of the NDR applies after the filament has necked and is flowing [1].

study that showed the combined effect of rate and temperature of deformation on the mechanical behavior of PET at large strains. Thomas [3] later conducted experiments at even higher temperatures ($\sim 100°C$) producing stress-strain curves at different roller drawing rates (50% to 444%/*min*). It was found that rapid draw rates resulted in large strain hardening of the material. X-ray photographs revealed high crystallinity in the drawn fibers. His conclusion was that strain hardening was attributed to the development of strain-induced crystallization.

In other work, Ward [4] studied the cold drawing of PET at room temperature over a wide range of test conditions and polymer constitution. The influence of preorientation, crystallinity, and chemical crosslinking was investigated. Experiments involving the determinations of the natural draw ratios and shrinkages of slightly preoriented fibers indicated that the NDR may be regarded as equivalent to stretching the network to a limiting total extension. Birefringences and moduli of the cold-drawn fibers were fitted by a model that assumed that the drawn fiber consists of an aggregate of optically and mechanically anisotropic units which are aligned by the drawing process. In later work, Ward, et. al. [5] examined the tensile yield behavior of isotropic amorphous PET sheets over a wide range of temperatures ($-25°C$ to $60°C$) and strain rates (0.00001/*s* to 0.1/*s*). In these works, it was recognized that PET undergoes orientation and also possibly crystallization during stretching, however, no clear distinction was made between the effects of orientation vs. the contributions of crystallization to the mechanical behavior. Also not addressed were the effects of the state of strain and strain history.

In a work on "stress-induced" crystallization, Misra and Stein [6] investigated the microstructure of quenched amorphous PET films stretched both below and above T_g by performing density measurements, small angle light scattering, and wide angle x-ray scattering measurements. In this study the strain rate (300%/*min*) was not changed while the

temperature and the amount of strain were varied. Considerable crystallinity was found to occur with stretching and the percent crystallinity increased when stretching was followed by annealing. It was found that for samples stretched at $80°C$ an increase in crystallinity was observed only beyond 80% nominal strain. This increase in crystallinity rose with increasing nominal strain, for example from 4% to 13% to 21% crystallinity at nominal strains of 80%, 200%, and 300%, respectively, and levelled off at higher strains (~380% strain).

In later work, Porter, et.al. [7]-[9] have conducted extensive tests on the deformation of PET and poly(ethylene2,6-naphthalate) (PEN) and have subsequently investigated the effects of extent of deformation and deformation temperature on the material microstructure. Ghanem and Porter [7] conducted isothermal solid-state coextrusion experiments on isotropic amorphous PEN both below and above its T_g and studied the behavior of the onset of cold crystallization (T_{cc}) with respect to extrusion temperature (ET) and extrusion draw ratio (EDR). DSC analysis showed that the T_{cc} decreased markedly with increasing EDR and goes through a minimum in the vicinity of the glass transition region. It was found that the percent crystallinity induced by draw, calculated from DSC analysis, increased continuously with increasing EDR and with increasing ET from 5% to 35% crystallinity. After this increase the crystallinity then reached a saturation value which was about 35% for an EDR of 2.3 at an ET of $150°C$. Guan, Wang and Porter [8] performed planar deformation of amorphous PET in equi-biaxial stretching and forging at temperatures above T_g ($80°C$ to $100°C$) and monitored the evolution of crystallinity with DSC, wide angle X-ray diffraction (WAXD), density and elastic recovery measurements. It was found that, at a temperature of $90°C$, as the biaxial draw ratio increases, the area of the cold crystallization exotherm decreases. This is a manifestation of the presence of strain-induced crystallization due to large deformations. They also observed that the percent

crystallinity measured by WAXD, found by comparing the areas of amorphous and crystalline portions of the WAXD scans, decreased as the stretching temperature was increased in biaxial stretching. This was attributed to the thermal relaxation process, which is competing with the chain orientation process, becoming more pronounced as the deformation temperature increases from T_g, and thus hinders crystallization. What was also shown was that the orientation and crystallization obtained from equi-biaxial stretching and uniaxial compression is essentially identical, as the only difference observed could be attributed to an effect of strain rate, which they were unable to maintain constant during their tests. In work by Sun, Pereira, and Porter [9], uniaxially drawn films were prepared from isotropic, amorphous PET by using solid-state coextrusion below its T_g ($50°C$ to $70°C$) at various draw ratios and the cold crystallization behavior was studied. It was found that T_{cc} decreases as the extrusion draw ratio increases. Also, it was found that for extrusion draw ratios up to 2.5 (which corresponds to a tensile logarithmic strain of 0.92), T_{cc} decreases with increasing extrusion temperature, but that this behavioral trend is reversed above this value and T_{cc} increases with increasing extrusion temperature.

In recent work, Jabarin, et. al. [10]-[11] have extensively investigated strain-induced crystallization in the rubbery region. The mechanical behavior of simultaneous and sequential biaxial stretching of initially amorphous PET films at temperatures ranging from 80-$110°C$, strain rates ranging from $0.05/s$ to $200/s$ and extension ratios from 4 to 5 (which correspond to a tensile logarithmic strain of 1.38 to 1.6) was found to depend on the deformation temperature and strain rate. Crystallinity was measured using DSC and was also studied, in some cases, using small angle light scattering and WAXD. Their results are consistent with the findings of Misra and Stein [6] and also Porter, et. al. [7]-[9] with respect to strain-induced crystallization. The crystallinity was found to develop a rod-like fibrillar structure depending on the extent of stretching. Mechanically, the strain-

induced crystallization can be observed by a noticeable increase in strain hardening that starts at a temperature and strain rate dependent level of strain. They call this strain the strain hardening parameter (SHP). They do, however, state that some crystallization does occur prior to SHP. When deformation is slow, strain-induced crystallization does not occur due to molecular relaxation having time to occur which inhibits orientation and subsequent crystallization. Mechanically, the strain hardening is very low or not present at all in these cases. This molecular relaxation phenomenon is consistent with the findings of Porter, et. al. [7]-[9]. This rate effect on strain-induced crystallization is very important with regard to understanding and being able to predict the mechanical behavior during processing. The work conducted by Jabarin [10] indicates that the rate effect is larger over the strain rate range examined as the temperature increases. However, if the strain rate is high enough at a given temperature, the strain hardening is nearly independent of rate. An important result of the investigation of Chandran and Jabarin [11] is the strong dependence of the strain state history on both crystallization and strain hardening. It was found that the stress-strain curves for specimens stretched in the simultaneous biaxial mode were always concave upward, indicative of an amorphous polymer. In contrast, when stretching in the sequential mode, if strain-induced crystallization occurred during the first stretch, exhibited by the characteristic upswing in the curve, then the stress-strain curves were convex upward, indicative of a semi-crystalline material. This can be attributed to a greater ability of the polymer chains to orient and crystallize under uniaxial tensile stretch conditions than under biaxial stretch conditions.

In more recent work, Buckley, et. al. [12] studied both uniaxial and constrained width (plane strain) drawing tests on PET film above T_g ($75°C$ to $120°C$) at strain rates ranging from $1/s$ to $16/s$ on a flexible film tester. The crystallinity content in the deformed specimen was monitored using density measurements. The overall stress level, at this strain rate

range, was found to increase with strain rate but there was no significant effect observed on the character of the strain hardening behavior. A significant temperature dependence was found, however, where hardening rate decreases with increasing temperature. There was not a very large difference in strain hardening between uniaxial and constrained width stretching. This was attributed to the nearly identical orientation obtained in these two stretch states.

In very recent work, Zaroulis and Boyce [13] studied the mechanical and crystallization behavior of PET over a wide range of strain rates (0.005/*s* to 0.5/*s*) and temperatures ($25°C$ to $80°C$) in both uniaxial and plane strain compression conditions. A dramatic drop was observed in both modulus and yield stress with temperature, accompanied by a drop in percentage softening after yield. The relative independence of hardening with temperature for the material over this temperature regime was also observed. DSC conducted on the deformed and undeformed samples show that the crystallization temperature decreases with strain and this occurs to a greater extent at higher temperatures of deformation. Comparison of the areas of these exotherms with the melt endotherm indicated, however, that there was no change in crystallinity content over this temperature range. It was concluded that for uniaxial compression, the strain hardening in this temperature regime is due to molecular orientation and not crystallization. However, DSC revealed that crystallization occurred during plane strain compression, which indicated that strain hardening during plane strain may be due to both orientation and crystallization. Additional experiments conducted at $80°C$ showed a dramatic change in the strain hardening behavior. At low strain rates (~0.005/*s*), the strain hardening behavior at $80°C$ is lower than that observed in the range of $60°C$ to $76°C$. At high rates (0.5/*s*), however, the hardening is dramatically higher. These results are consistent with the investigations of Porter, et. al. [7]-[9] and Jabarin [10]-[11]., which indicate that at longer times and higher temperatures,

a network relaxation occurs, while at higher rates, orientation does not have time to relax and therefore crystallization occurs. DSC on the $0.5/s$ and $80°C$ uniaxial compression sample confirmed that crystallization had indeed occurred. Similarly, the strain hardening in plane strain at $0.5/s$ and $80°C$ is also much higher than that observed in the $25°C$ to $76°C$ range.

Very interesting results were obtained by Blundell, et. al. [14]-[15] who studied structural changes during fast uniaxial drawing of PET by capturing simultaneous wide-angle x-ray scattering patterns using synchrotron radiation. Drawing was studied at $80°C$, $90°C$, $100°C$ and $110°C$ to a final draw ratio of ~4.1 at a draw rate of $\sim 10/s$. They found that essentially all crystallization occurred after final extension has been achieved and that crystallization does not occur below a critical draw ratio in the range of $80°C$ to $110°C$ and increases with the draw ratio beyond this point.

From the previous review, it is apparent that a comprehensive set of mechanical tests with subsequent microstructural analysis on the deformed material can provide a picture of the structural evolution of PET. Although the works described begin to determine the complex connection between deformation, time, temperature and crystallization, they have not individually spanned a range of homogeneous deformation states, rates of stretching, and temperatures. Increasing the extent of deformation acts to orient the molecular network, which, under favorable conditions such as high strain rates and temperatures, leads to strain-induced crystallization. This work builds on the work conducted by others and examines the mechanical behavior of initially amorphous PET in the rubbery region where there is a balance between strain-induced crystallization at high rates as well as network relaxation at low rates, as shown by Zaroulis and Boyce [13]. The experimental part of this investigation, which consists of mechanical tests and microstructural analy-

sis through DSC and WAXD, is presented in this chapter and serves as a basis for the constitutive modeling that is presented in the following chapters.

2.1.1 Material/Specimen Description

The material used in the experiments is nearly amorphous isotropic PET, with molecular weight $\overline{M}_w$ = 49,700. The PET was in sheet form and was supplied by Kodak. The material sheets, whose average thickness is 2.09*mm*, appear optically clear, implying a low crystallinity content. DSC measurements of the as-received material indicated a residual crystallinity content of about 10%. This small amount of residual crystallinity is a result of the practical difficulties encountered in quenching the polymer rapidly from the melt. These difficulties arise from controlling the film thickness, the temperature of the cooling drum, etc. in an effort to obtain amorphous material.

Uniaxial and plane strain compression tests were conducted in order to explore the mechanical behavior of the material. Compression tests were chosen over tension tests because it is relatively easy to achieve a controlled homogeneous deformation in compression. In previous compression tests on thermoplastics conducted by Arruda and Boyce [18] test specimens were machined from bulk and the tests were conducted using Teflon sheets as a lubricant between the specimen and the compression platen surface, which proved to provide excellent conditions for obtaining homogeneous deformations thereby resulting in accurate true stress vs. true strain data. In the work by Zaroulis and Boyce [13], PET sheets of similar dimensions (~1.73*mm* thickness) were used. It was found that the relatively small thickness of the specimens posed a problem of specimen size, particularly when considering that the material was compressed to a true compressive strain of -1.75, which causes a height reduction of the order of 85%. Trial experiments on commercially available polycarbonate (PC) were used to determine that samples with an initial height to diameter ratio in the range of 0.4-1.1 provided identical stress vs. strain results

indicating little influence of specimen size and/or friction on the measurement. Using these results, an initial height to diameter ratio of 0.51 was chosen for the PET sheet. In order to provide a test specimen of reasonable height, it was determined that a stack of three disks was needed to make one uniaxial compression specimen. To achieve the 0.51 initial height to diameter ratio, disks of 12.38*mm* diameter were machined from the PET sheets. Also, to eliminate the possibility of slippage between the disks for the duration of the experiment, the two disk-disk interfaces were roughened with coarse grid sand paper. To reduce the amount of friction between the disk-compression platen interfaces, teflon sheets and a common lubricant, WD40, were used. In order to avoid the possibility of WD40 coming between the disks, the WD40 was only sprayed between the teflon sheets and the compression platens. It was found previously by Zaroulis and Boyce[13] that increasing the number of disks helped in eliminating friction effects at higher strains but also introduced larger interface effects in terms of the potential sliding of disks over one another. Therefore, it was found that stacking three disks was the best compromise. The uniaxial compression specimens were found to give nearly homogeneous deformations to a final true strain of -2.0. Uniaxial compression tests were performed with one, two and three layers of disks to determine if there was an appreciable difference in the stress behavior. Figure 2.1 shows the stress-strain curves for the tests performed with different layers at $90°C$ at a strain rate of -1.0/*s*. As the figure shows, the mechanical behavior is repeatable for all three layer variations.

Plane strain compression specimens were machined in a similar manner. Each plane strain compression specimen consisted of a stack of three squares, in order to keep the possible effect of the interfaces the same for both experimental conditions. The squares were machined from the PET sheets with sides measuring 9.55*mm*. The initial height to width ratio for these specimens were approximately 0.65. The plane strain compression

specimens were found to give nearly homogeneous deformations to a final true strain of -1.6. Uniformity of deformation was verified by allowing the specimen to cool under the applied deformation and then unloading and examining the specimen. The specimen showed uniform deformation. Upon examination of specimen deformations which had been unloaded and then cooled, the specimens were found to exhibit some curling and uneven contraction from the nonuniform cooling (i.e. temperature gradient during cooling). Plane strain compression tests were also performed with one, two and three layers of disks to determine if there was an appreciable difference in the stress behavior. Figure 2.2 shows the stress-strain curves for the tests performed with different layers at $90°C$ at a strain rate of $-1.0/s$. As the figure shows, the mechanical behavior is not repeatable for the three layer variations and the stress response increases as the number of layers increases. It must also be stated that the thickness of the specimen for the 1 layer experiment at the end of the loading process is of the order of the 4 sheets of teflon used between the specimen and the top and bottom of the channel die. Therefore it is suspected that the stress-strain behavior of the 1 layer curve is not only sampling the PET specimen but the teflon sheets as well. This was not the case in uniaxial compression since only two layers of teflon were used. It is therefore postulated that the true mechanical behavior of the material in plane strain compression is exhibited by the test with two or three layers or possibly somewhere in between. It is difficult to surmise whether the stress-strain curve for 2 layers is also sampling the 4 teflon sheets, and, due to the small temperature gradient that sometimes exists as a result of the cooling liquid of the bottom actuator of the Instron, it is difficult to tell whether the stress-strain curve for 3 layers is a result of perfectly uniform deformation for all three layers.

2.1.2 Description of Mechanical Tests

Uniaxial and plane strain compression tests over a range of strain rates and temperatures were conducted in order to measure the stress vs. strain behavior of PET as a function of strain state, strain rate, and temperature. The temperature range spans from $25°C$ to $105°C$ where the glass transition temperature, T_g, is approximately $79°C$. The strain rate range spans from the slow isothermal rate of -0.005/*s* to the fast adiabatic rate of -2.0/*s*. Compression modes were chosen over the tensile mode due to several inhomogeneities that occur in the tensile mode. At some temperatures, tension typically results in inhomogeneous deformations (i.e. necking) at finite strains. Also, uniform specimen temperature is more easily maintained in compression than in tension tests. Therefore, compression experiments provide excellent conditions for the uniform homogeneous deformations necessary in examining the material constitutive behavior.

The mechanical tests were performed on an Instron 1350 servohydraulic machine using a Pentium computer running LabVIEW, a common data acquisition and control software package. The tests were performed in the strain control mode with a 2620-824 Instron extensometer in order to eliminate the Instron load train compliance errors and obtain the best accuracy in the measurement of deformation at high levels of true strain. For the duration of each experiment, logarithmic strain was monitored as a function of time and fed back to the controller in order to alter the actuator displacement rate to provide constant strain rate conditions. For the elevated temperature experiments, a radiant furnace was used to bring the sample to the desired experimental temperature. The time required for the environment of the furnace to reach thermal equilibrium was between 15 and 20 minutes. There was concern that this "equilibrating time" might induce crystallization in the specimens even before compression. This was determined not to be the case by conducting a DSC scan on a specimen that had been warmed in the furnace for the same time duration but not compressed.

In the uniaxial compression experiments, the specimen temperature was monitored with four type-K thermocouples. Two thermocouples were cemented to both the top and bottom compression platen, with all four thermocouples spaced evenly about the circumference of the platens 90 degrees apart. In the plane strain compression experiments, only one thermocouple was needed, which was positioned inside the channel die fixture in contact with the specimen. The fact that the lower actuator head was cooled by the actuator fluid inside and the upper actuator head was not caused a temperature difference to develop between the two compression platens that manifested itself if the furnace was used for an extended period of time. This temperature difference was allowed to be no more than $2°C$ above or below the target temperature, at which point the testing was stopped and the upper actuator head allowed to cool.

Due to the range of the strain rates utilized in these experiments, the actual duration of the experiments varied from approximately 0.8 seconds for the -2.0/*s* rate, to 400 seconds for the -0.005/*s* rate. The inelastic nature of the deformation results in heat dissipation that may or may not produce a temperature rise in the specimen during the test, depending on the strain rate and the experimental temperature of the test. Obviously, the faster the rate of the experiment, the less time for heat transfer, thus the more important the adiabatic effects. Also, the higher the temperature, the smaller the value of the plastic work input to the sample, and hence the lower the temperature rise due to deformation. In this work, an experiment is classified as isothermal, thermomechanically coupled, or adiabatic by comparing the duration of the loading part of the experiment, t_{exp}, to the time required for the conduction of heat out of the specimen, t_{cond}. The first order analysis used to determine these classifications follows.

In the uniaxial compression experiments, the dominant mode of heat transfer during the course of the experiments is the conduction of heat from the uniaxially compressed

sample to the compression platens. Let h_{inst} be the instantaneous height of the specimen during a compression experiment. Then the characteristic length that controls the heat transfer is the distance from the platen to the center of the specimen, which is half the current specimen height, $h_{char}=h_{inst}/2$. Thus, the time required for heat to conduct out of the sample, t_{cond}, is given as:

$$t_{cond} = \frac{(h_{char}/2)^2}{2\kappa/\rho c} \tag{2.1}$$

where $\kappa = 0.218 W/mK$ is the thermal conductivity, $\rho = 1330 g/cm^3$ is the density of amorphous PET, and $c = 1300 J/kgK$ is the specific heat capacity[2]. For a constant strain rate test the loading time required to reach the final strain, t_{exp}, can be calculated by dividing the final strain, $\varepsilon_f = -2.0$ by the strain rate, $\dot{\varepsilon}$. Table 2.1 shows the heat transfer calculations for the uniaxial compression experiments. It can be seen that the experimental time is much longer than the conduction time for the -0.005/*s* and -0.01/*s* rates, hence the heat transfer conditions during those experiments are expected to be isothermal. Similarly, since the experimental time is about as long as the conduction time for the -0.05/*s* and -0.1/*s* rates, the heat transfer conditions during those experiments are expected to be thermomechanically coupled. Lastly, since the experimental time is much shorter than the conduction time for the -0.5/*s* strain rate and faster strain rates, the heat transfer conditions during these experiments are expected to be adiabatic.

$\dot{\varepsilon}(1/s)$	$t_{exp}(s)$	$t_{cond}(s)$	$\frac{t_{exp}}{t_{cond}}$	heat transfer condition
-0.005	400	9.837	40.7	isothermal

Table 2.1: Comparison of heat transfer conditions at different strain rates for Uniaxial Compression Experiments

2. Property values extracted from the Polymer Handbook [16]

$\dot{\varepsilon}(1/s)$	$t_{exp}(s)$	$t_{cond}(s)$	$\frac{t_{exp}}{t_{cond}}$	heat transfer condition
-0.01	200	9.837	20.3	isothermal
-0.05	40	9.837	4.1	coupled
-.01	20	9.837	2.0	coupled
-0.5	4	9.837	0.41	adiabatic
-1.0	2	9.837	0.203	adiabatic
-1.5	1.3	9.837	0.132	adiabatic
-2.0	1	9.837	0.102	adiabatic

Table 2.1: Comparison of heat transfer conditions at different strain rates for Uniaxial Compression Experiments

The same first order analysis can be applied to the plane strain compression experiments. In the plane strain channel die conduction occurs in two directions simultaneously: (1) to the side walls and (2) to the top and bottom of the steel plane strain fixture. The dominant heat transfer time is the smaller of the two conduction times, and, therefore, corresponds to the smaller of the two controlling dimensions, height and width. Since the height of the specimen is the smaller of the two controlling dimensions, the characteristic length that controls the heat transfer is the distance from the side wall of the channel die to the center of the specimen, which is half the instantaneous specimen height, $h_{char}=h_{inst}/2$. Thus the time required for heat to conduct out of the sample, t_{cond}, in the plane strain case is found using Equation 2.1 and is the same as in the uniaxial case since the initial specimen height was the same for both cases. Table 2.2 shows the heat transfer calculations for the plane strain compression experiments.

$\dot{\varepsilon}(1/s)$	$t_{exp}(s)$	$t_{cond}(s)$	$\frac{t_{exp}}{t_{cond}}$	heat transfer condition
-0.005	320	9.837	32.54	isothermal

Table 2.2: Comparison of heat transfer conditions at different strain rates for Plane Strain Compression Experiments

$\dot{\varepsilon}(1/s)$	$t_{exp}(s)$	$t_{cond}(s)$	$\frac{t_{exp}}{t_{cond}}$	heat transfer condition
-0.01	160	9.837	16.27	isothermal
-0.05	32	9.837	3.25	coupled
-0.1	16	9.837	1.63	coupled
-0.5	3.2	9.837	0.33	adiabatic
-1.0	1.6	9.837	0.16	adiabatic
-1.5	1.07	9.837	0.11	adiabatic
-2.0	0.8	9.837	0.08	adiabatic

Table 2.2: Comparison of heat transfer conditions at different strain rates for Plane Strain Compression Experiments

The temperature rise of the specimen for both the uniaxial and plane strain case for a fully adiabatic strain rate is a function of the strain. This temperature rise can be estimated by two methods using the true stress and true strain measured by the mechanical testing machine. The first method is a function of the current stress and strain:

$$\Delta T_1 = \frac{1}{\rho c_p}\int_0^{\varepsilon_f} \sigma \varepsilon d\varepsilon \tag{2.2}$$

The second method is a function of the initial yield stress, σ_{y_o}, and strain:

$$\Delta T_2 = \frac{1}{\rho c_p}\int_0^{\varepsilon_f} \sigma_{y_o} \varepsilon d\varepsilon \tag{2.3}$$

where ρ and c_p are the density of amorphous PET and the specific heat capacity, respectively, as given earlier. In this second method, the strain hardening process is not taken to be dissipative. For these two methods, in uniaxial compression at $90°C$, the approximate temperature rise due to adiabatic heating is $7°C$ for the first method and $1.5°C$ for the second method. It is also important to note that the exothermic nature of the crystallization that may be occurring with strain is also not taken into account. An increase in crystallinity from 5% to 31% would result in a temperature rise of about $14°C$.

2.1.3 Description of DSC Measurements

Differential Scanning Calorimetry was used to monitor the rate of change of specimen enthalpy as a function of increasing temperature at a given heating rate. Information on the microstructure and internal energy content of the material can be obtained from the DSC scan through proper data reduction and interpretation. Aspects of the DSC scan, for example the exact location of the glass transition temperature, are somewhat dependent on the imposed heating rate and the kinetic effects cannot be eliminated from the DSC readings. Thus, the heating rate must be chosen with care and only thermograms with the same rate should be compared with one another when interpreting the enthalpy content of a polymer. A compromise should be sought between a fast rate, which would cause non-uniform heating of the sample, and a very slow rate, which could cause sample aging in the DSC pan. Heating rates of 5-20$°C/min$ are typically used in testing with polymers[17]. For these reasons, DSC scans were performed at a rate of 10$°C/min$. DSC specimens with masses ranging from 3mg to 10mg were cut from the center of the deformed specimens using an Buehler Isomet low speed saw. Care was taken not to impart additional deformation to the specimens as they were cut. DSC specimens were cut from the centers of the deformed samples in order to eliminate any end effect phenomena from the compression tests on the subsequent DSC readings.

All DSC measurements were performed on a Perkin-Elmer DSC-7A with water as the cooling medium. The instrument was calibrated at the same heating rate with two known materials, indium and zinc. A baseline run was then conducted also at the same heating rate in order to measure the residual enthalpy rate between the reference and sample pans. The baseline was then subtracted from subsequent thermograms of the polymer specimens. A baseline run was conducted every few hours to take into account any possible heating of the cooling water. It must be noted that this quantitative analysis from DSC

thermograms requires fully corrected data. Elimination of residual enthalpy readings from the signal, normalization of the thermogram by the specimen weight, and an appropriate choice of integration limits is very important since the accuracy of the method is heavily dependent on the measurement of the crystallization and melting areas with respect to the fully corrected baseline[3]. With respect to the baseline, in many of the DSC thermograms taken the curves are slanted in an inconsistent manner due to the nonrepeatability of the baseline. However, the crystallinities calculated from the thermograms were found to be repeatable regardless of the slant of the thermogram. Great care was taken to conduct a baseline scan every couple of hours and to subtract the most recent baseline from each scan. Therefore, despite the fact that the baselines were not repeatable, the crystallinities calculated from the thermograms were repeatable. This is shown in greater detail in Appendix A.

DSC thermograms were taken on the as-received material as well as on the specimens deformed at different strain states, strain rates and temperatures in order to assess the effects of deformation conditions on crystallization. For all DSC thermograms, the strain level referenced for each thermogram refers to the applied strain in the corresponding mechanical compression test.

2.1.4 Description of Wide Angle X-ray Diffraction Measurements

Wide Angle X-ray Diffraction (WAXD) was used to analyze the structure and morphology developed in the specimens due to deformation. A Rigaku RU200 185*mm* Diffractometer was used to perform the x-ray diffraction measurements. Equatorial scans were conducted in the range of $2\theta = 10°–50°$ with intensity data collected every $0.1°$ for a period of 1 second. Since the deformation of the uniaxial compression specimens is

---

3. The several methods for the measurement of crystallinity such as N.M.R., X-ray diffraction, density etc. are covered comprehensively in reference [23].

axially symmetric, only two x-ray scans were performed on these specimens, whereas three scans were performed on the plane strain compression specimens. For uniaxial compression specimens the first scan was conducted in transmission, with the x-ray beam positioned perpendicular to the plane of the specimen (load direction, LD), and the second scan in reflection, with the x-ray beam positioned at a glancing angle to the plane of the specimen (flow direction, FD). For the plane strain compression specimens, the first scan was conducted in transmission, with the x-ray beam positioned perpendicular to the plane of the specimen and the specimen positioned in order to sample the constrained direction (CD). The second scan was also in transmission, with the x-ray beam also perpendicular to the plane of the specimen but with the specimen positioned in order to sample the flow direction (FL). The third scan was performed in reflection, with the x-ray beam positioned at a glancing angle to the plane of the specimen in order to sample the load direction (LD). For all WAXD measurements, the strain level referenced for each scan refers to the applied strain in the corresponding mechanical compression test.

2.2 Experimental Results

Results from the mechanical tests, the DSC measurements, and the WAXD measurements are presented here. Effects of strain rate, temperature and strain state are discussed separately for the uniaxial and plane strain mechanical tests. Cold crystallization phenomena and percent crystallinity are discussed for the DSC measurements. Evolution of crystallinity, size and number of crystallites are explored for the WAXD measurements.

2.2.1 Results from Mechanical Tests

Uniaxial compression and plane strain compression tests were conducted at temperatures of $25°C$ to $105°C$ and strain rates of -0.005/s to -2.0/s. Several tests were conducted at each testing condition to verify repeatability. These repeatability results can be found in Appendix B. The results of these tests are plotted in terms of true stress vs. true strain. The

true strain, ε, is defined as the natural logarithm of the current height, h, to the initial height, h_o, given as follows:

$$\varepsilon = \ln(h/h_o) \tag{2.4}$$

The true stress is the ratio of the current force F to the current area A:

$$\sigma = F/A \tag{2.5}$$

where the current area is calculated using the measured current height and assuming incompressibility of inelastic deformation.

Uniaxial compression tests: Figures 2.3 to 2.14 show the uniaxial compression loading-unloading curves at different strain rates at a temperature of $25°C$, $70°C$, $80°C$, $90°C$, $100°C$, and $105°C$, respectively, with a blow-up following each figure of the same curves to a strain of -1.0. The uniaxial compression tests at $25°C$ and $70°C$ were conducted to a final strain of -1.4 instead of -2.0 due to the capacity of the load cell on the Instron machine. The load capacity of the load cell is about $48kN$, which dictated the final strain that the experiments could be taken to. For the uniaxial compression tests conducted at higher temperatures ($80°C$ to $105°C$) however, the PET is softer, thereby permitting a final strain of -2.0 for those temperatures.

The deformation curves shown in Figure 2.3 and Figure 2.5 exhibit the behavior of a polymer in the glassy region, with blown-ups shown in Figures 2.4 and 2.6. Initially, the deformation is linear elastic with the stress increasing proportionally with strain. Then there is a nonlinear region prior to yield where the stress reaches a maximum. The yield stress increases with increasing strain rate. After yield the stress decreases with increasing strain, which is termed strain softening. This strain softening continues until it reaches a minimum, called the flow stress. The strain softening phenomena in uniaxial compression was also observed in PET as well as other glassy polymers: poly(methyl-methacrylate)

(PMMA), polystyrene (PS), and polycarbonate (PC) by Arruda and Boyce [18], Hasan and Boyce [19] and Zaroulis and Boyce [13]. After strain softening, a monotonic increase in the true stress with true strain is observed in the material, which is termed strain hardening. The strain hardening is observed to be nonlinear and increases slightly with increasing strain rate at the slower strain rates. At faster strain rates, the apparent amount of strain hardening decreases due to the adiabatic heating effect. The unloading profiles of the tests show that during unloading the material initially behaves in a linear elastic manner followed by nonlinear recovery.

As previously mentioned, the glass transition temperature, T_g, for this material is about $79°C$ as determined by DSC. Thus, as expected, the deformation curves for tests conducted at $90°C$, $100°C$ and $105°C$, shown in Figures 2.9 to 2.14, exhibit the behavior of a polymer in the rubbery region. The PET flows with no clearly apparent yielding. The adiabatic heating effect is also present at a deformation temperature of $90°C$ at the faster strain rates, but at $100°C$ and $105°C$ the adiabatic heating does not have as much of an effect.

The deformation curves at $80°C$ shown in Figures 2.7 and 2.8 exhibit the behavior of a glassy polymer at the faster strain rates and that of a rubbery polymer at the slower strain rates. This is as expected since the deformation temperature, $80°C$, is so close to the glass transition temperature. At very low strain rates the PET acts as a rubbery polymer with no apparent yielding, but at the higher strain rates, the PET acts as a glassy polymer with observable yielding and even some strain softening before strain hardening at higher strains. Since the deformation temperature is so close to T_g and T_g is rate dependent, the faster strain rates cause the material to act in a manner consistent with being below T_g (in the leathery region) and the slower rates cause the behavior to be consistent with being above T_g.

Effects of strain rate in uniaxial compression: At all deformation temperatures, the flow stress increases with increasing strain rate. At temperatures below and near the glass transition, the yield stress increases with increasing strain rate as seen in Figures 2.3 to 2.8. The initial strain hardening slope increases as the strain rate is increased, as can be seen in Figures 2.10, 2.12 and 2.14. At a strain of -1.0, the slope of the curves increases as the strain rate is increased. Also, as seen in Figures 2.7 to 2.14, the amount of strain hardening increases with increasing strain rate when the rates are isothermal, but as the tests become more adiabatic the strain hardening slope decreases. Therefore, at a given deformation temperature, the amount of strain hardening increases as the strain rate increases for isothermal tests. But as the tests become more adiabatic and there is less heat conducted out of the specimen to the platens, the apparent amount of strain hardening decreases due to the simultaneous occurrence of thermal softening. These findings prove to be consistent with the first order analysis presented earlier. When comparing Figures 2.7 and 2.9 to Figures 2.11 and 2.13, it can be seen that adiabatic heating has more of an effect at deformation temperatures of $80°C$ and $90°C$ than at $100°C$ and $105°C$. This is as expected since the adiabatic softening contribution decreases with increasing deformation temperatures.

The most interesting result comes from the deformation of PET in the rubbery regime shown in Figures 2.9 to 2.14. In the rubbery regime the plasticity mechanism is effectively inactive and hence the related phenomena, such as yield and strain softening, are nearly absent. The "yield" or flow stress is only on the order of $1MPa$. The most distinct difference between the rapid rates (-2.0/s, -1.5/*s*, -1.0/*s*, -0.5/*s*, -0.1/*s*, and -0.05/*s*) and the slow rates (-0.01/*s* and -0.005/*s*) occurs in the strain hardening behavior. The behavior at the high strain rates exhibits large strain hardening suggesting the presence of strain-induced crystallization or at least more effective molecular orientation. The hardening rate at the

low strain rates is lower than that observed at the lower temperatures ($25°C$ and $70°C$) suggesting a molecular relaxation process dominating as temperatures get higher and strain rates slower. These results are consistent with the experimental observations of Jabarin et. al. [11].

Effects of deformation temperature in uniaxial compression: Figures 2.15, 2.16, 2.17, and 2.18 show uniaxial compression in the rubbery region at $80°C$, $90°C$, $100°C$ and $105°C$ at strain rates of -0.005/*s*, -0.01/*s*, -0.1/*s*, and -1.0/*s*, respectively. It can be seen that as the deformation temperature increases the stress decreases. Also, as the deformation temperature increases the amount of recovery upon unloading decreases.

What is most interesting in these figures is the amount of strain hardening occurring with respect to temperature. The initial strain hardening slope increases as the temperature is decreased, as can be seen in Figures 2.15 to 2.18. At a strain of -1.0, the slope of the curves increases as the temperature is decreased. In Figures 2.15 and 2.16 the strain rates are isothermal. It can be seen that the deformations occurring at $100°C$ and $105°C$ at these low strain rates do not exhibit the dramatic upturn in the curve that signifies strain hardening. Whereas in Figures 2.17 and 2.18 at the higher strain rates, the deformation occurring at these same two temperatures does exhibit the upturn in the curve that signifies either a locking phenomenon with respect to molecular orientation and/or the occurrence of strain-induced crystallization. At all four strain rates, the deformation curves at $80°C$ and $90°C$ all exhibit strain hardening.

Plane strain compression tests: Figures 2.19 to 2.22 show the plane strain compression loading-unloading curves at different strain rates at a temperature of $25°C$, $80°C$, $90°C$ and $100°C$, respectively. The plane strain compression tests at $25°C$ were conducted to a final strain of -1.2 due to the capacity of the load cell on the Instron machine.

For the plane strain compression tests conducted at higher temperatures ($80°C$ to $100°C$) however, the PET is softer, thereby permitting a final strain of -1.6 for those temperatures.

As with the uniaxial compression tests performed at $25°C$ shown in Figure 2.3, the deformation curves in plane strain compression shown in Figure 2.19 exhibit the behavior of a polymer in the glassy region. Initially, the deformation is linear elastic with the stress increasing proportionally with strain. Then there is a nonlinear region prior to yield where the stress reaches a maximum. The yield stress increases with increasing strain rate. After yield the material strain softens. This strain softening continues until it reaches the flow stress. This strain softening phenomena in plane strain compression was also observed in PET by Zaroulis and Boyce [13]. After strain softening, the material strain hardens. The strain hardening is observed to be nonlinear and is slightly dependent on the strain rate. At faster strain rates, the amount of strain hardening decreases due to the adiabatic heating effect. The unloading profiles of the tests show that during unloading the material initially behaves in a linear elastic manner followed by nonlinear recovery.

As previously mentioned, the glass transition temperature, T_g, for this material is about $79°C$. Thus, as expected, the deformation curves shown in Figure 2.21 and Figure 2.22 exhibit the behavior of a polymer in the rubbery region. The PET flows with no apparent yield point.

As with the uniaxial compression curves at $80°C$ shown in Figure 2.7, the deformation curves shown in Figure 2.20 exhibit the behavior of a glassy polymer at the faster strain rates and that of a rubbery polymer at the slower strain rates. Again, this is as expected since the deformation temperature, $80°C$, is so close to the glass transition temperature. At the slower strain rates, the PET acts as a rubbery polymer with no apparent yielding, but at the higher strain rates, the PET acts as a glassy polymer with observable yielding and even some strain softening before strain hardening at higher strains. Since the

deformation temperature is so close to T_g, the faster strain rates cause the material to act as though it were below T_g in the leathery region.

Effects of strain rate in plane strain compression: At all deformation temperatures, the stress increases with increasing strain rate. At temperatures below and near the glass transition, the yield stress increases with increasing strain rate as seen in Figures 2.19 and Figure 2.20. Also, as seen in Figures 2.20, 2.21, and 2.22, the amount of strain hardening increases with increasing strain rate when the rates are isothermal, but as the tests become more adiabatic the strain hardening slope decreases. Therefore, at a given deformation temperature, the amount of strain hardening increases as the strain rate increases for isothermal tests. But as the tests become more adiabatic and there is more heat conducted from the specimen, the amount of strain hardening decreases. These findings prove to be consistent with the first order analysis presented earlier. When comparing Figures 2.20 to Figures 2.21 and 2.22, it can be seen that adiabatic heating has more of an effect at a deformation temperature of $80°C$. This is as expected since the adiabatic softening contribution decreases with increasing deformation temperatures.

The most interesting result comes from the deformation of PET in the rubbery regime shown in Figures 2.21 and 2.22. In the rubbery regime the plasticity mechanism is nearly inactive and hence the related phenomena, such as a prominent yield point followed by strain softening, are absent. In the figures, the initial strain hardening slope increases as the strain rate is increased. At a strain of ~1.0, the slope of the curves increases as the strain rate is increased. It can also be seen that the curves take a severe upturn at the onset of strain hardening and that this onset occurs at an earlier strain as the strain rate increases. This strain hardening response suggests strain-induced crystallization.

Effects of deformation temperature in plane strain compression: Figures 2.23, 2.24, 2.25, and 2.26 show the plane strain compression in the rubbery region at $80°C$, $90°C$

and $100°C$ at strain rates of -0.01/s, -0.1/s, -1.0/s and -2.0/s, respectively. The initial strain hardening slope increases as the temperature is decreased. Also, the onset of dramatic strain hardening occurs at a larger strain as the temperature increases. It is also evident that as the deformation temperature increases, the strain level at which the unloading portion of the curves reaches zero stress decreases. This is a measure of the recovery of the specimen after loading and unloading. Therefore, as the deformation temperature increases, the amount of recovery upon unloading decreases.

Effects of state of strain: Figures 2.27, 2.28 and 2.29 show a direct comparison between uniaxial and plane strain compression in the rubbery region for strain rates of -1.0/s, -0.1/s, and -0.01/s at deformation temperatures of $80°C$, $90°C$ and $100°C$, respectively. The deformation curves at $80°C$ show that the "yield stress" is slightly higher in plane strain compression than in uniaxial compression. It can be observed that for the same deformation conditions of temperature and strain rate, the plane strain stress is always greater than the uniaxial stress at any given strain. This is due to the fact that the deformation in uniaxial compression allows the material to flow in two directions, whereas the deformation in plane strain compression allows the material to flow in only one direction. The macromolecules are more constrained in plane strain compression, therefore the load required to move, align, and stretch them is more than the load required in uniaxial compression. It is also apparent from the figures that the strain hardening in plane strain is much more severe than in uniaxial compression. Again, this is attributed to the evolution in molecular orientation with state of strain for polymers that rem amorphous after deformation. These results have also been found by Arruda, et. al.[2] for PMMA and PC. In the case of PET, this difference in strain hardening is also attributable in part to strain-induced crystallization. The effects of deformation on the degree of crystallinity are evident from the DSC measurements discussed in the following section.

2.2.2 Results from Differential Scanning Calorimetry Measurements

DSC thermograms were taken on specimens in the as-received condition as well as specimens that had been loaded and unloaded in uniaxial and plane strain compression at different strain rates, to different final strains and at different temperatures. The DSC thermograms enable the assessment of percent crystallinity content through analysis of the cold crystallization behavior. Table 2.3 summarizes the data calculated from the DSC thermograms taken of the as-received specimen and the uniaxial compression specimens by giving the onset of the cold crystallization exotherm, T_{cc}, and the weight percent crystallinity, p_{cr}.

Mechanical Test Conditions	T_{cc} ($°C$)	p_{cr} (%)
As-received PET	137	10
Uniaxial, 25$°C$, $\dot{\varepsilon}$=-0.005/s, ε_f=-1.4	121	11
Uniaxial, 70$°C$, $\dot{\varepsilon}$=-0.005/s, ε_f=-1.4	117	11
Uniaxial, 80$°C$, $\dot{\varepsilon}$=-0.01/s, ε_f=-1.4	106	13
Uniaxial, 80$°C$, $\dot{\varepsilon}$=-1.0/s, ε_f=-1.4	112	11
Uniaxial, 80$°C$, $\dot{\varepsilon}$=-0.01/s, ε_f=-2.0	92	21
Uniaxial, 80$°C$, $\dot{\varepsilon}$=-1.0/s, ε_f=-2.0	108	24
Uniaxial, 90$°C$, $\dot{\varepsilon}$=-0.005/s, ε_f=-2.0	104	31
Uniaxial, 90$°C$, $\dot{\varepsilon}$=-0.1/s, ε_f=-2.0	97	33
Uniaxial, 90$°C$, $\dot{\varepsilon}$=-1.0/s, ε_f=-2.0	100	27
Uniaxial, 100$°C$, $\dot{\varepsilon}$=-0.005/s, ε_f=-2.0	124	11
Uniaxial, 100$°C$, $\dot{\varepsilon}$=-0.1/s, ε_f=-2.0	104	26
Uniaxial, 100$°C$, $\dot{\varepsilon}$=-1.0/s, ε_f=-2.0	117	37
Uniaxial, 105$°C$, $\dot{\varepsilon}$=-0.01/s, ε_f=-2.0	109	14
Uniaxial, 105$°C$, $\dot{\varepsilon}$=-0.1/s, ε_f=-2.0	98	30
Uniaxial, 105$°C$, $\dot{\varepsilon}$=-1.0/s, ε_f=-2.0	108	36
Uniaxial, 105$°C$, $\dot{\varepsilon}$=-2.0/s, ε_f=-2.0	108	37

Table 2.3: Uniaxial Compression data reduced from DSC thermograms

Table 2.4 summarizes the data calculated from the DSC thermograms taken of the plane strain compression mechanical test specimens.

Mechanical Test Conditions	T_{cc} (°C)	p_{cr} (%)
Plane Strain, 25°C, $\dot{\varepsilon}$=-0.01/s, ε_f=-1.2	102	14
Plane Strain, 25°C, $\dot{\varepsilon}$=-0.1/s, ε_f=-1.2	97	12
Plane Strain, 25°C, $\dot{\varepsilon}$=-1.0/s, ε_f=-1.2	92	24
Plane Strain, 80°C, $\dot{\varepsilon}$=-0.01/s, ε_f=-1.6	89	35
Plane Strain, 80°C, $\dot{\varepsilon}$=-0.1/s, ε_f=-1.6	88	36
Plane Strain, 80°C, $\dot{\varepsilon}$=-1.0/s, ε_f=-1.6	95	38
Plane Strain, 80°C, $\dot{\varepsilon}$=-2.0/s, ε_f=-1.6	97	38
Plane Strain, 90°C, $\dot{\varepsilon}$=-0.01/s, ε_f=-1.6	95	36
Plane Strain, 90°C, $\dot{\varepsilon}$=-0.1/s, ε_f=-1.6	98	36
Plane Strain, 90°C, $\dot{\varepsilon}$=-1.0/s, ε_f=-1.6	100	38
Plane Strain, 90°C, $\dot{\varepsilon}$=-2.0/s, ε_f=-1.6	102	41
Plane Strain, 100°C, $\dot{\varepsilon}$=-0.01/s, ε_f=-1.6	100	38
Plane Strain, 100°C, $\dot{\varepsilon}$=-0.1/s, ε_f=-1.6	104	40
Plane Strain, 100°C, $\dot{\varepsilon}$=-1.0/s, ε_f=-1.6	116	40
Plane Strain, 100°C, $\dot{\varepsilon}$=-2.0/s, ε_f=-1.6	119	41

Table 2.4: Plane Strain Compression data reduced from DSC thermograms

Figure 2.30 shows a standard thermogram resulting from a DSC thermogram of the as-received material. The thermogram shows the variation of heat flow into the sample as a function of increasing temperature at a constant heating rate of $10°C/min$ on the as-received PET sheet. At this heating rate, the glass transition temperature T_g is observed at approximately $79°C$. This value is consistent with the mechanical experiments performed at $80°C$ which show glass-like polymer behavior at fast strain rates and rubber-like behavior at slow strain rates. This behavior can be explained by time-temperature superposition, which states that a polymer in the vicinity of its glass transition is rubber-like with a

high compliance at higher temperatures or low strain rates and becomes glassy with a low compliance as the temperature is reduced or the strain rate increased [20]. The glass transition in Figure 2.30 does not exhibit a smooth enthalpic transition indicating that the material has undergone physical aging, which manifests itself as the endothermic overshoot at T_g. As the temperature is increased beyond T_g the material begins to crystallize in the DSC pan, where the onset of the cold crystallization exotherm, T_{cc}, is observed at $137°C$ at this heating rate and the area of cold crystallization, A_{cc}, is observed to be $-29J/g$. As the temperature increases even more, the crystals begin to melt at the onset of the melting endotherm, T_m, observed at $251°C$. The melting continues through the melting endotherm, reaching a peak maximum at $258°C$ and having a peak area, A_m, of $41J/g$.

Based on a two-phase (crystalline-amorphous) peak area method [22], the weight percent crystallinity of the material can be estimated. The weight percent crystallinity, p_{cr}, is given by:

$$p_{cr} = \frac{\Delta H_m - \Delta H_{cc}}{\Delta H_f} \tag{2.6}$$

where ΔH_{cc} is the enthalpy released during cold crystallization, ΔH_m is the enthalpy required for melting and ΔH_f is the enthalpy of fusion of PET crystals, taken to be equal to $120J/g$ [13]. The enthalpy released during cold crystallization is taken to be equal to the area of cold crystallization, $\Delta H_{cc} = A_{cc}$. Similarly, the enthalpy required for melting is taken to be equal to the area of the melting peak, $\Delta H_m = A_m$. Equation 2.4 gives an initial crystallinity for the as-received material of about 10%. This value for the crystallinity is inconsistent with the WAXD scan of the as-received material, which will be shown later. In the WAXD scan, there were no crystalline peaks, indicating no crystallinity in the as-received material.

DSC trends in uniaxial compression: Figure 2.31 shows the effect of deformation temperature in the glassy region. The figure shows the DSC thermograms of the as-received PET, and PET deformed at -0.005/*s* to a final strain of -1.4 at $25°C$ and $70°C$, respectively. It can be seen that as the deformation temperature increases, staying below the glass transition temperature, the cold crystallization peak shifts to the left as well as the glass transition. What is also noticeable is that the percent crystallinity does not increase to any significant degree due to these imparted strains. Thus it can be concluded that strain-induced crystallization does not occur at temperatures below the glass transition in uniaxial compression even at large strains where strain hardening is present, as shown in Figures 2.3 and 2.5. Therefore, the strain hardening observed in uniaxial compression below the glass transition is due to molecular orientation only.

Figure 2.32 shows the effect of different levels of final strain in the glass transition region of $80°C$. The figure shows the DSC thermograms of PET deformed in uniaxial compression to final strains of -1.4 and -2.0 at strain rates of -0.01/*s* and -1.0/*s*. It can be seen that the cold crystallization peak shifts to the left as well as becoming smaller as the final strain is increased. Also, as the strain rate is decreased the cold crystallization peak shifts to the left. It can also be observed that the glass transition has also shifted to the left for all four thermograms. The glass transition temperature for the deformations to a final strain of -2.0 is $76°C$, whereas the glass transition temperature for the deformations to a final strain of -1.4 is $74°C$, which is the same for the deformations performed at $25°C$ and $70°C$ shown in Figure 2.31. Thus, it can be concluded that the imparted final strain, and less dramatically the strain rate, determines how far the glass transition is shifted to the left from the as-received glass transition. Due to the decrease in the area of the cold crystallization peak as the imparted strain is increased, the percent crystallinity also increases. It can be seen that, at this deformation temperature, and probably at deformation

temperatures below $80°C$, the strain rate during deformation does not have much of an effect on the percent crystallinity content of the material and increases only slightly with increasing strain rate when the final strain is -2.0. The uniaxial compression deformation to a final strain of -1.4 does not seem to induce much increase in crystallinity whereas the deformation to a final strain of -2.0 seems to have induced a crystallinity increase to about 22%. This correlates with the strain hardening behavior shown in Figure 2.7. In the figure, for a strain of -1.4 not much strain hardening has occurred yet, but as the strain reaches -2.0 there is much more strain hardening occurring.

Figures 2.33, 2.34 and 2.35 show the DSC thermograms for various strain rates to a final strain of -2.0 at deformation temperatures of $90°C$, $100°C$ and $105°C$. At a deformation temperature of $90°C$, the different strain rates do not seem to have much of an effect on the percent crystallinity. The percent crystallinity is approximately 30% for all strain rates. This is not the case for deformation temperatures of $100°C$ and $105°C$ as shown in Figures 2.34 and 2.35, respectively. At $100°C$ the crystallinity content increases with increasing strain rate and at $105°C$ the crystallinity content increases from 14% to 30% as the strain rate is increased by just one order of magnitude. This correlates with the stress-strain curves presented earlier. Examination of the stress-strain curves in uniaxial compression at a deformation temperature of $90°C$ shown in Figure 2.9, one can see that at all strain rates, the curves exhibit strain hardening. Also, the percent crystallinity at a strain rate of -1.0/*s* is less than the crystallinities at strain rates of -0.005/*s* and -0.1/*s* due to the adiabatic heating effect. This is evident in the stress-strain curve in Figure 2.9. The curve for -1.0/*s* shows a decrease in the amount of strain hardening, thus manifesting itself as having lower percent crystallinity in the DSC thermogram. Figure 2.11 shows the stress-strain curves that pertain to the DSC thermograms in Figure 2.34 for uniaxial compression performed at $100°C$. In Figure 2.34 the crystallinity content increases for each

increase in strain rate. This correlates to the strain hardening behavior in the stress-strain curves. One can see an increase in the strain hardening slope as the strain rate increases from -0.005/*s* to -0.1/*s* and finally to -1.0/*s*. This manifests itself in the gradual increase in percent crystallinities at these strain rates as will be discussed in more detail later in the discussion section of this chapter. Figure 2.13 shows the stress-strain curves that pertain to the DSC thermograms in Figure 2.35 for uniaxial compression performed at $105°C$. In Figure 2.35 the crystallinity content is 14% for -0.01/s, which is not much greater than the as-received crystallinity of 10%. For the strain rate of -0.1/*s*, the crystallinity jumps to 30%, then for the strain rates of -1.0/*s* and -2.0/*s* the crystallinities are about the same at 36% and 37%, respectively. Again, this can be correlated to the slope of the strain hardening portion of the stress-strain curves which can be seen in Figure 2.13. At a strain rate of -0.01/*s* it can be seen that the curve does not exhibit the upturn that signals the level of strain hardening that is apparent in the curves at faster strain rates. Also, the fact that the stress-strain curves at strain rates of -2.0/*s* and -1.0/*s* are parallel explains why they have about the same percent crystallinity of 36% and 37%, respectively. The slope of the stress-strain curve at -0.1/*s* is less than the slopes of the curves at -2.0/*s* and -1.0/*s*, thus the percent crystallinity is lower.

In all of the DSC thermograms performed at $90°C$, $100°C$ and $105°C$ it is evident that as the area of the cold crystallization peak decreases due to strain-induced crystallization, the peak shifts more to the left until it is indistinguishable from the glass transition endotherm. It is important to note that, although the strain hardening behavior and the crystallization measurements correlate, it does not indicate which one causes the other.

DSC trends in plane strain compression: The plane strain compression DSC results show considerable increase in crystallinity when compared to the uniaxial compression results. Figure 2.36 shows the DSC thermograms performed on samples deformed in

plane strain compression at $25°C$ to a final strain of -1.2. It is observable from the thermograms that the crystallinity content is nearly the same for the isothermal rates of -0.01/*s* and -0.1/*s*, but increases at the higher strain rate of -1.0/*s* perhaps as a result of the rise in temperature due to the adiabatic heating. The rise in temperature from plastic dissipation is estimated to be approximately $46°C$ integrating over the entire stress-strain curve as shown in Equation 2.2, or $55°C$ integrating with the initial yield stress as shown in Equation 2.3. It is important to remember that these temperature rise calculations do not include any change in temperature from crystallization. Note that although strain-induced crystallization occurred at the high rate, the strain hardening behavior was similar for all rates as shown earlier in Figure 2.19.

Figures 2.37, 2.38 and 2.39 show the DSC thermograms of the plane strain specimens deformed to a final strain of -1.6 at strain rates of -0.01/*s*, -0.1/*s*, -1.0/*s* and -2.0/*s* at deformation temperatures of $80°C$, $90°C$ and $100°C$, respectively. It can be seen from these DSC thermograms that the crystallinity content increased from the straining at all temperatures and that the increase in crystallinity as the strain rate is increased is very slight. This can be correlated to the stress-strain curves shown in Figures 2.20 to 2.22. In these figures the strain hardening slopes slightly increase as the strain rate increases resulting in slightly increasing crystallinities with increasing strain rate. The average crystallinity after straining at each temperature was approximately 37% at $80°C$, 38.5% at $90°C$, and 40% at $100°C$. The increase in crystallinity content with increasing deformation temperature is a result of the greater mobility of the molecular chains at higher temperatures. It can be concluded that plane strain compression performed in the rubbery region to a final strain of -1.6 results in a large amount of strain-induced crystallization and that this crystallization increases very slightly as the strain rate increases and as the deformation temperature increases.

In order to determine if this large amount of strain-induced crystallization is dependent on the final strain imparted, an additional set of mechanical experiments were conducted. Figure 2.40 shows the stress-strain curves for plane strain compression experiments performed at $90°C$ to different levels of final strain of -1.0, -1.2, -1.4 and -1.6. Figure 2.41 shows the DSC thermograms of these experiments. It can be seen that even at a strain level as low as -1.0 the strain-induced crystallinity content is still about 37%. There is still ambiguity as to whether crystallization took place during straining or during the cool down period (i.e. an annealing effect). But, it is still observed that the strain-induced crystallization of PET occurs at a level of imparted strain lower than -1.0 in plane strain compression, where the stretch state for an imparted strain of -1.0 is $\lambda_1 = 0.37$, $\lambda_2 = 2.72$, and $\lambda_3 = 1.0$. This was also discovered by previous investigators Misra and Stein [6], and Jabarin [10]. Misra and Stein stretched strips of amorphous PET above the glass transition temperature and found that strain-induced crystallization only occurred if the samples were stretched past 80% elongation. This is equivalent to 0.6 true strain. Jabarin stretched strips of PET to a final nominal strain of 1.1 at three different strain rates and found that the strain-induced crystallization occurs when samples are stretched to amounts below the strain hardening region of the force-extension curve.

2.2.3 Results from Wide Angle X-ray Diffraction Measurements

WAXD scans were taken on a specimen in the as-received condition as well as specimens that had been loaded and unloaded in uniaxial and plane strain compression at different strain rates, final strains and temperatures. The WAXD scans enable the assessment of the nature and evolution of the texture, and thus the crystallinity, through comparison and analysis of the peaks corresponding to crystallographic planes. The WAXD scans conducted for the specimens are all shown in Appendix C.

The crystal structure of PET has a triclinic unit cell shown in Figure 2.42[27]. Figure 2.43 shows the triclinic unit cell structure with the crystallographic diffracting planes. The unit cell parameters are $a = 0.45nm$, $b = 0.59nm$, $c = 10.7nm$, $\alpha = 100°$, $\beta = 118°$ and $\gamma = 112°$ [21]. In the case of PET, chain slip can occur on the (100) plane, the (010) plane and the $(\bar{1}05)$ plane. For PET, the diffraction peaks at $2\theta = 17°$, $26°$, and $43°$ are identified with the crystallographic planes (010), (100), and $(\bar{1}05)$, respectively. The other diffraction peaks that might be of interest in PET at $2\theta = 16°$, $21°$, and $23°$ are identified with the crystallographic planes $(0\bar{1}0)$, $(1\bar{1}1)$, and $(\bar{1}10)$, respectively.

The WAXD scan of isotropic semi-crystalline PET in Figure 2.44[27] reveals a number of crystalline reflections. The PET specimen had been annealed at $190°C$ in order to crystallize the material. In Bellare, et. al[27], the PET had then been highly textured via plane strain compression at $190°C$. The WAXD scans of this fully textured semi-crystalline PET scanned perpendicular to the CD, FD, and LD directions are shown in Figure 2.45[27]. The scans in Figure 2.45 reveal increased diffracted intensity of the (100), (010), and $(\bar{1}05)$ planes in the three respective directions relative to the other crystal reflections. The LD scan indicates that the (100) plane is lying perpendicular to the load direction, the CD scan indicates that the (010) plane is lying perpendicular to the constrained direction, and the FD scan indicates that the $(\bar{1}05)$ plane is lying perpendicular to the flow direction. Figures 2.44 and 2.45 will serve as a reference to the WAXD scans performed in this investigation.

Figure 2.46 shows the WAXD scan of the isotropic as-received material. WAXD scans of amorphous solids are characterized by an almost complete lack of periodicity and a tendency to "order" only in the sense that the atoms are fairly tightly packed together and show a statistical preference for a particular atomic distance; the result is an x-ray scatter-

ing curve showing no distinct peaks and only one or two broad maxima[22]. When compared to the peaks in the scan of the isotropic semi-crystalline PET in Figure 2.44, one can see how the amorphous material lacks any periodicity. Figure 2.47[28] shows typical WAXD scans of other amorphous polymers. These scans indicate that the scans conducted on the as-received PET shown in Figure 2.46 are scans typical of an amorphous polymer, as expected.

In Figure 2.46, the scan in the flow direction (FD) is a scaled version of the scan in the load direction (LD). This is expected due to the isotropic nature of the material. The FD scan intensity is on a smaller scale than the LD scan intensity because the FD scan is performed in reflection whereas the LD scan is performed in transmission, in which the x-rays measured travel through the material rather than reflecting off of it.

WAXD results in uniaxial compression: WAXD scans were performed on specimens that were uniaxially compressed at: (1)$80°C$ to a final strain of -2.0 at a strain rate of -0.01/*s*, and (2)$80°C$ to a final strain of -1.4 at a strain rate of -0.01/*s*. As shown in the DSC scans of Figure 2.32, increasing the final strain from -1.4 to -2.0 at a deformation temperature of $80°C$ increases the crystallinity content to 20%. The stress-strain curves corresponding to these scans are shown in Figure 2.7. The WAXD scans were performed in both the through and edge directions and can be seen compared to the scans of the as-received material in Figure 2.48. The specimens deformed at $80°C$ depict an evolution in the packing and a developing bias with direction, thus indicating molecular orientation. The figure shows that the broad peak in the load direction decreases from the as-received scan, whereas the broad peak in the flow direction increases from the as-received scan. This is indicative of the molecular orientation occurring with increasing strain level. However, these scans do not exhibit any peaks and thus indicate no crystallinity. According to the corresponding DSC scan in Figure 2.32, the crystallinity of the specimen deformed at

$80°C$ to a final strain of -2.0 at a strain rate of -0.01/*s* has a degree of crystallinity of 20%. While DSC and WAXD data generally do not agree precisely with regard to measuring the percent crystallinity, the discrepancy evident here between the DSC indicating a crystallinity of 20% and the WAXD indicating alignment but no crystallinity (evidenced by the absence of distinct peaks) is quite disturbing. There are a few possible explanations for this discrepancy:

- One explanation would be that the DSC is more sensitive to the presence of the crystals and is indeed providing a more accurate indication of crystallinity development. If this is the case, then the WAXD is not detecting a rather important level of crystallinity which is possible if the crystals formed are very small.
- An alternative explanation is that the WAXD data is correct and that while there is molecular orientation, there is no crystallinity. The DSC data must then be indicating that the preferential orientation and packing leads to a reduction in the crystallization enthalpy.

Both of these explanations are reasonable, yet directly in conflict with one another. Thus, there is ambiguity regarding the matter of whether the $80°C$ uniaxial compression specimens did or did not undergo strain-induced crystallization. It is clear, however, that molecular orientation and packing did occur. The investigation conducted by Jabarin [10] found similar results in their WAXD and DSC measurements of PET stretched at $100°C$ at 50.8*mm/s* with no annealing. Jabarin's results indicated an increase in crystallinity as measured by DSC but a WAXD scan with no distinct peaks, indicating no crystallinity.

In contrast to the $80°C$ uniaxial compression WAXD scans, the WAXD scans for the deformation conducted at $90°C$ in Figure 2.49 show the beginnings of the peaks indicative of semi-crystalline PET, clearly indicating the presence of crystallinity. The DSC

measured crystallinity content of the specimen deformed at $90°C$ was about 33%. This manifests itself as the peaks clearly seen in Figure 2.49. In order to help in the understanding of the directions of deformation in Figure 2.49 and in later figures, a schematic of the deformation directions are shown in Figure 2.50, indicating the flow and load directions for uniaxial compression and the flow, load, and constrained directions for plane strain compression. In Figure 2.49, the development of a prominent (100) peak in the load direction (LD) along with the development of a prominent (010) peak in the flow direction (FD) indicates that the material crystallizes in a preferential texture that is consistent with the development of molecular orientation. Under uniaxial compression, a biaxial orientation develops with strain which tends to align the molecular chains normal to the direction of the load. The (100) plane is perpendicular to the LD indicating that the crystals are aligned with their chain direction perpendicular to the LD and, in particular, with the benzene ring of the molecular chains lying flat in the plane.

Figure 2.51 shows the WAXD scans performed on specimens uniaxially compressed at $100°C$ to a final strain of -2.0 at strain rates of -0.005/*s*, -0.1/*s*, and -1.0/*s*. In the figure, the evolution of the texture with increasing strain rate can be seen. The peaks become more defined and apparent, evolving from the amorphous oriented pattern at -0.005/*s* to the peaks signifying crystallinity at -1.0/*s*. As in the WAXD scans performed on the specimen deformed at $90°C$ in Figure 2.49, the deformation at $100°C$ results in the (100) planes of the crystals lying perpendicular to the load direction (LD), and the (010) and $(\bar{1}05)$ planes of the crystals lying parallel to the load direction. Figure 2.52 shows how the crystals are oriented in a uniaxially compressed specimen that has undergone crystallization. The (100) planes of the crystals are oriented perpendicular to the load direction, and the (010) and $(\bar{1}05)$ planes are oriented randomly perpendicular to the flow direction. Increased intensity of the prominent reflections is observed in specimens deformed at

higher strain rates. This leads to the conclusion that the crystallinity increases as the strain rate increases. This is the same conclusion reached from the DSC scans of the same specimens shown in Figure 2.34. In the DSC scans the crystallinity content calculated increased as the strain rate increased.

WAXD results in plane strain compression: In Figure 2.53 the WAXD scans of the specimen deformed in plane strain compression at $80°C$ to a final strain of -1.6 at a strain rate of -0.1/s are shown. These WAXD scans show several prominent peaks clearly indicating the presence of crystallinity. The DSC crystallinity content of this specimen was about 36% as shown in Figure 2.37. The WAXD scans in Figure 2.53 show a prominent (100) peak in the load direction (LD), a prominent (010) peak in the constrained direction (CD), and a prominent $(\bar{1}05)$ peak in the flow direction (FD). While this preferential crystallographic texture differs from that observed in specimens deformed by uniaxial compression, it is consistent with the manner in which molecular orientation develops under these loading conditions. In the CD curve in Figure 2.53, the (010) crystallographic reflection is prominent, indicating that the (010) plane of the crystals is oriented perpendicular to the constrained direction. In the FD curve, the $(\bar{1}05)$ crystallographic reflection is very prominent, indicating that the $(\bar{1}05)$ plane of the crystals is oriented perpendicular to the flow direction. In the LD curve, the (100) crystallographic reflection is very prominent, indicating that the (100) plane of the crystals is oriented perpendicular to the load direction. These orientations make sense if one thinks of the unit cell in Figure 2.43 as one typical crystal. The crystal orientations in a specimen that undergoes crystallization in plane strain compression are shown in Figure 2.54. The deformation results in the (100) plane lying perpendicular to the load direction and parallel to the compression platens (making the benzene rings parallel to the compression platens), the (010) plane lying perpendicular to the constrained direction and parallel to the walls of the channel die, and the $(\bar{1}05)$

plane lying perpendicular to the flow direction and perpendicular to both the compression platens and the channel walls thus showing the chain direction of the crystals to be in the flow direction.

A similar texture was observed in the WAXD scans of the semi-crystalline PET which had been fully textured by plane strain deformation shown earlier in Figure 2.45. Although the two textures of Figures 2.45 and 2.53 are similar, they were obtained by different processing routes. In Figure 2.45, the material began in an isotropic semi-crystalline state and was then deformed. Therefore, the crystallographic texture had evolved from one of randomly oriented crystals to one of preferentially oriented crystals. Alternatively, in Figure 2.53, the material began in an isotropic amorphous state. The deformation acted to preferentially orient the amorphous molecular network which then led to the crystallization where the crystallization occurred in a preferential crystallographic orientation consistent with molecular orientation.

In Figure 2.55 the WAXD scans of specimens deformed in plane strain compression at $90°C$ to a final strain of -1.6 at strain rates of -0.01/s, -0.1/s, and -1.0/s are shown in the constrained, flow, and load directions respectively. As was shown in the WAXD scans of uniaxial compression at $100°C$ in Figure 2.51, the crystalline peaks become more defined and apparent as the strain rate is increased. As in the WAXD scans performed on the specimen deformed at $80°C$ in Figure 2.53, the deformations at $90°C$ result in the (100) plane of the crystals lying perpendicular to the load direction, the (010) plane of the crystals lying perpendicular to the constrained direction, and the $(\bar{1}05)$ plane of the crystals lying perpendicular to the flow direction. The increase in strain rate results in more diffraction from crystallographic planes thereby increasing the intensity of these reflections. Thus Figure 2.55 shows that the crystallinity increases with increasing strain rate. This increase in crystallinity with increasing strain rate agrees with the DSC scans on the same speci-

mens shown in Figure 2.38, although the WAXD scans show this increase in crystallinity more dramatically than the DSC scans do.

Figure 2.56 shows the WAXD scans of specimens deformed in plane strain compression at $90°C$ at a strain rate of $-0.1/s$ to final strains of -1.0, -1.2, -1.4, and -1.6. As can be seen in the figure, the crystalline peaks become more defined and apparent as the strain is increased. The development of texture found in Figure 2.55 for increasing strain rates also applies in this figure for increasing levels of final strain. The deformations result in the (100) plane of the crystals lying perpendicular to the load direction, the (010) plane of the crystals lying perpendicular to the constrained direction, and the $(\bar{1}05)$ plane of the crystals lying perpendicular to the flow direction. The increase in final strain level results in more diffraction from crystallographic planes thereby increasing the intensity of these reflections. Therefore, the crystallinity increases with increasing levels of final strain. This increase in crystallinity does not agree with the DSC scan on the same specimens shown in Figure 2.41. The discrepancy between the DSC scans in Figures 2.38 and 2.41 and their WAXD counterparts in Figures 2.55 and 2.56 is most likely due to the difficulty in deciphering the cold crystallization area at high crystallinity content in the DSC scans. These cold crystallization peaks are very small and blend with the glass transition endothermic overshoot, making it difficult to measure their areas.

Figure 2.57 shows the WAXD scans of specimens deformed in plane strain compression at a strain rate of $-0.1/s$ to a final strain of -1.6 at deformation temperatures of $80°C$, $90°C$ and $100°C$. The scans in the CD and the LD show marked differences in texture with respect to deformation temperature, whereas the scan in the FD does not show much of a difference. The CD and LD scans show that the specimen deformed at $80°C$ exhibits less texture, and therefore less crystallinity, than those deformed at $90°C$ and $100°C$. The specimens deformed at $90°C$ and $100°C$ exhibit well-defined peaks for both the (010)

and $(\bar{1}10)$ crystallographic reflections in the CD scans indicating that these planes in the crystals are oriented perpendicular to the constrained direction and that there is more diffraction from these planes as the deformation temperature is increased from $80°C$. In the LD scan, the (100) peak becomes more defined as the deformation temperature is increased, indicating that the (100) plane is oriented perpendicular to the load direction and that there is more diffraction from this plane as the deformation temperature is increased. According to the DSC scans for these specimens shown in Figure 2.58, the crystallinities at these temperatures are 36% for $80°C$, 36% at $90°C$ and 40% for $100°C$. This agrees with the WAXD scans which show that the peaks are more defined at $100°C$ than at $80°C$ or $90°C$. This trend is best observed in the LD scan.

The greater degree of texture resulting from plane strain compression than from uniaxial compression allowed the crystallite widths to be calculated from the WAXD scans in the three crystallographic directions for the plane strain compression specimens. The crystallite width is measured in a direction perpendicular to a particular set of reflecting planes. The width of the diffraction peak increases as the thickness of the crystallite decreases. The width of the crystallite can be calculated with the Scherrer equation:

$$w = \frac{0.9\lambda}{B\cos\theta_B} \tag{2.7}$$

where $\lambda = 1.54nm$ is the wavelength of the x-rays, B is the full width at half peak maximum (also known as FWHM), and θ_B is the Bragg angle[24]. After WAXD scans were taken of the plane strain specimens, JADE, a data analysis software package for x-ray diffraction curves, was used to determine B and θ_B. Using the values of B and θ_B from JADE, the crystallite widths could be calculated. In the WAXD scans for the plane strain specimens, the (010) plane was most evident in the CD scan, the $(\bar{1}05)$ plane was most evident in the FD scan, and the (100) plane was most evident in the LD scan, therefore the

crystallite width corresponding to each plane was calculated using the appropriate scan. Before discussing the WAXD scans performed for this investigation, it is important to review the reference scans in Figures 2.44 and 2.45 of isotropic semi-crystalline PET and fully textured semi-crystalline PET, respectively. A rough estimate was calculated of the crystallite widths from these WAXD scans. For the isotropic case, the crystallite width is about $12nm$ in the (100) plane and also about $12nm$ in the (010) plane. The peak for the $(\bar{1}05)$ plane is barely discernible to calculate a crystallite width. For the fully textured case, the crystallite width is about $10nm$ in the (100) plane, about $15nm$ in the (010) plane and about $13nm$ in the $(\bar{1}05)$ plane.

Figure 2.55 shows the crystallite widths as a function of strain rate and scan direction for specimens deformed at 90 $°C$ to a final strain of -1.6. For each of the scan directions, the crystallite widths are about the same regardless of strain rate. This shows that the increasing crystallinity with increasing strain rate, as evidenced by the increasing peak definition with increasing strain rate discussed earlier and by the DSC results in Figure 2.38, is due to an increase in the number of crystallites rather than an increase in the size of the crystallites.

Figure 2.56 shows the crystallite widths as a function of final strain level and scan direction for specimens deformed at 90 $°C$ at a strain rate of $-0.1/s$. For each of the scan directions, the crystallite widths are about the same regardless of strain level. This also shows that the increase in crystallinity with increasing strain level, as evidenced by the increasing peak definition with increasing strain level discussed earlier and by the DSC results in Figure 2.41, is also due to an increase in the number of crystallites rather than an increase in the size of the crystallites.

Figure 2.57 shows the crystallite widths as a function of deformation temperature and scan direction for specimens deformed at a strain rate of $-0.1/s$ to a final strain of -1.6. The

figure shows that the crystallite widths for the $100°C$ specimens differ markedly from the crystallite widths for the $80°C$ and $90°C$ specimens. It seems that at $100°C$, the crystallite widths are greater in the (010) and (100) planes, but smaller in the $(\bar{1}05)$ plane when compared to $80°C$ and $90°C$. This seems to suggest that, well into the rubbery region, the crystallite size changes as the deformation temperature is increased and that this change is characterized by an increase in the crystallite width in the (010) and (100) planes but a decrease in the crystallite width in the $(\bar{1}05)$ plane.

The crystallite widths found in Figures 2.55, 2.56 and 2.57 are in agreement with the range of crystallite widths found by Salem[25] and Peszkin and Schultz[26]. Peszkin and Schultz[26] found the crystallite widths in PET fibers that had been annealed for different lengths of time at $100°C$ under tension to be in the range of $3nm$ to $5nm$. Salem [25] found the crystallite widths in PET films that had been stretched at $90°C$ at different strain rates to be $2.3nm$ to $3.0nm$ normal to the (100) planes and $2.8nm$ to $4.0nm$ normal to the (010) planes.

Texture in uniaxial compression vs. plane strain compression: In plane strain compression, the texture that develops is similar to the texture that develops in uniaxial compression. In both uniaxial and plane strain compression, the (100) plane is oriented perpendicular to the load direction. However, in uniaxial compression, the (010) plane is oriented perpendicular to the direction of flow, whereas in plane strain compression it is oriented perpendicular to the constrained direction. Physically, this is interpreted in the following manner. Within the plane strain compression specimens, the (100) planes of the crystals are parallel to the compression platens, the (010) planes are parallel to the channel die walls and the $(\bar{1}05)$ planes are parallel to the free end of the channel die. However, within the uniaxial compression specimens, the (100) planes of the crystals are also parallel to the compression platens, but the (010) planes lie perpendicular to the compression

platens and in random directions. In both uniaxial and plane strain compression, the chains axes go in the direction of flow. The differing crystal orientations in each case can be seen by comparing the crystals shown in Figure 2.52 for uniaxial compression to the crystals shown in Figure 2.54 for plane strain compression. Therefore, in plane strain compression, the crystals lie in all three directions in the same way, whereas, in uniaxial compression, the crystals lie in only one direction the same way, the load direction, and lie randomly in the other two directions.

This leads to the question of what texture would develop in a specimen that undergoes crystallinity by plane strain compression and is then subjected to stretching in the previously constrained direction. It is postulated that the texture that would develop would be very similar to the texture in the uniaxial compression specimens. The orientation of the (100) planes would not change, but the orientation of the (010) and the $(\bar{1}05)$ planes would become randomized, resembling the texture of a uniaxial compression specimen.

2.3 Discussion and Conclusions

The mechanical tests and the microstructural analyses conducted by DSC and WAXD show that the mechanical behavior of PET is a strong function of deformation temperature, strain rate and strain state. The following trends can be observed from the data shown in the previous sections.

- In uniaxial and plane strain compression, at fixed deformation temperatures below the glass transition, as the imparted strain increases the material deforms elastically, yields, strain softens, flows and eventually strain hardens. As the deformation temperature increases and/or the strain rate decreases, the elastic modulus, yield stress and flow stress decrease. DSC scans show that strain-induced crystallization does not occur in uniaxial compression in specimens deformed at these glassy temperatures,

even at rapid strain rates and large final strains. However, the DSC scans of the specimens deformed in plane strain compression at $25°C$ exhibit an increase in crystallinity only at the fastest strain rate signifying either a locking phenomenon with respect to molecular orientation and/or the occurrence of strain-induced crystallization at room temperature at very rapid strain rates. However, the stress-strain curve at this temperature and strain rate did not exhibit an increase in strain hardening.

- At a deformation temperature of $80°C$, which is in the leathery region, the deformation is very strain rate dependent. In both uniaxial and plane strain compression, the stress-strain curves at the rapid strain rates exhibit the behavior of a polymer deforming below T_g in the leathery region, with an apparent yield phenomenon, whereas the stress-strain curves at slow strain rates exhibit the behavior of a polymer deforming above T_g in the leathery region, with no yield stress at all. The strain hardening slopes increase as strain rate is increased, but then decrease at faster strain rates due to the adiabatic heating effect. DSC scans show that an increase in crystallinity content does occur in uniaxial compression at $80°C$ but only after a strain of -1.4. However, WAXD scans do not show that any crystallization has occurred in uniaxial compression at this deformation temperature and strain level. Two possible explanations were given to explain this discrepancy, however, it is clear that molecular orientation and packing does occur at this deformation temperature and strain level. DSC and WAXD scans of specimens deformed at $80°C$ in plane strain compression, however, both exhibit marked increases in crystallinity content. The DSC and WAXD scans also show that there is a very slight increase of crystallinity with strain rate.
- The most interesting results were obtained in the rubbery region at deformation tem-

peratures of $90°C$ and above. The uniaxial and plane strain stress-strain curves exhibit increasing strain hardening slopes with increasing strain rate until adiabatic heating causes the strain hardening slopes to decrease at the higher strain rates. Due to more severe chain orientation, the plane strain compression curves exhibit much more strain hardening than the uniaxial compression curves. DSC scans of the uniaxial specimens showed that an increase in crystallinity content does occur at these deformation temperatures, but they also showed that at the same strain rates and final strains, the crystallinities at $90°C$ were about the same regardless of strain rate, whereas at $100°C$ and $105°C$ the crystallinities were an increasing function of strain rate. This makes sense when the stress-strain curves for these specimens are reviewed to find that this correlates with the amount of strain hardening that has occurred at these deformation temperatures and strain rates. The crystallinity at each strain rate at $90°C$ was about the same correlating to the fact that they had all undergone some strain hardening, but at $100°C$ and $105°C$ at the slower strain rates there is very little strain hardening correlating to very little crystallinity. The DSC scans of the plane strain specimens exhibited not only a large increase in crystallinity content, but that this crystallinity content increased only slightly with increasing strain rate. The WAXD scans exhibited much more strain rate dependence in the crystalline peaks. Mechanical tests, DSC scans and WAXD scans also showed that, in plane strain, the increase in crystallinity occurs before a final strain of -1.0 at $90°C$ and that the percent crystallinity increases with increasing final strain.

- The WAXD scans showed that there is a difference in the resulting crystallographic textures between uniaxial compression and plane strain compression. In plane strain

compression, the crystals lie in all three directions in the same orientation, whereas, in uniaxial compression, the crystals lie in only one direction in the same orientation, the load direction, and lie randomly in the other two directions. However, in both cases, the chains axes go in the direction of flow. It was also postulated that the texture that would develop in a specimen that undergoes crystallinity by plane strain compression and then is subjected to stretching in the previously constrained direction, would be very similar to the texture in the uniaxial compression specimens. The orientation of the (100) planes would not change, but the orientation of the (010) and the $(\bar{1}05)$ planes would become randomized, resembling the texture of a uniaxial compression specimen.

The strain rate, strain state and temperature dependence of the material behavior of PET play an integral role during the processing of the material. It is important to be able to predict the mechanical behavior of the material in order to reduce cost and material waste. Therefore, it is important that a constitutive model of the mechanical behavior of the material be able to capture the essence of the strain rate, strain state and temperature dependencies. In the next chapter, the development of a constitutive model which captures these dependencies is developed.

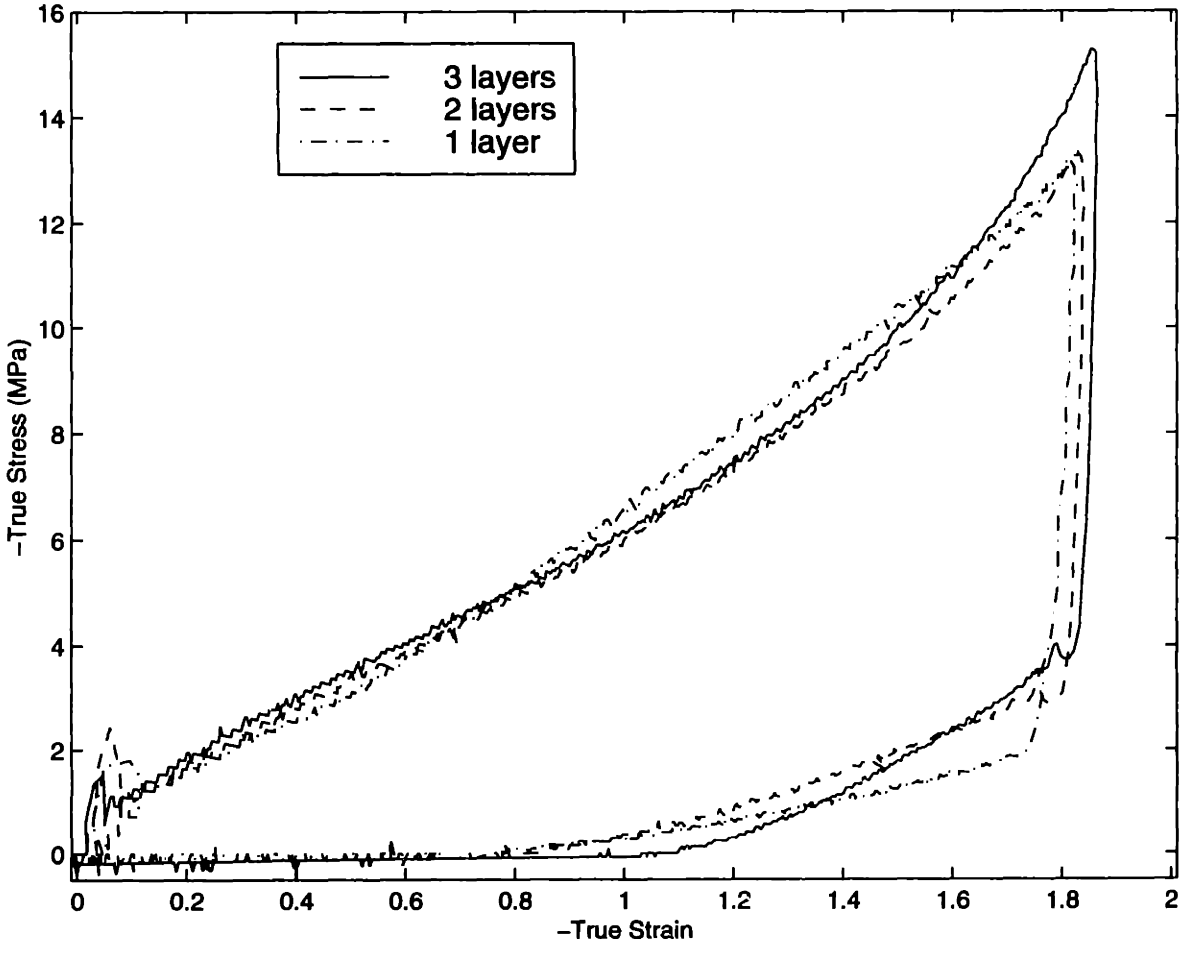

Figure 2.1: Uniaxial Compression tests, comparison of tests performed with various layers of PET. Tests performed at $90°C$ at a strain rate of -1.0/*s*.

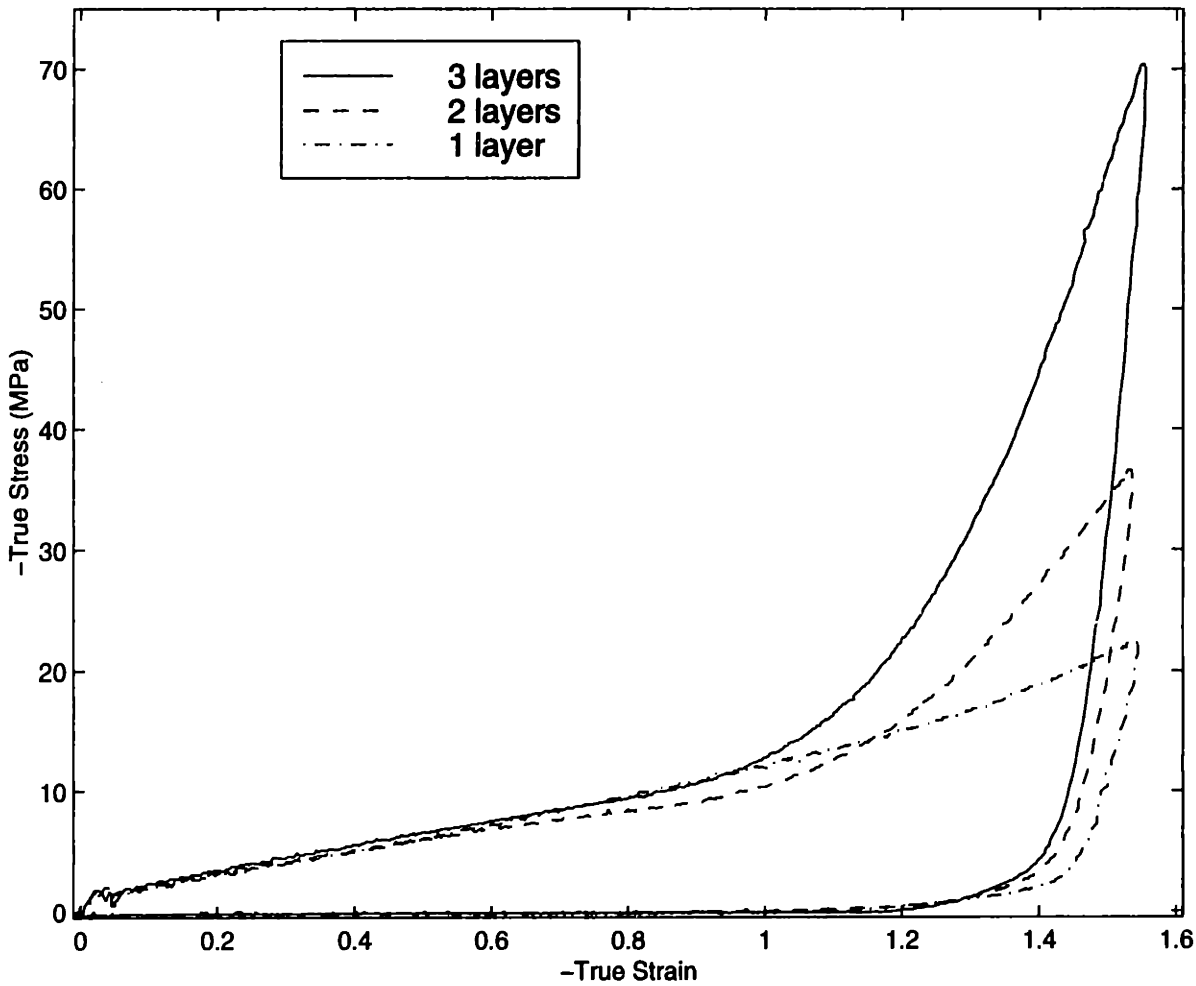

Figure 2.2: Plane Strain Compression tests, comparison of tests performed with various layers of PET. Tests performed at $90°C$ at a strain rate of -1.0/s.

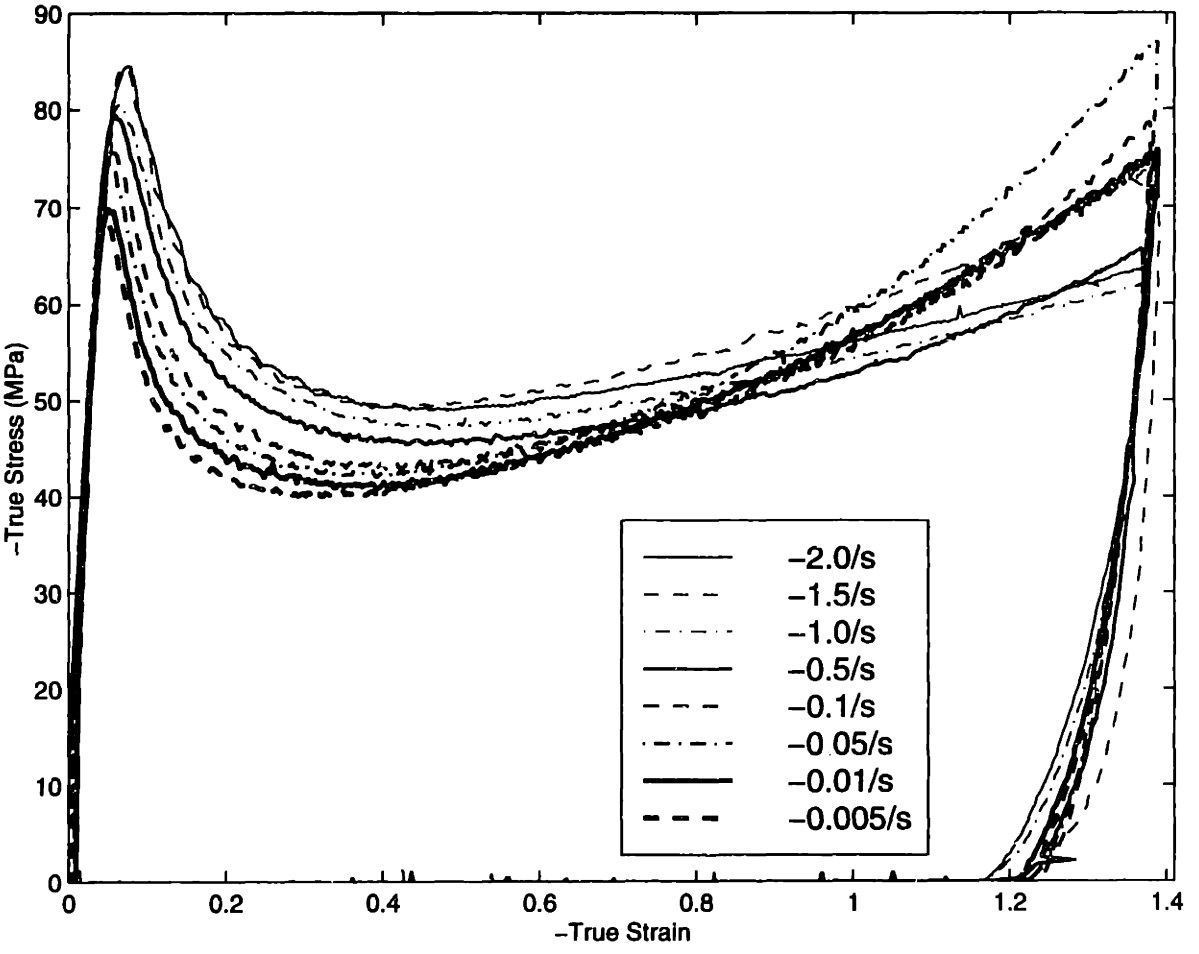

Figure 2.3: Uniaxial Compression Data, Temperature = $25°C$

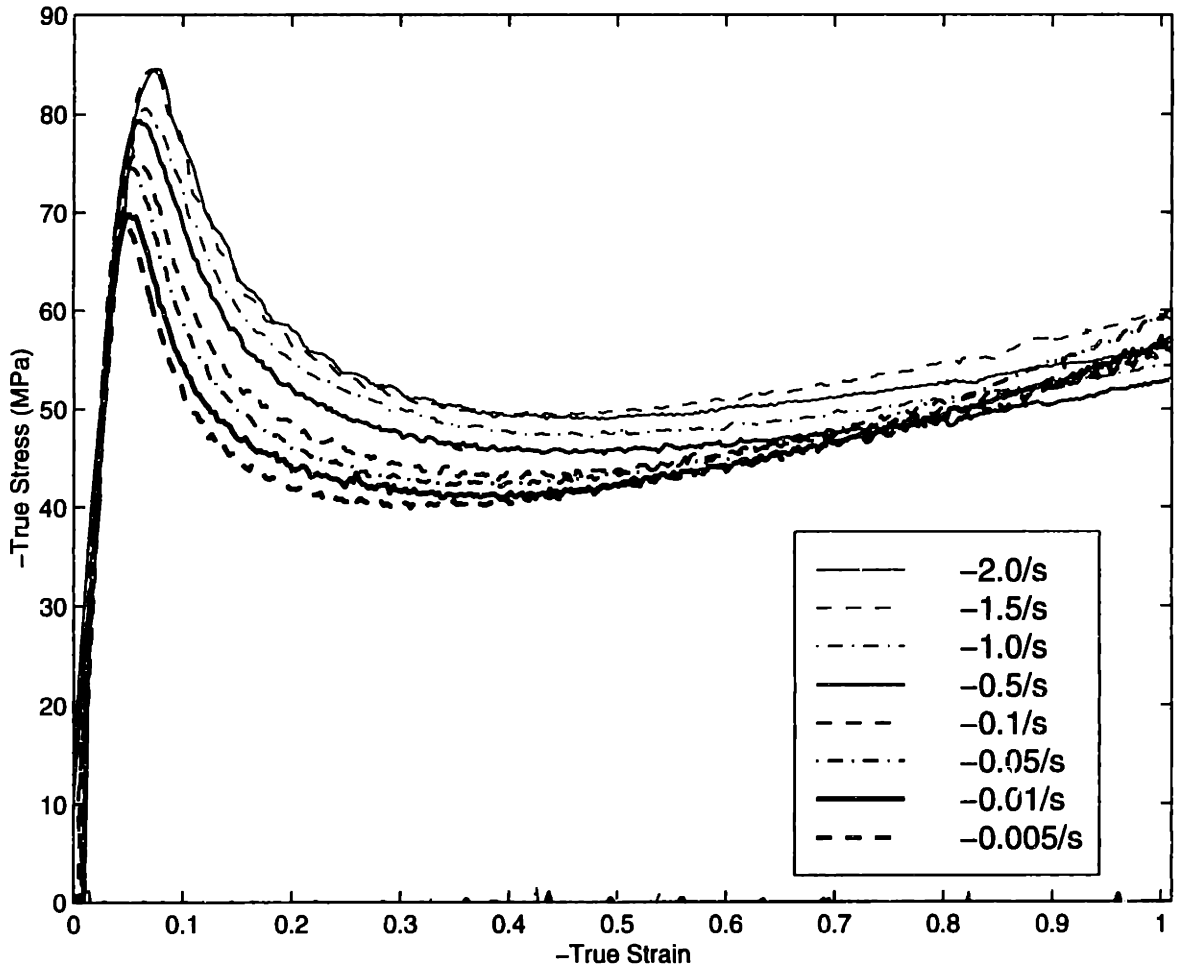

Figure 2.4: Uniaxial Compression Data, Temperature = $25\,^{\circ}C$, blown up to a final strain of -1.0

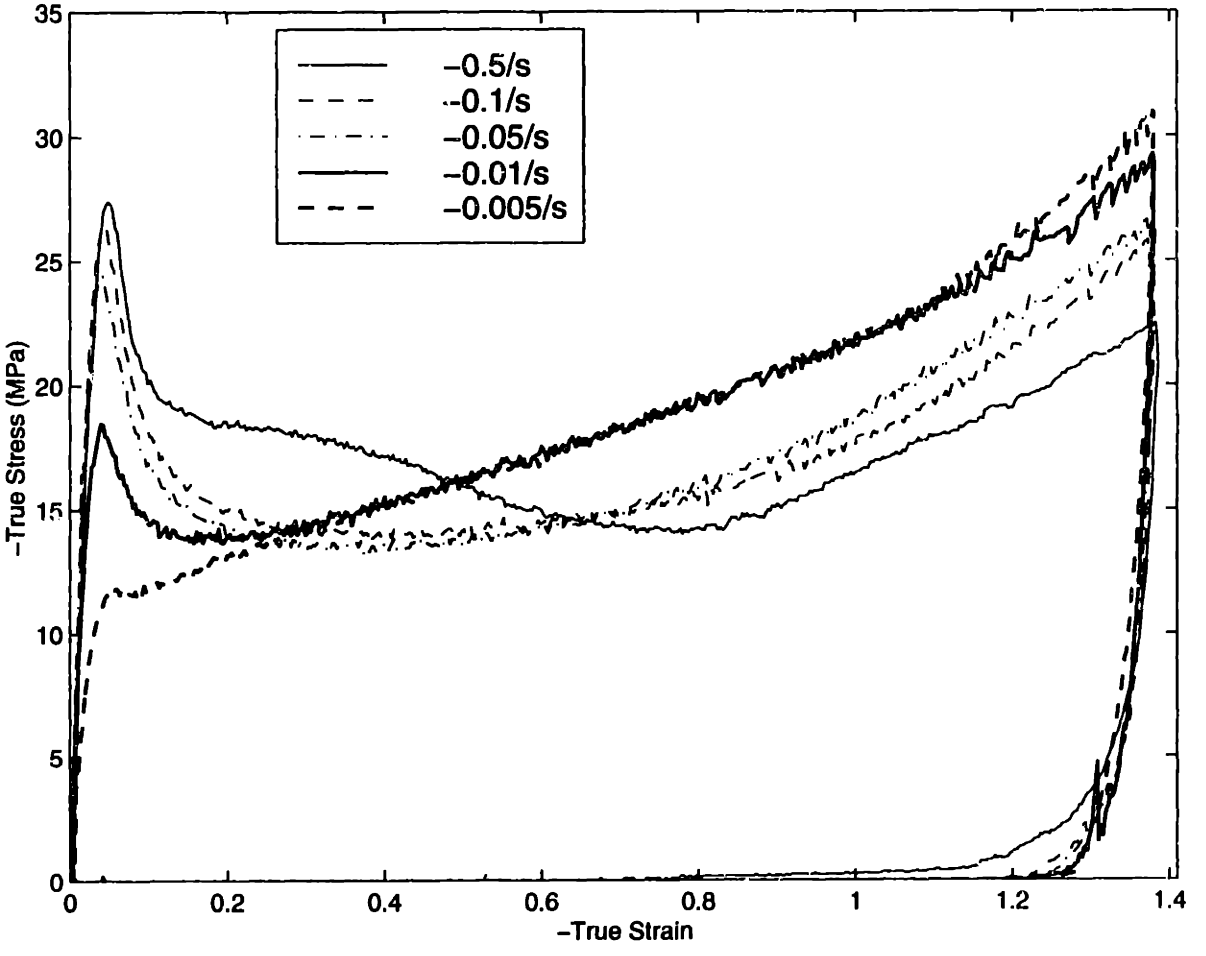

Figure 2.5: Uniaxial Compression Data, Temperature = $70°C$

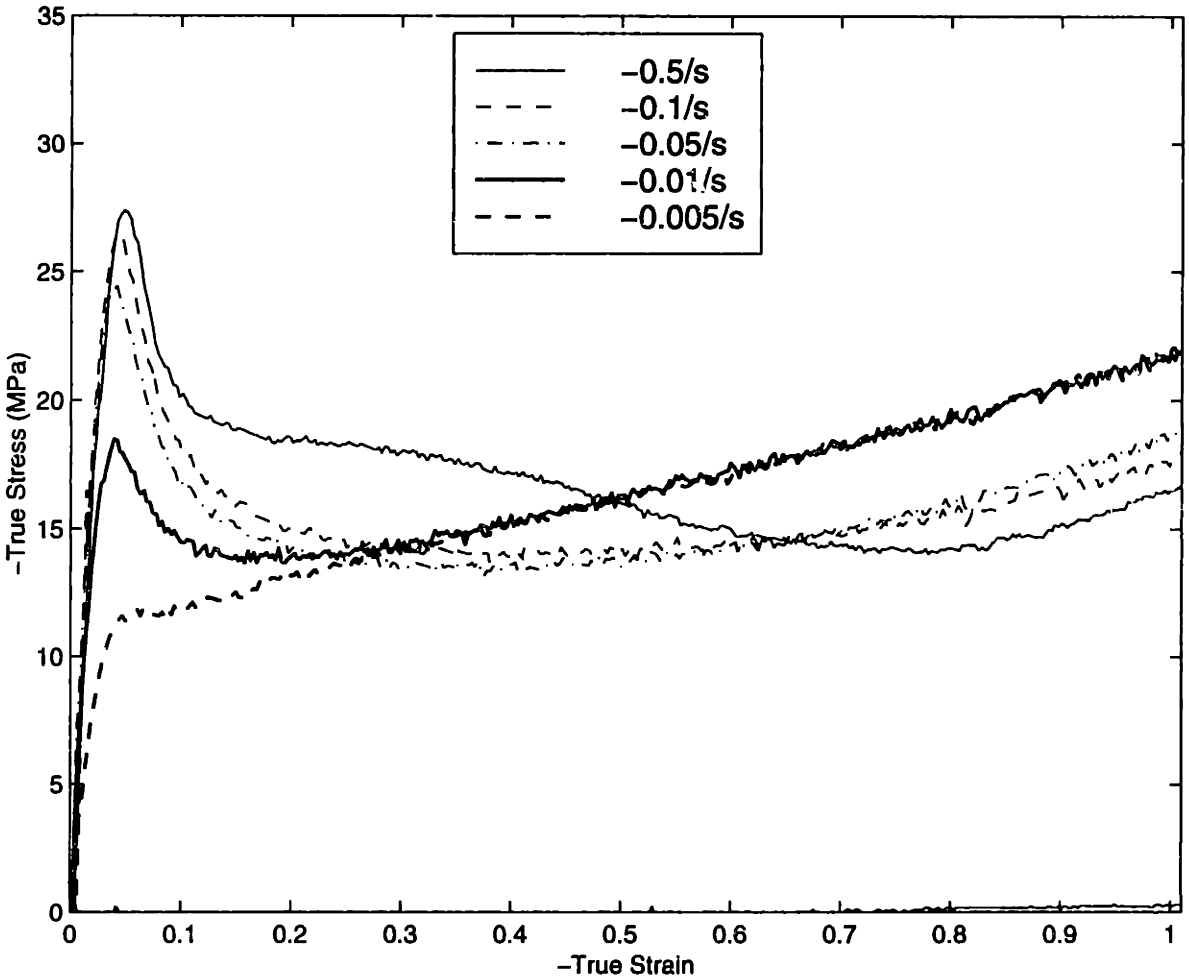

Figure 2.6: Uniaxial Compression Data, Temperature = $70°C$, blown up to a final strain of -1.0

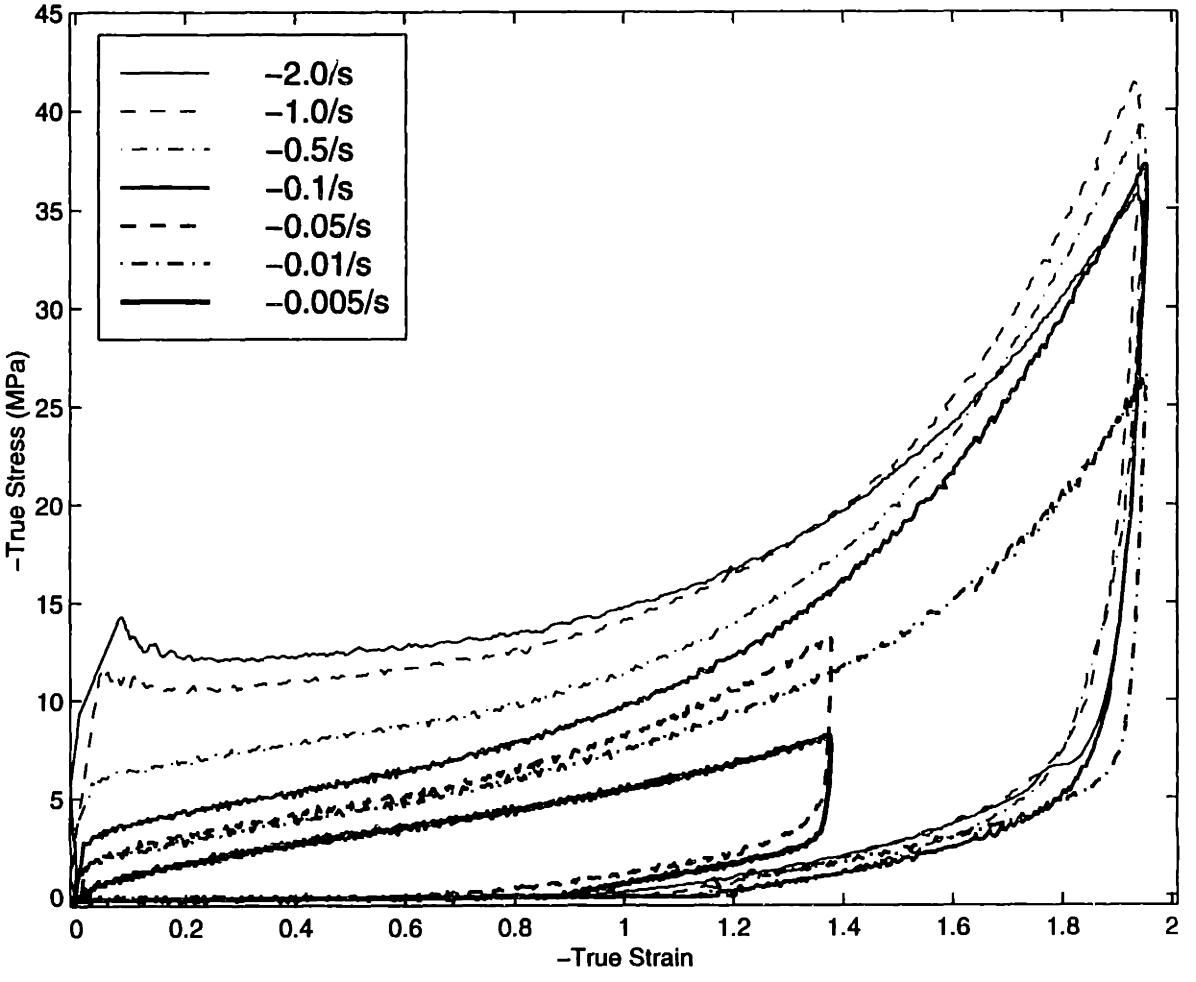

Figure 2.7: Uniaxial Compression Data, Temperature = $80°C$

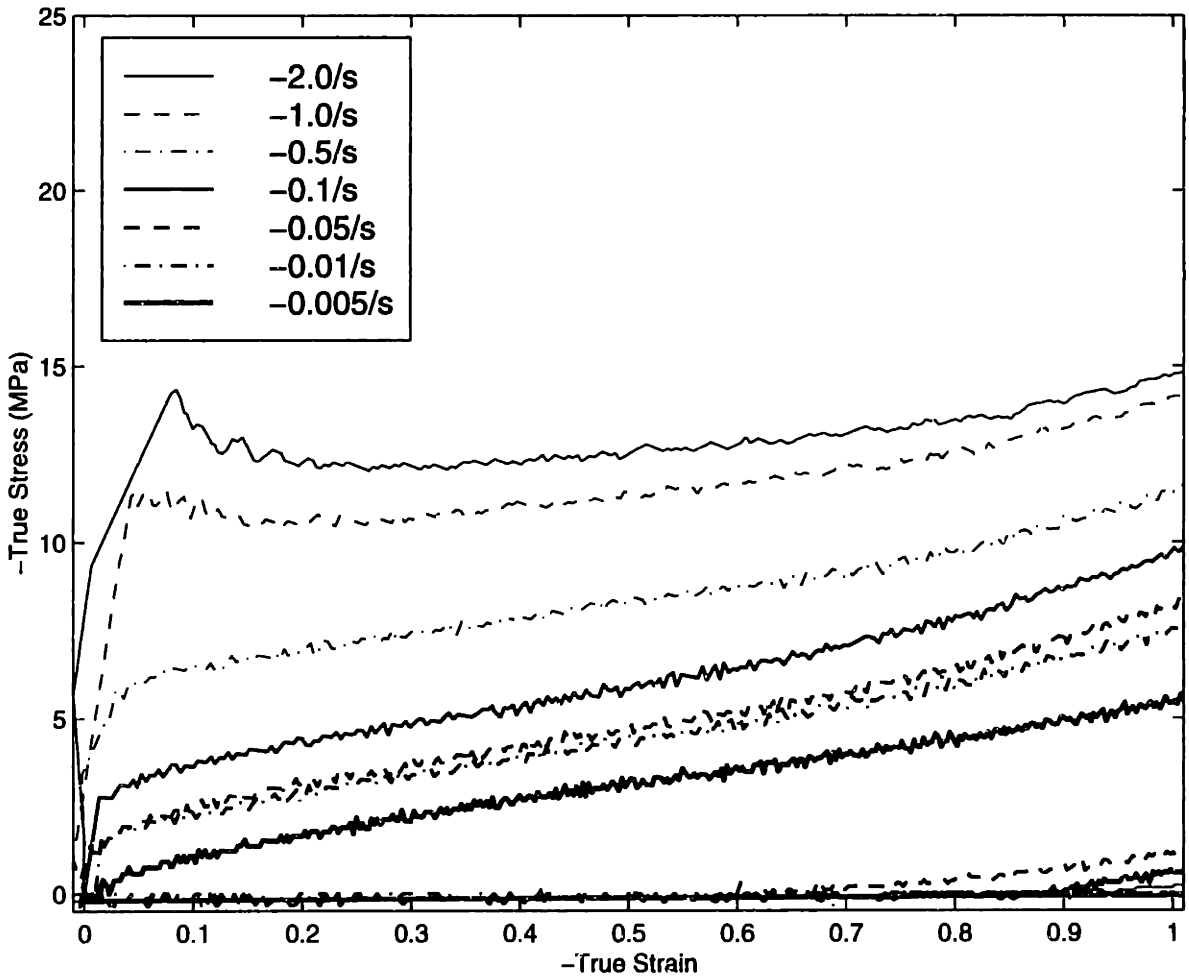

Figure 2.8: Uniaxial Compression Data, Temperature = $80°C$, blown up to a final strain of -1.0

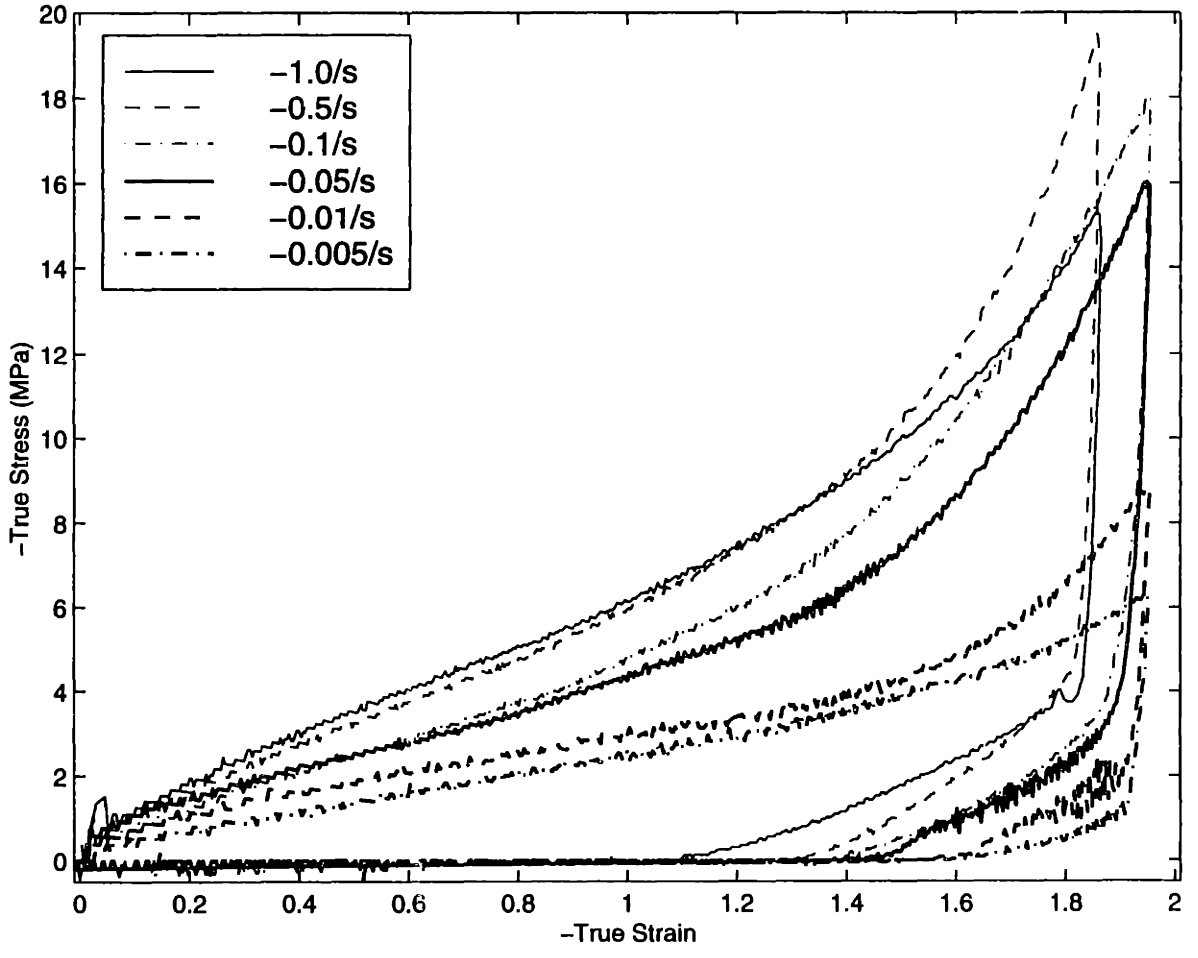

Figure 2.9: Uniaxial Compression Data, Temperature = $90°C$

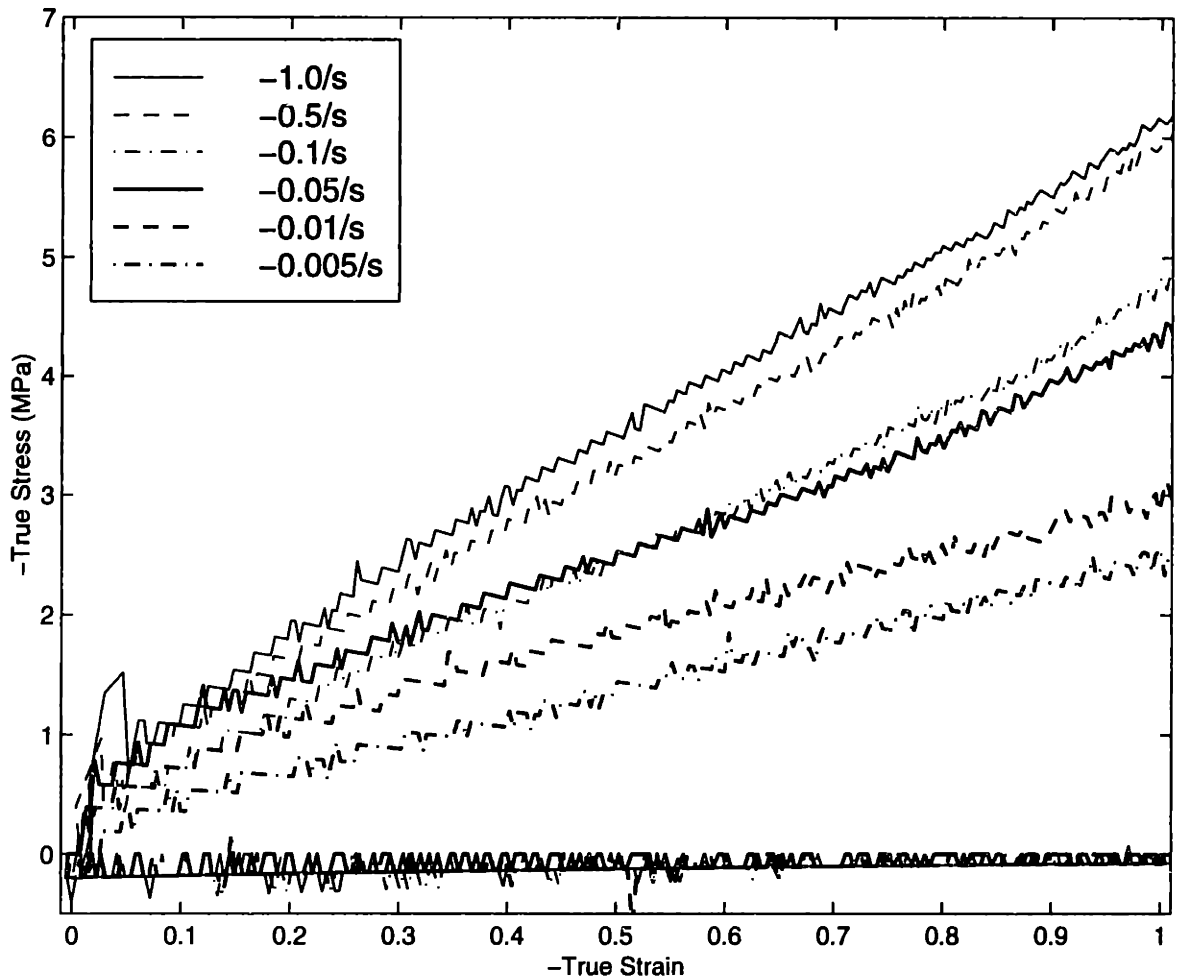

Figure 2.10: Uniaxial Compression Data, Temperature = $90°C$, blown up to a final strain of -1.0

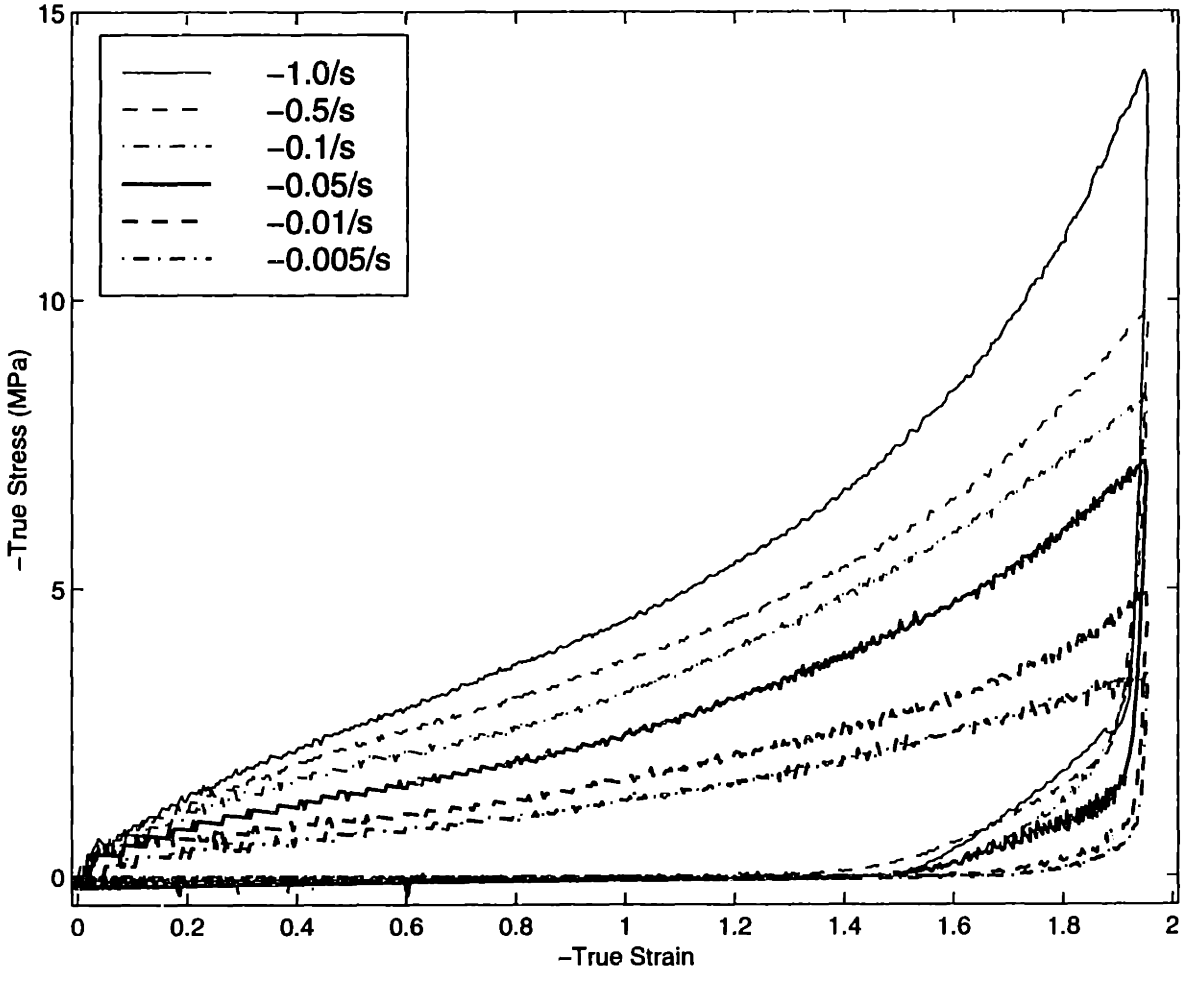

Figure 2.11: Uniaxial Compression Data, Temperature $100°C$

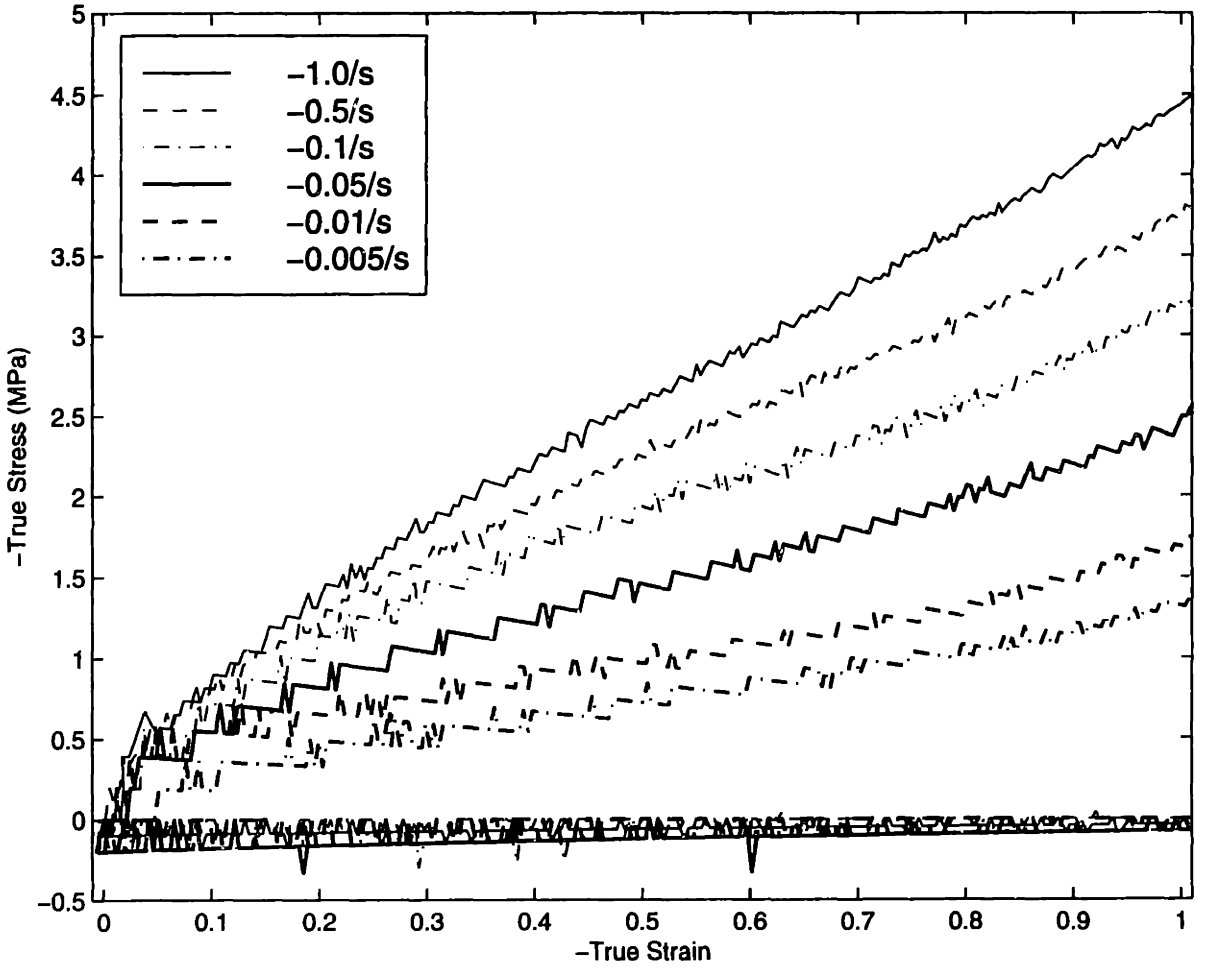

Figure 2.12: Uniaxial Compression Data, Temperature = $100°C$, blown up to a final strain of -1.0

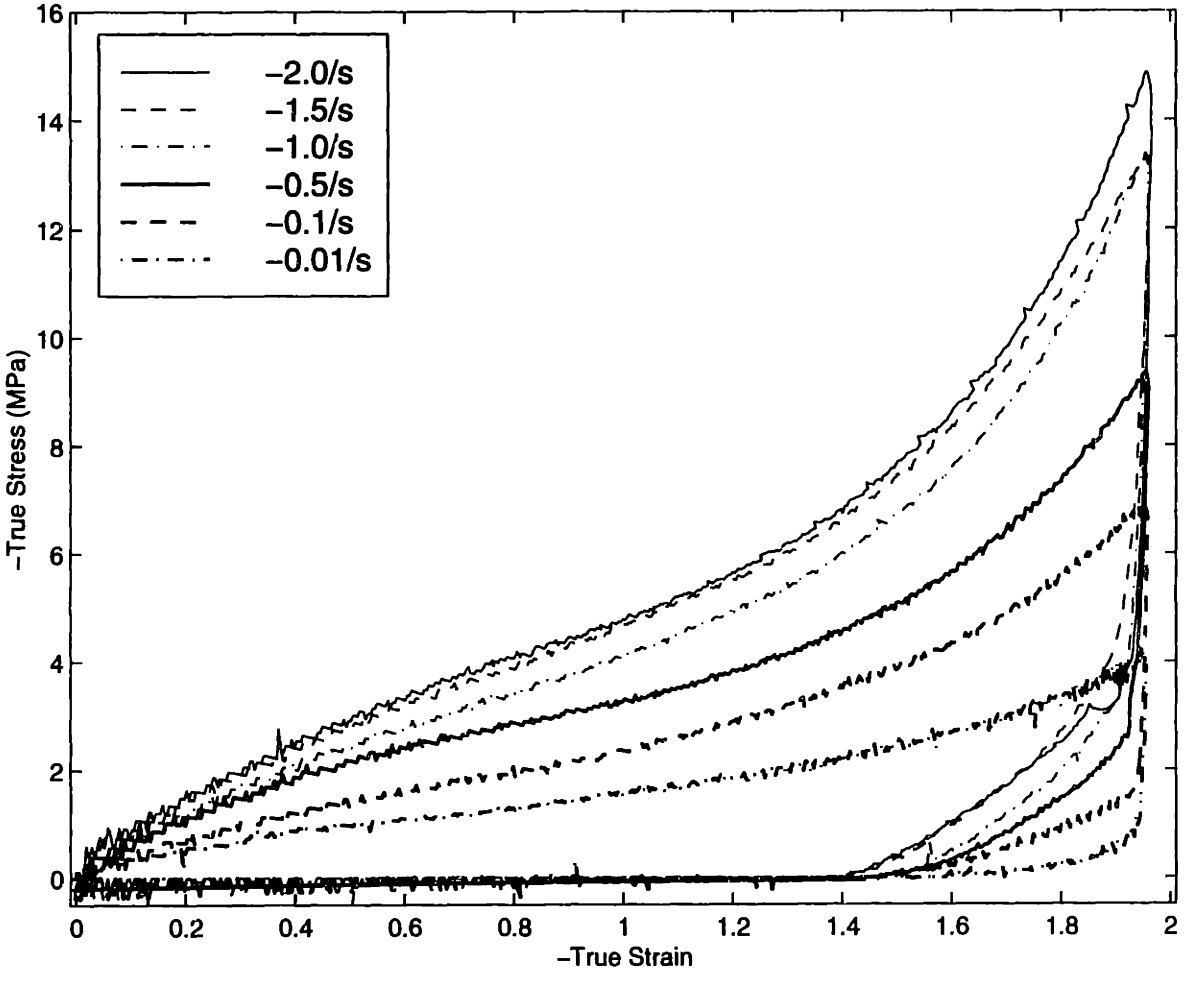

Figure 2.13: Uniaxial Compression Data, Temperature = $105°C$

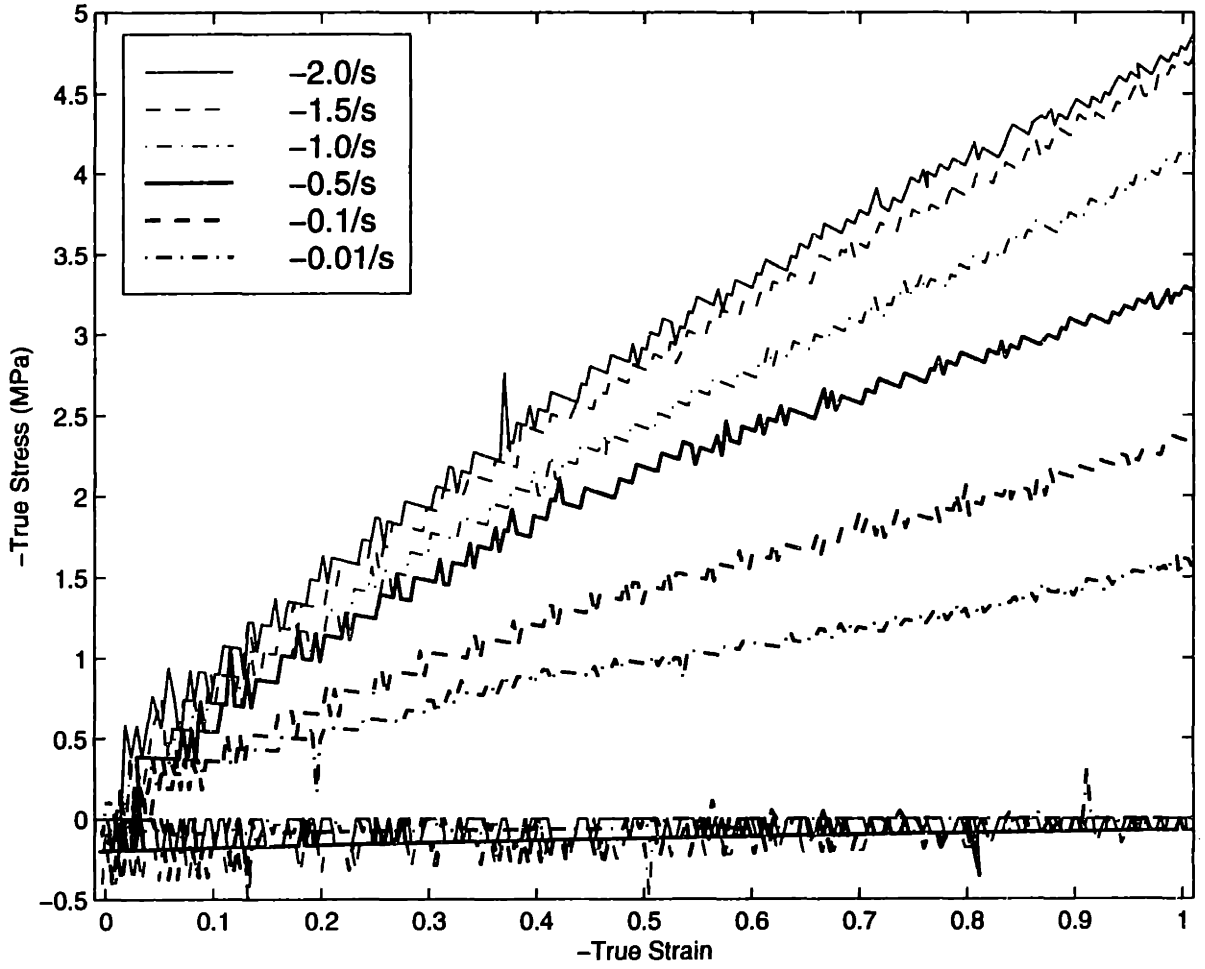

Figure 2.14: Uniaxial Compression Data, Temperature = $105°C$, blown up to a final strain of -1.0

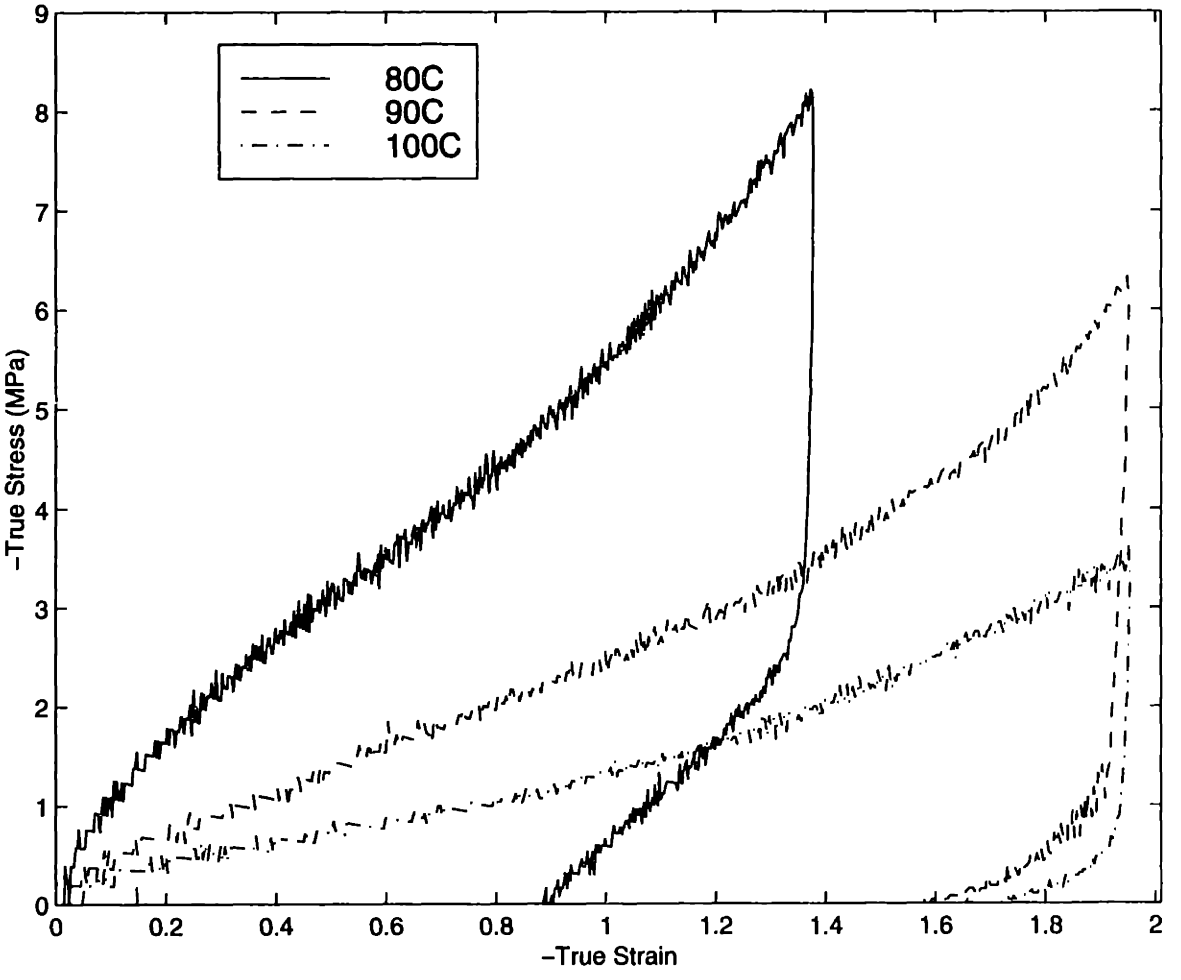

Figure 2.15: Uniaxial Compression Data, $\dot{\epsilon} = -0.005/s$

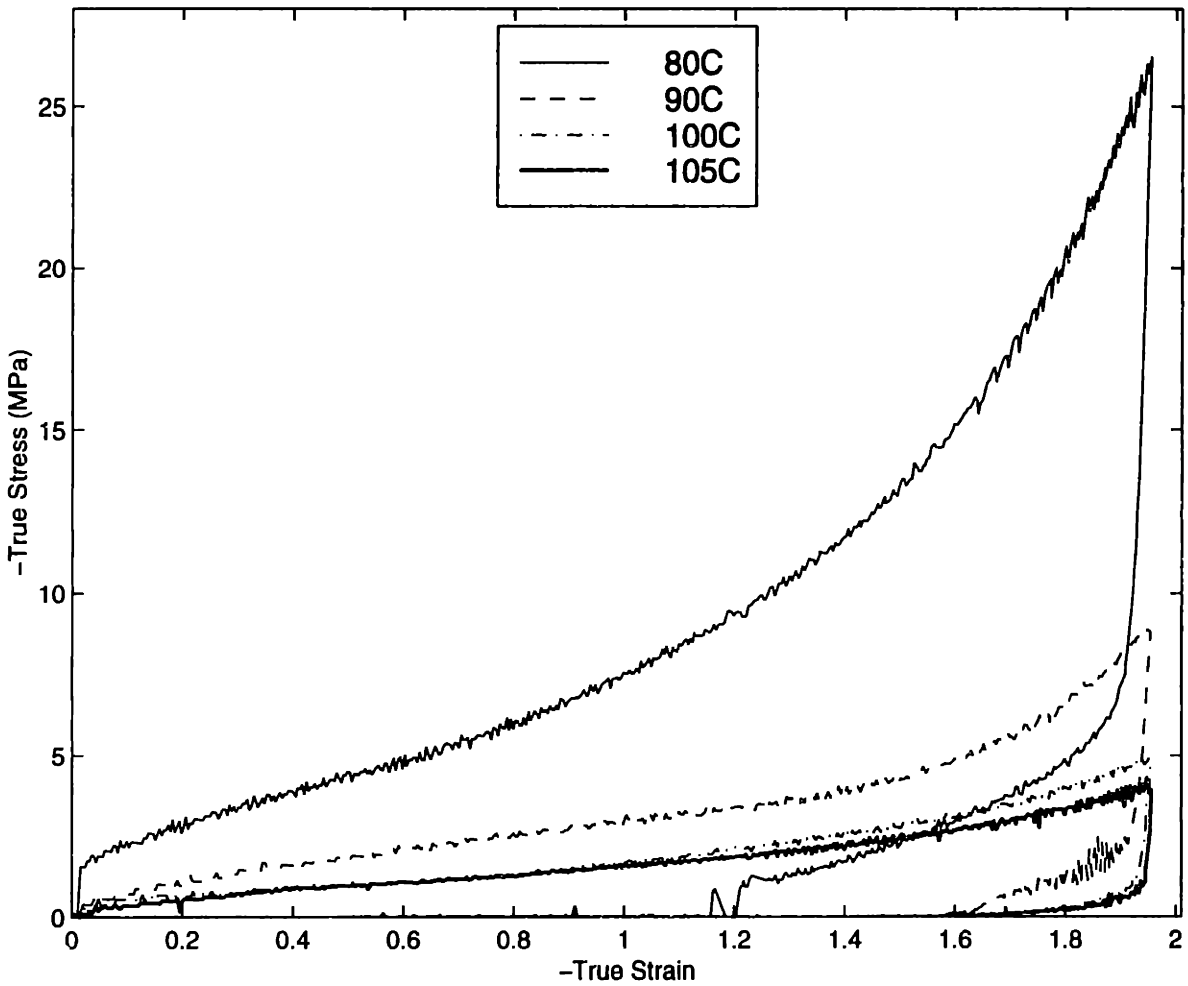

Figure 2.16: Uniaxial Compression Data, $\dot{\varepsilon} = -0.01/s$

, various deformation temperatures

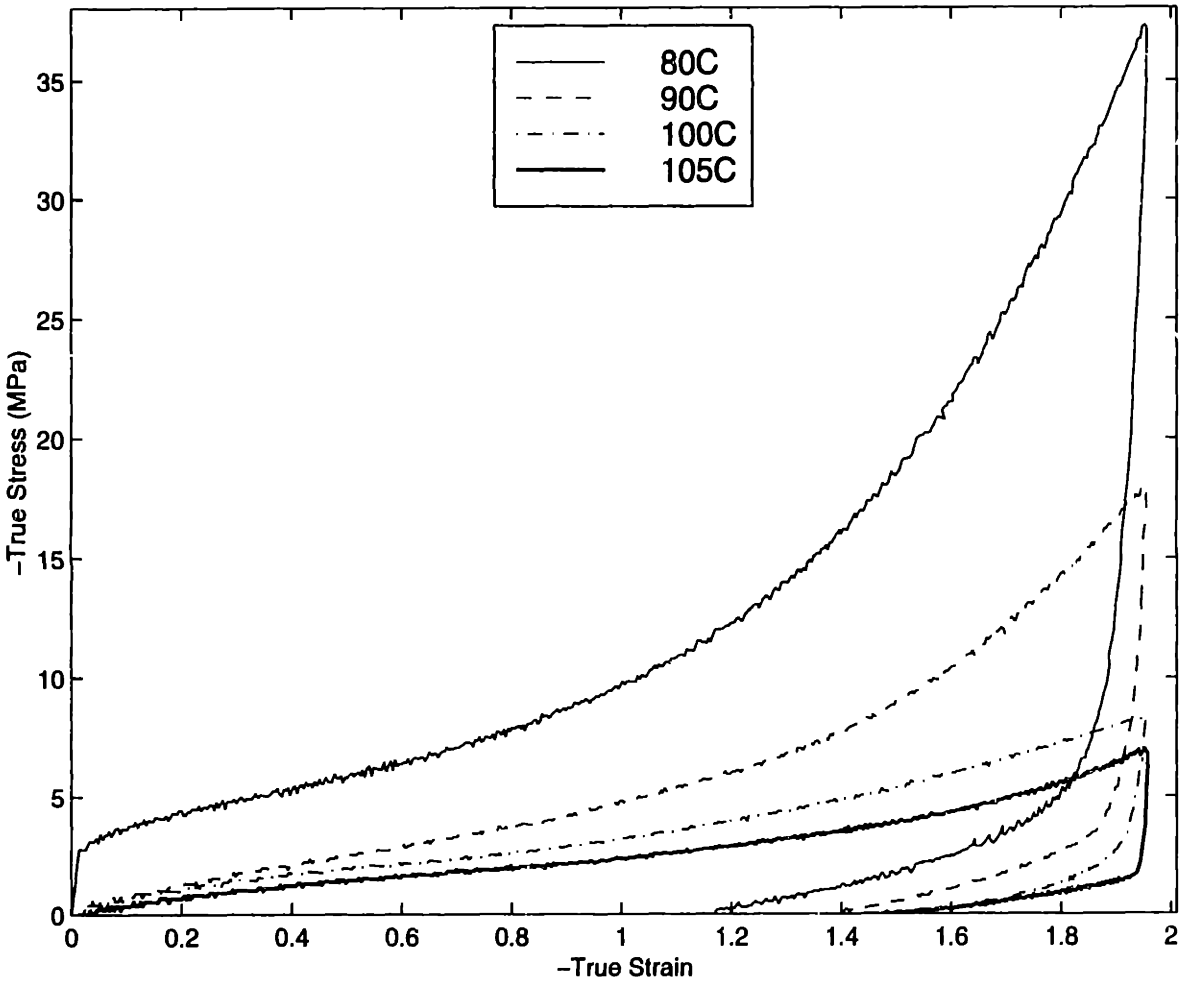

Figure 2.17: Uniaxial Compression Data, $\dot{\epsilon} = -0.1/s$

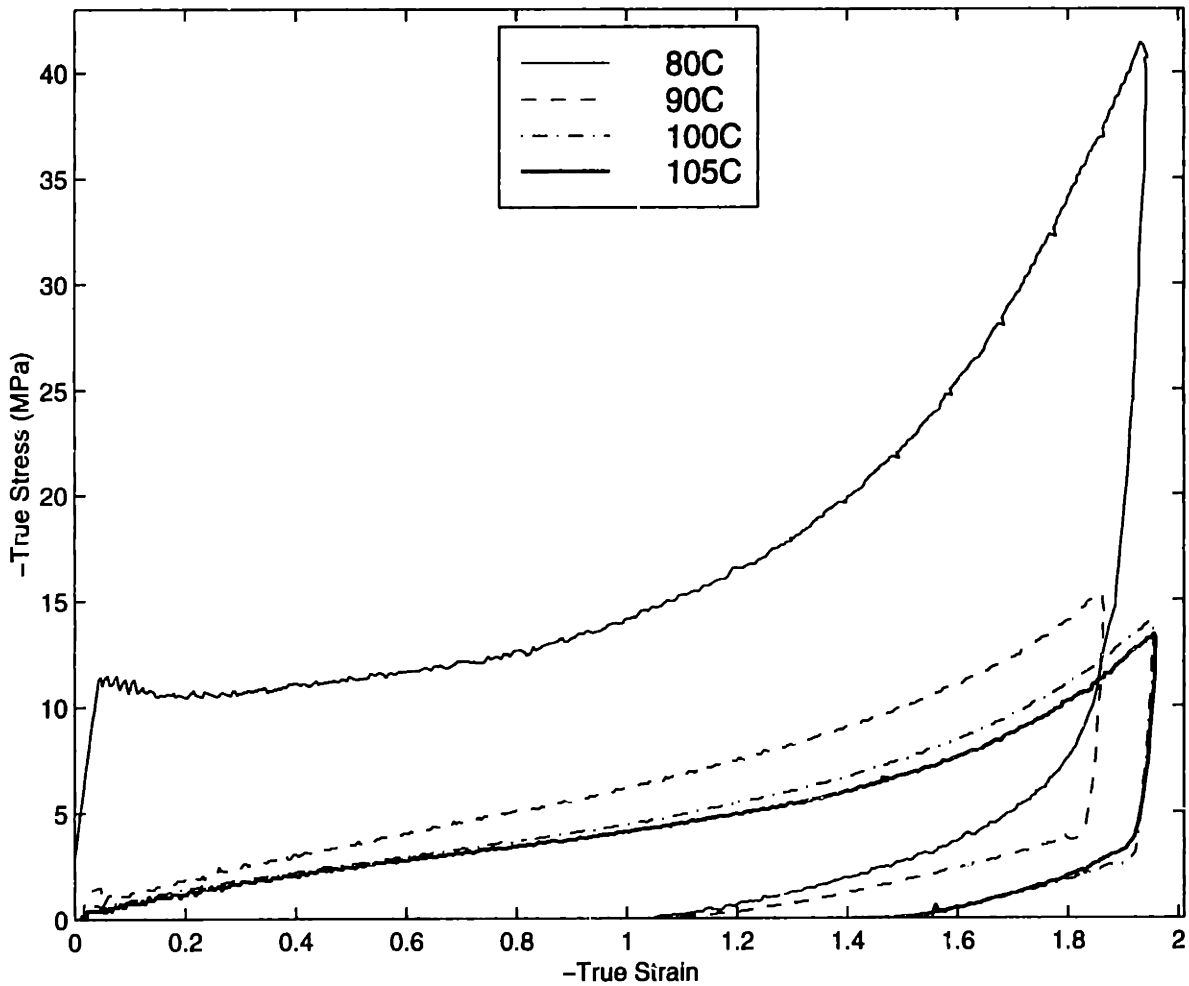

Figure 2.18: Uniaxial Compression Data, $\dot{\epsilon} = -1.0/s$

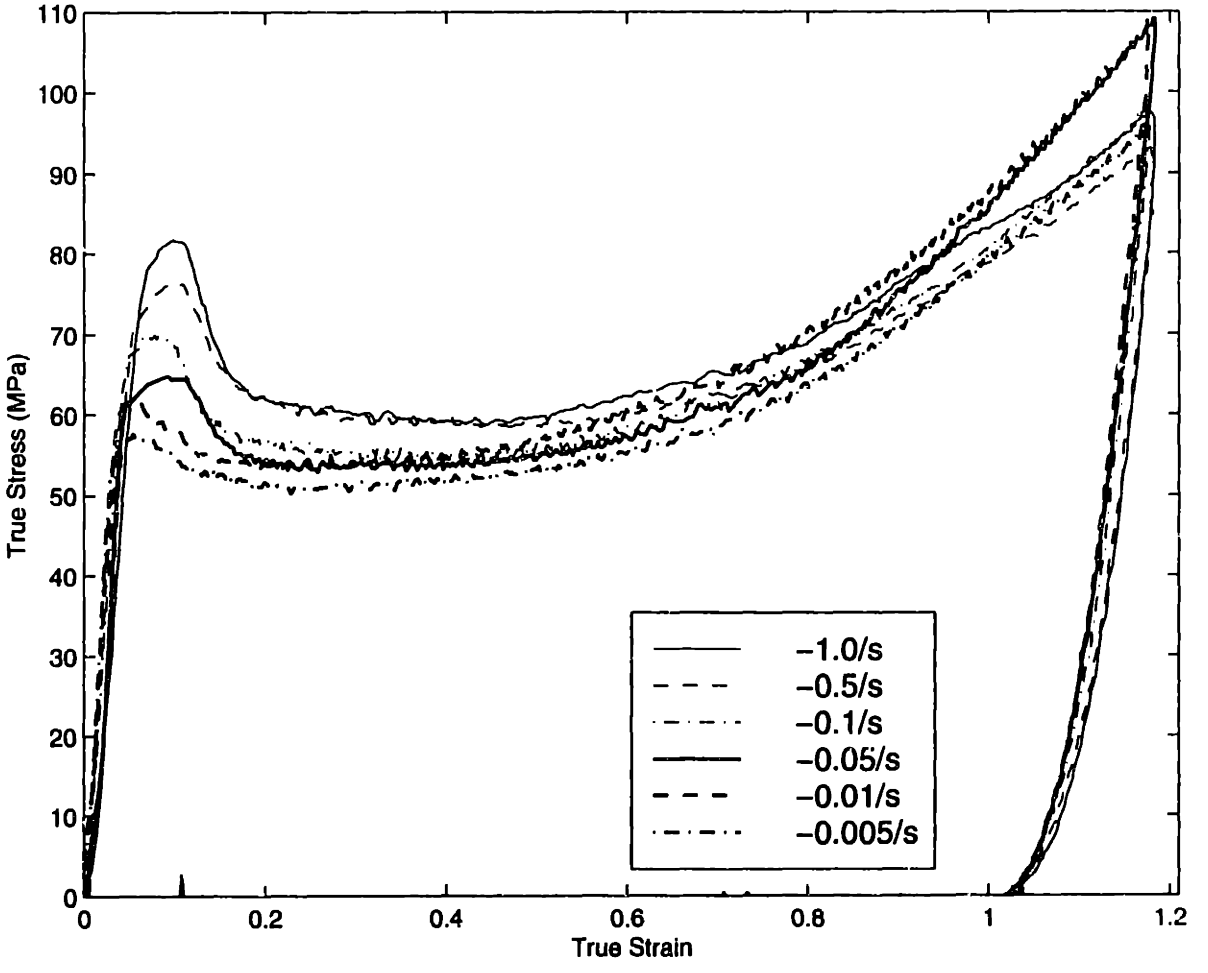

Figure 2.19: Plane Strain Compression Data, Temperature = $25°C$

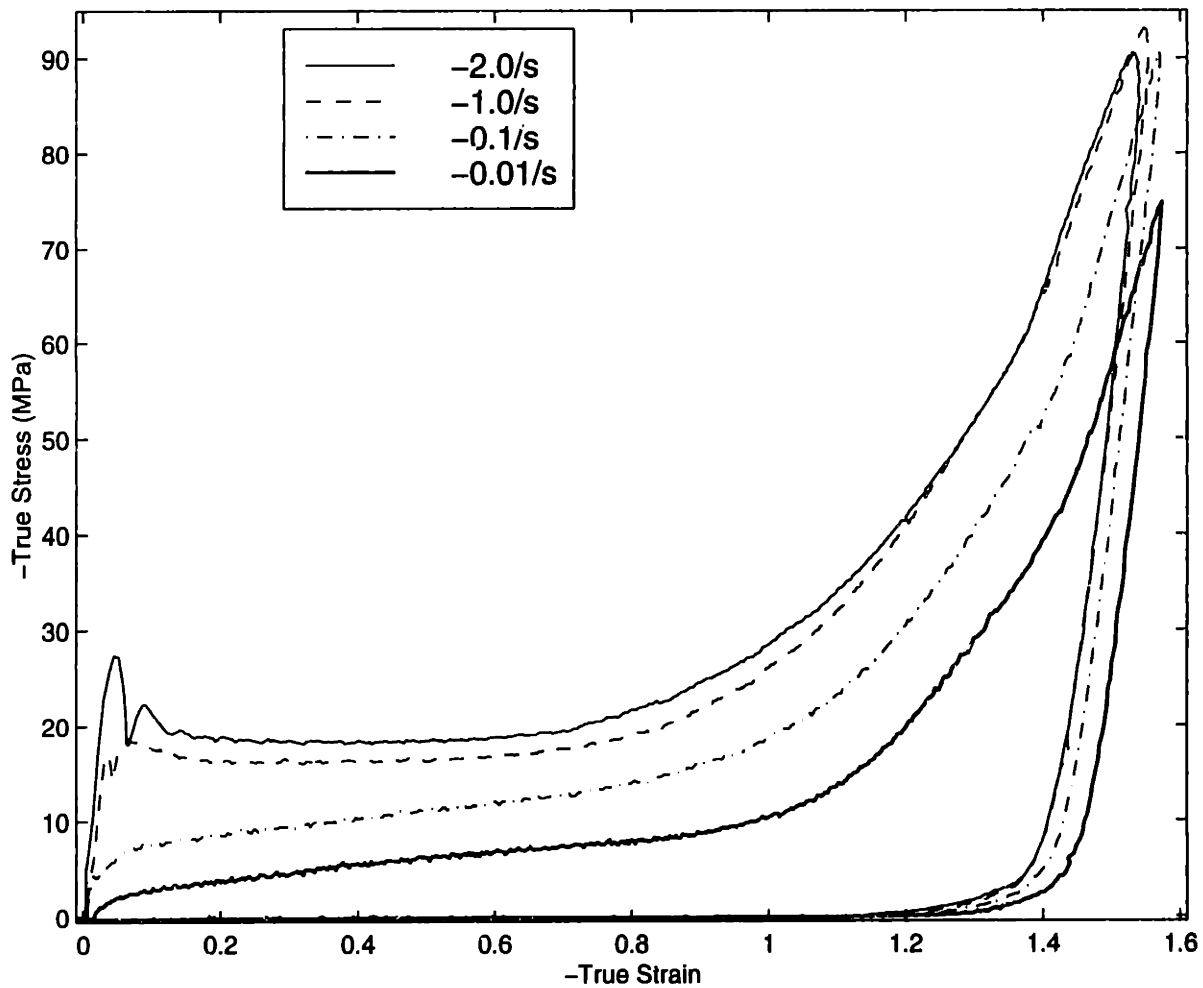

Figure 2.20: Plane Strain Compression Data, Temperature = 80°*C*

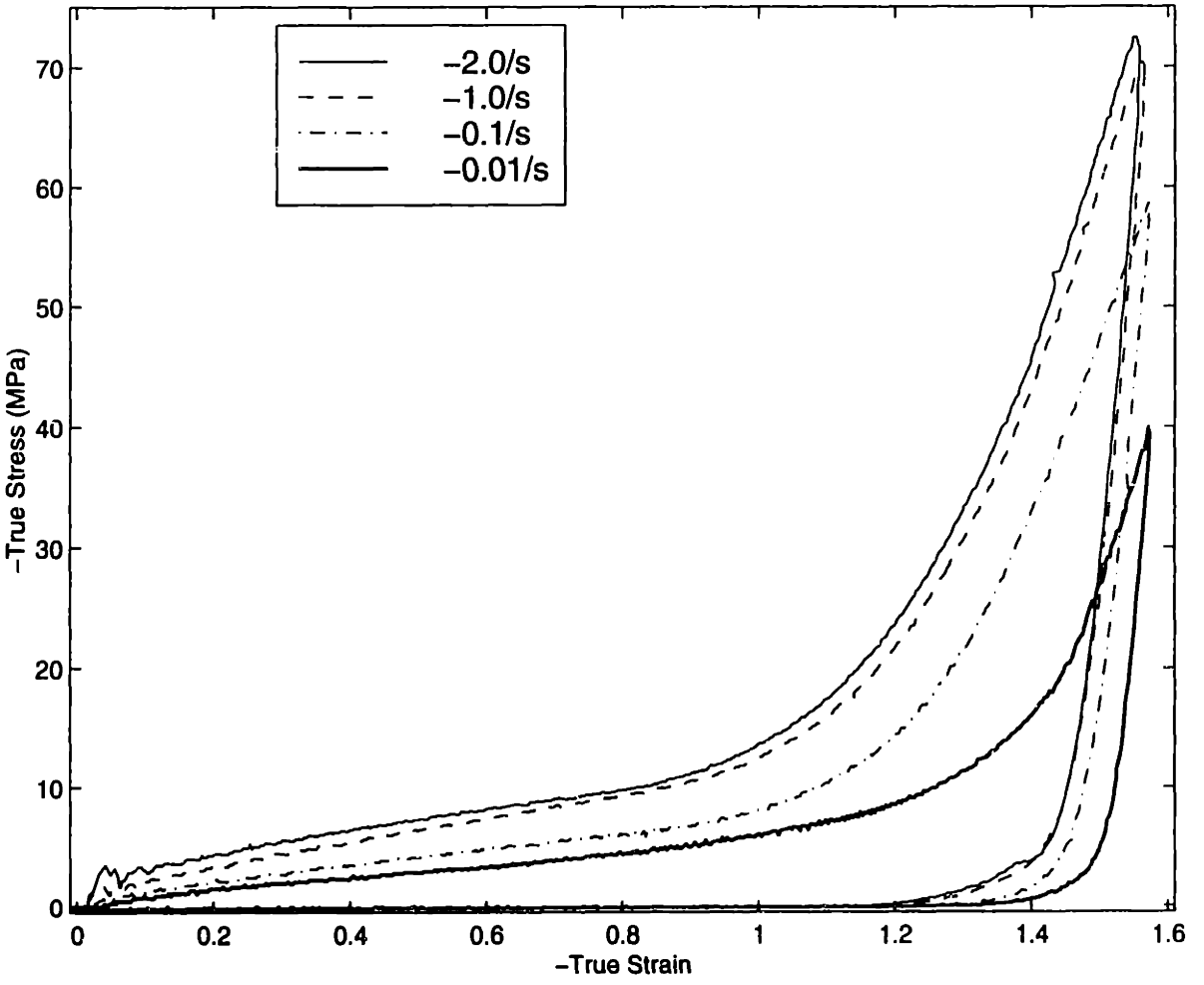

Figure 2.21: Plane Strain Compression Data, Temperature =90°*C*

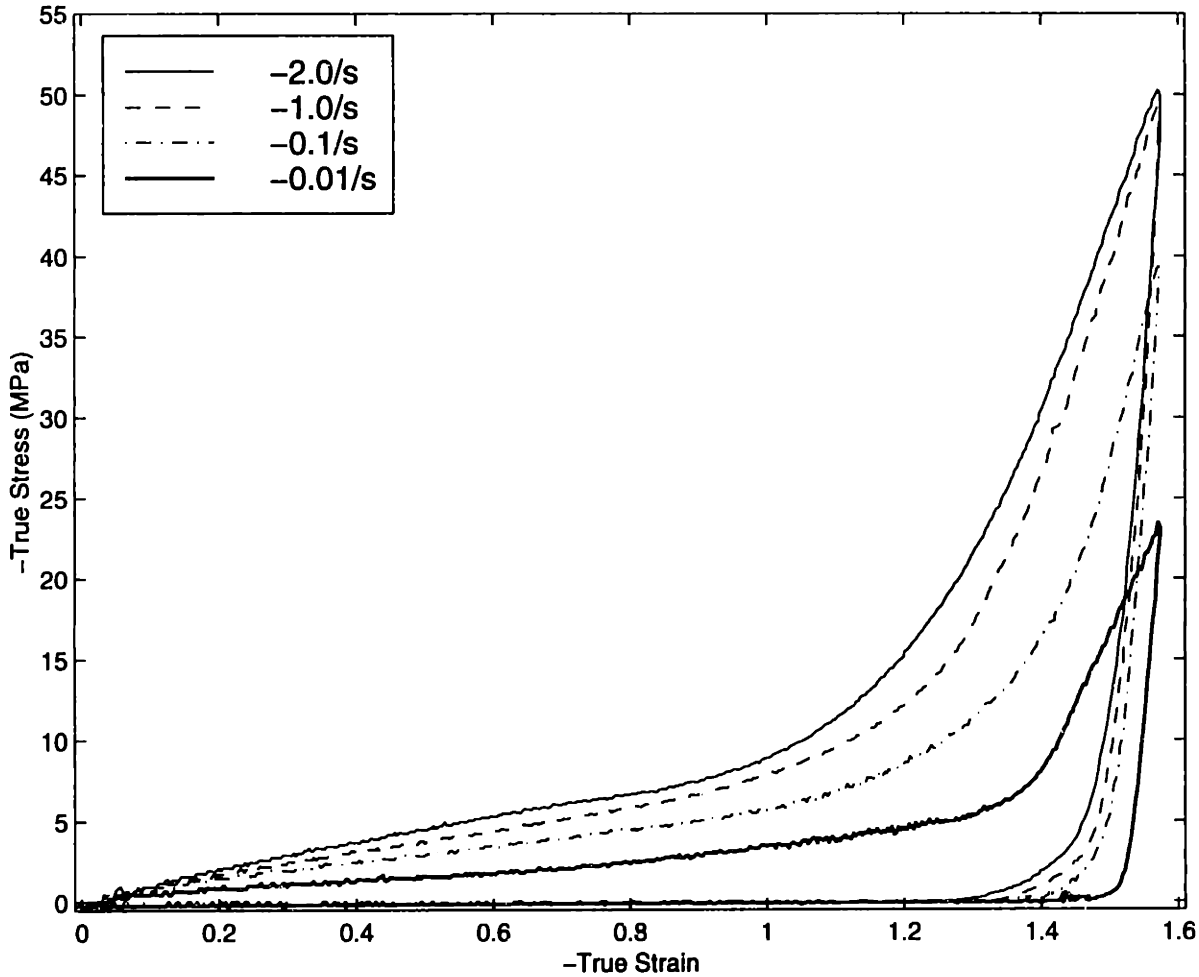

Figure 2.22: Plane Strain Compression Data, Temperature = $100°C$

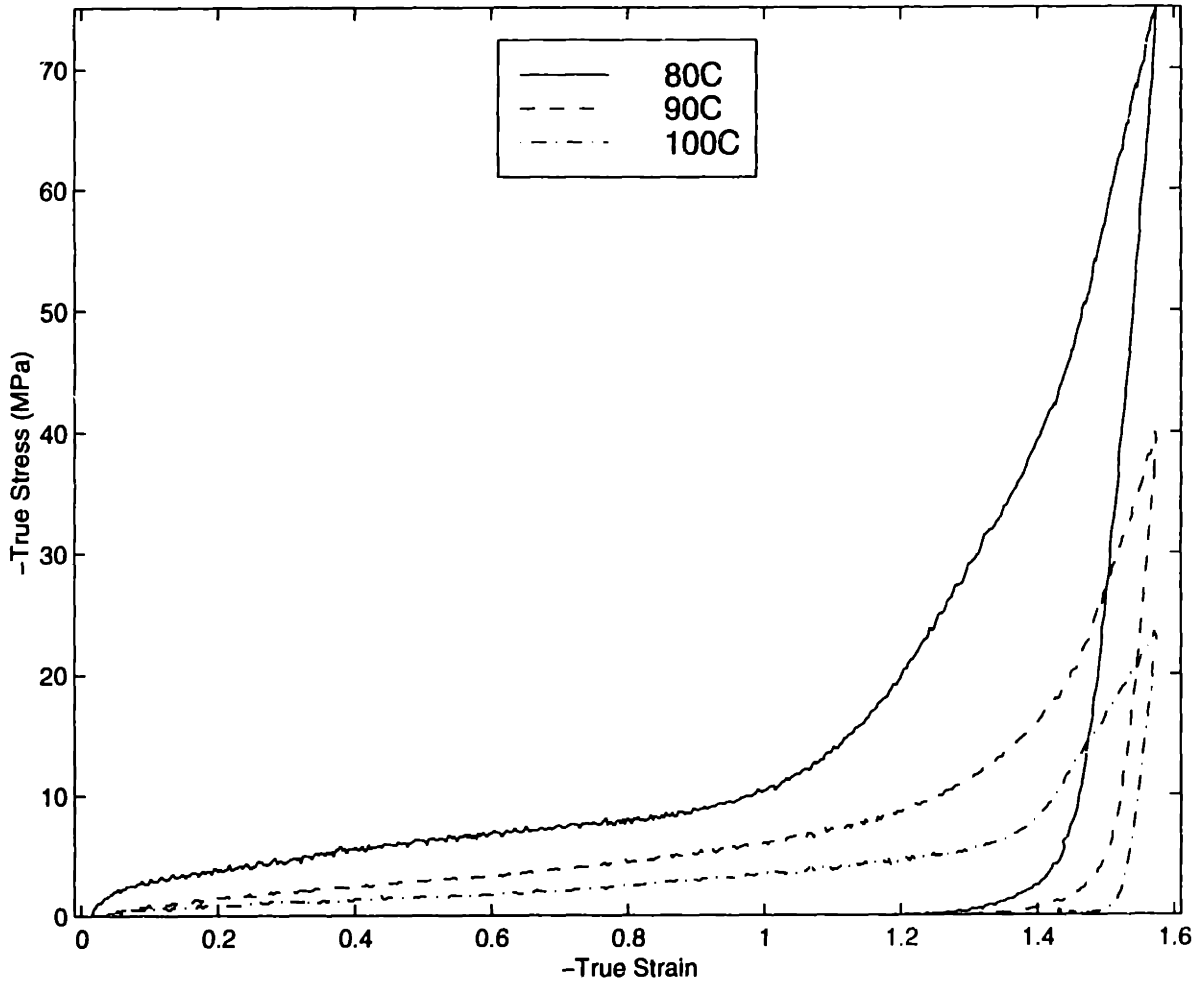

Figure 2.23: Plane Strain Compression Data, $\dot{\epsilon} = -0.01/s$

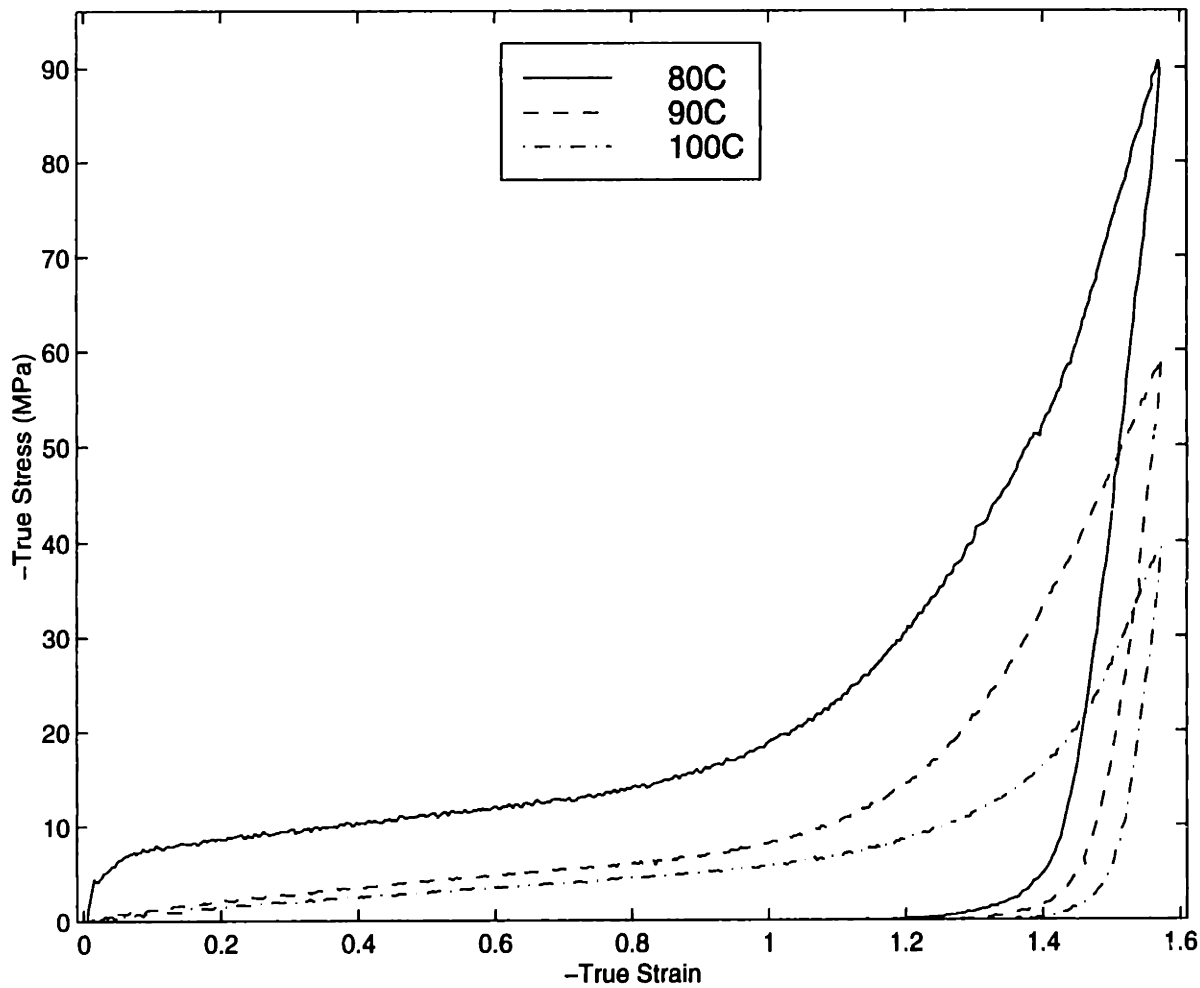

Figure 2.24: Plane Strain Compression Data, $\dot{\epsilon} = -0.1/s$

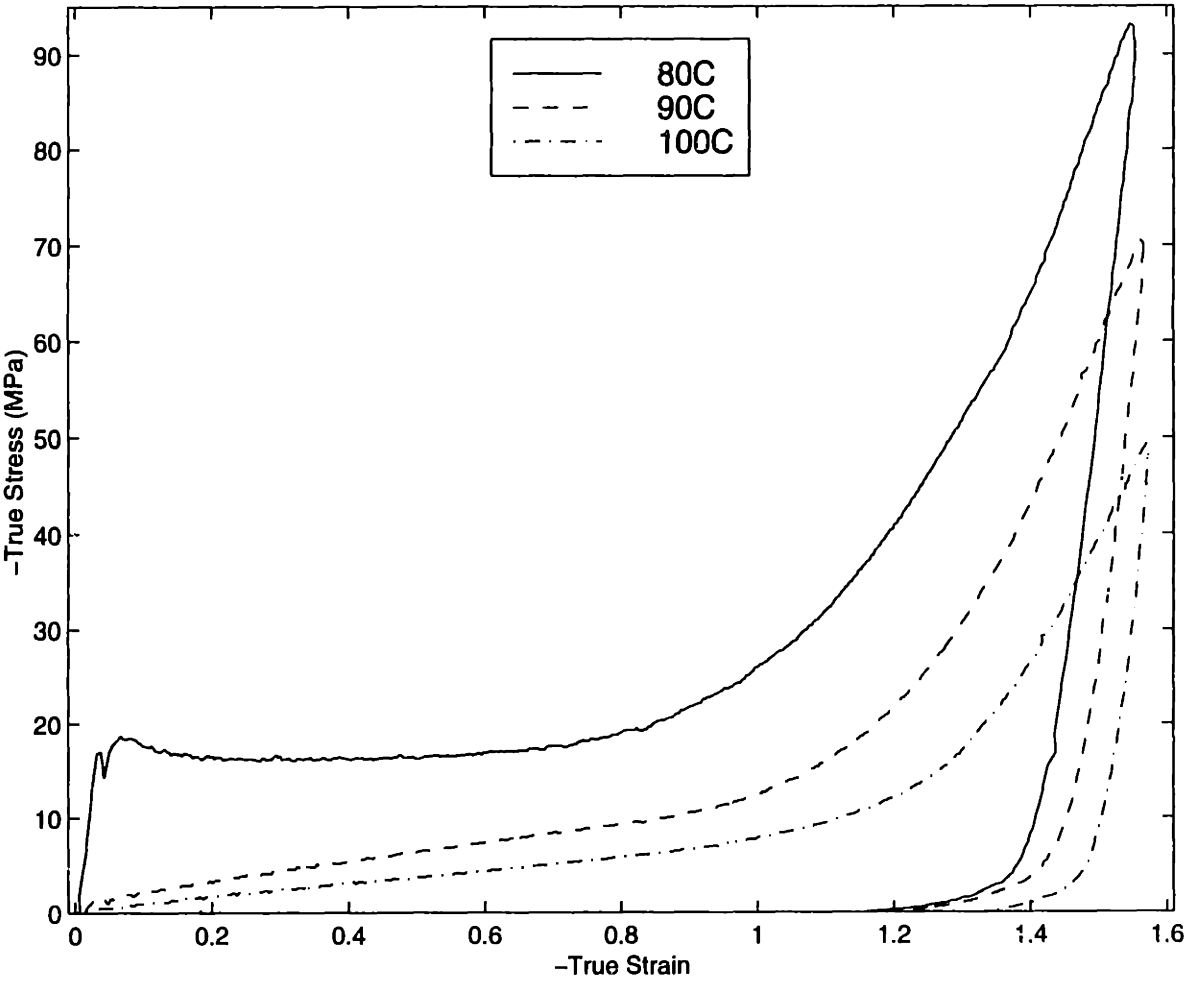

Figure 2.25: Plane Strain Compression Data, $\dot{\epsilon} = -1.0/s$

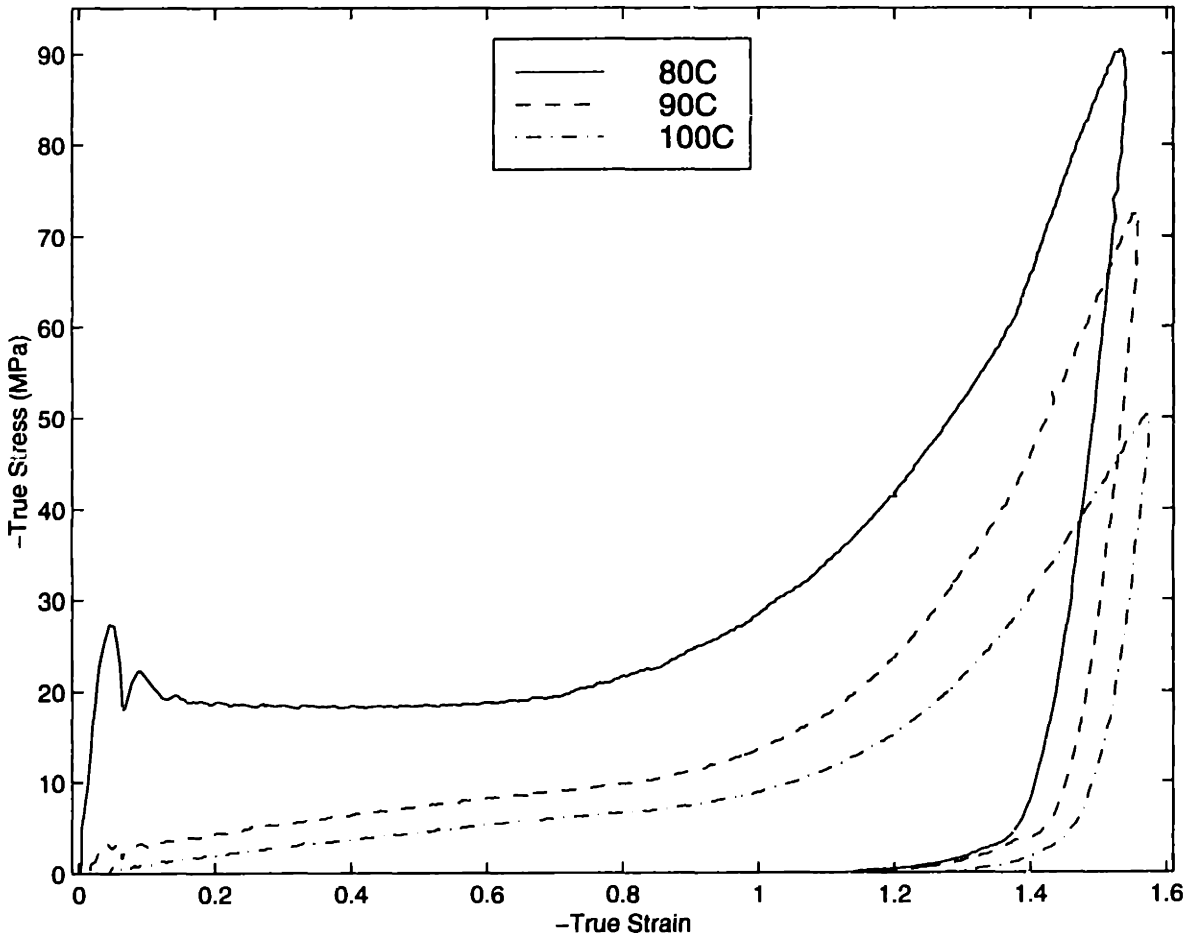

Figure 2.26: Plane Strain Compression Data, $\dot{\epsilon} = -2.0/s$

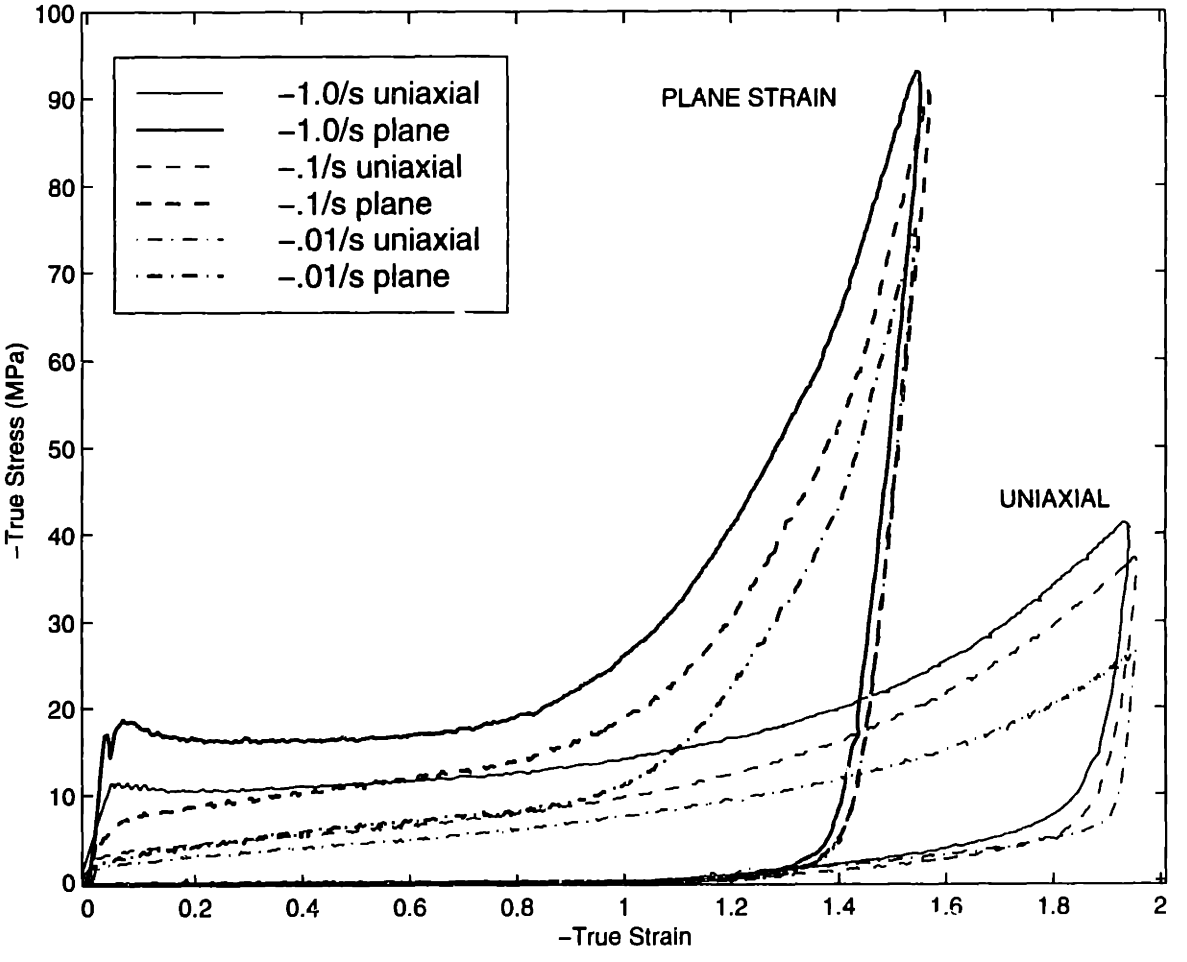

Figure 2.27: Comparison of plane strain and uniaxial compression at $80°C$

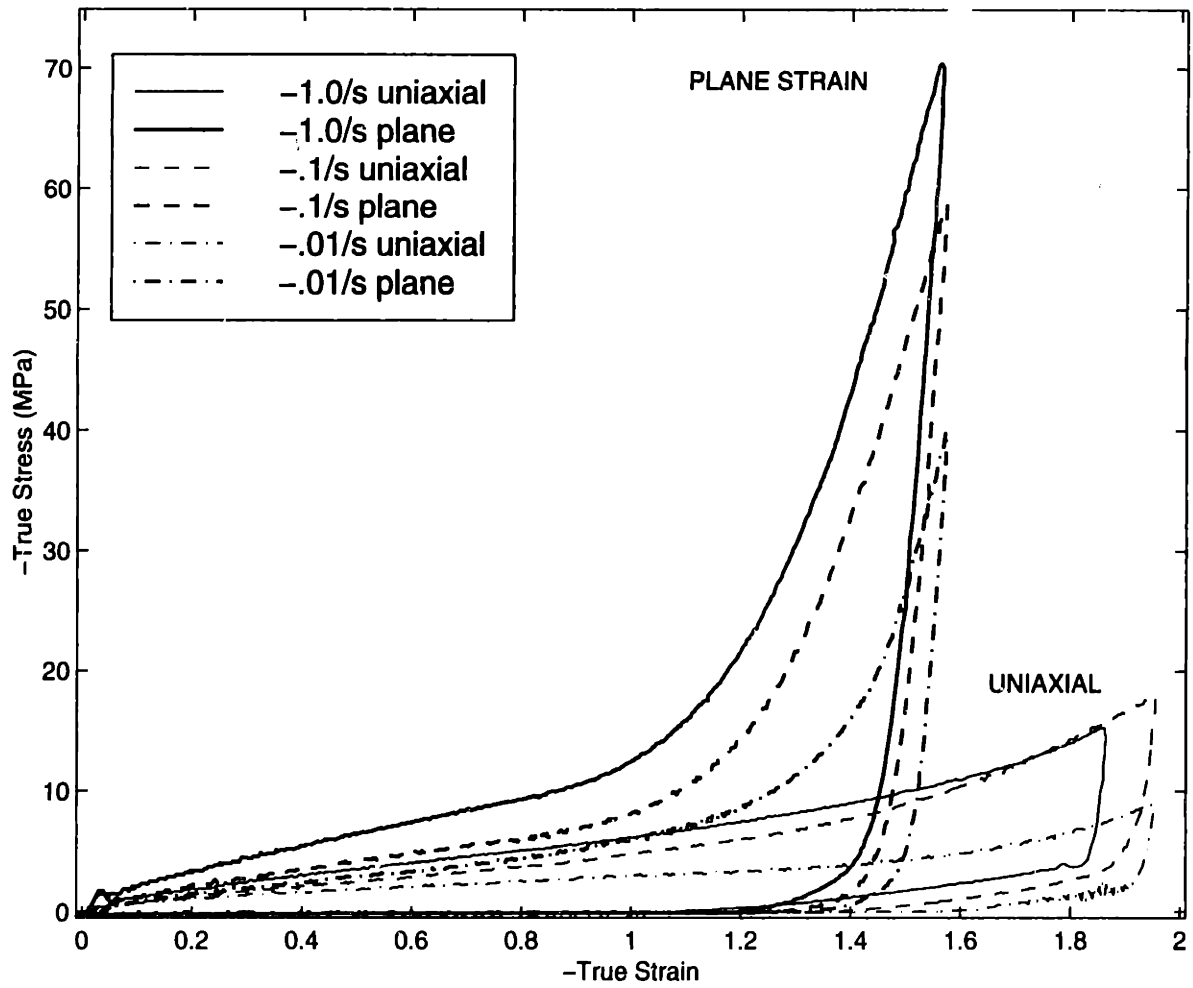

Figure 2.28: Comparison of plane strain and uniaxial compression at $90°C$

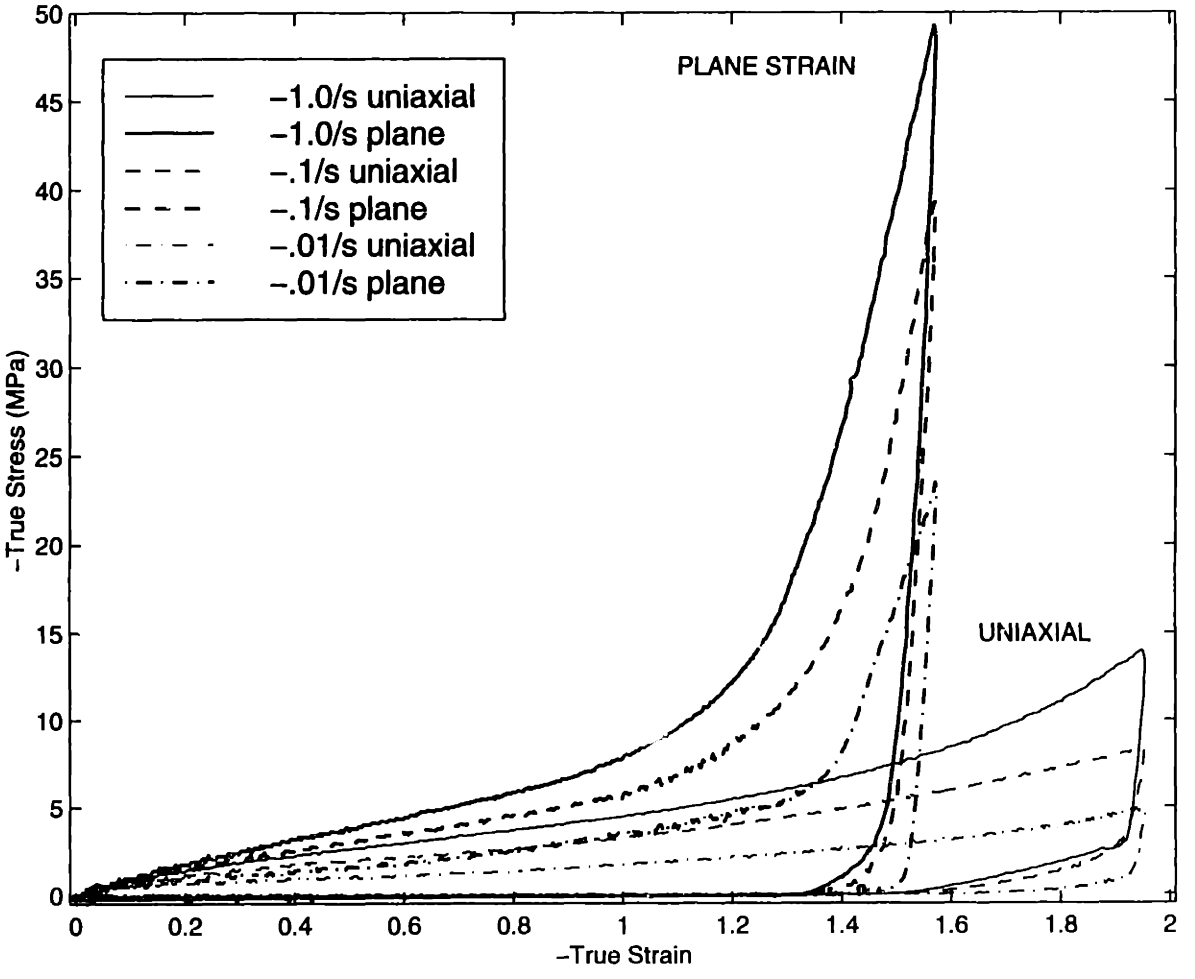

Figure 2.29: Comparison of plane strain and uniaxial compression at $100°C$

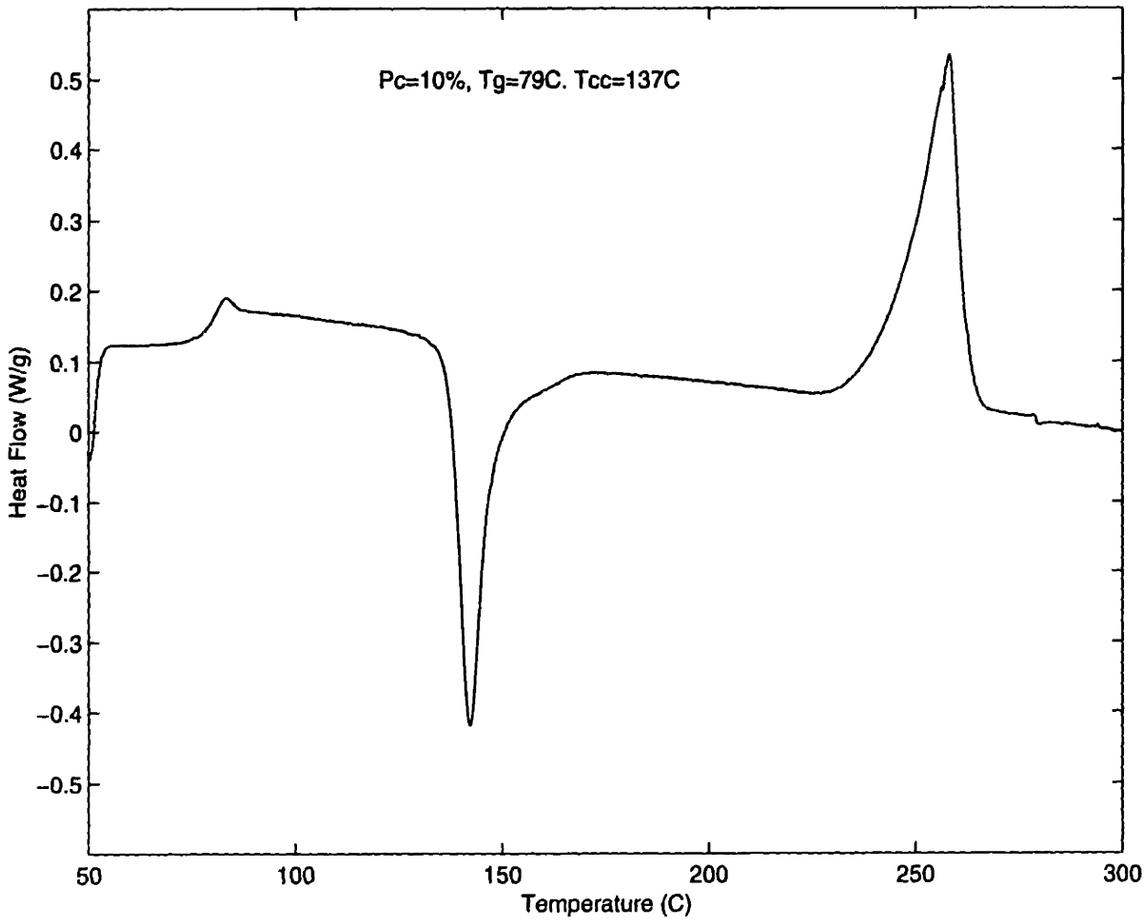

Figure 2.30: DSC thermogram of as-received, undeformed PET conducted at a constant heating rate of $10°C/min$ with crystallinity and glass transition as indicated

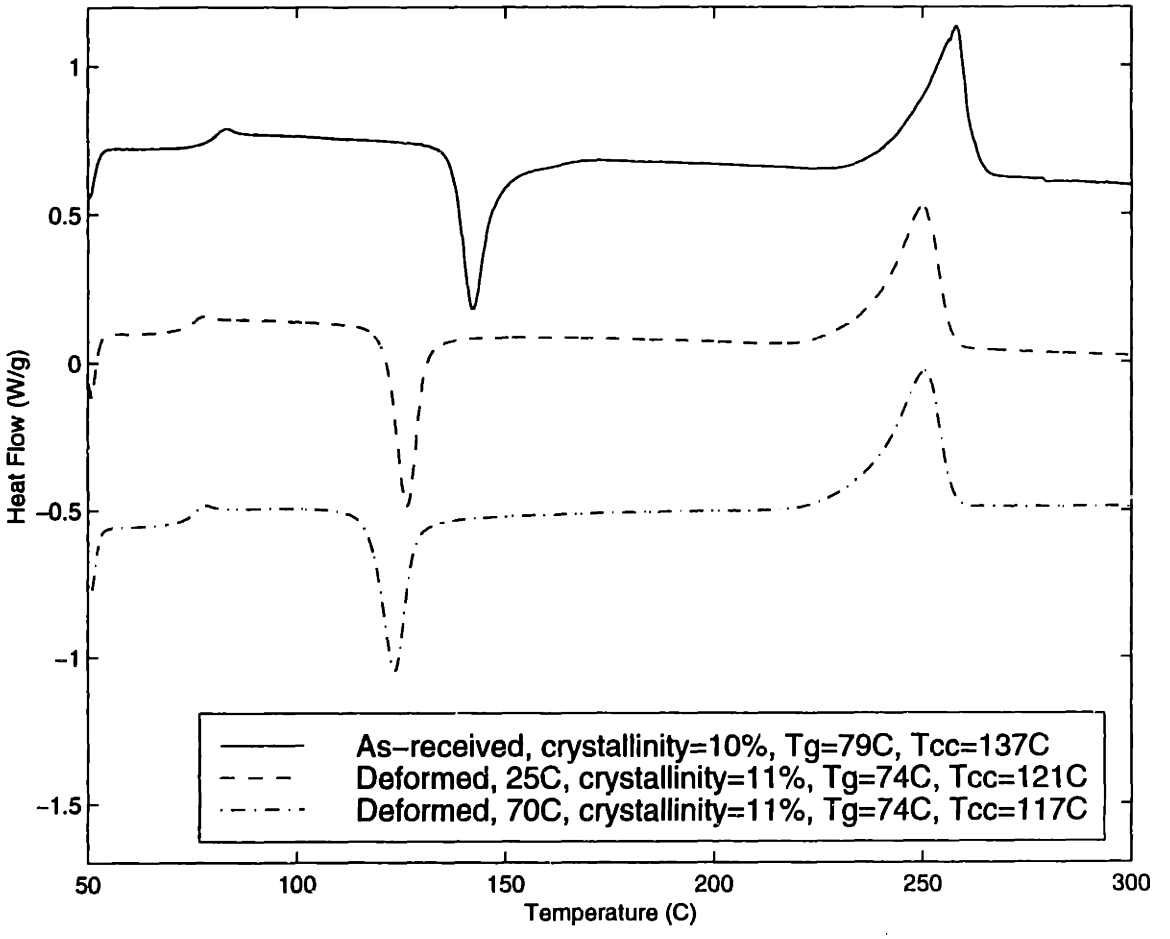

Figure 2.31: DSC thermograms of specimens deformed at $25°C$ and $70°C$ in uniaxial compression at a strain rate of -0.005/*s*, to a final strain of -1.4 compared to the DSC thermogram of the as-received PET with crystallinities and glass transitions as indicated

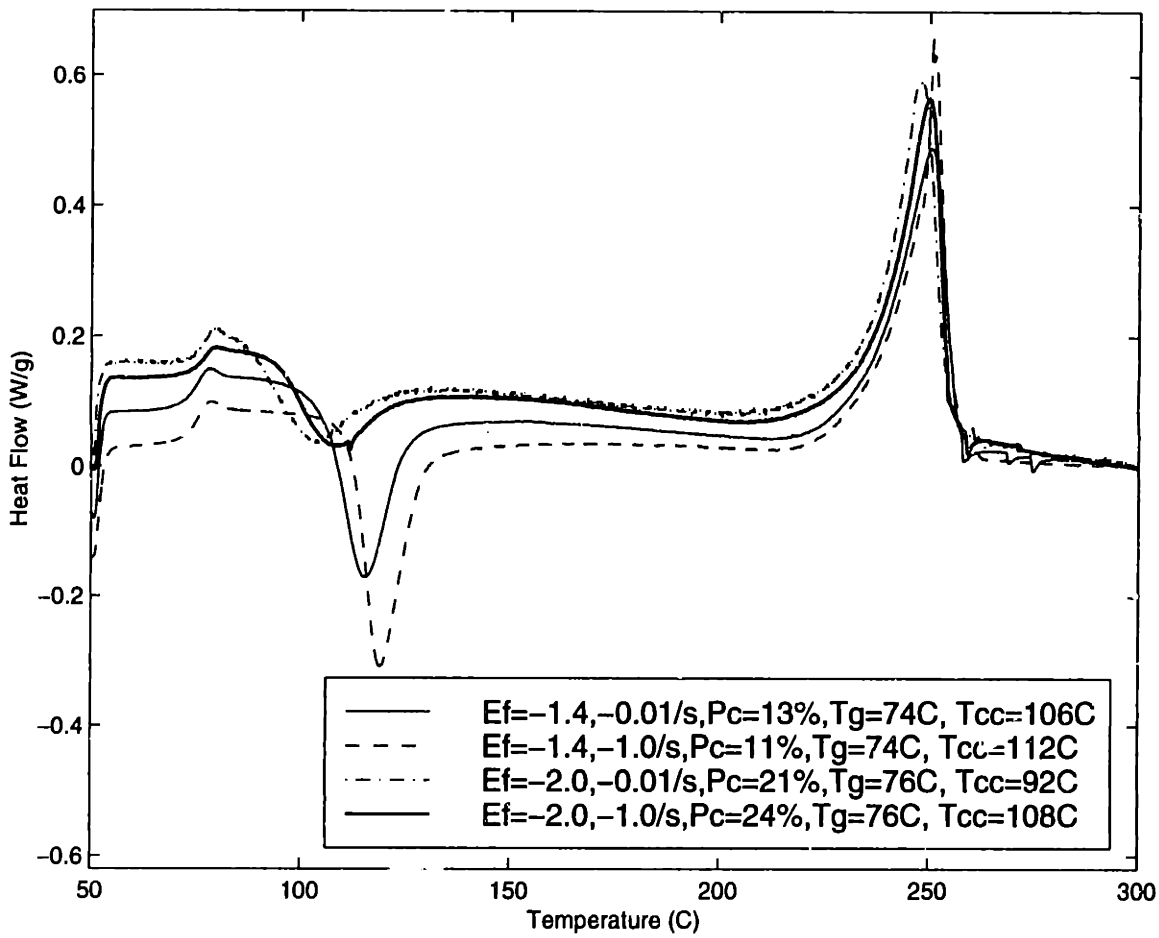

Figure 2.32: DSC thermograms of specimens deformed in uniaxial compression at $80°C$ with final strain levels of -1.4 and -2.0 and strain rates of -0.01/*s* and -1.0/*s*, and crystallinities and glass transitions as indicated

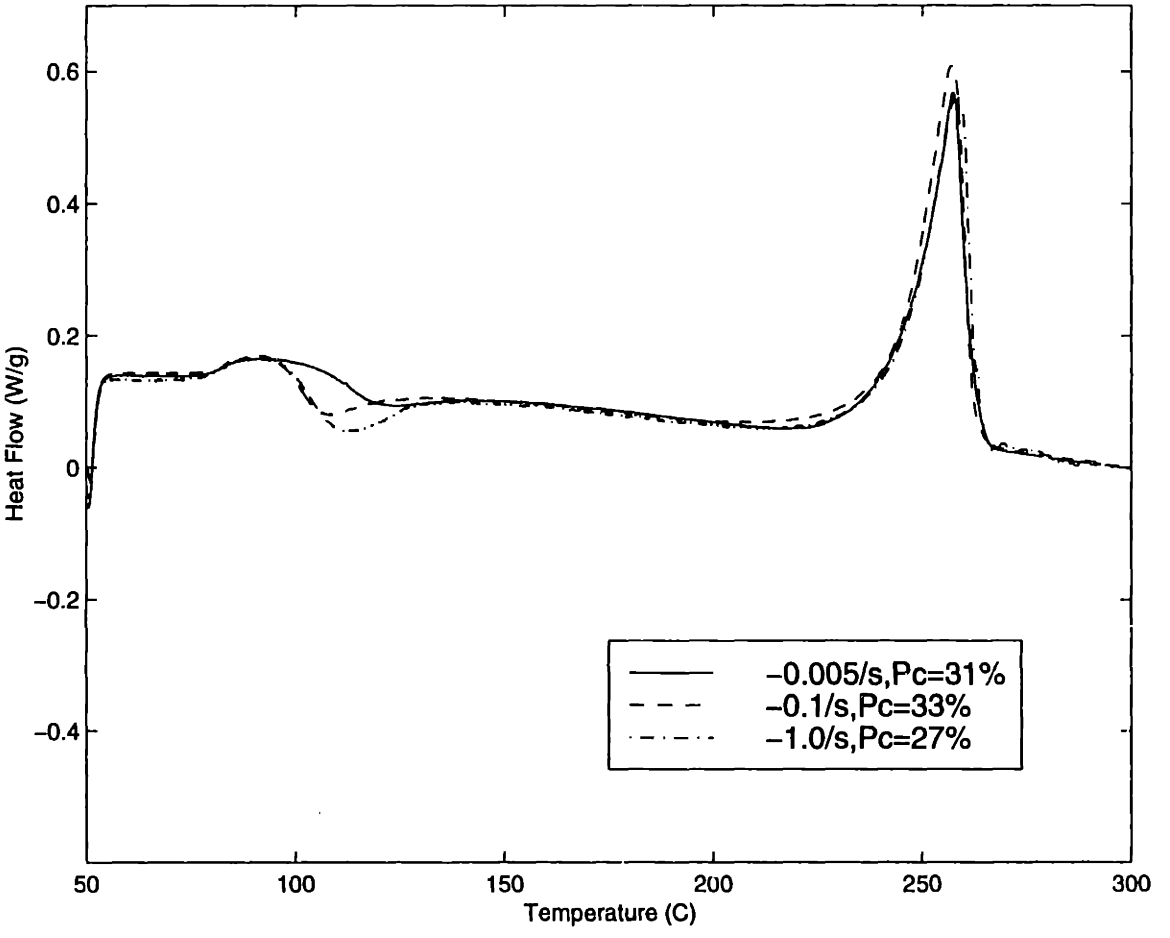

Figure 2.33: DSC thermograms of specimens deformed in uniaxial compression at $90°C$ with a final strain level -2.0, and crystallinities as indicated

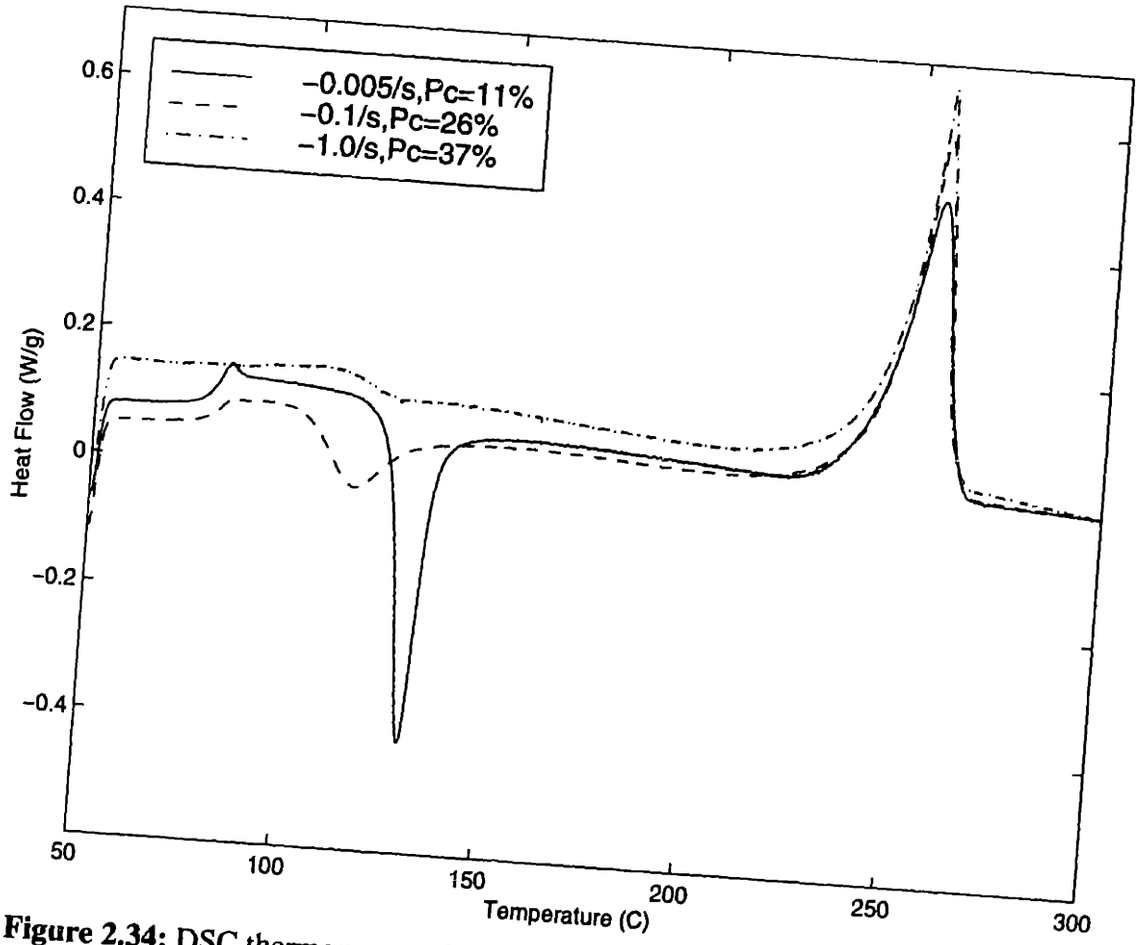

Figure 2.34: DSC thermograms of specimens deformed in uniaxial compression at $100°C$ with a final strain level -2.0, and crystallinities as indicated

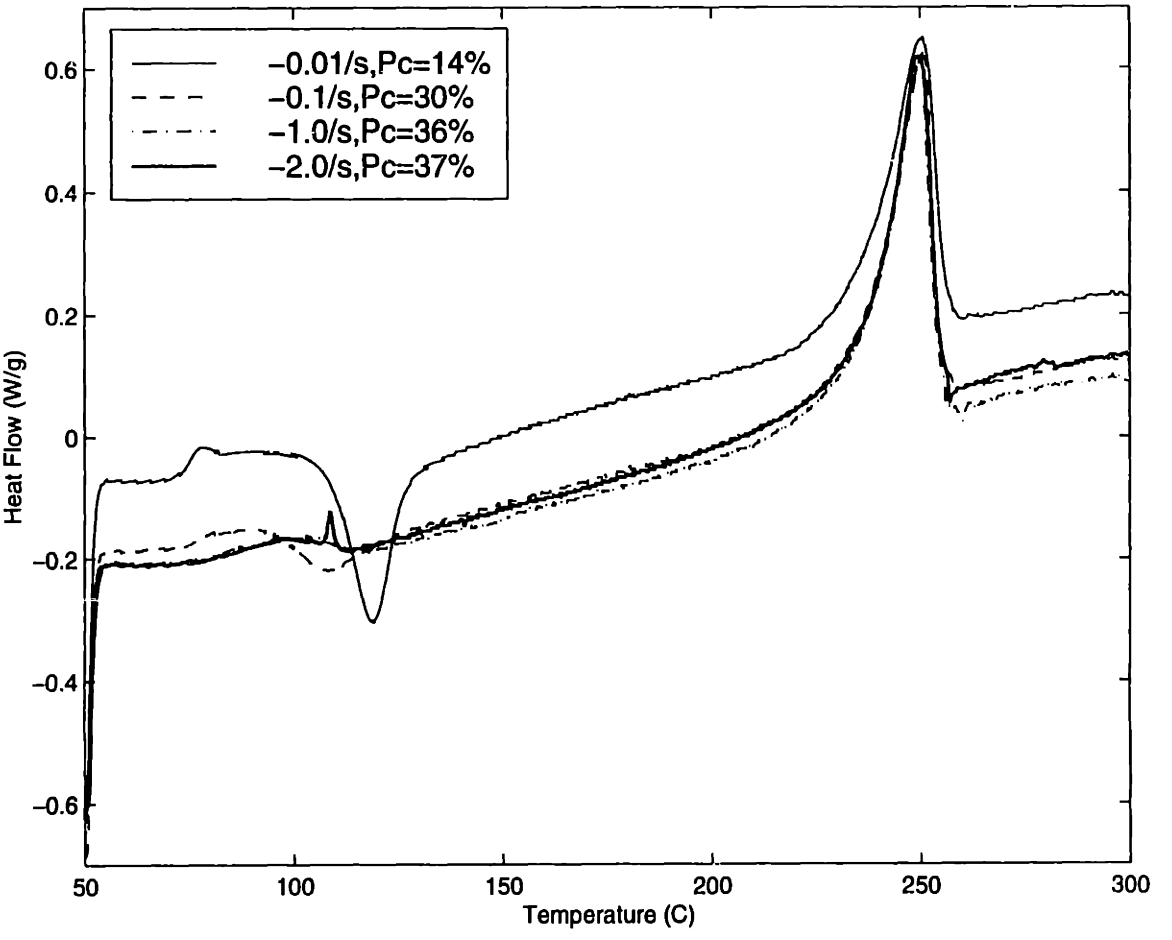

Figure 2.35: DSC thermograms of specimens deformed in uniaxial compression at $105°C$ with a final strain level -2.0, and crystallinities as indicated

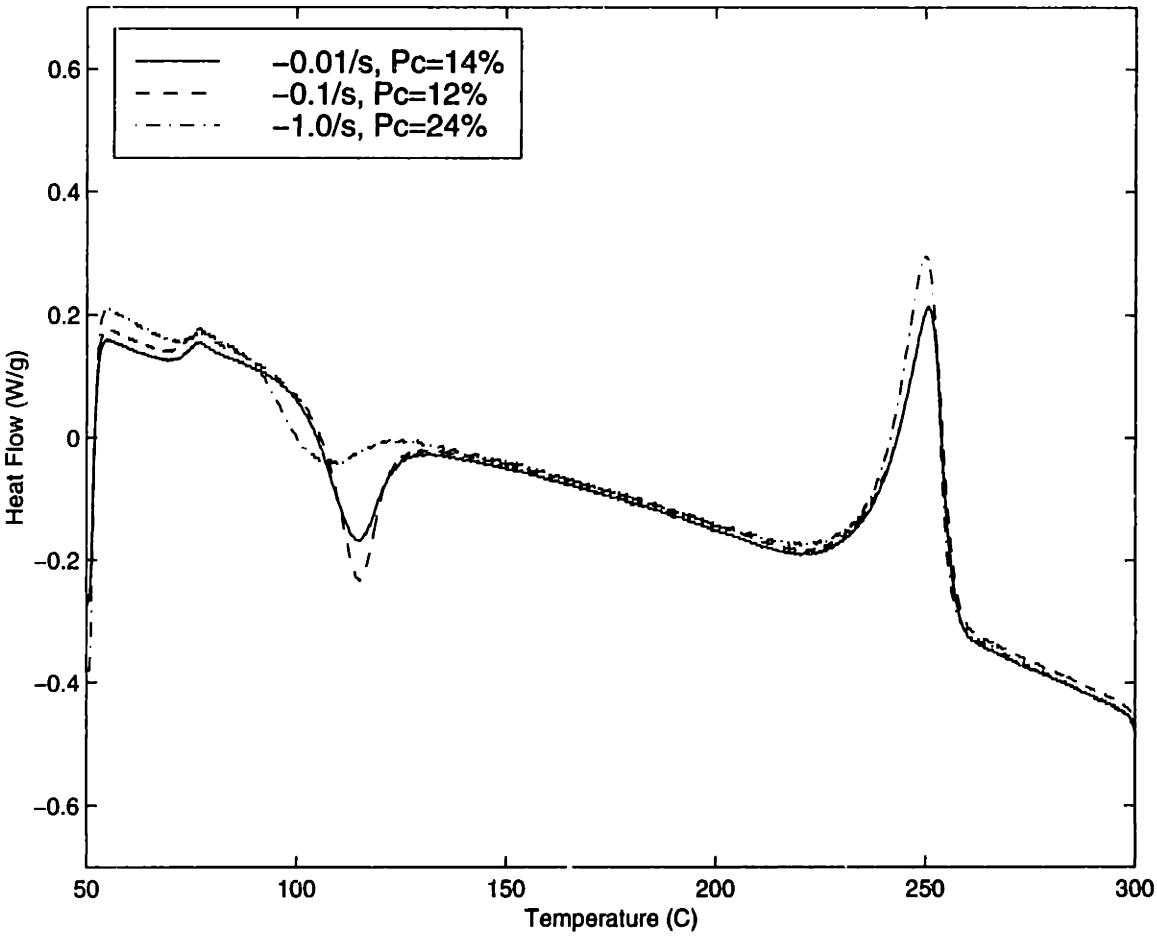

Figure 2.36: DSC thermograms of specimens deformed in plane strain compression at $25°C$ with a final strain level -1.2, and crystallinities as indicated

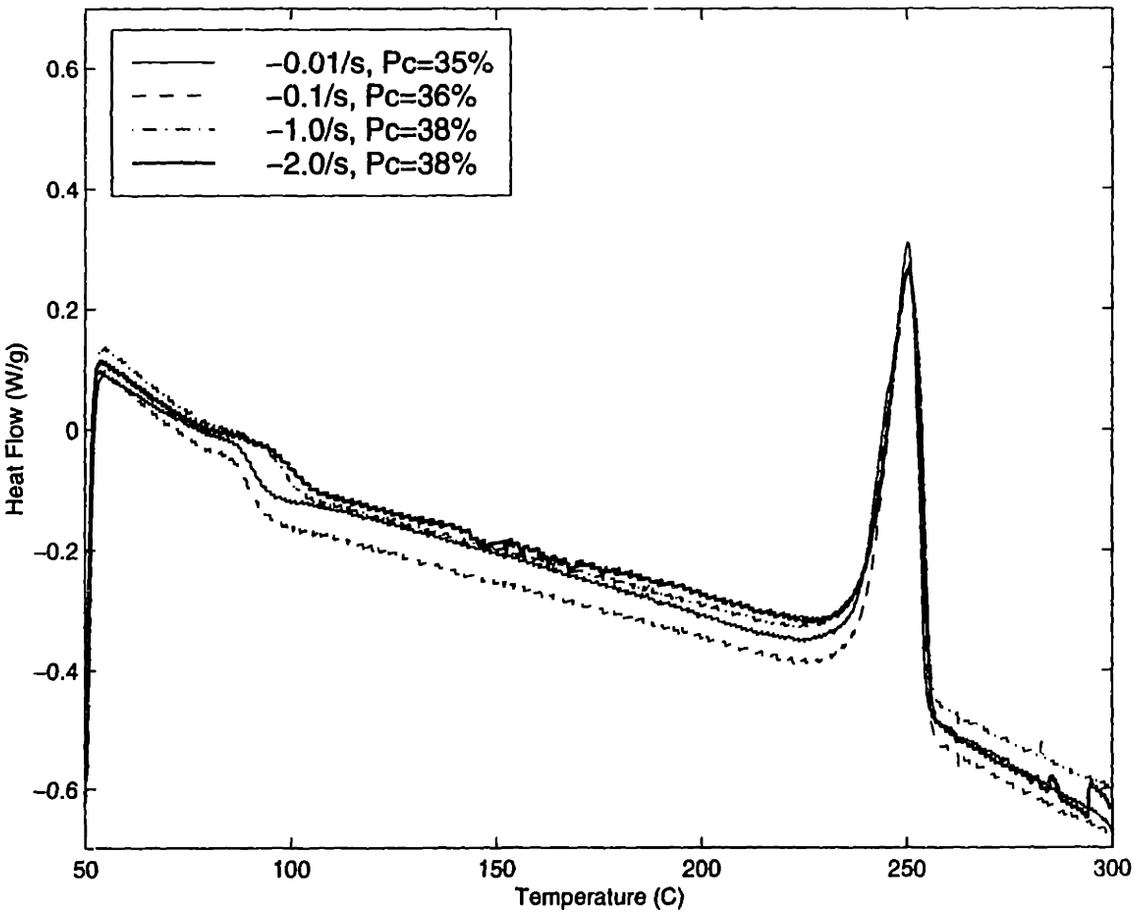

Figure 2.37: DSC thermograms of specimens deformed in plane strain compression at $80°C$ with a final strain level -1.6, and crystallinities as indicated

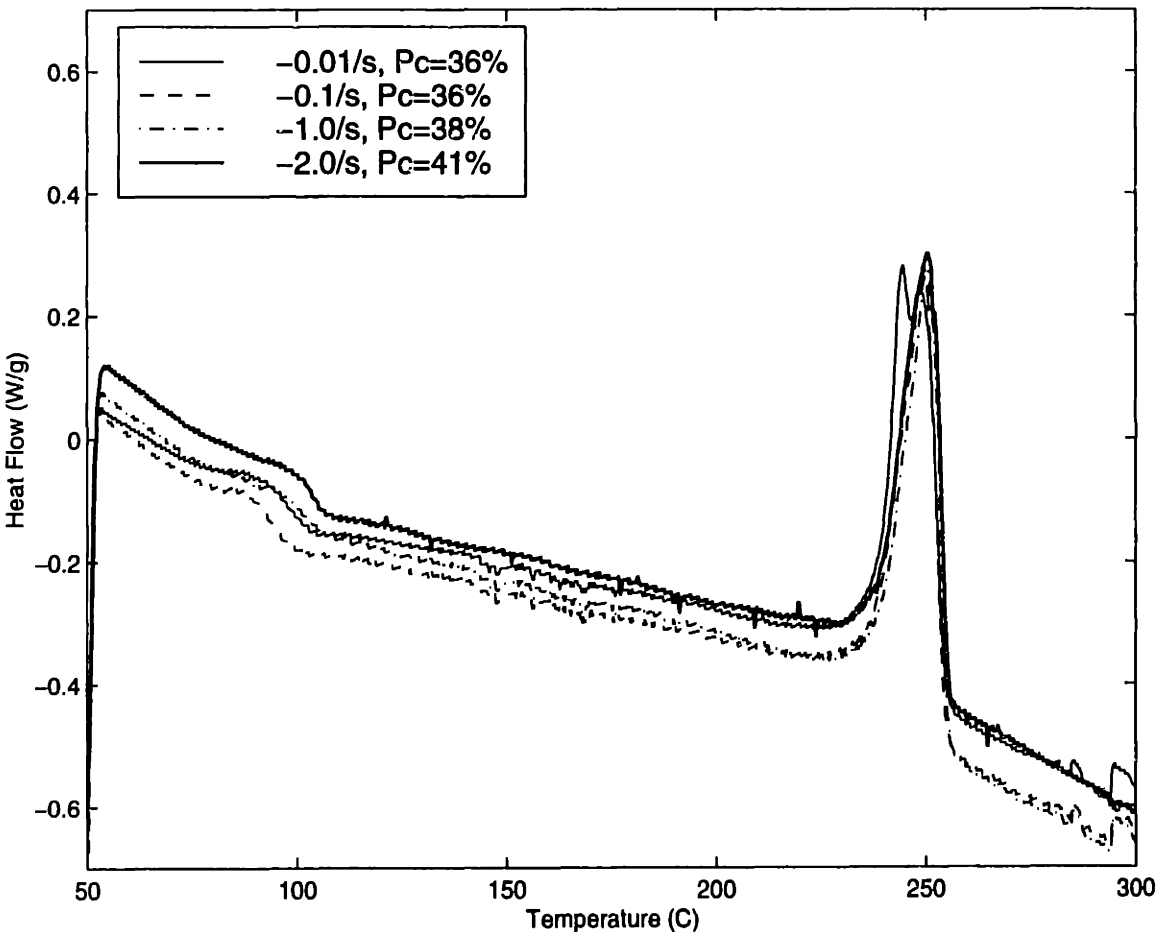

Figure 2.38: DSC thermograms of specimens deformed in plane strain compression at $90°C$ with a final strain level -1.6, and crystallinities as indicated

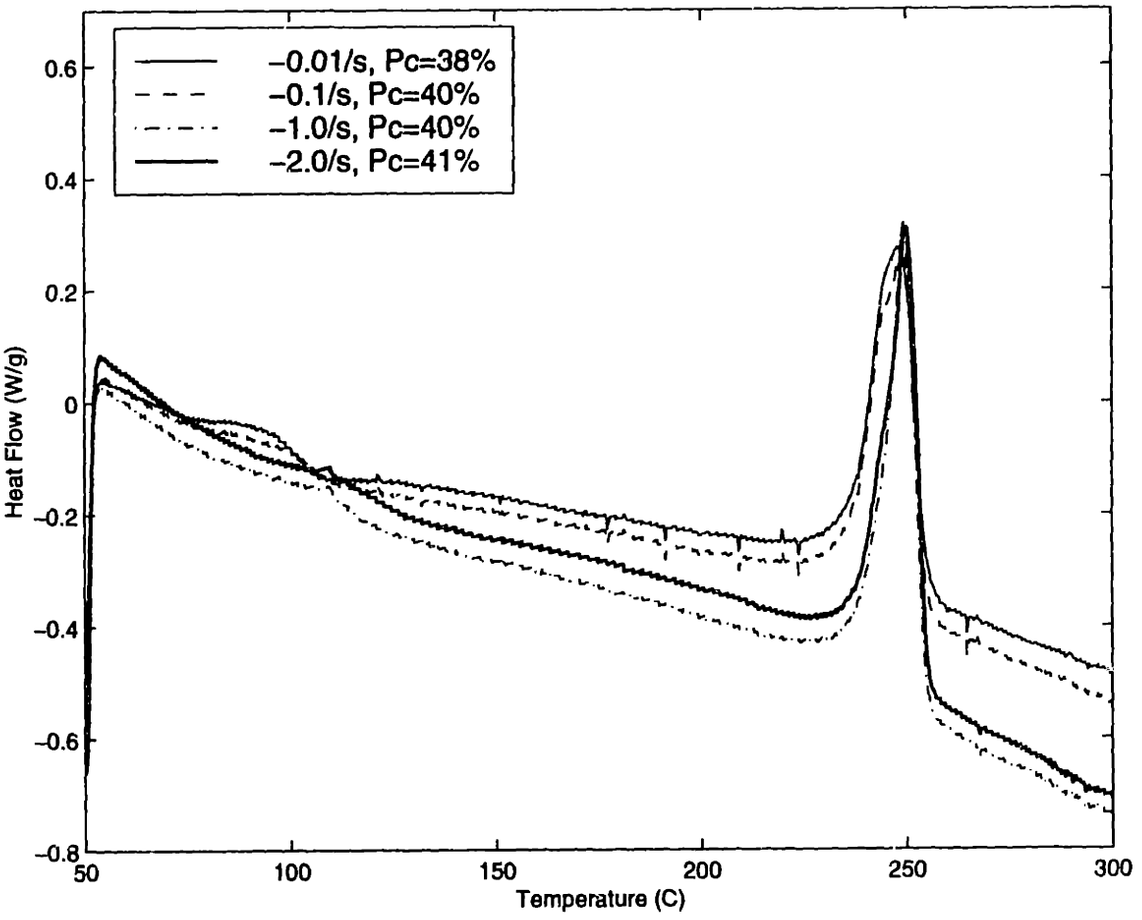

Figure 2.39: DSC thermograms of specimens deformed in plane strain compression at $100°C$ with a final strain level -1.6, and crystallinities as indicated

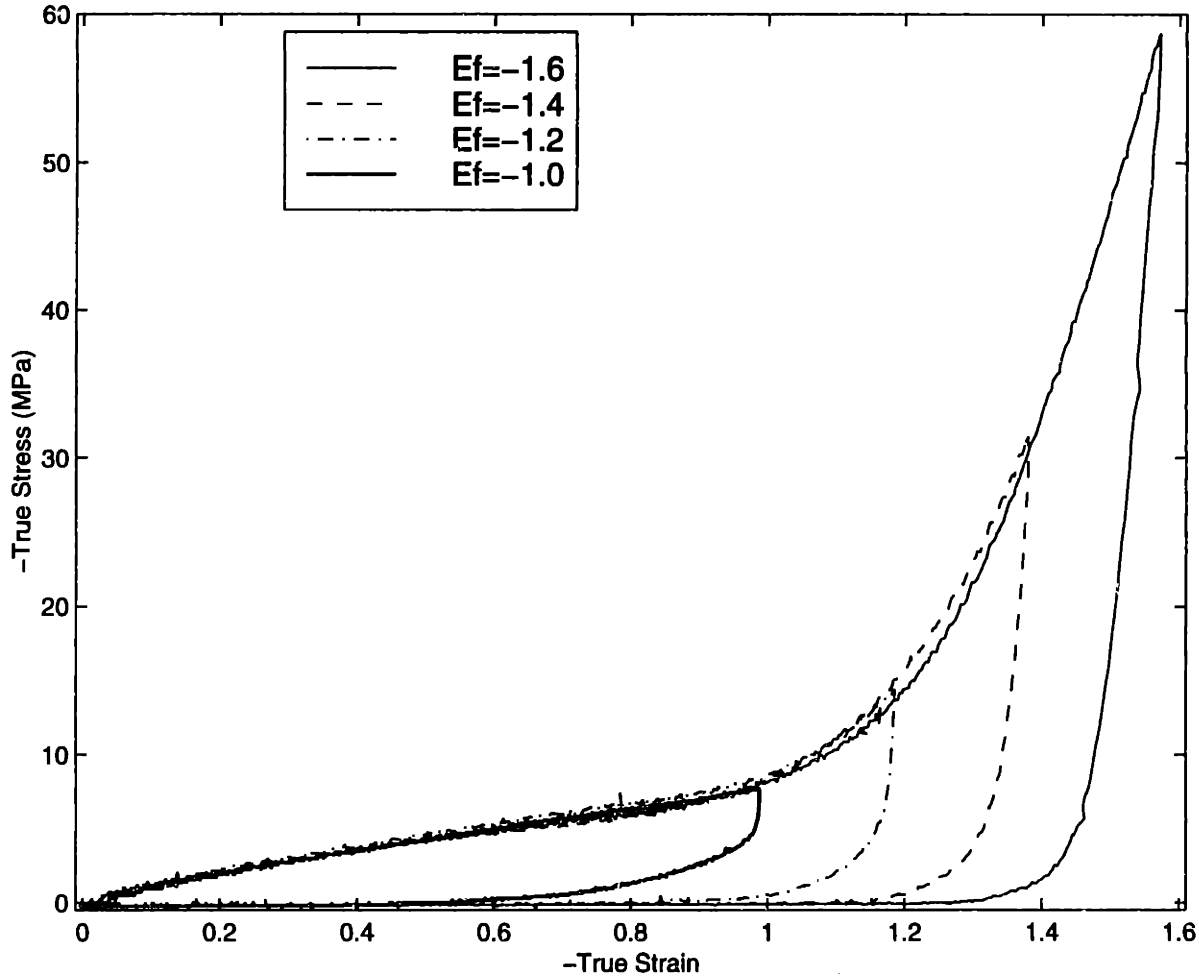

Figure 2.40: Plane Strain Compression Data, Temperature $=90°C$, $\dot{\varepsilon} = -0.1/s$, at different final strains

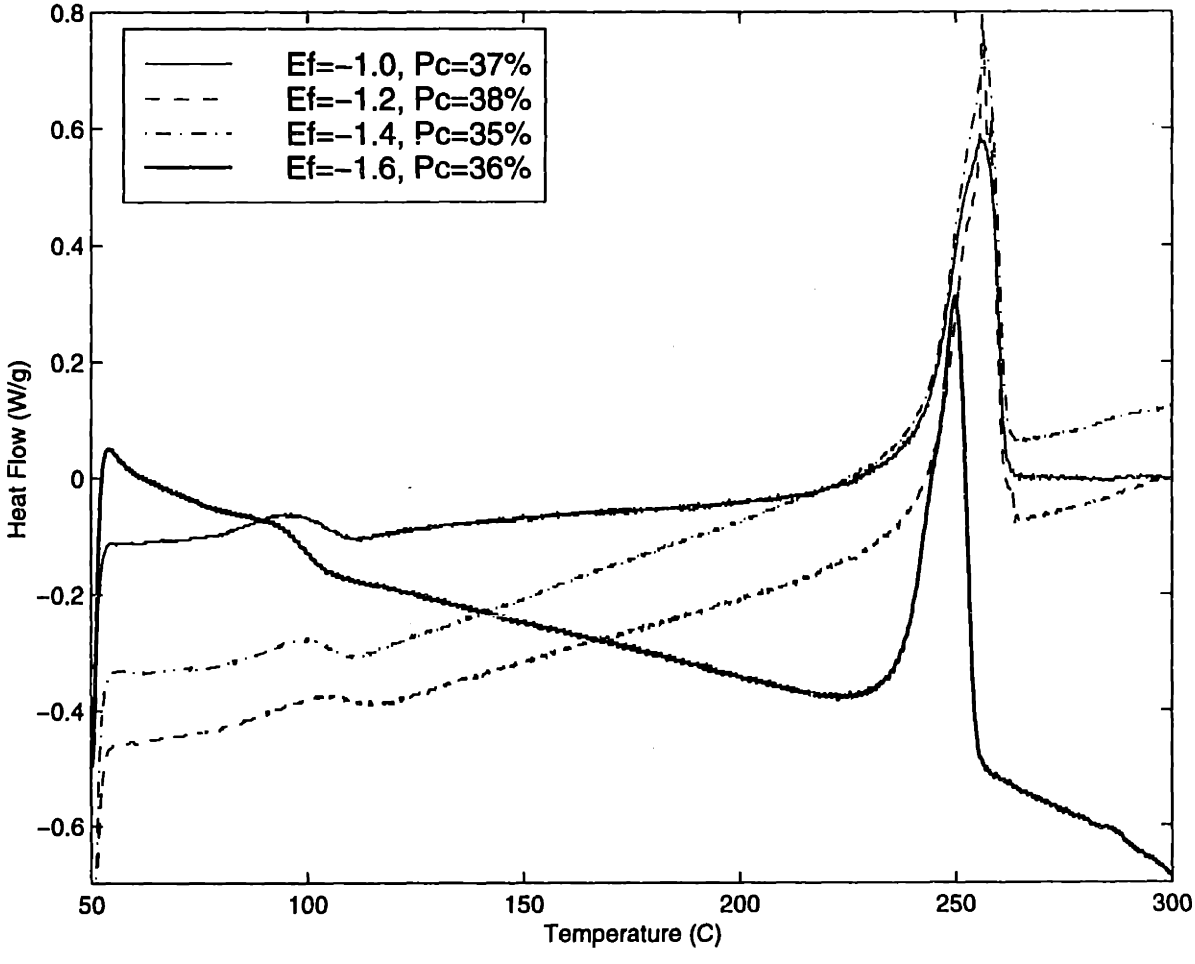

Figure 2.41: DSC thermograms of plane strain compression at $90°C$, $\dot{\varepsilon} = -0.1/s$, at different final strains with indicated crystallinities

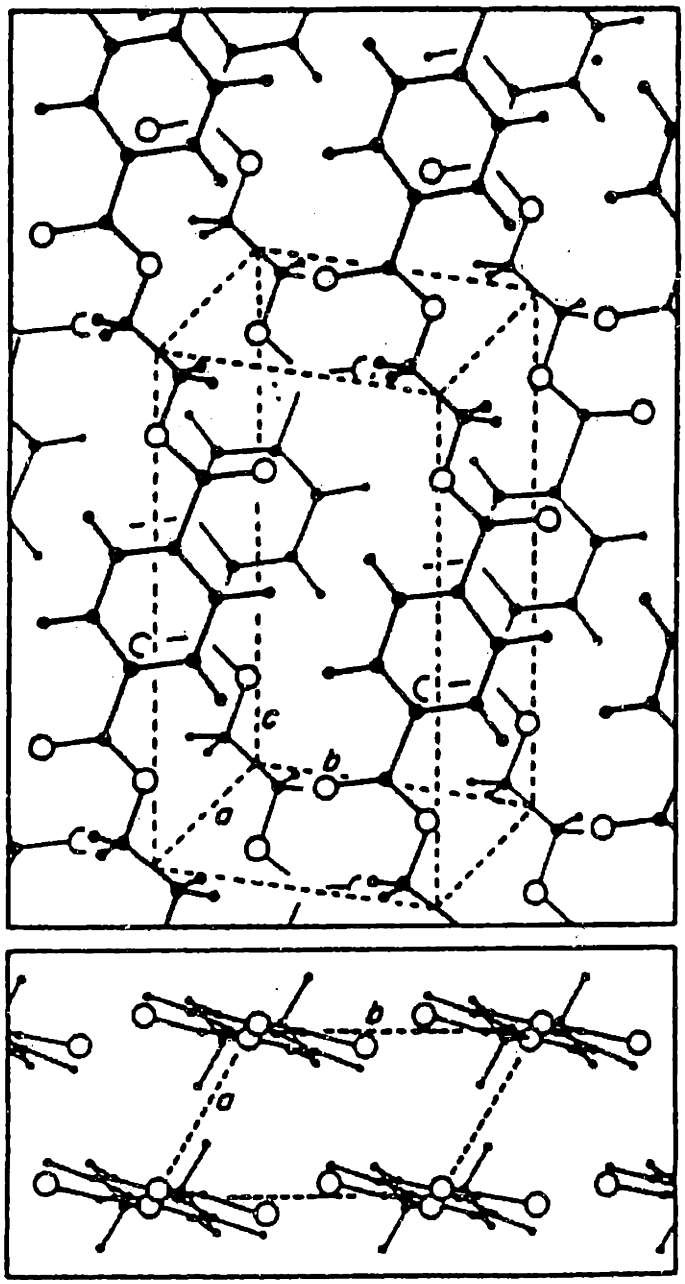

Figure 2.42: Triclinic crystal structure of PET[31]

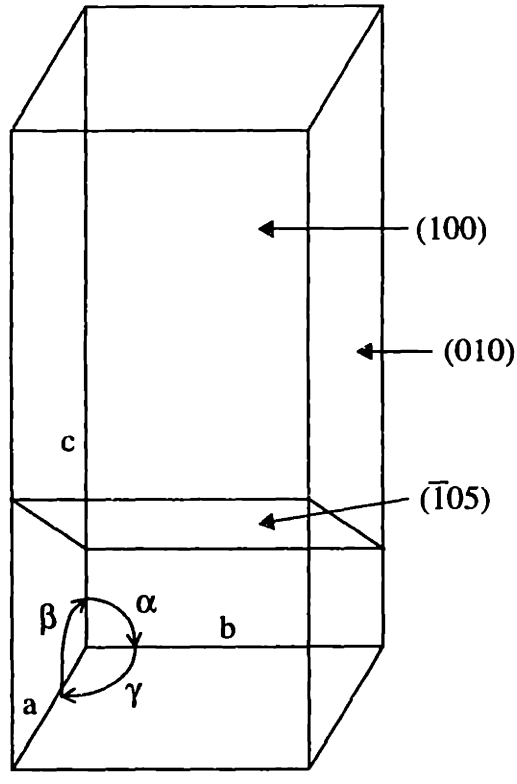

Figure 2.43: PET triclinic unit cell structure with crystallographic slip planes

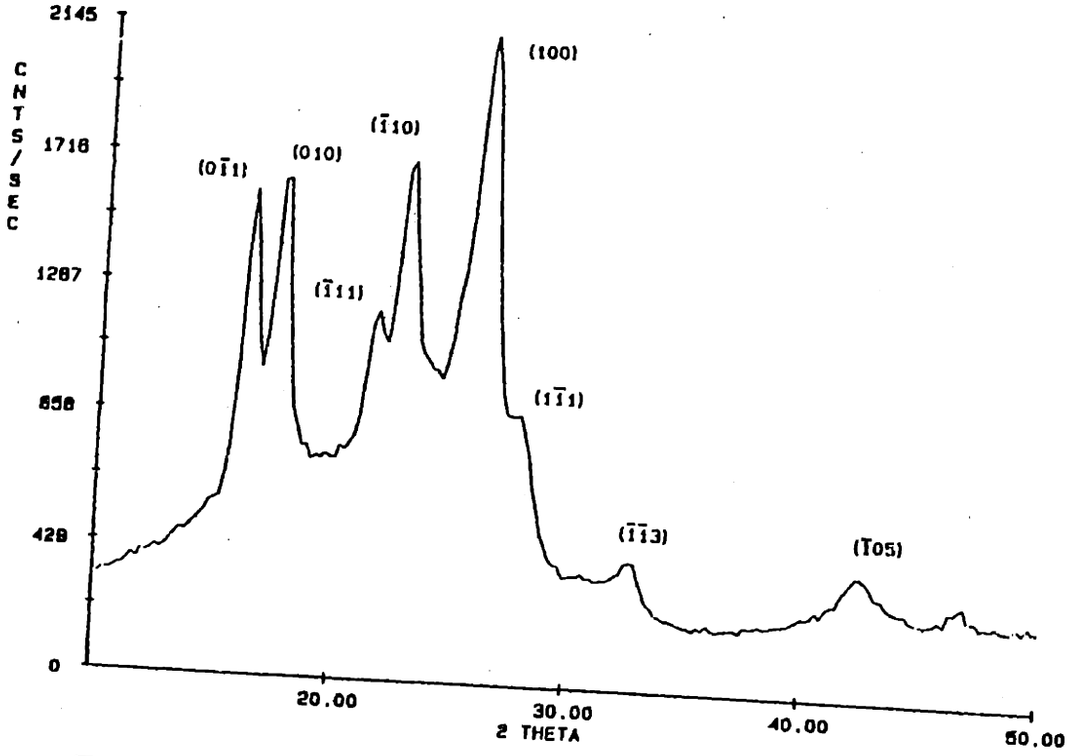

Figure 2.44: WAXD scan of isotropic semi-crystalline PET[31]

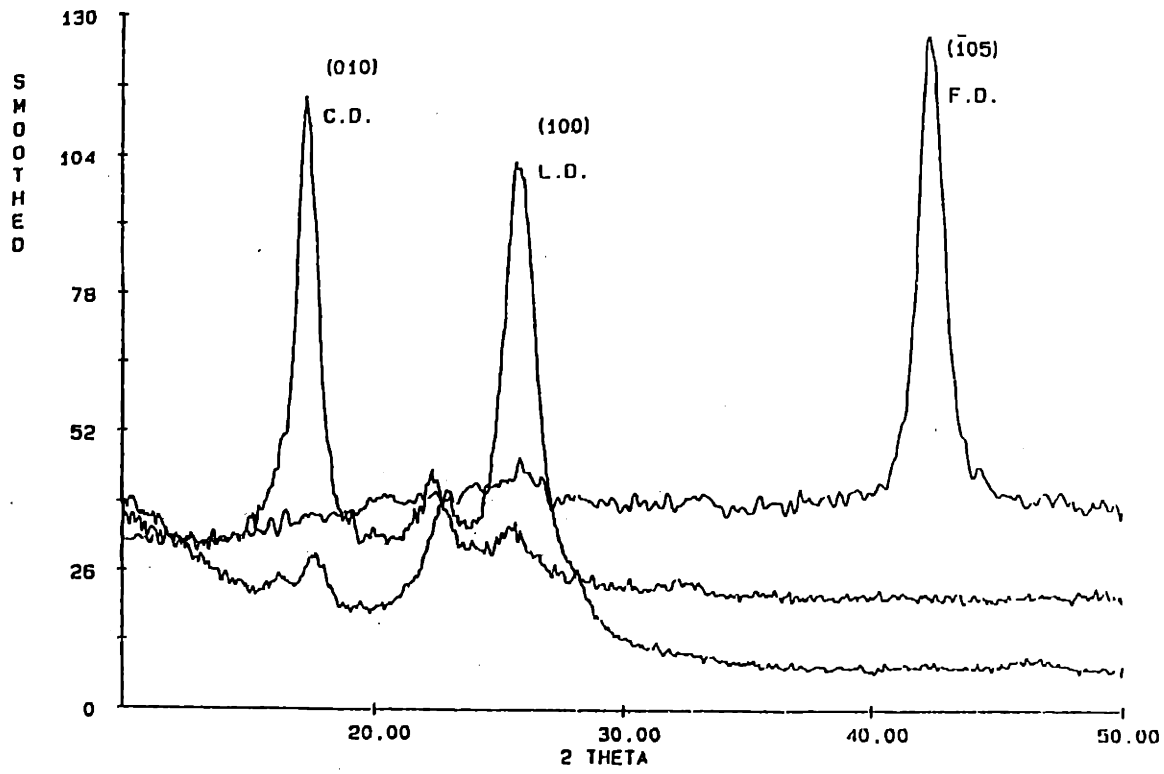

Figure 2.45: WAXD scan of fully textured semi-crystalline PET[31]

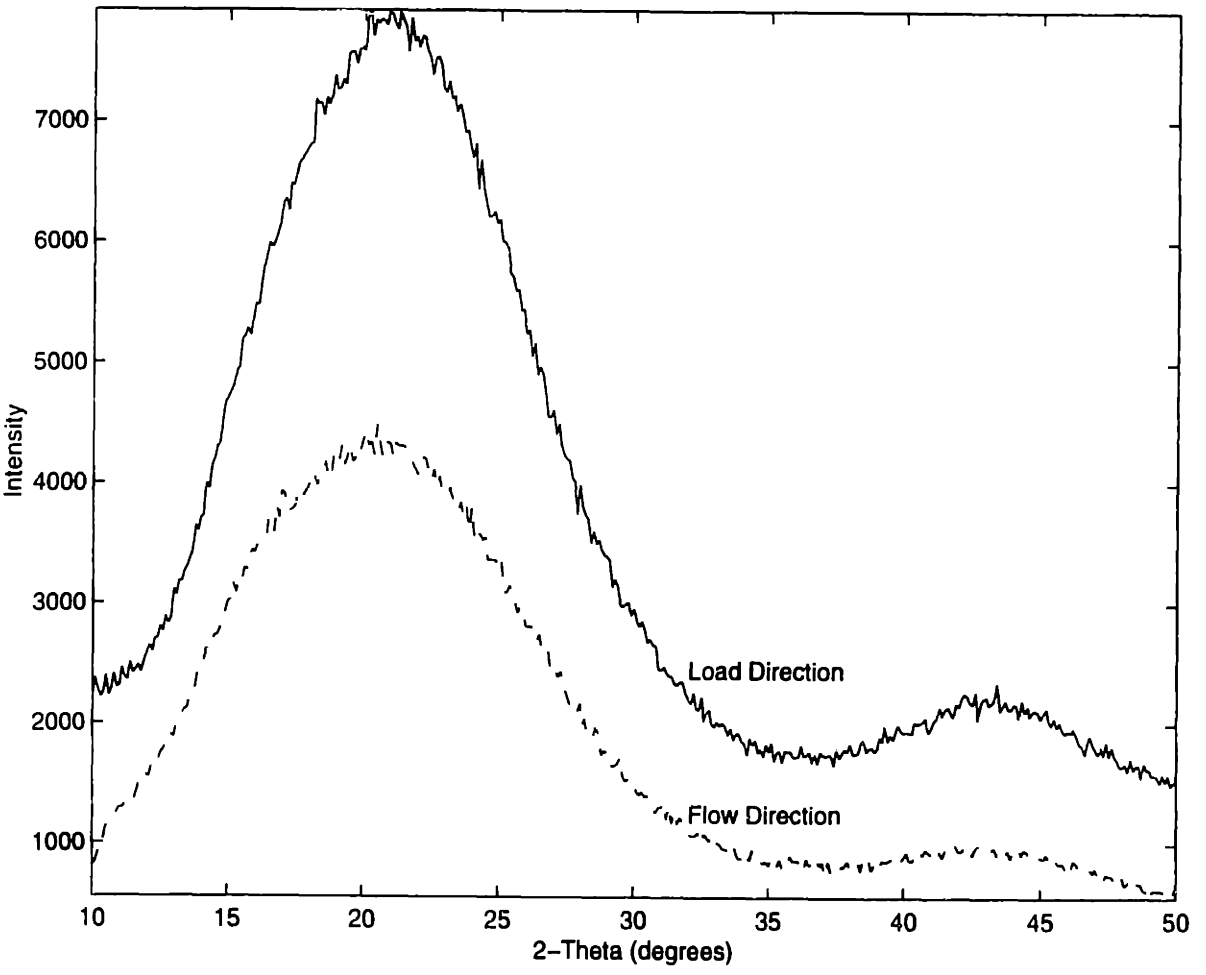

Figure 2.46: WAXD scan of the as-received PET

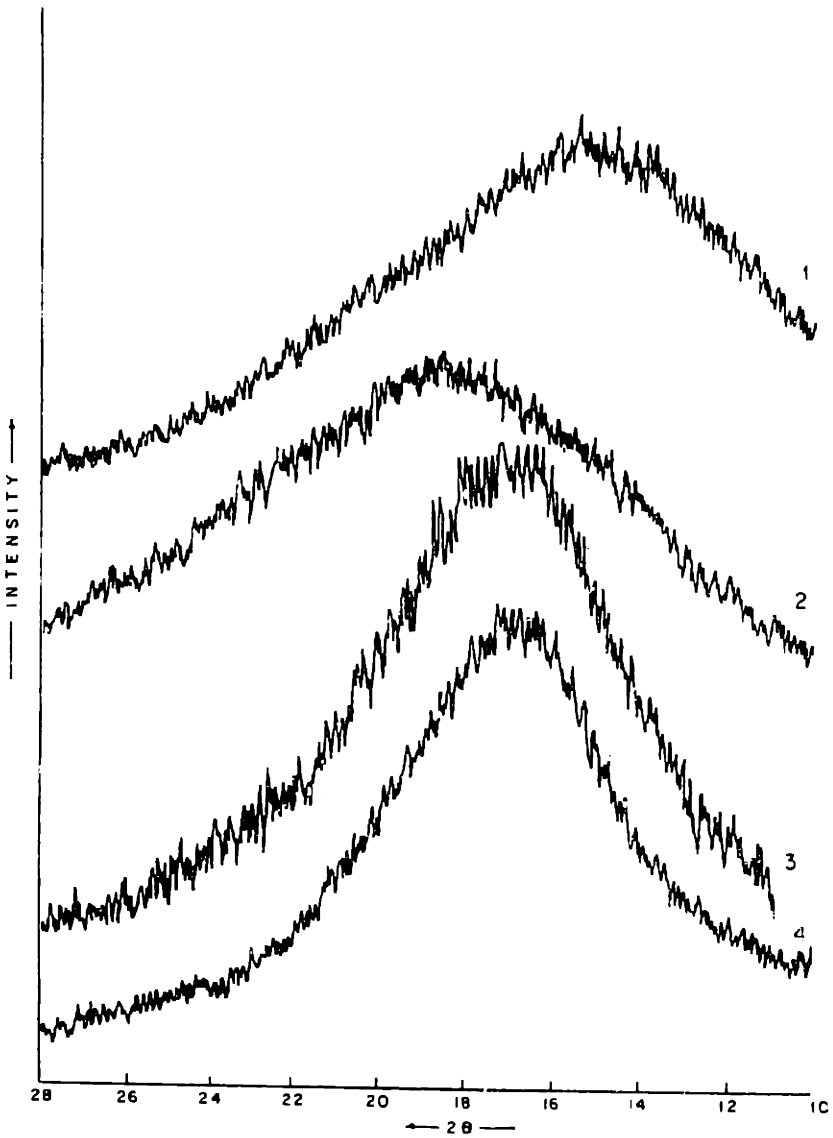

Figure 2.47: Typical WAXD scans of other amorphous polymers, where the polymers are: (1) TM Bis-IPC/TPC, (2) PhPha-IPC/TPC, (3) Bis-A-IPC/TPC, (4) Polycarbonate [28]

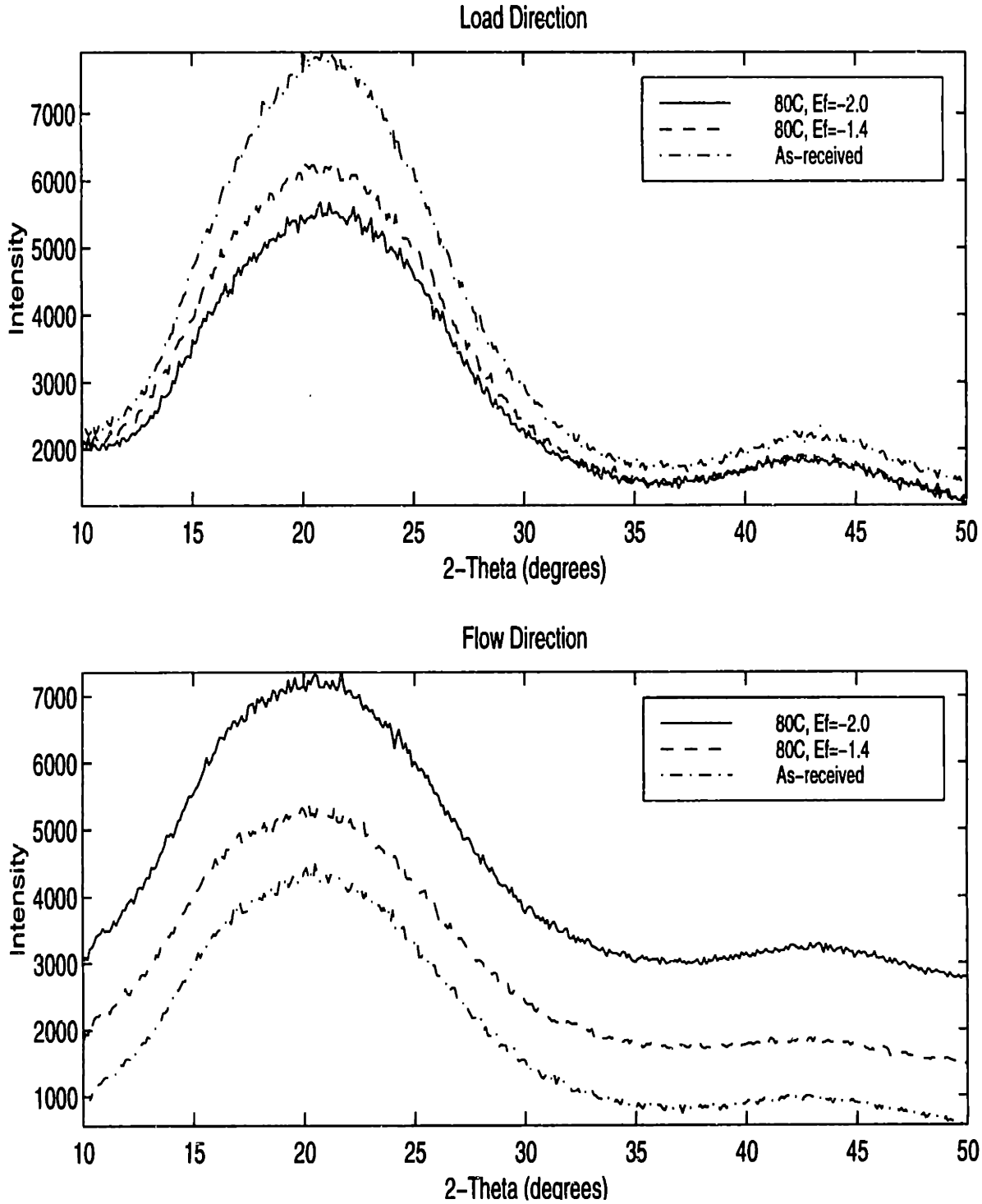

Figure 2.48: WAXD scans of specimens deformed in uniaxial compression at (1)80°C, -0.01/s, final strain of -2.0, (2)80°C, -0.01/s, final strain of -1.4, and (3)as-received material

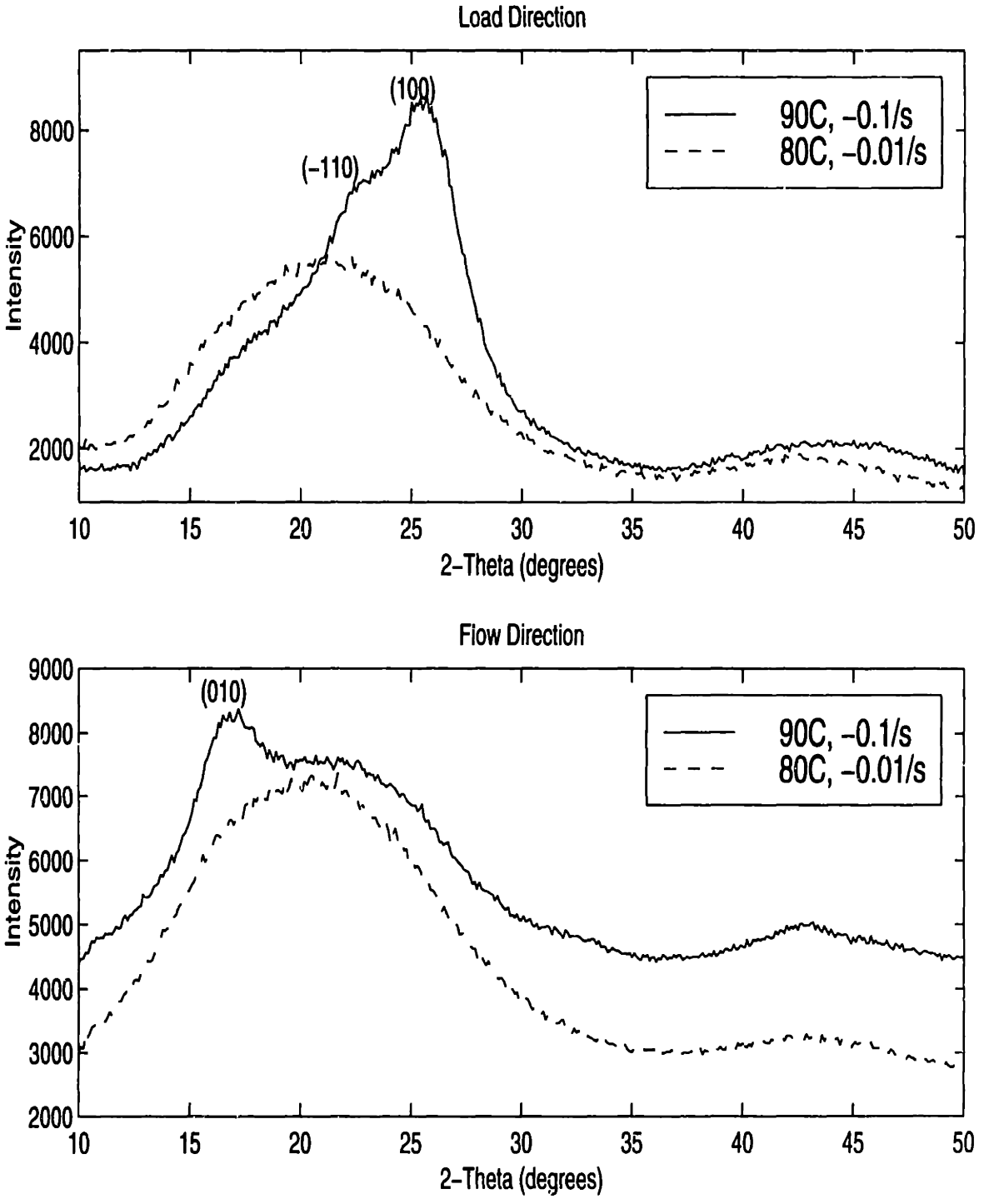

Figure 2.49: WAXD scans of specimens deformed in uniaxial compression to a final strain of -2.0 at (1) 90°C at a strain rate of -0.1/s and (2) 80 °C at a strain rate of -0.01/s

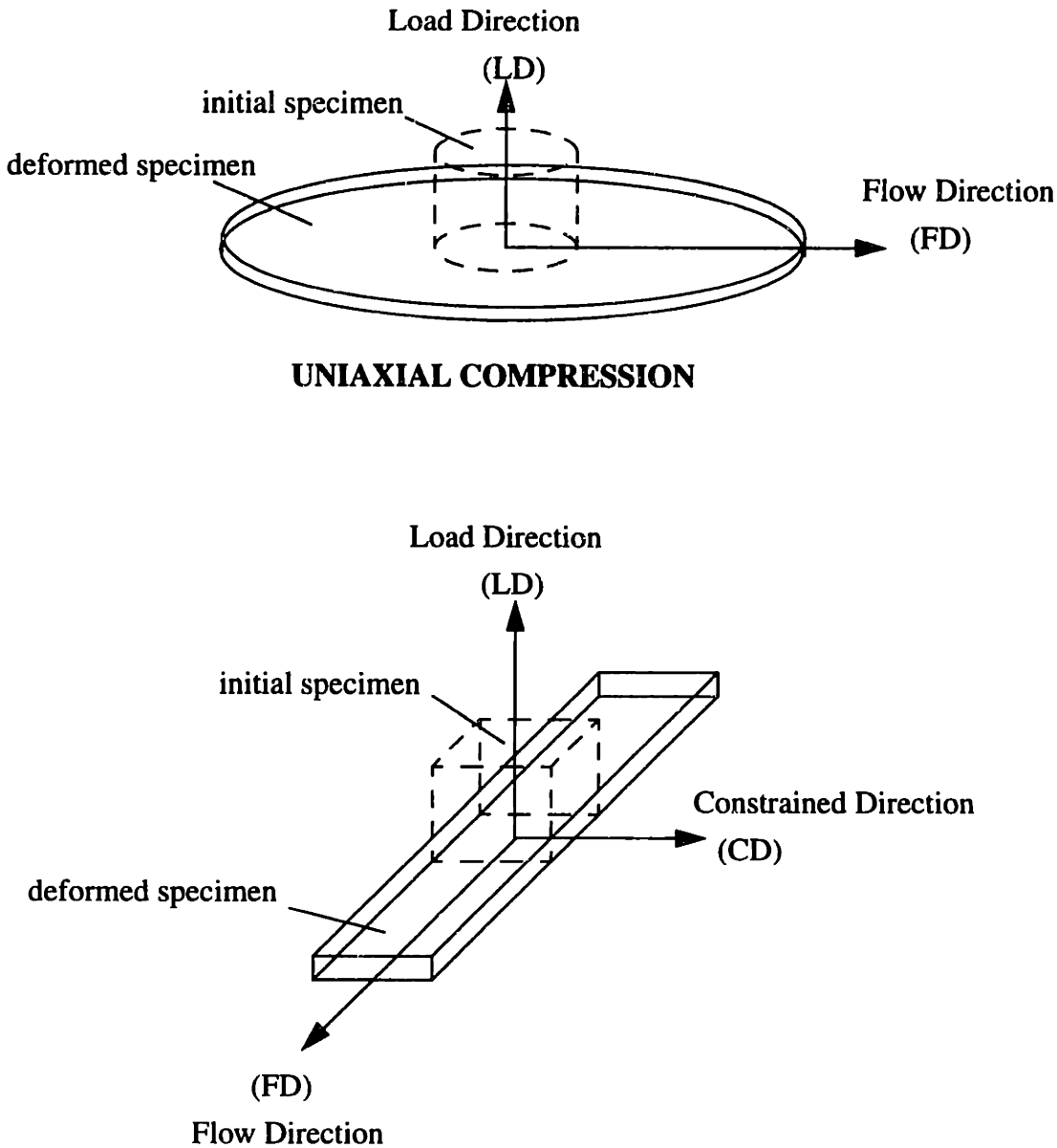

Figure 2.50: Uniaxial and plane strain deformation directions

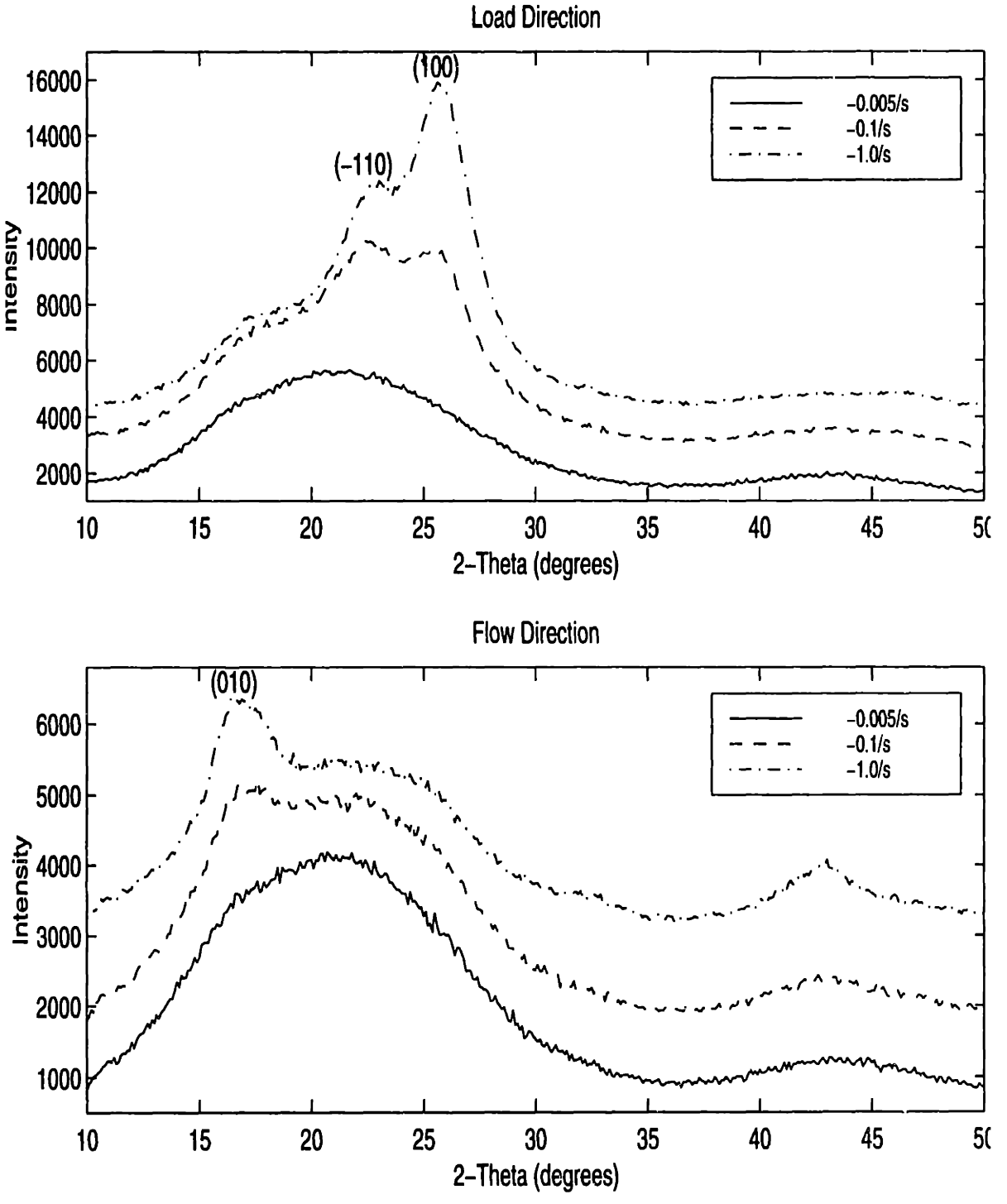

Figure 2.51: WAXD scans of specimens deformed in uniaxial compression at $100°C$ to a final strain of -2.0

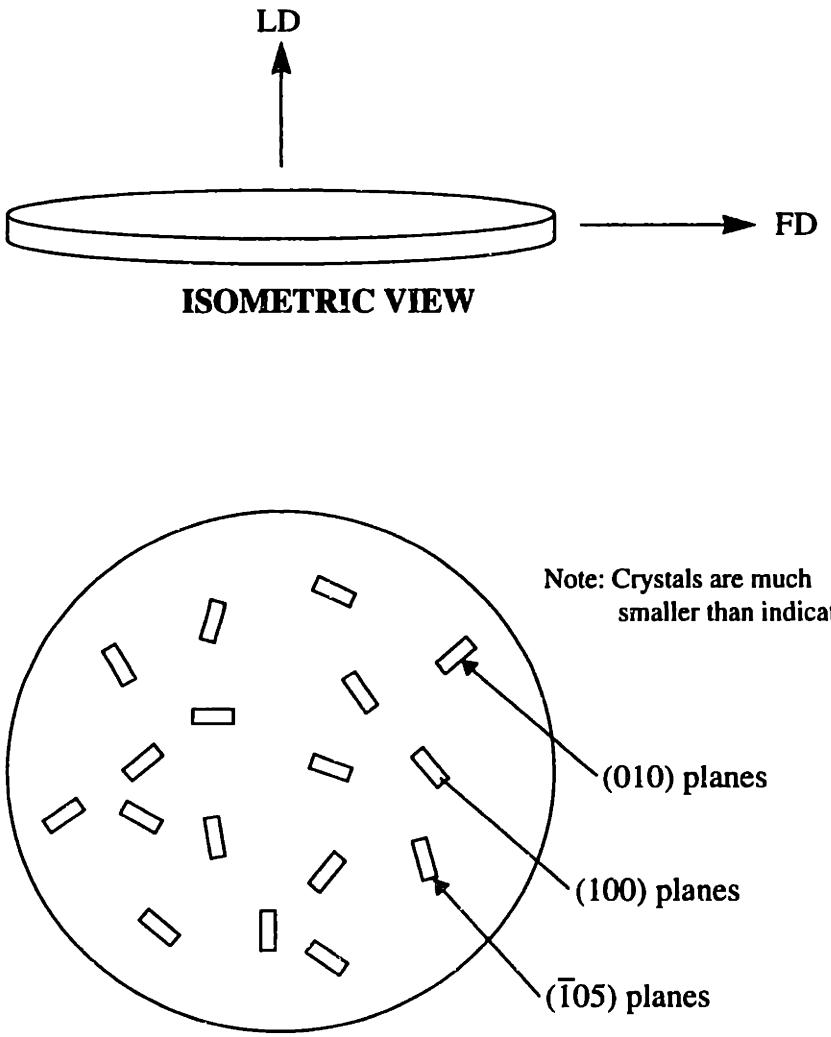

Figure 2.52: Orientation of the crystals in specimens deformed in uniaxial compression; crystals are oriented with the (100) planes perpendicular to the load direction, and the (010) and $(\bar{1}05)$ planes perpendicular to the page with their normals pointing in random directions parallel to the flow direction

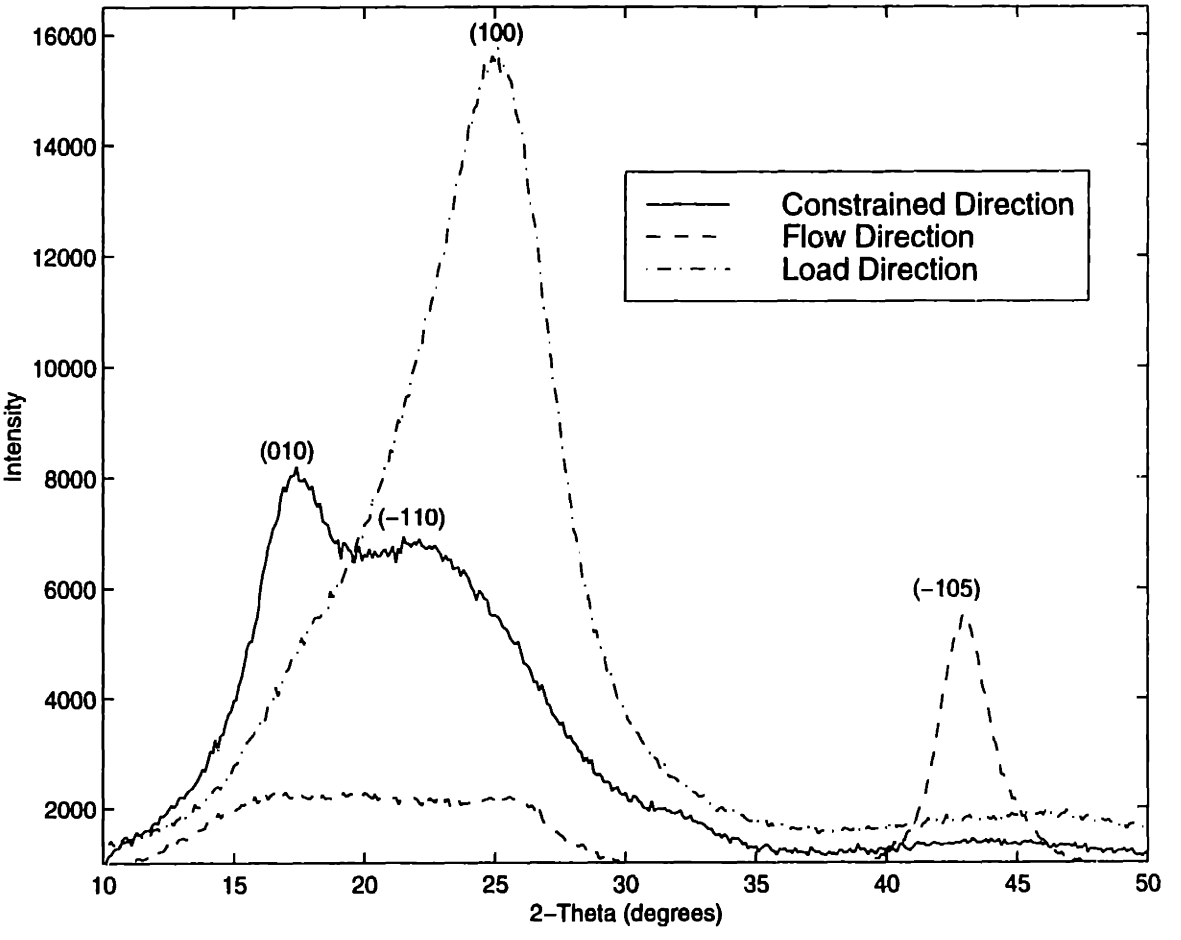

Figure 2.53: WAXD scans of a specimen deformed in plane strain compression at $80°C$ at a strain rate of -0.1/*s* and to a final strain of -1.6

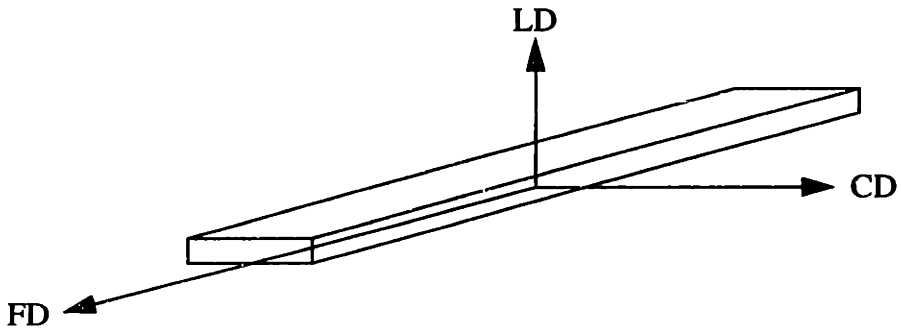

ISOMETRIC VIEW

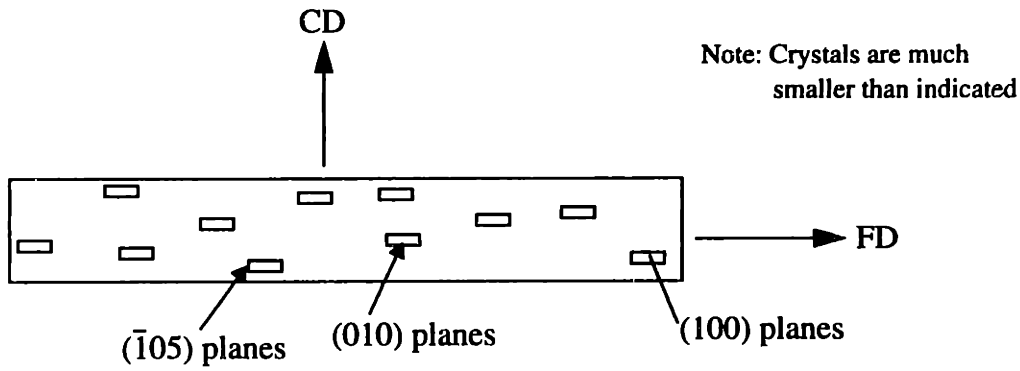

TOP VIEW
(LD coming out of the plane of the page)

Figure 2.54: Orientation of the crystals in specimens deformed in plane strain compression; crystals are oriented with the (100) planes perpendicular to the load direction, the (010) planes perpendicular to the constrained direction, and the $(\bar{1}05)$ perpendicular to the flow direction

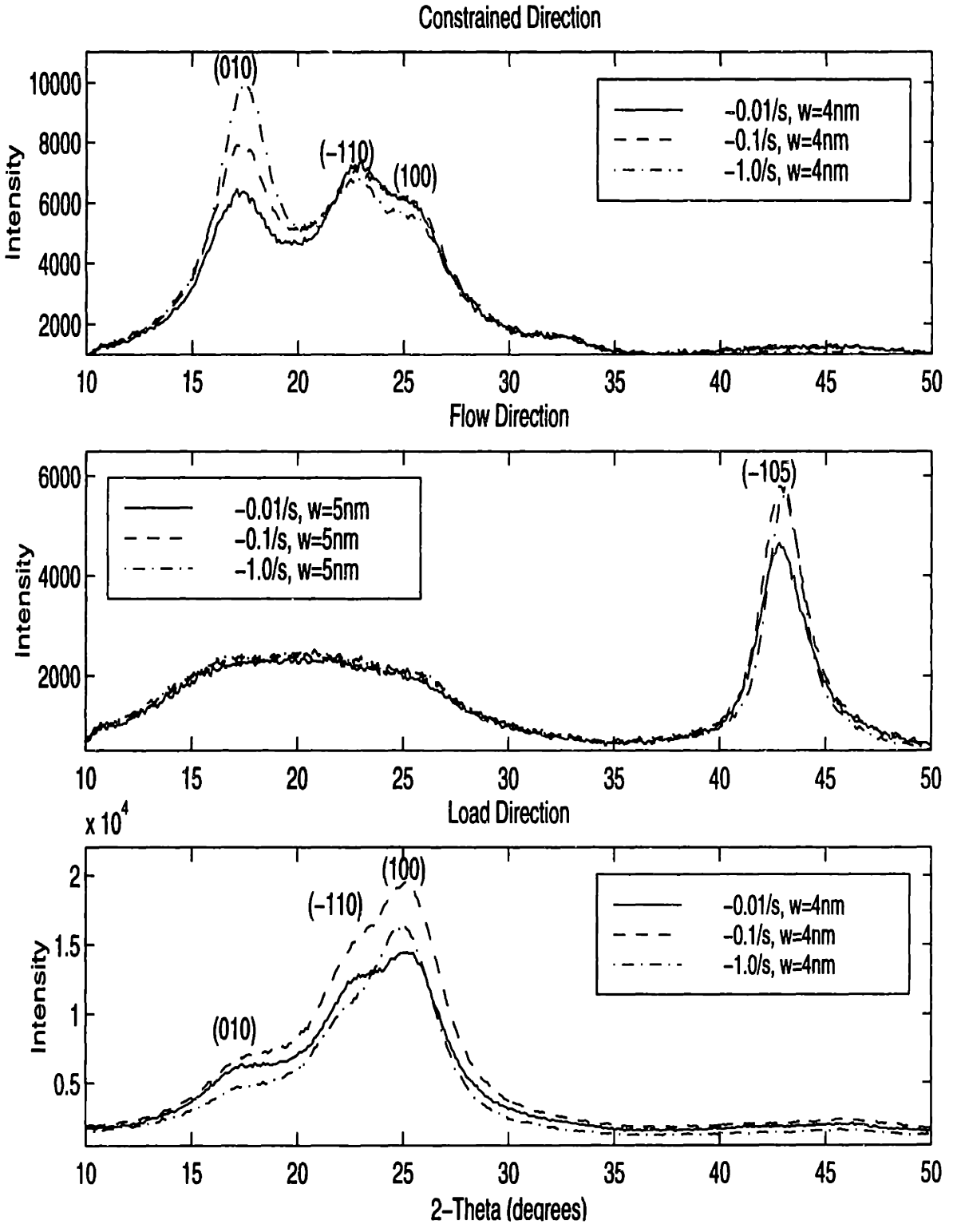

Figure 2.55: WAXD scans of specimens deformed in plane strain compression at 90°C to a final strain of -1.6

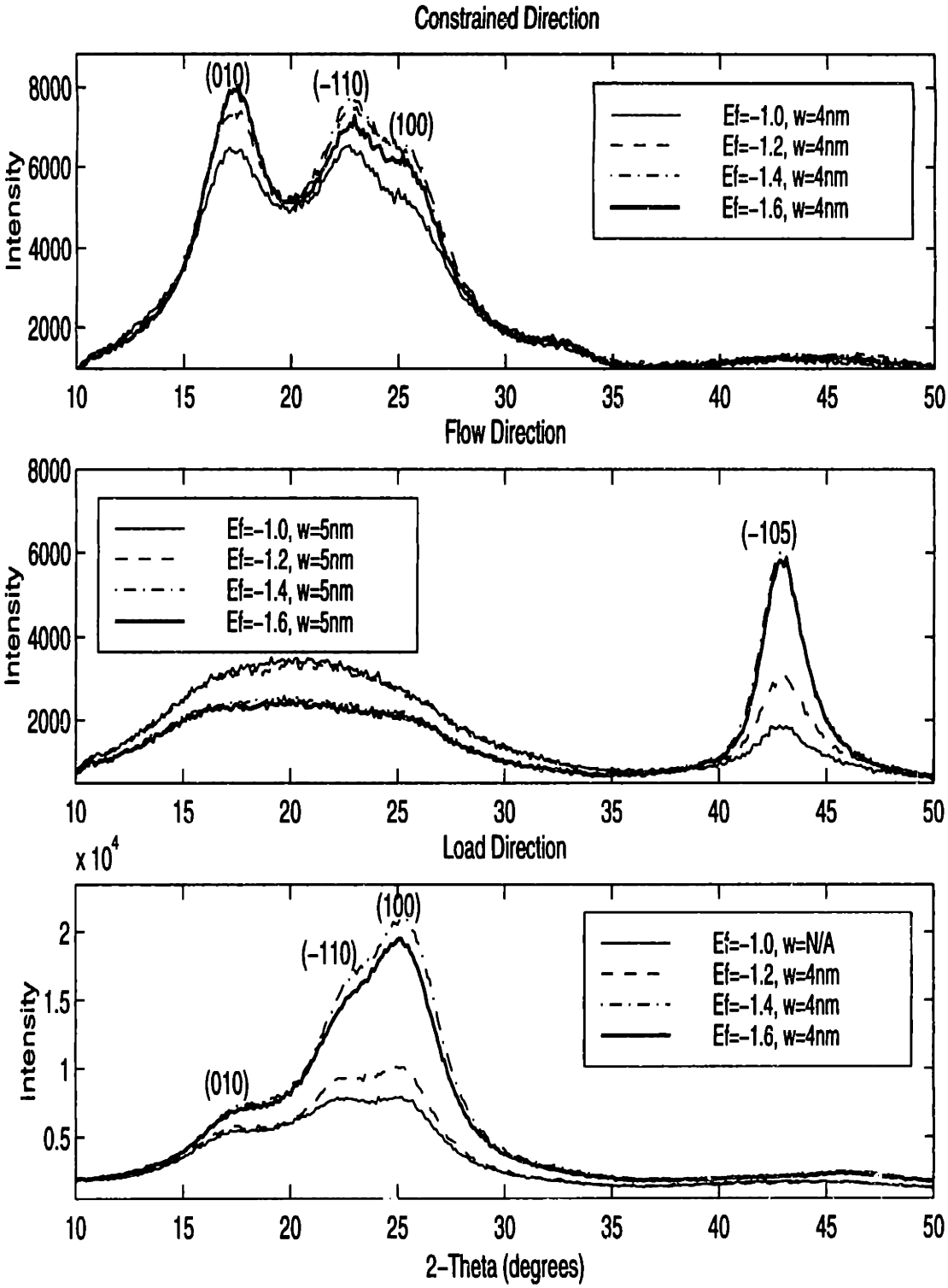

Figure 2.56: WAXD scans of specimens deformed in plane strain compression at $90°C$ at a strain rate of -0.1/s to different final strains

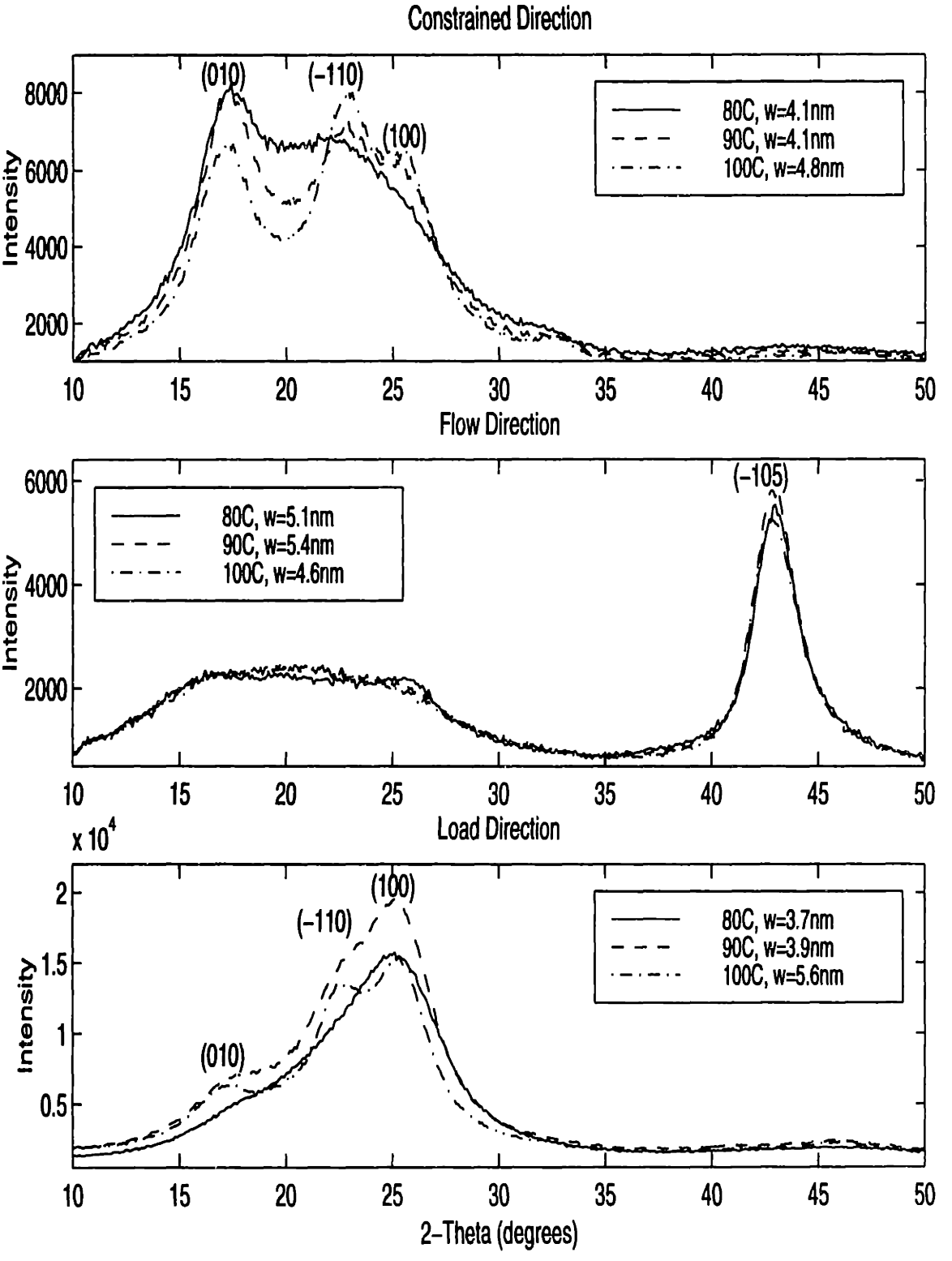

Figure 2.57: WAXD scans of specimens deformed at a strain rate of -0.1/s to a final strain of -1.6

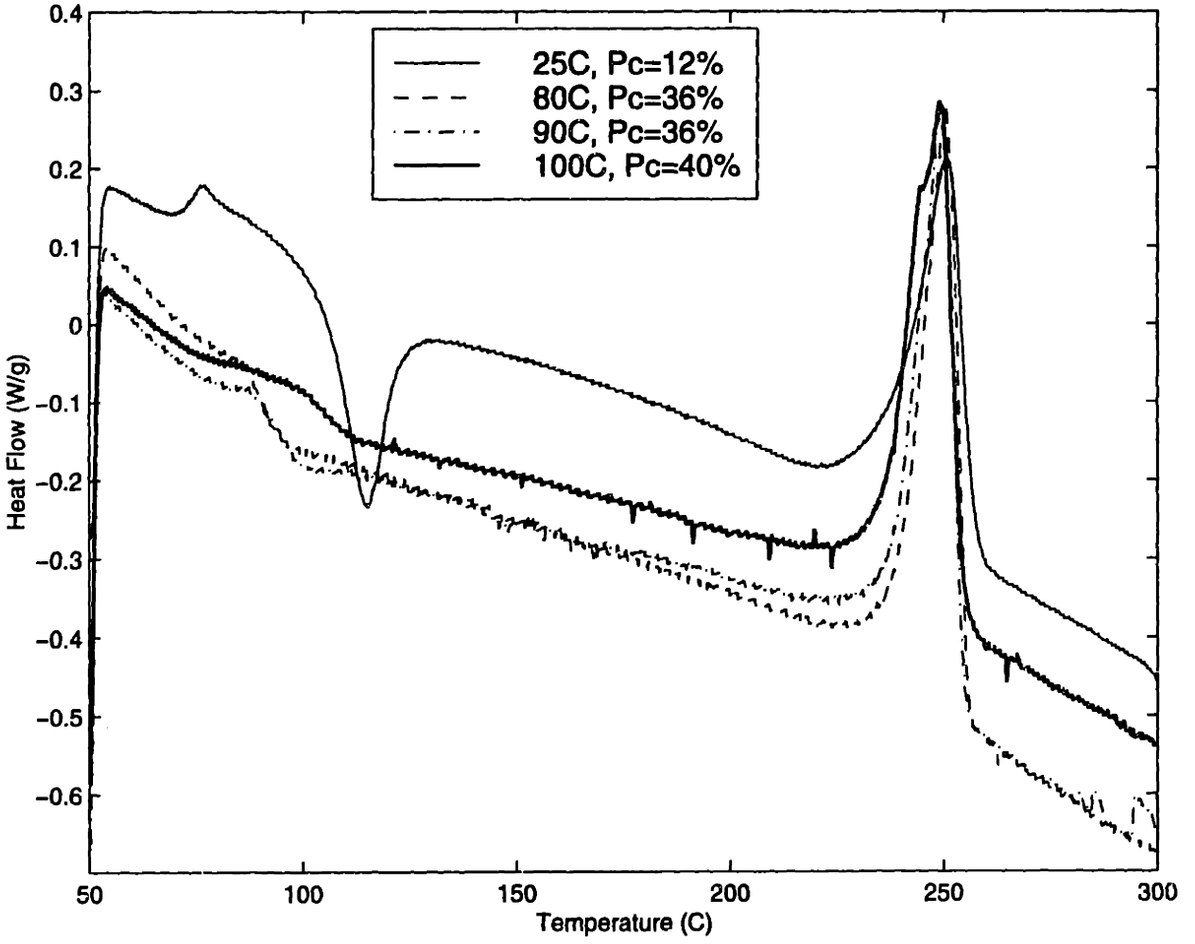

Figure 2.58: DSC thermograms of specimens deformed in plane strain compression at a strain rate of -0.1/s to a final strain of -1.6

Chapter 3

Constitutive Model

3.1 Background

The elastic-viscoplastic behavior of amorphous polymers has been modeled by several investigators. One of the earliest attempts to model the temperature dependent yield behavior of amorphous polymers in the glass transition regime was made by Robertson [29]-[30]. Robertson considered the deformation resistance to arise from intramolecular interactions. The theory presented by Robertson was based on the idea that the applied shear stress induces structural changes in the chain configuration decreasing the intramolecular energy barrier amplitude. The work done by the shear stress decreases the energy amplitude between the two rotational states, *trans*, or low-energy state, and *cis*, or flexed state. The maximum shear strain rate, $\dot{\gamma}_{max}$, induced by the shear stress, τ, is given approximately by

$$\dot{\gamma}_{max} = \frac{\tau}{\eta_g} \exp\left\{2.303\left[\left(\frac{c_1^{\,g} c_2^{\,g}}{\theta_1 - T_g - c_2^g}\right)\left(\frac{\theta_1}{T}\right) - c_1^{\,g}\right]\right\} \tag{3.1}$$

where η_g is the viscosity of a glass at the glass transition temperature, c_1^g and c_2^g are the two WLF equation parameters, T is the temperature, θ_1 is a fictive temperature where the polymer is structurally equivalent to that of the melt, and T_g is the glass transition temperature [30]. A pressure sensitive modification of the Robertson theory was introduced by Duckett, et al. [5] that predicted the yield behavior of isotropic amorphous PMMA and PET over deformation ranges below the glass transition temperatures for both polymers. Though successful in its predictions, the modified model did not account for any intermolecular interactions that are the major source of deformation resistance below the glass transition.

Recognizing the dominant role of intermolecular over intramolecular interactions well below T_g, Argon [31]-[32], based his intermolecular theory of yielding of glassy polymers on thermally-activated production of local molecular kinks located in an elastic matrix initiating inelastic shear transformations. Argon obtains the activation free enthalpy of this process by modeling the intermolecular energy barrier as resulting from the stress fields of two equal and opposite closely spaced wedge disclination loops extending over the molecular cross section at the points of rotation of the molecular kinks. The model suggested by Argon for the plastic shear strain rate is an activation energy barrier Arrhenius expression:

$$\dot{\gamma}_p = \dot{\gamma}_0 \exp\left(-\frac{\Delta G^*}{kT}\right) \tag{3.2}$$

where the free energy barrier is given by[33]

$$\Delta G^* = \Delta G\left[1 - \left(\frac{\tau}{s}\right)^{p/q}\right] \tag{3.3}$$

where $\dot{\gamma}_0$ is the pre-exponential factor, ΔG^* is the amplitude of the free energy barrier to segment rotation and thus inelastic deformation, ΔG is the stress-unbiased Helmholtz free energy, k is Boltzmann's constant, T is the absolute deformation temperature, τ is the applied equivalent shear stress, s is the athermal shear resistance, and p and q are experimentally determined fitted or theoretically derived coefficients[1]. In the Argon model: $p = 5/6$, $q = 1$. The theory in this form has been successful in predicting the yield behavior of amorphous polymers such as PET, PMMA, PC, and polystyrene (PS) for temperatures at least 15K below their respective glass transition temperatures and over decades of strain rates. However, in the immediate vicinity of the glass transition temperature, Robertson's model has been found to provide a better fit to experimental data[32].

Recently, Argon, et al. [34]-[35] have investigated molecular level computer simula-

1. Best fits typically result in $0 < p < 1$ and $1 < q < 2$ for a wide range of materials.

tions of the inelastic deformation of polypropylene (PP) based on the early model introduced by Theodorou and Suter [36]. The model, which makes no assumptions about structure and modes of molecular segment relaxations, is based on systematic static energy minimizations in a small periodic cell representing a typical molecular environment. Their simulation shows that plastic relaxation is by the repeated nucleation of shear transformations in a very large group of segments in a cooperative manner.

The past work on modeling the strain hardening behavior of polymers is also quite extensive. It is widely accepted that the strain hardening of glassy polymers is due to the evolution in molecular orientation with strain. Evolution in molecular orientation is also the underlying mechanism of the large strain elastic behavior of elastomeric materials. An excellent review of the mechanics and physics of rubber elasticity up to the mid 1970's can be found in the works by Treloar [37]-[38]. Mathematical models that attempt to describe the stress-strain relation for rubber elastic materials can be classified into two different approaches. The first is the phenomenological, invariant-based approach and the second is the statistical mechanics, network-based approach. The primary criticism of phenomenological theories, for example those developed by Rivlin [39], Valanis-Landel [40], and Ogden [41], is that they lack a direct physical connection to the mechanisms of deformation. They lack the connection to real structural descriptors which can enable them to be predictive under conditions of complex thermal and mechanical loading conditions. The alternative approach of statistical mechanics results in network-based models built on Gaussian statistics of chain configurations, such as the models suggested by Flory and Rehner [42] and Edwards and Vilgis [43]. There are more advanced network models based on Langevin statistics, such as the model developed by Wang and Guth [44] and more recently by Arruda and Boyce [45]. These statistical models have enjoyed considerable success in modeling rubber elastic deformation of elastomeric materials as well as the

strain hardening behavior of amorphous glassy thermoplastics deformed in a variety of strain states.

Given accurate constitutive descriptions of the deformation resistances, combinations of them in a single kinematic framework can be used in simulations of polymer deformation. The work of Boyce et al. [46] and the work of Zaroulis and Boyce [13] has progressed in this direction.

A similar approach with emphasis above the glass transition region is that of Buckley et al. [47]. In their work they have employed a model based on Eyring type plastic flow to explain viscoelasticity and the Edwards and Vilgis network model to describe strain hardening during stretching of initially amorphous PET at high strain rates and temperatures above the glass transition.

In more recent work, Bergstrom and Boyce [48] developed a constitutive model for the large strain time-dependent behavior of elastomers. The foundation of their model is that the mechanical behavior can be decomposed into two parts. The first part is an equilibrium network corresponding to the state that is approached in long time stress relaxation tests. The second part is a network capturing the nonlinear rate-dependent deviation from the equilibrium state. The time-dependence of the second network is assumed to be governed by the reptational motion of molecules having the ability to change conformation significantly thereby relaxing the overall stress state. This model predicts the rate-dependence and relaxation behavior of elastomeric materials very well.

As mentioned previously in Chapter 1, PET is typically processed in the solid state at temperatures above its glass transition temperature. Therefore, the modeling effort will focus on the prediction of the mechanical behavior above the glass transition temperature. Various aspects of the models described above will be useful in the development of the constitutive model for PET, however, it is important to recognize that there are differences

in the behavior of PET above the glass transition from the behavior of the materials modeled in the previous investigations.

There are significant characteristics of the mechanical behavior of PET that were observed in the previous chapter that need to be captured in the constitutive model. Figure 3.1 shows a schematic plot of a representative stress-strain curve of PET in the rubbery regime. This schematic defines certain characteristic features of the stress-strain curve such as the initial modulus, E, the flow stress, σ_{flow}, the initial strain hardening slope, h, and the dramatic strain hardening. The experimental data from the mechanical tests conducted above the glass transition in both uniaxial compression and plane strain compression are shown again in Figures 3.2 to 3.11. The characteristics of the mechanical behavior summarized below refer to these figures as well as Figure 3.1. The characteristics of the mechanical behavior exhibited by PET above the glass transition temperature are:

- Initial stiffness and flow resistance depend on both strain rate and deformation temperature. This is evident in the stress-strain curves shown in Figures 3.3, 3.5, 3.7, 3.9 and 3.11, which show the stress-strain behavior up to strains of -1.0. The flow stress increases with increasing strain rate for all of the figures and it decreases with increasing temperature, for example at $90°C$, $-0.01/s$ the flow stress is 0.5 MPa, whereas at $100°C$, $-0.01/s$ it is 0.25 MPa.
- Figure 3.1 shows a schematic plot of a representative stress-strain curve of PET in the rubbery regime. Once the flow stress is reached, which is characterized by a roll over in the stress-strain curve as shown in the schematic, the stress gradually increases with strain. This is termed the strain hardening regime since the stress required to continue to deform the material increases with strain. It is also referred to as the strain stiffening region since the slope, which is the tangent stiffness, also gradually

increases with increasing strain. The initial slope of the strain hardening regime, h_i, strongly depends on strain rate and deformation temperature. This can be seen in the blow-ups of the experimental data shown in Figures 3.3, 3.5, 3.7, 3.9 and 3.11.

- The strain hardening slope gradually increases with increasing strain until a logarithmic strain of approximately -1.0, whereupon the strain hardening slope increases rather dramatically with strain, as shown in Figures 3.2, 3.4, 3.6, 3.8 and 3.10. These figures also show that the strain at which this dramatic increase in strain hardening slope with strain begins is dependent on strain rate and deformation temperature.
- All aspects of the stress-strain behavior are very strongly dependent on the state of strain as is evident when comparing the uniaxial compression data shown in Figures 3.2-3.7 to the plane strain compression data shown in Figures 3.8-3.11.

It is important that a constitutive model of the mechanical behavior of the material capture the essence of the strain rate, strain state and temperature dependencies of the material behavior as tabulated above. In the following sections, the development of a constitutive model which captures these dependencies is detailed. The model takes advantage of the success of prior models in capturing similar dependencies but addresses the specific characteristics observed in the behavior of PET above the glass transition temperature. Model simulation results are also compared to the experimental data in order to ascertain the model's ability to predict the mechanical behavior.

3.2 Development of the Constitutive Model

The stress-strain behavior of PET above the glass transition is observed to have two distinct resistances: (1) a resistance to initial flow, and (2) an evolving resistance to continued flow (exhibited by strain hardening). Both of these resistances are observed to depend on strain rate and deformation temperature. In modeling this behavior, a framework similar to

that used by Bergstrom and Boyce [48] in modeling the rate-dependent deformation of elastomeric materials is adopted.

As mentioned earlier, the model developed by Bergstrom and Boyce is a dual network model that decomposes the mechanical behavior of the material into two distinct parts: an equilibrium network and a time-dependent network [48]. The equilibrium network governs the equilibrium response and the time-dependent network governs the time-dependent deviation from equilibrium. A one-dimensional representation of this model is shown in Figure 3.12. The model consists of a parallel structure between the A and B networks. The A network captures the equilibrium response of the material and the B network captures the time-dependent deviation from the equilibrium state. Network A is modeled by a single spring element. Resistance B is modeled as a spring in series with a time-dependent dashpot which acts to relieve the strain on the perfect network with time. In this model, the spring elements in both networks A and B are modeled using the Arruda-Boyce 8-chain model [45] mentioned in the previous section and the dashpot element is modeled using a reptational model. This model predicts the rate-dependence and relaxation behavior of elastomeric materials very well. A framework similar to that shown in Figure 3.12 is adopted for the model developed in this work.

3.2.1 Dual Resistance Model

In order to model the two resistances operating in mechanically deforming PET above the glass transition temperature, a spring and dashpot framework similar to that used by Bergstrom and Boyce [48] was utilized, as shown in Figure 3.12, but with different models used to constitutively describe the springs and the dashpot. This dual resistance model consists of a parallel structure between the A network, which models the strain hardening that occurs with large strains, and the B resistance, which captures the rate and temperature dependence of the initial modulus and flow stress. Network A is modeled by a single

spring element. Resistance B is modeled as a spring in series with a time-dependent dashpot whereupon, once the stress level is significant enough, the dashpot absorbs most of the deformation. The spring element in network A is modeled using the Arruda-Boyce 8-chain model [45] mentioned in the previous section, the spring element in resistance B is modeled using the classical Neo-Hookean model, and the dashpot element is modeled using a thermal activation model.

3.2.2 The Arruda-Boyce 8-Chain Model

The Arruda-Boyce 8-chain model is based on a unit cube in which eight non-Gaussian chains are united at the center. Each chain extends from the center of the cube to one of the eight corners. As a result of this symmetry, all eight chains undergo the same deformation during different types of loading. This symmetry is the essence of the model and provides its computational simplicity.

Each chain in the unit cube is represented as a Langevin statistical chain to account for large deformations. The strain energy is proportional to entropy changes due to deformation since enthalpy considerations are negligible. Thus, the change in entropy is expressed for a deformed chain as a function of the inverse Langevin function and the chain vector length, r_{chain}. The Langevin function is expressed as:

$$L[\beta] = \coth\beta - \frac{1}{\beta} \tag{3.4}$$

and the chain vector length is expressed in terms of the principal stretches based on the geometry of the deformed eight chain network:

$$r_{chain} = \frac{1}{\sqrt{3}}\sqrt{N}l(\lambda_1^2 + \lambda_2^2 + \lambda_3^2)^{\frac{1}{2}} = \frac{1}{\sqrt{3}}\sqrt{N}lI_1^{\frac{1}{2}} \tag{3.5}$$

where I_1 is the first stretch invariant. In Equation 3.5, r_{chain} is proportional to I_1, as a result, the strain energy expression is a function of I_1 only. In Equation 3.5, the expression

$\sqrt{N}l$ represents the initial chain length. The resulting strain energy function can be expressed in terms of Equations 3.4 and 3.5:

$$W = nk\Theta\left(\frac{r_{chain}}{Nl}\beta + \ln\frac{B}{\sinh B}\right) - \Theta_{c'} \tag{3.6}$$

where n is the chain density, k is Boltzmann's constant, Θ is the temperature, and c' is a constant. Differentiation of W then leads to a stress-stretch relationship written in terms of a difference between two principal stretches in order to cancel the constant pressure term:

$$\sigma_1 - \sigma_2 = \frac{nk\Theta}{3}\sqrt{N}L^{-1}\left[\frac{\lambda_{chain}}{\sqrt{N}}\right]\frac{(\lambda_1^2 - \lambda_2^2)}{\lambda_{chain}} \tag{3.7}$$

where λ_{chain} is r_{chain} divided by the initial length.

3.2.3 The Neo-Hookean Model

The Neo-Hookean model is a phenomenological model that expresses the strain energy function in the following form:

$$W = \mu_B(I_1 - 3) \tag{3.8}$$

where μ_B is the parameter that is found by calculating the tangent modulus of the experimental data.

3.2.4 Thermal Activation Model

The dashpot element is a rate and temperature dependent term which governs plastic flow. This component models the isotropic resistance to chain segment rotation of the material and is expressed in terms of an activation energy barrier Arrhenius expression that is the result of combining Equations 3.2 and 3.3 mentioned earlier:

$$\dot{\gamma}_p = \dot{\gamma}_0 \exp\left\{-\frac{\Delta G}{kT}\left[1 - \left(\frac{\tau}{s}\right)^{p/q}\right]\right\} \tag{3.9}$$

Upon examination of this expression, it is clear that the τ/s is the key to the "activation"

of this component of the model. As the effective shear strength approaches the athermal shear strength, the coefficient of the exponential approaches zero, and the entire term approaches the pre-exponential factor.

3.2.5 Determination of the Dual Resistance Model Parameters

Thus far, the dual resistance model has been described in one dimension so that the contributions of the elements can be easily understood. In order to formulate the entire constitutive model in three dimensions, the individual contributions must be thought of in terms of finite strain deformation continuum mechanics. The finite strain kinematics of the physics for the final form of the constitutive model will be discussed later in Section 3.4 in order not to disturb the flow of the development of the constitutive model. After the three-dimensional equations have been formulated, the model is coded as a user defined material, or *UMAT, to interface with the ABAQUS finite element solution routine. The *UMAT requires calculating and returning values for the incremental stress and the Jacobian matrix.

There are 5 parameters needed to fully determine the dual resistance model: $\mu_A = nk\Theta/3$ and N for the Arruda-Boyce element; μ_B from Equation 3.8 for the Neo-Hookean element; and ΔG and $\dot{\gamma}_0$ for the thermal activation element, where p/q was taken to be equal to 1.0 and $s = 0.1\mu_B$. It was decided to model the material behavior in uniaxial compression at $100°C$ first, as shown in Figures 3.4 and 3.5, due to the relative absence of adiabatic heating effect at this temperature and the repeatability of the tests with different layers in uniaxial compression.

The value for μ_A can be estimated by corresponding its value to the tangent modulus of the stress-strain curve after the initial yield. The value of N is a function of the stretch, λ_{lim}, at which the stress starts to increase without limit:

$$N = \frac{1}{3}\left[\lambda_{lim}^2 + \frac{2}{\lambda_{lim}}\right] \tag{3.10}$$

The value for μ_B can be estimated by corresponding its value to the initial modulus of the stress-strain curve and subtracting the corresponding value found earlier for μ_A. The thermal activation parameters are the only parameters that introduce rate-dependence and temperature-dependence into this model. Experimental data at two different strain rates is required to determine these two parameters. The value of τ is estimated through the Mises relationship as:

$$\tau = \frac{Y}{\sqrt{3}} \tag{3.11}$$

where Y is the tensile "yield" stress of the material. Similarly, $\dot{\gamma}_p$ is estimated as the strain rate multiplied by $\sqrt{3}$. The athermal shear strength s can be estimated as one tenth of μ_B. Using the stress-strain data from two different strain rate tests, two equations of the form of Equation 3.9 in terms of the two unknowns, ΔG and $\dot{\gamma}_0$ can be found. These two equations can be solved simultaneously to determine the two unknowns.

3.2.6 Discussion of Model Predictions

The following table shows the model parameters determined for the uniaxial compression tests conducted at $100°C$.

Model Parameter	Value Determined from Data
μ_A	1.5 *MPa*
N	5.0
μ_B	5.9 *MPa*
$\dot{\gamma}_0$	$2.7/s$[a]
$\Delta G/kT$	4.9

Table 3.1: Model parameters used in the dual resistance model at a temperature of $100°C$

a. Note that $\dot{\gamma}_0$ is a rather small value, most likely because of the high temperature (above the glass transition). In the glassy state, $\dot{\gamma}_0$ is more typically on the order of $10^{10}/s$.

In Figures 3.13 and 3.14, the uniaxial compression stress-strain curves conducted at $100°C$ at three different strain rates are plotted against the dual resistance model prediction. As shown, the initial yield is captured well, as well as the strain hardening behavior for the fastest strain rate. However, the strain rate dependence of the strain hardening behavior is not captured. Therefore, a modification to the dual resistance model was needed in order to fully capture the rate-dependent strain hardening behavior of the material.

3.3 Proposed Constitutive Model

In order to fully capture the strong rate-dependence of the material behavior, a delay of the upturn in the stress-strain curve would have to be implemented. The strain hardening behavior is observed to be strongly dependent on the strain rate; as the strain rate decreases, the deformation is occurring over longer periods of time apparently allowing some form of molecular relaxation to occur and thus not providing as much stretching of the network. It is the stretching of this network that provides the initial strain hardening.

In order to more clearly illustrate the rate dependent strain hardening behavior, the strain hardening portion of each experimental curve was isolated and plotted in Figures 3.15, 3.16 and 3.17 for $90°C$, $100°C$ and $105°C$, respectively. In these plots, the contribution to the overall stress from the B resistance has been subtracted out, thus leaving the equivalent network stress vs. applied strain. As shown in Figures 3.15, 3.16 and 3.17, the strain hardening behavior is clearly rate dependent in terms of both the initial hardening slope and the upswing at larger strains.

In order to capture the rate dependent behavior, the strain is envisioned to be accommodated not only by the stretching of the network A, but also by some form of molecular relaxation which will be termed viscous flow. Schematically, the viscous flow and network

stretch can be expressed as a dashpot (viscous flow) in series with a spring (network stretch) as shown in Figure 3.18. Mathematically, the stretch will be composed of both a flow component, Λ_F, and a network stretch, Λ_N:

$$\Lambda = \Lambda_N \Lambda_F \tag{3.12}$$

Data reduction was conducted to determine, at different strain rates, what part of the total stretch goes to the network and what part goes to the flow, as a function of the imparted stretch, or strain.

3.3.1 Data Reduction of the Experimental Data

It was assumed that for deformation conducted at -1.0/*s*, the fastest strain rate, the total stretch is composed entirely of the network stretch with no flow stretch involved. This is a valid assumption since the uploading part of the test takes only 2 seconds to complete and since the stress-strain curves for the tests conducted at -1.0/s and -2.0/s were very close, indicating that the amount of flow stretch in the -1.0/*s* curve is very small. Working on this assumption and using the reduced data of Figures 3.15, 3.16 and 3.17, an equivalent network stress vs. network strain curve was plotted from the -1.0/*s* strain rate data in uniaxial compression at $100°C$. This curve is shown in Figure 3.19. The network strain, ε_{N11}, was taken to be equivalent to the imparted strain at this strain rate since there is assumed to be no flow taking place. Therefore, this curve is exactly the same curve as the -1.0/*s* rate curve in Figure 3.16. Using this equivalent network stress vs. network strain curve, the network strains for the strain rates of -0.1/*s* and -0.01/*s* were determined by using the corresponding values of the equivalent network stress calculated earlier. At this point, we have the equivalent network stress vs. network strain behavior for each of the three strain rates. The network strain is a function of the network stretch as shown in the following:

$$\Lambda_{N11} = \exp(\varepsilon_{N11}) \tag{3.13}$$

A similar function for the total stretch in terms of the total strain and for the flow stretch in terms of the flow strain applies. Using Equation 3.13, the network stretch can be calculated from the network strain for each of the three strain rates.

Working on the assumption that the deformation at the fastest strain rate is composed entirely of the network stretch, then the flow stretch is always 1.0 for this strain rate. Therefore, the network stretch is equivalent to the total stretch for the fastest strain rate. Using this value for the total stretch, the flow stretch for the -0.1/*s* and -0.01/*s* strain rates can be calculated by the following expression:

$$\Lambda_{F11}\Big|_{-0.1/s,\,-0.01/s} = \Lambda_{N11}^{-1}\Big|_{-0.1/s,\,-0.01/s}\Lambda_{11} \tag{3.14}$$

where the total stretch, Λ_{11}, is equivalent to the network stretch for the fastest strain at the corresponding strain.

Figures 3.20 to 3.22 are plots of Λ_{F11} vs. Λ_{11}, Λ_{F11} vs. Λ_{N11}, and Λ_{F11} vs. $\overline{\sigma_N}$, respectively, for each of the three strain rates. What is most noticeable upon examination of these plots is that the flow stretch for the two lower strain rates levels off and reaches a saturation point and that this saturation point is the same for both strain rates in terms of the equivalent network stress and the network stretch, as shown in Figures 3.22 and 3.21. This saturation point occurs at what is termed the critical equivalent network stress, σ^*, as shown in Figure 3.22, and the critical equivalent network stretch, Λ_N^*, as shown in Figure 3.21. The linearity of the flow stretch in the three figures up until the saturation point suggests that the form of the plastic shear strain expression for the dashpot in the A network might be one of linear viscosity.

3.3.2 Linear Viscosity Dashpot Incorporated into the Model

The linear viscous dashpot element introduced into the dual resistance model is governed by the following expressions:

$$\dot{\gamma}_p^A = C\overline{\sigma_N} \;,\; \overline{\sigma_N} < \sigma^* \tag{3.15}$$

$$\dot{\gamma}_p^A = 0 \;,\; \overline{\sigma_N} \geq \sigma^* \tag{3.16}$$

In this element, the plastic shear strain rate of the dashpot in network A is a linear function of the equivalent network stress, $\overline{\sigma_N}$, the stress found in the spring in network A. After this equivalent network stress reaches the critical value, the dashpot deactivates. This adds two more model parameters to the list of 5 discussed earlier resulting in 7 total model parameters for the dual resistance model. The values for the first 5 parameters are the same values discussed previously and are determined in the same manner. The value for the critical stress can be determined from the data reduction plot of Figure 3.22. The model parameter for the linear viscous element, C, is a proportionality constant and was found by plotting Λ_{F11} vs. t as shown in Figure 3.23, where t is the current time of the experiment (i.e. how long the experiment has been running) and is given by the following expression:

$$t = \frac{1}{\dot{\varepsilon}} \ln \Lambda = \frac{1}{\dot{\varepsilon}} \ln(\Lambda_N \Lambda_F) \tag{3.17}$$

The value of C can be determined from the slope of the curves up until the saturation point. From Figure 3.23 is can be seen that C can have two different values, depending on which curve is chosen (giving an indication that linear viscosity will not work). Table 3.2 shows the model parameters used for the four-component dual network model using a linear viscous element in network A. In Table 3.2, the two different values of C were tried in order to determine which best fit the experimental data.

Model Parameter	Value Determined from Data
μ_A	1.5 *MPa*

Table 3.2: Model parameters used in the dual network model using a linear viscous element in network A, in uniaxial compression at $100°C$

Model Parameter	Value Determined from Data
N	5.0
μ_B	5.9 *MPa*
$\dot{\gamma}_0$	2.7/*s*
$\Delta G/kT$	4.92
σ^*	2.3 *MPa*
C	0.031 *MPa*, 0.006 *MPa*

Table 3.2: Model parameters used in the dual network model using a linear viscous element in network A, in uniaxial compression at 100°*C*

Figure 3.24 shows the results of the model compared to experimental data using the value of *C* determined from the slope of the -0.1/*s* stress-strain curve in Figure 3.23. Figure 3.25 shows the results of the model compared to experimental data using the value of *C* determined from the slope of the -0.01/*s* stress-strain curve in Figure 3.23. As shown by the figures, the model using the higher value of *C* fits the -0.1/*s* data very nicely, as expected, but completely underpredicts the -0.01/*s* data. Conversely, the model using the lower value of *C* fits the -0.01/*s* data reasonably well, as expected, but completely overpredicts the -0.01/*s* data.

Clearly, a linear viscous element for the dashpot in the dual resistance model does not predict the material behavior. When fit to the data at -0.1/*s* it allows for too much flow at -0.01/*s*, thereby underpredicting that data, and conversely, when fit to the data at -0.01/*s*, it does not allow for enough flow at -0.1/*s*, thereby overpredicting that data. This outcome motivated the replacement of the linear viscous element with a nonlinear viscous element.

3.3.3 Nonlinear Viscosity Dashpot Incorporated into the Model

The first nonlinear expression attempted gave the dependence of the plastic shear strain rate of the dashpot element in network A as a function of the equivalent network stress to some power, *p*:

$$\dot{\gamma}_p = C\overline{\sigma_N^p} \tag{3.18}$$

This resulted in predictions similar to the predictions for the linear viscous element. This is not surprising since the stresses for each of the three strain rates are of the same order.

Therefore, a model for the dashpot in network A was needed that took into account the increasing entanglement drift occurring with decreasing strain rate, but not to the extent that the linear viscous dashpot model did. It was postulated that the plastic shear strain rate of the dashpot was not only a function of the equivalent network stress but also a function of the average flow stretch; physically, this acts to capture the phenomenon that the flow becomes increasingly difficult as it occurs. The dashpot is taken to deactivate at an average network stretch, $\overline{\Lambda_N}$, equal to the critical network stretch. Where the average network stretch is given by:

$$\overline{\Lambda_N} = \sqrt{\frac{\lambda_{N11}^2 + \lambda^2{}_{N22} + \lambda^2{}_{N33}}{3}} \tag{3.19}$$

The expression corresponding to this type of dependence is given as follows:

$$\dot{\gamma}_p^A = C\frac{\overline{\sigma_N}}{(\overline{\Lambda_F})^p} \;,\; \overline{\Lambda_N} < \Lambda_N{}^* \tag{3.20}$$

$$\dot{\gamma}_p^A = 0 \;,\; \overline{\Lambda_N} \geq \Lambda_N{}^* \tag{3.21}$$

where the average flow stretch, $\overline{\Lambda_F}$, is the root mean square of the principle stretches given by the following:

$$\overline{\Lambda_F} = \sqrt{\frac{\lambda_{F11}^2 + \lambda^2{}_{F22} + \lambda^2{}_{F33}}{3}} \tag{3.22}$$

The average flow stretch is always greater than or equal to 1.0 due to the fact that the principle stretches are either greater than or less than 1.0. Therefore, the inverse of the average

flow stretch was needed in order to have the viscosity increase with increasing average flow stretch. This was in hopes of slowing down the response of the dashpot at the slower strain rate without affecting the faster rates. Raising the average flow stretch to a power merely amplifies this effect.

A total of 8 model parameters are needed for this model. The first 5 parameters are calculated as mentioned previously in Section 3.2.5 and shown in Section 3.2.6. This form of the nonlinear viscous element model adds 3 model parameters to the initial 5-parameter model: the proportionality constant, C, the critical network stretch, Λ_N^*, and the exponent, p. The critical network stretch is found from the plot of Λ_{F11} vs. Λ_{N11} and is taken to be the equivalent stretch when $\Lambda_{N11} = \Lambda_{N11}^*$. The proportionality constant can be found from taking the slope of the -0.1/s curve in the Λ_{F11} vs. t plot. The exponent is found by trial and error after all other parameters have been determined. Table 3.3 gives the model parameters calculated from the data reduction:

Model Parameter	Value Determined from Data
μ_A	1.5 *MPa*
N	5.0
μ_B	5.9 *MPa*
$\dot{\gamma}_0$	2.7/*s*
$\Delta G/kT$	4.92
Λ_N^*	1.2
C	0.031 *MPa*
p	15

Table 3.3: Model parameters used in the dual network model using a nonlinear viscous element in network A, in uniaxial compression at $100°C$

Figure 3.26 shows the model predictions for the stress-strain behavior plotted with the

experimental data. Figure 3.27 shows the model predictions for the flow stretch and network stretch behavior plotted with increasing strain for each strain rate. In Figure 3.26, the model prediction is excellent for all strain rates with only a small underprediction in the strain hardening at the fastest strain rate and a slight overprediction in the slower strain rates. There is also a slight overprediction of the initial flow stress at the fastest strain rate and a slight underprediction of the initial flow stress at the slowest strain rate. Figure 3.27 shows the contribution of both the flow stretch and the network stretch to the total stretch as the strain increases. As expected, at -1.0/*s*, the total stretch is almost entirely made up of network stretch with very little flow stretch involved, however, at -0.1/*s*, the stretch is a combination of both the flow stretch and the network stretch, with the saturation point being reached at a strain of approximately -1.0. Alternatively, at -0.01/*s*, the stretch is mostly made up of flow stretch until a strain of approximately -1.5, near the saturation point. This figure is predicting that at the fastest strain rate, the molecules do not have enough time to relax, and thus the flow stretch is nearly zero. As the strain rate is increased, however, the molecules have more time the relax, and thus the flow stretch contribution increases.

It is important to note that the model does not specifically include strain-induced crystallization and the hardening is modeled as a network stretch phenomenon. The cessation of viscous flow at a critical network stretch level could be interpreted as some onset of crystallization; however it could just as easily be interpreted as a molecular orientation effect. If crystallization does indeed occur during the straining process, then additional deformation mechanisms in the form of crystal slip resistances would have to be incorporated and, indeed, could explain the failure of the model to predict as steep a strain hardening slope at the high rates as seen in Figure 3.26 (and as will be seen in some of the plane strain compression results to be discussed later). Recall that the $100°C$ uniaxial compres-

sion data showed no crystallization at the rate of -0.01/*s*, but some at both -0.1/*s* and -1.0/*s*.

Due to the success with which the model predicted the data for uniaxial compression at $100°C$, it was concluded that the four-component dual network model incorporating a nonlinear viscous element as the dashpot in network A would be the nature of the constitutive model. Prior to exploring the effectiveness of the model in capturing the data at other temperatures and states of strain, the full three-dimensional finite strain kinematics of the model are discussed.

3.4 Kinematics of Finite Strain Deformation and Constitutive Representation of the Model

The reference configuration of an initially amorphous non-oriented polymer is an isotropic state (i.e., randomly oriented physically entangled macromolecules). The mechanics of fully three-dimensional large strain deformation involves the total deformation gradient **F**, which maps a material point of the reference configuration into the current configuration:

$$\mathbf{F} = \text{Grad}\, \boldsymbol{x} = \nabla_X \boldsymbol{x} \tag{3.23}$$

where X represents the reference position of a material point, $\boldsymbol{x}$ represents the current position, and ∇ is the gradient. This deformation gradient acts on both network A and resistance B:

$$\mathbf{F} = \mathbf{F}_\mathrm{A} = \mathbf{F}_\mathrm{B} \tag{3.24}$$

The deformation gradient on both networks can be further decomposed into elastic and plastic parts:

$$\mathbf{F}_A = \mathbf{F}_A^e \mathbf{F}_A^p \tag{3.25}$$

$$\mathbf{F}_B = \mathbf{F}_B^e \mathbf{F}_B^p \tag{3.26}$$

where the elastic deformation gradients, $\mathbf{F}_A^e$ and $\mathbf{F}_B^e$, represent the configuration obtained

by a complete virtual elastic unloading of the corresponding network to a stress-free state.

3.4.1 Kinematics and Constitutive Representation of Network A

The total velocity gradient of resistance B is given by:

$$\mathbf{L}_A = \dot{\mathbf{F}}_A \mathbf{F}_A^{-1} \tag{3.27}$$

This velocity gradient can be similarly decomposed into elastic and plastic components:

$$\mathbf{L}_A = \mathbf{L}_A^e + \mathbf{F}_A^e \mathbf{L}_A^p \mathbf{F}_A^{e-1} = \mathbf{L}_A^e + \tilde{\mathbf{L}}_A^p \tag{3.28}$$

where

$$\mathbf{L}_A^p = \dot{\mathbf{F}}_A^p \mathbf{F}_A^{p-1} = \mathbf{D}_A^p + \mathbf{W}_A^p \tag{3.29}$$

$$\tilde{\mathbf{L}}_A^p = \tilde{\mathbf{D}}_A^p + \tilde{\mathbf{W}}_A^p \tag{3.30}$$

The velocity gradient of the relaxed configuration, $\mathbf{L}_A^p$, may be represented as the sum of symmetric and skew-symmetric tensors, $\mathbf{D}_A^p$ and $\mathbf{W}_A^p$, where $\mathbf{D}_A^p$ is the rate of shape change in the relaxed configuration and $\mathbf{W}_A^p$ is the spin in this configuration.

The unloading process relating the deformed state with the relaxed state is not uniquely defined since an arbitrary rigid body rotation of the relaxed configuration still leaves the relaxed configuration stress free. The unloaded configuration can be made unique by prescribing that $\tilde{\mathbf{W}}_A^p = 0$, as developed by Boyce, Weber and Parks [49]. This, in general, results in elastic and plastic deformation gradients which both contain rotations. The left elastic stretch tensor, $\mathbf{V}_B^e$, is symmetric positive definite and can therefore be decomposed into its spectral representation:

$$\mathbf{V}_A^e = \mathbf{Q}_A^e \left[\sum_{i=1}^{3} \lambda_i^{(Ae)} \mathbf{e}_i \otimes \mathbf{e}_i \right] (\mathbf{Q}_A^e)^T = \sum_{i=1}^{3} \lambda_i^{(Ae)} \mathbf{l}_i^{(Ae)} \otimes \mathbf{l}_i^{(Ae)} \tag{3.31}$$

where $\mathbf{Q}_A^e$ is proper orthogonal. The stress acting in network A is then:

$$\mathbf{T}_A = \sum_{i=1}^{3} \sigma_i^{(Ae)} \mathbf{l}_i^{(Ae)} \otimes \mathbf{l}_i^{(Ae)} \tag{3.32}$$

where the stress is given constitutively by a compressible version of the Arruda-Boyce 8-chain network model:

$$\sigma_i^{(A)} = \mu_A \sqrt{N} L^{-1}\left[\frac{\lambda_{chain}}{\sqrt{N}}\right]\left(\frac{\lambda_i^2 - \lambda_{chain}^2}{\lambda_{chain}}\right) + B \ln \sqrt{I_3^{(A)}} \tag{3.33}$$

where

$$\mu_A = \frac{nk\Theta}{3} \tag{3.34}$$

$$I_3^{(A)} = (\lambda_1^{(A)} \lambda_2^{(A)} \lambda_3^{(A)})^2 \tag{3.35}$$

and where λ_{chain} and the Langevin were defined in Section 3.2.2.

The rate of shape change of network A can now be constitutively described by

$$\tilde{\mathbf{D}}_A^p = \dot{\gamma}_A \mathbf{N}_A \tag{3.36}$$

where $\mathbf{N}_A$ gives the direction of the driving stress state of the relaxed configuration convected to the loaded configuration and $\dot{\gamma}_A$ is an effective creep rate given constitutively by:

$$\dot{\gamma}_A = C \frac{\overline{\sigma_N}}{(\overline{\Lambda_F})^p}, \ \overline{\Lambda_N} < \Lambda^* \tag{3.37}$$

$$\dot{\gamma}_A = 0, \ \overline{\Lambda_N} \geq \Lambda^* \tag{3.38}$$

Since $\mathbf{T}_A$ is calculated in the loaded configuration, the driving stress state on the relaxed configuration expressed in the loaded configuration is then given by:

$$\mathbf{T}_A^* = \mathbf{T}_A \tag{3.39}$$

where the deviatoric part of the driving stress state on the relaxed configuration is:

$$\mathbf{T}_A{}^{*\prime} = \mathbf{T}_A{}^* - \frac{1}{3}tr(\mathbf{T}_A{}^*) \tag{3.40}$$

and the equivalent effective shear stress is:

$$\tau_A = \sqrt{\frac{1}{2}tr(\mathbf{T}_A{}^{*\prime}\mathbf{T}_A{}^{*\prime})} \tag{3.41}$$

The direction of the driving stress, $\mathbf{N}_A$ is calculated from:

$$\mathbf{N}_A = \frac{1}{\sqrt{2}\tau_A}\mathbf{T}_A{}^{*\prime} \tag{3.42}$$

3.4.2 Kinematics and Constitutive Representation of Resistance B

The finite strain kinematics for resistance B is exactly the same as for network A since the networks are both composed of a spring and dashpot element in series. However, the constitutive equations governing the spring and dashpot elements are quite different and are given here.

The stress in resistance B is given constitutively by the Neo-Hookean model:

$$\sigma_i^{(B)} = \mu_B\lambda_i^2 + B\ln\sqrt{I_3^{(B)}} \tag{3.43}$$

Thus, the total stress in resistance B can be written as:

$$\mathbf{T}_B = \sum_{i=1}^{3} \sigma_i^{(Be)}\mathbf{l}_i^{(Be)} \otimes \mathbf{l}_i^{(Be)} \tag{3.44}$$

The total stress in the system then simply becomes $\mathbf{T} = \mathbf{T}_A + \mathbf{T}_B$.

The effective creep rate for resistance B is constitutively described by the thermal activation model as:

$$\dot{\gamma}_B = \dot{\gamma}_0 \exp\left\{-\frac{\Delta G}{kT}\left[1 - \left(\frac{\tau}{s}\right)^{p/q}\right]\right\} \tag{3.45}$$

with the rate of deformation given by:

$$\tilde{\mathbf{D}}_B^p = \dot{\gamma}_B \mathbf{N}_B \tag{3.46}$$

where $\mathbf{N_B}$ is calculated from:

$$\mathbf{N}_B = \frac{1}{\sqrt{2}\tau_B}\mathbf{T}_B^{*'} \tag{3.47}$$

3.5 Comparison of Model with Experimental Data

In the model proposed, the temperature dependence is taken into account by the thermal activation model. To determine the model parameters for a test conducted in uniaxial compression at $90°C$, a method similar to the method described in Section 3.2.5 is used. The values for μ_A and μ_B are calculated in exactly the same manner, by looking at the tangent moduli of the experimental curves before and after the yield. The value for s is calculated by taking one tenth of μ_B. The pre-exponential factor is taken to be exactly the same as the factor calculated for $100°C$. The temperature dependence is introduced by taking the value for $\Delta G/kT$ and scaling it by the temperature ratio in the following manner:

$$\left.\frac{\Delta G}{kT}\right|_{90°C} = \left(\left.\frac{\Delta G}{kT}\right|_{100°C}\right)\left(\frac{363K}{373K}\right) \tag{3.48}$$

The other model parameters are found in exactly the same manner as described previously. Table 3.4 gives the model parameters calculated for uniaxial compression at $90°C$.

Model Parameter	Value Determined from Data
μ_A	1.95 *MPa*
N	3.0
μ_B	12.7 *MPa*
$\dot{\gamma}_0$	2.7/*s*
$\Delta G/kT$	5.06

Table 3.4: Model parameters used for uniaxial deformation at $90°C$

Model Parameter	Value Determined from Data
Λ^*	1.3
C	0.008 MPa
p	15

Table 3.4: Model parameters used for uniaxial deformation at $90°C$

Figure 3.28 shows the model predictions for the stress-strain behavior plotted with the experimental data in uniaxial compression at $90°C$. Figure 3.29 shows the model predictions for the flow stretch and network stretch behavior plotted with increasing strain for each strain rate. In 3.28 the model prediction is excellent for all strain rates. There is, however, a slight overprediction of the yield stress at the faster strain rates and a slight underprediction of the yield stress at the slowest strain rate. It is important to remember that the experimental data taken at this temperature at the faster strain rates was affected greatly by adiabatic heating effects and crystallization effects. Since these were not taken into consideration by the model then the model would not be expected to predict the high rate experimental behavior exactly at the larger strains, where adiabatic heating and crystallization effects are manifested. As shown in Figure 3.29, there is very little flow stretch contribution for -1.0/s and -0.1/s strain rates, correlating to the fact that their corresponding stress-strain curves in Figure 3.28 are nearly parallel, indicating similar contributions for the flow stretch and the network stretch. Again, this is due to the fact that adiabatic heating and crystallization effects were not taken into account.

The same model parameters found in Table 3.3 were used to predict the behavior of plane strain compression experiments conducted at $100°C$. Figure 3.30 shows the model predictions of the stress-strain behavior plotted with the experimental data. Figure 3.31 shows the model predictions for the flow stretch and network stretch behavior plotted with increasing strain for each strain rate. Similarly, the same model parameters found in Table

3.4 were used to predict the behavior of plane strain compression experiments conducted at $90°C$. Figure 3.32 shows the model predictions of the stress-strain behavior plotted with the experimental data. Figure 3.33 shows the model predictions for the flow stretch and network stretch plotted with increasing strain for each strain rate. In Figures 3.30 and 3.32, the model predicts the stress-strain behavior very well until the dramatic strain hardening region. The model underpredicts the strain hardening behavior for every strain rate at $100°C$ but overpredicts the strain hardening behavior for the faster strain rates at $90°C$ due to the adiabatic heating and crystallization effects in the data that is not taken into account in the model. This was expected due to the ambiguity of the plane strain compression data in terms of the nonrepeatability of the stress-strain curves of different layers of PET as shown in Figure 2.2. Also, since the effects of crystallization are much more dramatic in plane strain compression than in uniaxial compression, the model's predictions in plane strain compression would not be expected to be as accurate as in uniaxial compression. Figures 3.31 and 3.33 show the model predictions of the contributions of the flow stretch and the network stretch in plane strain compression at $90°C$ and $100°C$, respectively. As shown in these figures, the contributions at each strain rate are similar to the contributions in uniaxial compression shown in Figures 3.27 and 3.29. These figures exhibit how the model fails to predict the plane strain compression data as well as the uniaxial compression data. The saturation point at the faster strain rates occurs sooner since the critical average network stretch is reached at smaller strains. Therefore, the model predicts dramatic strain hardening to begin at smaller strains than actually observed for the two higher rates. However, it is important to remember that the two higher strain rate tests result in the heating of the material from both plastic dissipation and crystallization. This heating thus provides some thermal softening of the material, which is not taken into account in the model. As the number of crystallites increases, the material dramati-

cally strain hardens. This would explain why the model is overpredicting the stress in the range of -0.7 to -1.2 and underpredicting the stress in the dramatic strain hardening region for the faster strain rates where crystallization effects are more prominent.

3.6 Further Refinements to the Proposed Model

In order to make the model more robust in its ability to predict the temperature dependence not just in the initial resistance to flow, but also in the strain hardening behavior, a refinement to the model in terms of the constitutive relation for the dashpot in network A was introduced. The viscosity model for the dashpot in network A was altered by multiplying it with an activation energy barrier Arrhenius expression:

$$\dot{\gamma}_A = C^* \exp\left(-\frac{\Delta Q}{kT}\right) \frac{\overline{\sigma_N}}{(\overline{\Lambda_F})^p} \quad , \quad \overline{\Lambda_N} < \Lambda^* \tag{3.49}$$

$$\dot{\gamma}_A = 0 \quad , \quad \overline{\Lambda_N} \geq \Lambda^* \tag{3.50}$$

where the new constant, C^*, multiplied by the activation energy barrier Arrhenius expression, is equivalent to the former constant, C:

$$C = C^* \exp\left(-\frac{\Delta Q}{kT}\right) \tag{3.51}$$

This refinement results in a total of 9 model parameters, with C^* replacing C, and $\Delta Q/k$ as an additional parameter. These two parameters can be found by simultaneously solving two equations of the form of Equation 3.51 for these two unknowns, using the values of C calculated earlier from the reduction of the uniaxial compression data at $90°C$ and $100°C$. The values for these two parameters thus apply to all temperatures. The new parameters for the refined model are given in Tables 3.5 and 3.6 for both $100°C$ and

$90°C$, respectively.

Model Parameter	Value Determined from Data
μ_A	1.5 *MPa*
N	5.0
μ_B	5.9 *MPa*
$\dot{\gamma}_0$	2.7/*s*
$\Delta G/kT$	4.92
Λ^*	1.2
C^*	$9.18*10^{13}$ *MPa*
p	15
$\Delta Q/k$	9725.5/°*K*

Table 3.5: Model parameters used in the dual network model using a temperature-dependent nonlinear viscous element in network A, in uniaxial compression at $100°C$

Model Parameter	Value Determined from Data
μ_A	1.95 *MPa*
N	3.0
μ_B	12.7 *MPa*
$\dot{\gamma}_0$	2.7/*s*
$\Delta G/kT$	5.06
Λ^*	1.3
C^*	$9.18*10^{13}$ *MPa*
p	15
$\Delta Q/k$	9725.5/°*K*

Table 3.6: Model parameters used in the dual network model using a temperature-dependent nonlinear viscous element in network A, in uniaxial compression at $90°C$

These new model parameters give exactly the same results as the previous model parameters and, therefore, the model predictions are the same as those discussed previously for Figures 3.26 to 3.33 for uniaxial compression and plane strain compression at $90°C$ and $100°C$. However, the motivation for altering the model to this form was to make it more applicable at different temperatures, and therefore more robust. This capability of the model is shown by its prediction of the uniaxial compression data at $105°C$. The model parameters used to predict the mechanical behavior in uniaxial compression at this temperature were the same parameters used for uniaxial compression at $100°C$. The difference in temperature was taken into account by the two energy barrier expressions of the constitutive relations for the dashpots The model parameters used are given in the following table:

Model Parameter	Value Determined from Data
μ_A	1.5 *MPa*
N	5.0
μ_B	5.9 *MPa*
$\dot{\gamma}_0$	2.7/*s*
$\Delta G/kT$	4.86
Λ^*	1.2
C^*	$9.18*10^{13}$ *MPa*
p	15
$\Delta Q/k$	9725.5/°*K*

Table 3.7: Model parameters used in the dual network model using a temperature-dependent nonlinear viscous element in network A, in uniaxial compression at $105°C$

In Table 3.7, the model parameters are exactly the same as those used for uniaxial compression at $100°C$, with the exception of the temperatures. Figure 3.34 shows the model

predictions for the stress-strain behavior plotted with the experimental data in uniaxial compression at $105°C$. Figure 3.35 shows the model predictions for the flow stretch and network stretch behavior plotted with increasing strain for each strain rate. As shown in Figure 3.34, the model predicts the stress-strain behavior reasonably well, especially when considering that the same parameters from the uniaxial compression at $100°C$ were used with only a modification with respect to temperature. Again, the stress-strain behavior is underpredicted in the strain hardening region for the fastest strain rate and overpredicted for the slowest strain rate. This is understandable when considering that adiabatic heating and crystallization effects were not taken into account. The evolution of the flow stretch and the network stretch are similar to that found for uniaxial compression at $100°C$, as expected.

The ability to predict the $105°C$ response without using data reduced from the $105°C$ experimental curves demonstrates the potential predictive capability of this form of model in terms of covering a wide range of temperatures with the same material constants. Future work should address working with the form of model to determine appropriate constants that predict the strain hardening behavior spanning from $90°C$ to $120°C$, the typical processing range for PET.

3.7 Conclusions

The deformation of initially amorphous, unoriented PET above its glass transition has been modeled through the use of a dual resistance model. The two distinct resistances are: (1) a resistance to initial flow, and (2) an evolving resistance to continued flow (exhibited by strain hardening). Both of these resistances are observed to depend on strain rate and deformation temperature. The model incorporates the following constitutive relationships to act together to predict the mechanical behavior:

- a Neo-Hookean law to dictate the initial stiffness of the material that is independent of strain rate
- a thermal activation law for the temperature and strain rate dependence of the initial flow stress
- the Arruda-Boyce 8-chain model for the strain hardening behavior of the material; physically, this model is based on the idea of a network of chains orienting cooperatively during deformation until reaching a limiting chain extensibility
- a viscosity model that governs the strain rate dependence as well as the temperature dependence of the strain hardening behavior; this model takes into account the entanglement drift and relaxation of molecules that occurs at lower strain rates and/or higher temperatures in the material, but also provides for a critical network stretch where this entanglement drift/relaxation ceases

The constitutive model was found to predict the experimental data reasonably well. Also, since the constitutive model did not specifically incorporate the effects of strain-induced crystallization, it is best termed a network stretch model. The refinement to the model proved effective in predicting the behavior at another temperature without altering the model parameters. There was better agreement with the uniaxial compression data than with the plane strain compression data, and better agreement at lower strain rates. The better agreement is understandable since the model did not take adiabatic heating or crystallization effects into account.

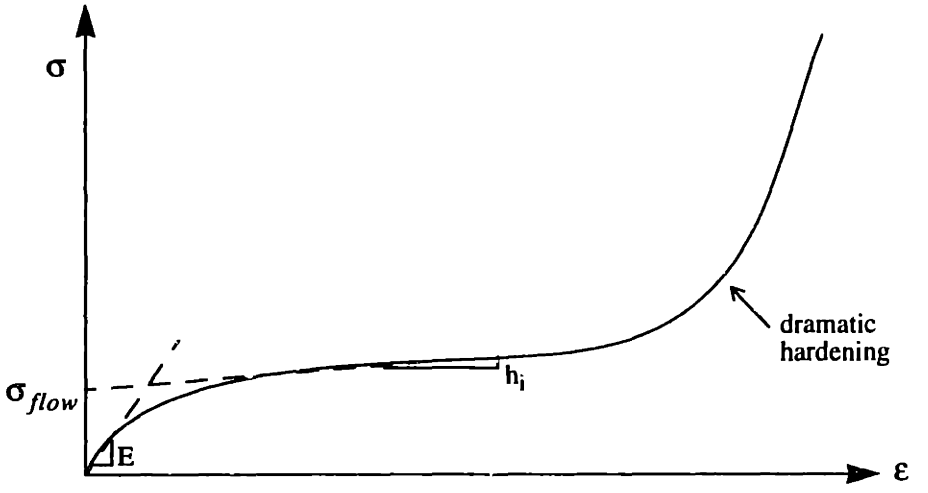

Figure 3.1: Schematic plot of a representative stress-strain curve of PET in the rubbery regime indicating the flow stress σ_{flow}, initial stiffness E, initial strain hardening modulus h_i, and dramatic strain hardening

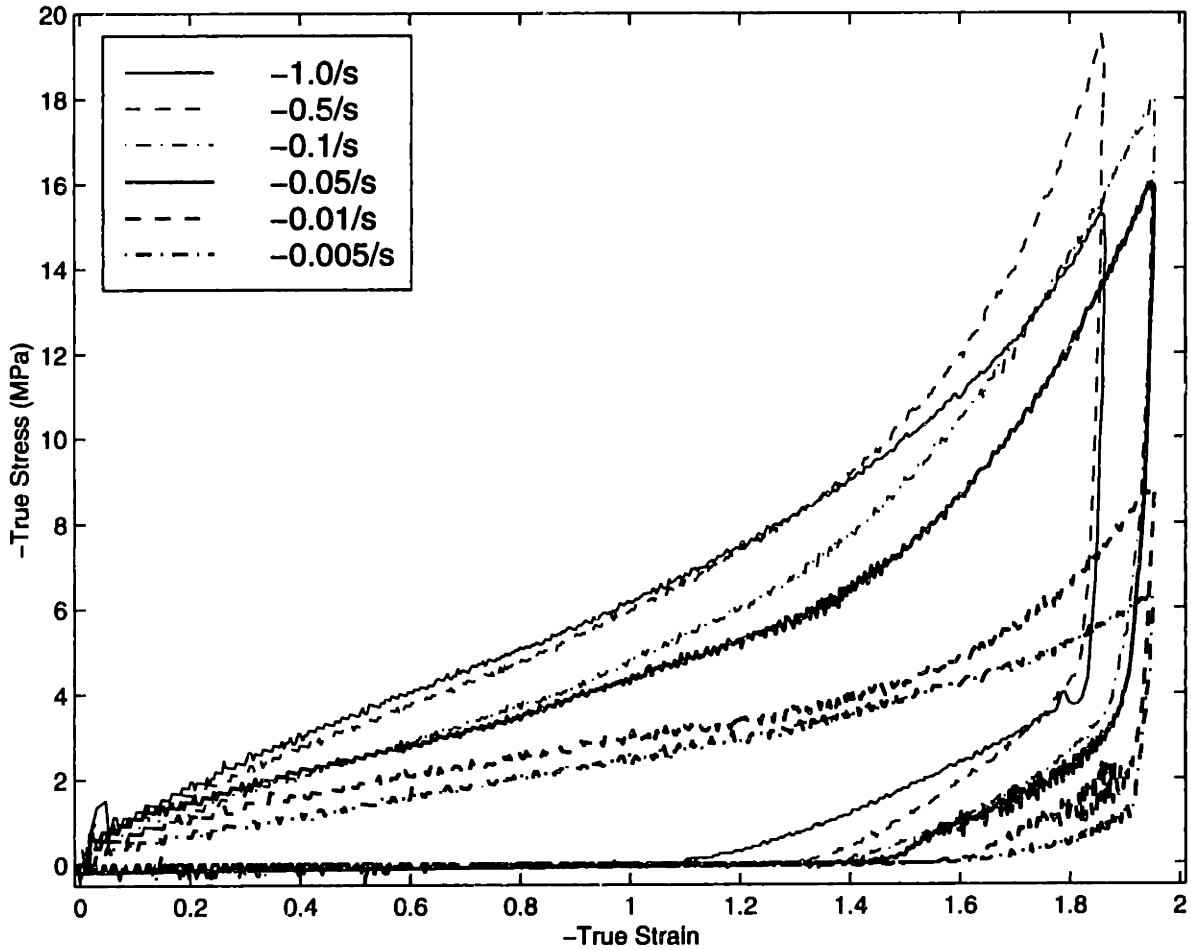

Figure 3.2: Uniaxial Compression Data, Temperature = $90°C$

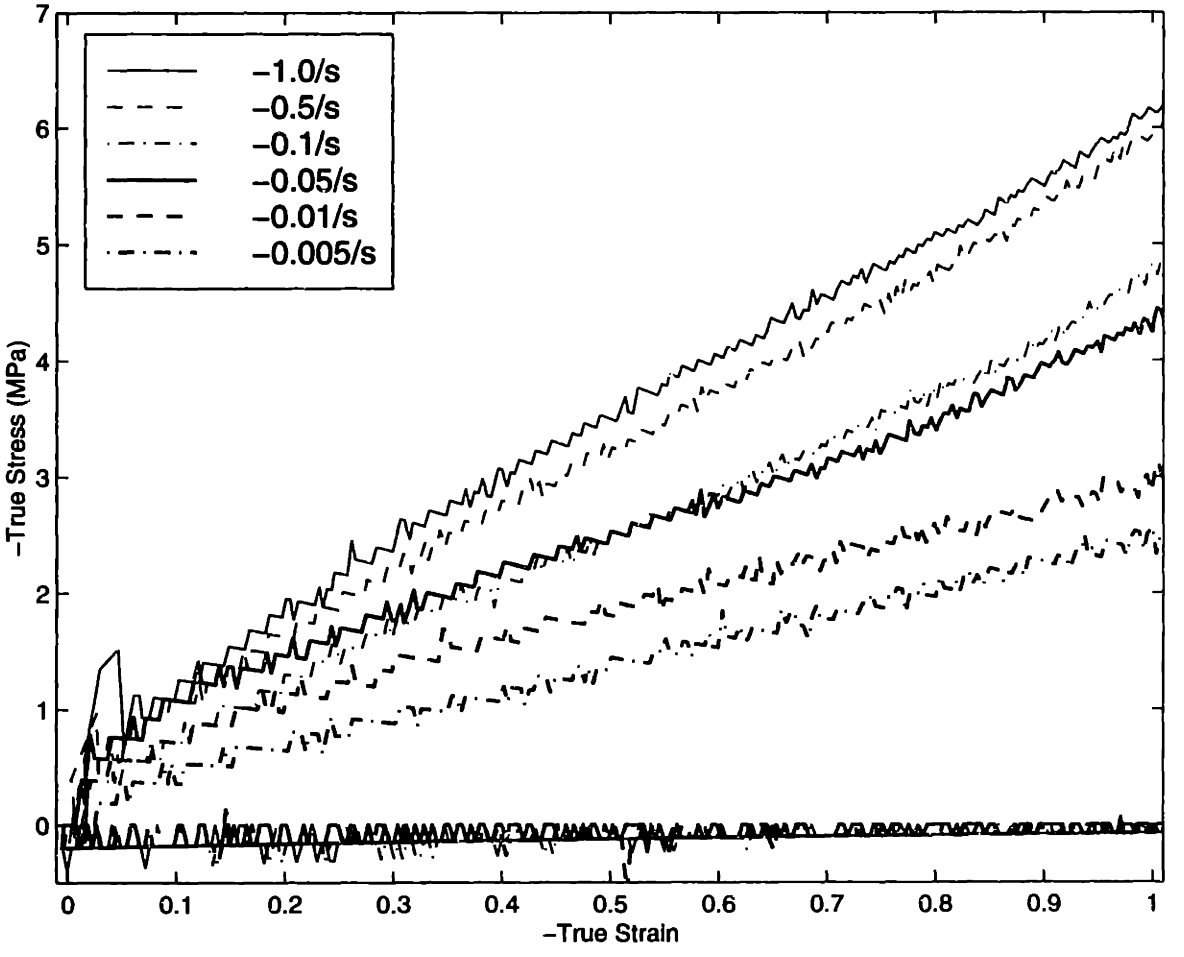

Figure 3.3: Uniaxial Compression Data, Temperature = $90°C$, blown up to a final strain of -1.0

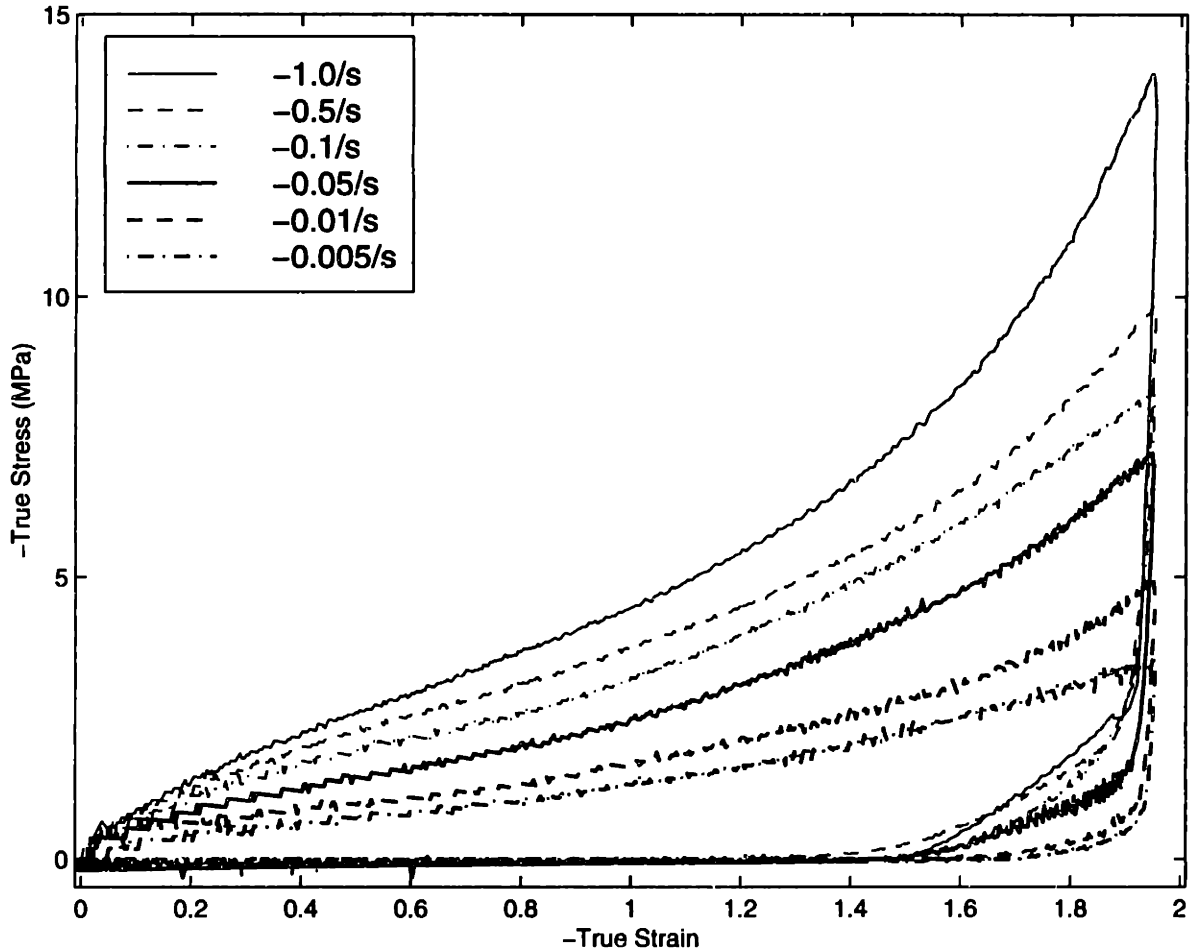

Figure 3.4: Uniaxial Compression Data, Temperature = $100°C$

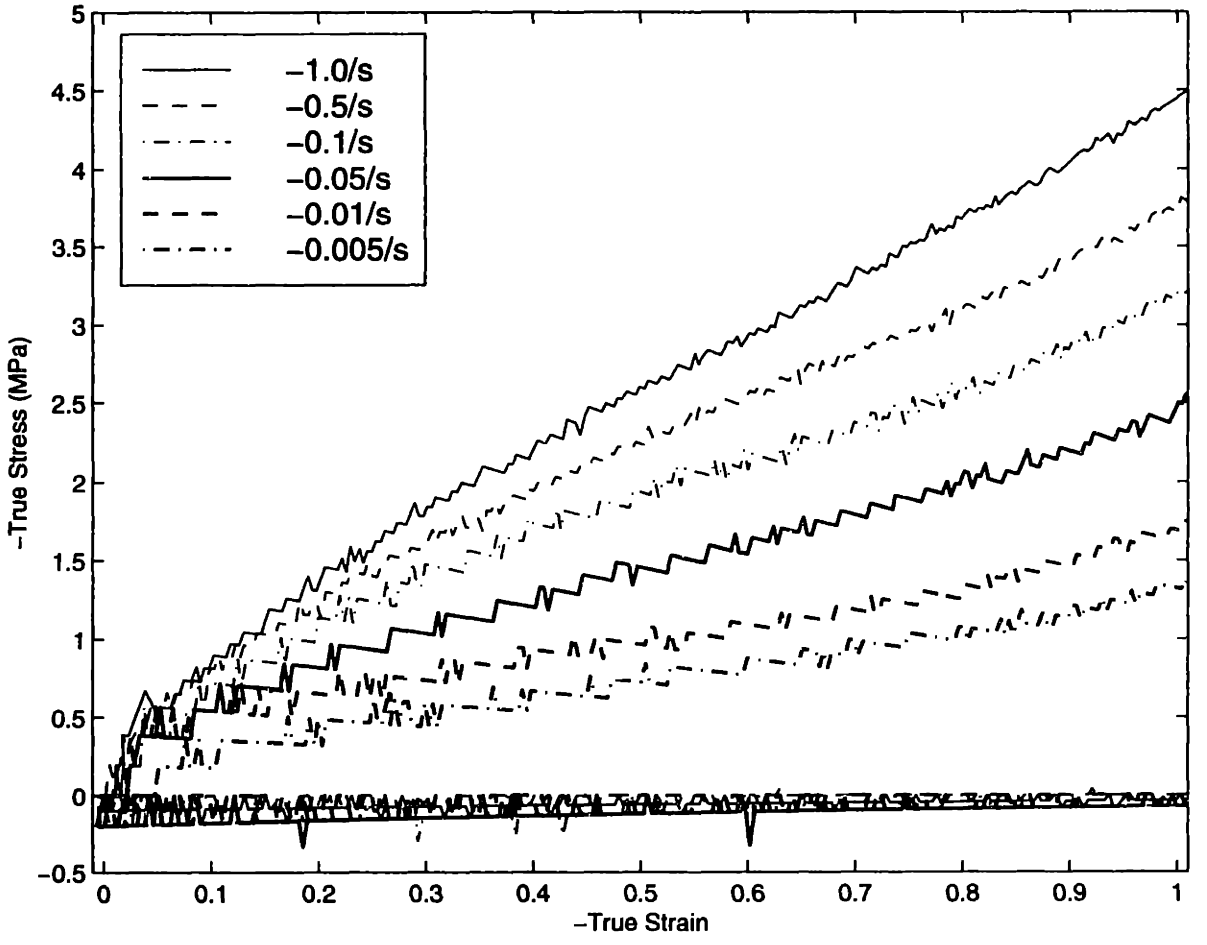

Figure 3.5: Uniaxial Compression Data, Temperature = $100°C$, blown up to a final strain of -1.0

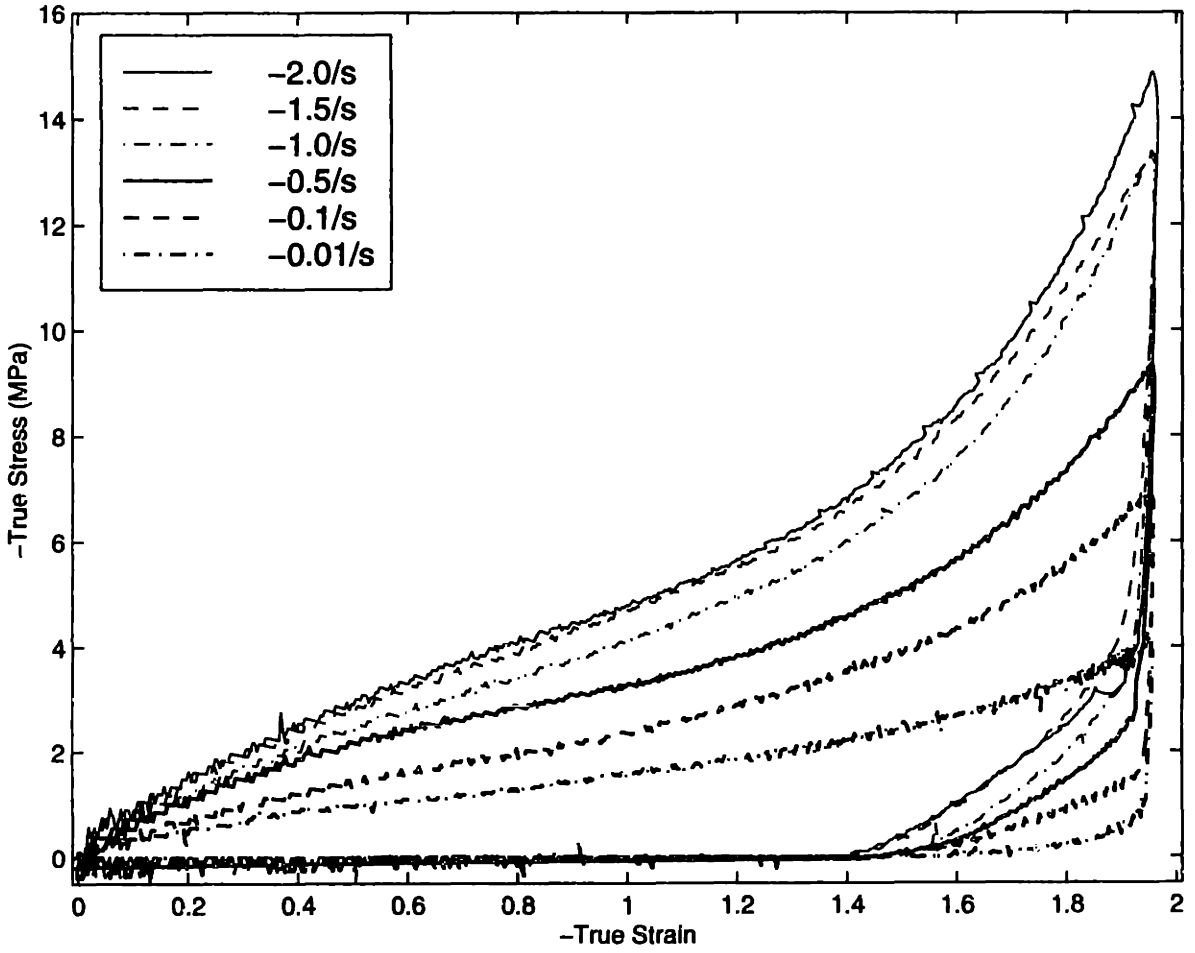

Figure 3.6: Uniaxial Compression Data, Temperature = $105°C$

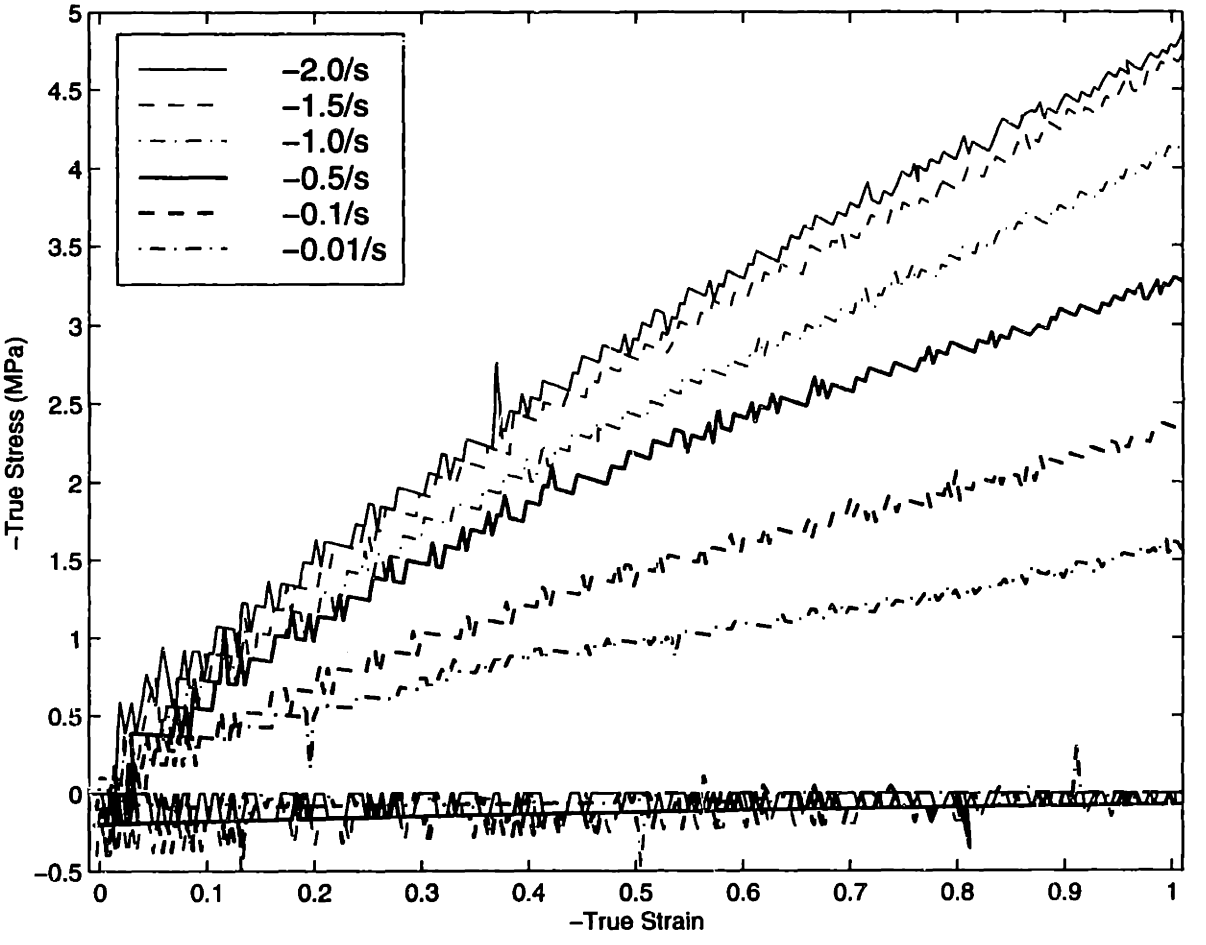

Figure 3.7: Uniaxial Compression Data, Temperature = $105°C$, blown up to a final strain of -1.0

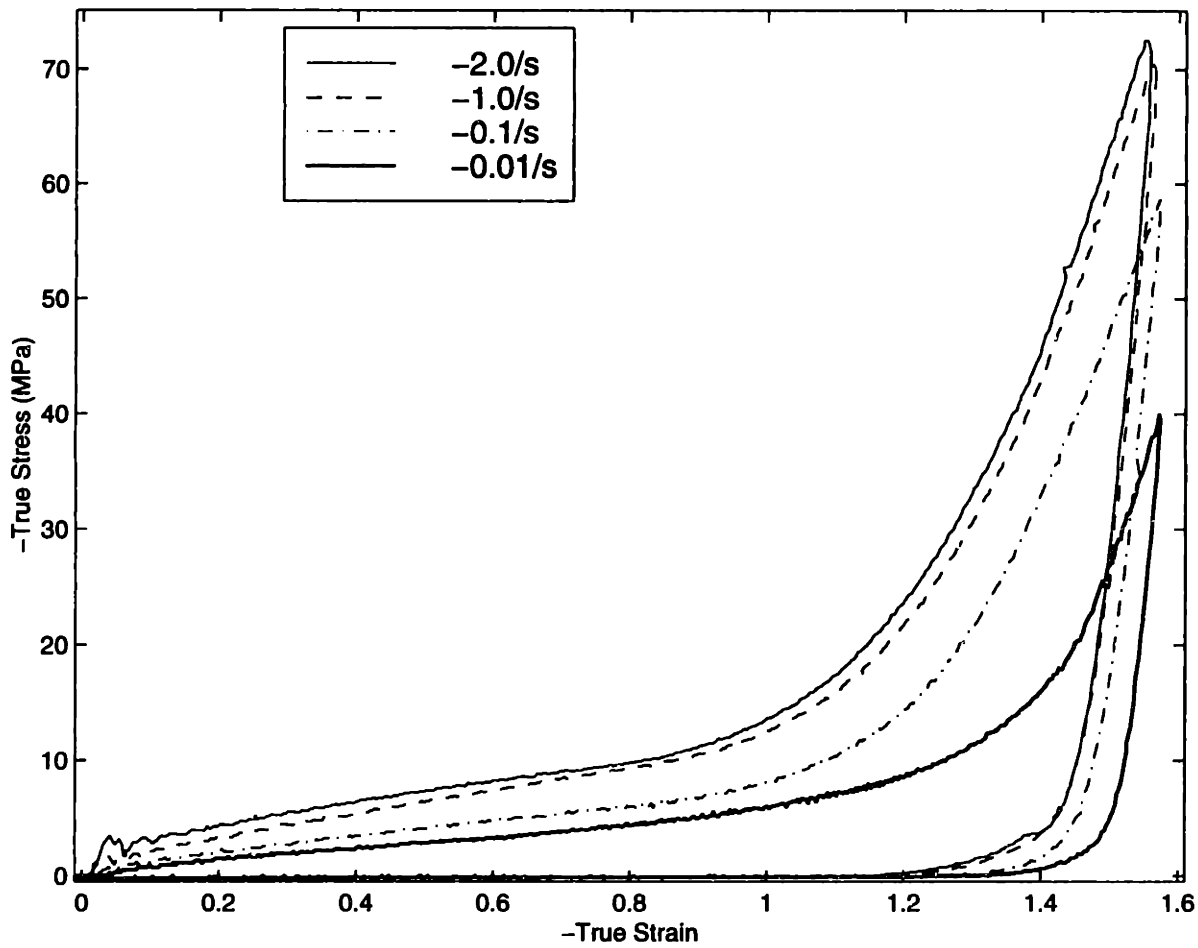

Figure 3.8: Plane Strain Compression Data, Temperature = $90°C$

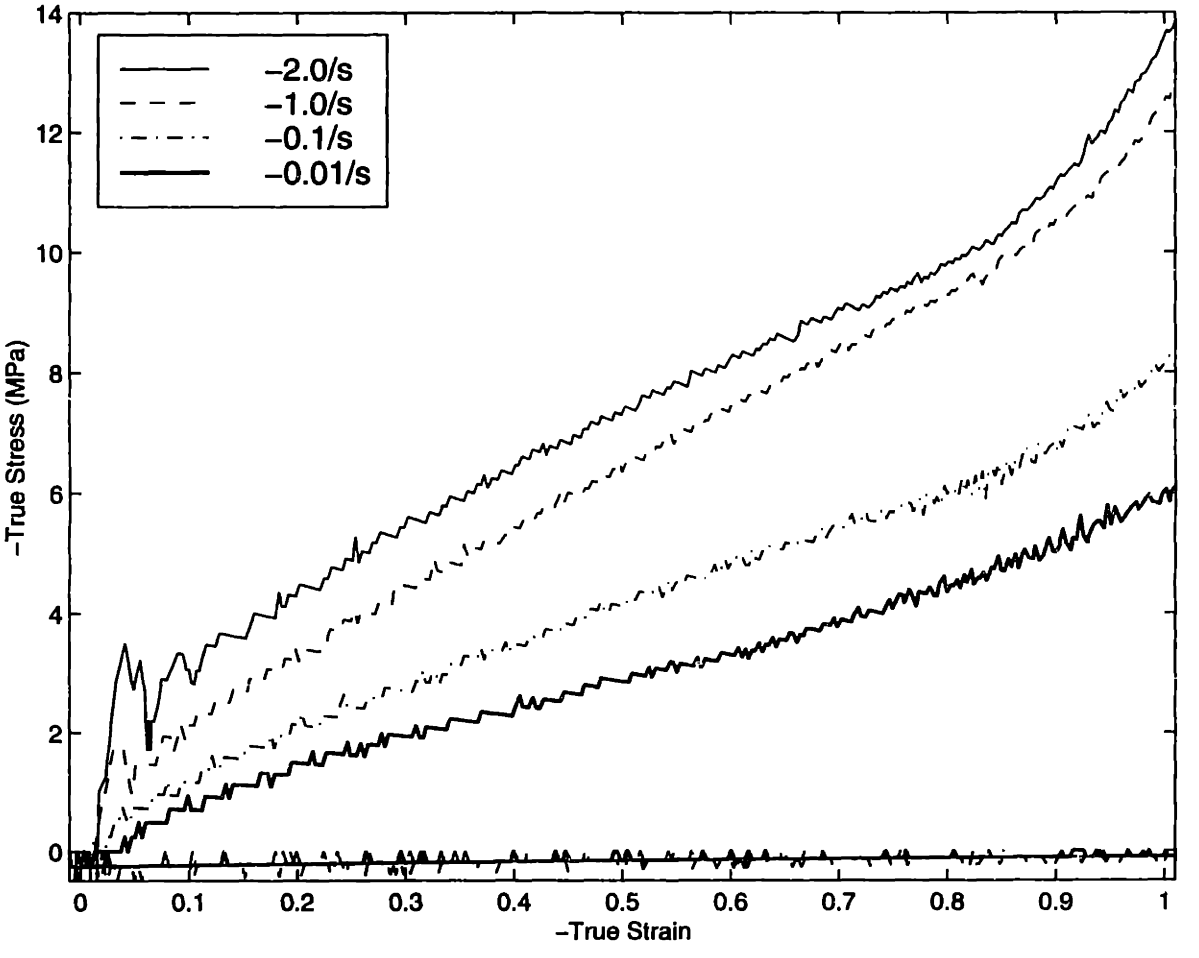

Figure 3.9: Plane Strain Compression Data, Temperature = $90°C$, blown up to a final strain of -1.0

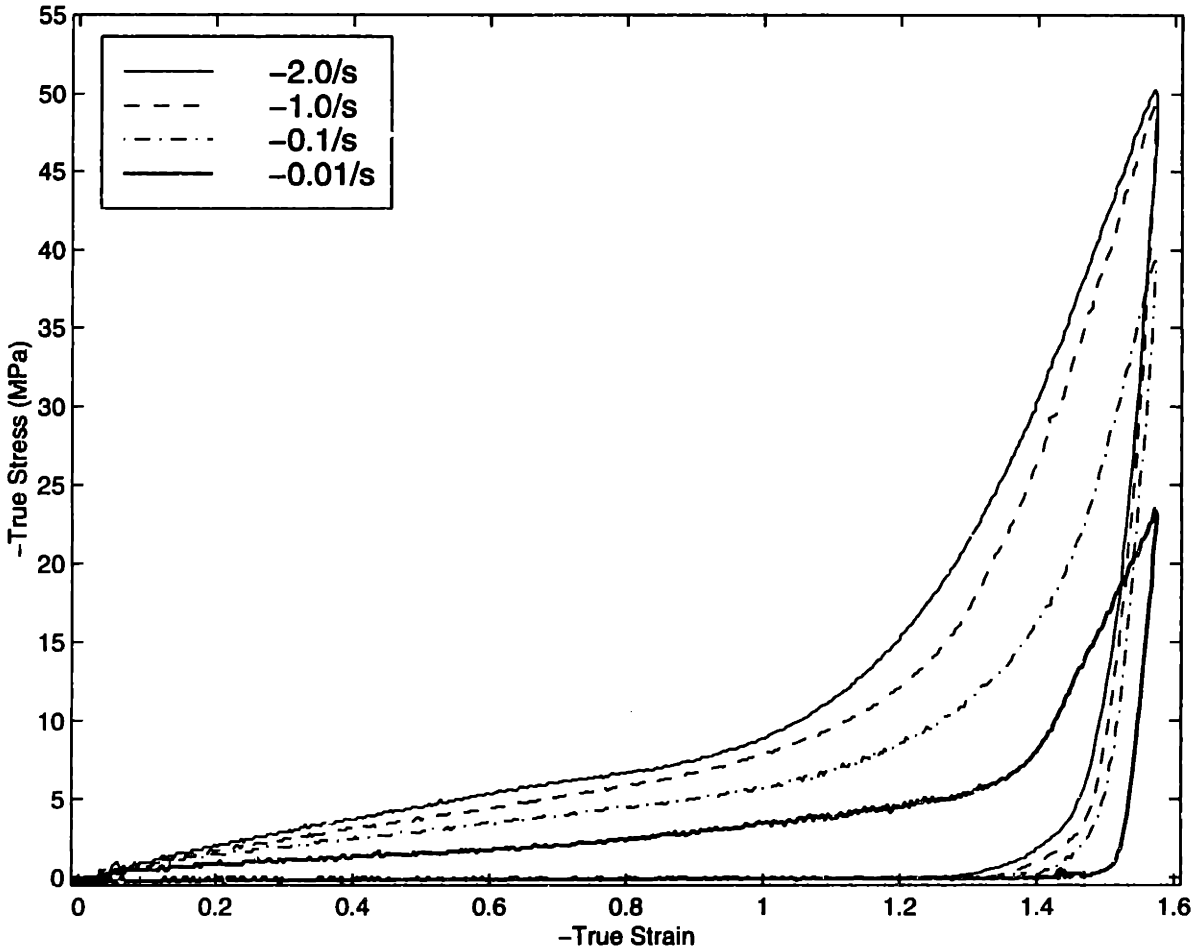

Figure 3.10: Plane Strain Compression Data, Temperature = $100°C$

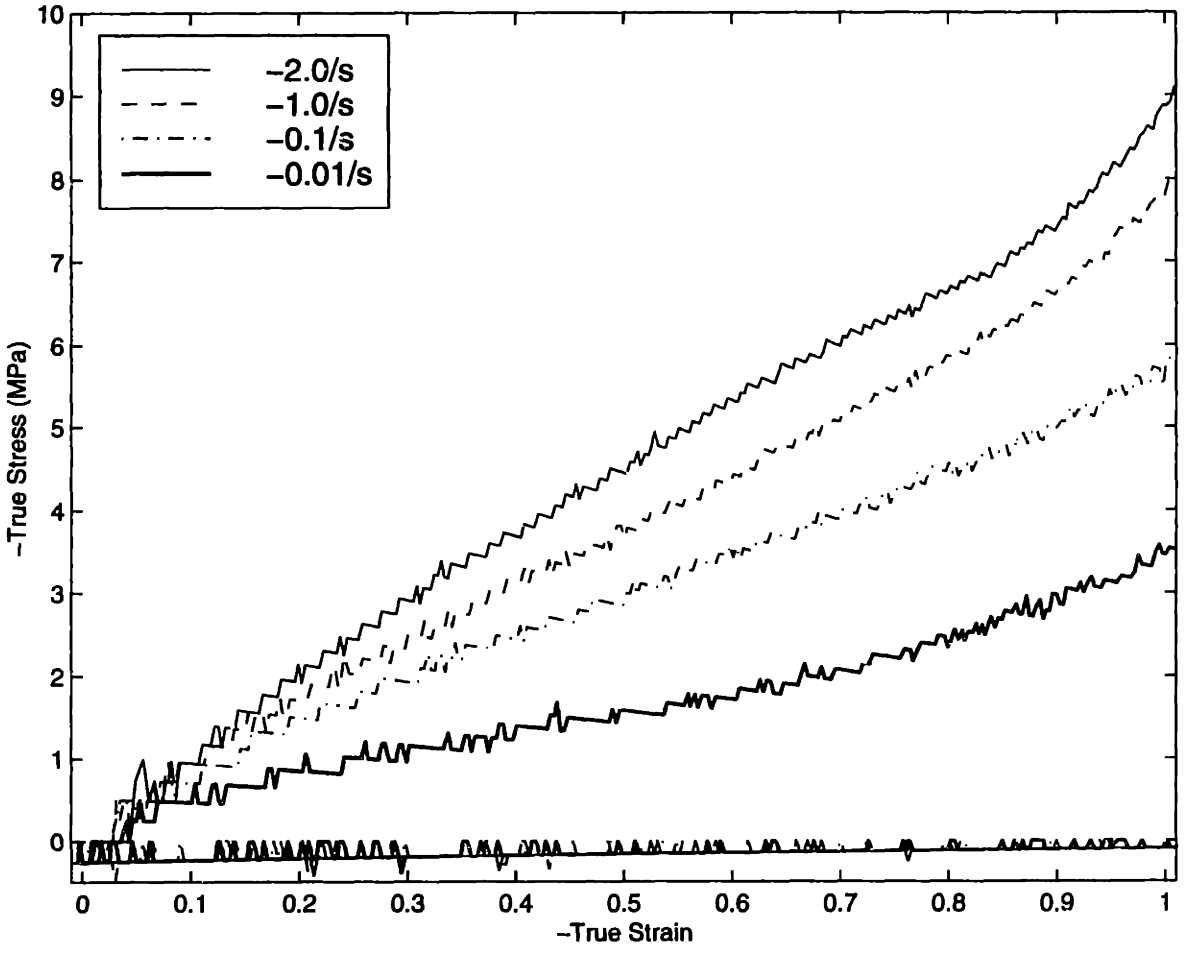

Figure 3.11: Plane Strain Compression Data, Temperature = $100°C$, blown up to a final strain of -1.0

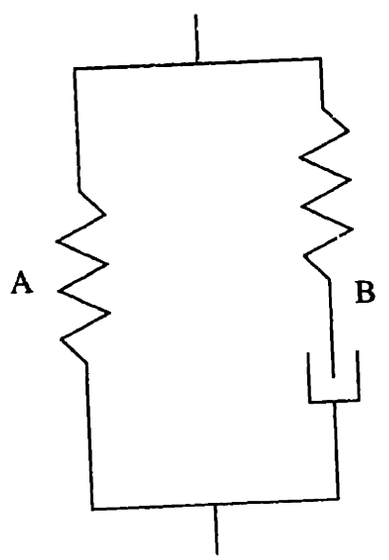

Figure 3.12: Spring and dashpot framework used by Bergstrom and Boyce [48]

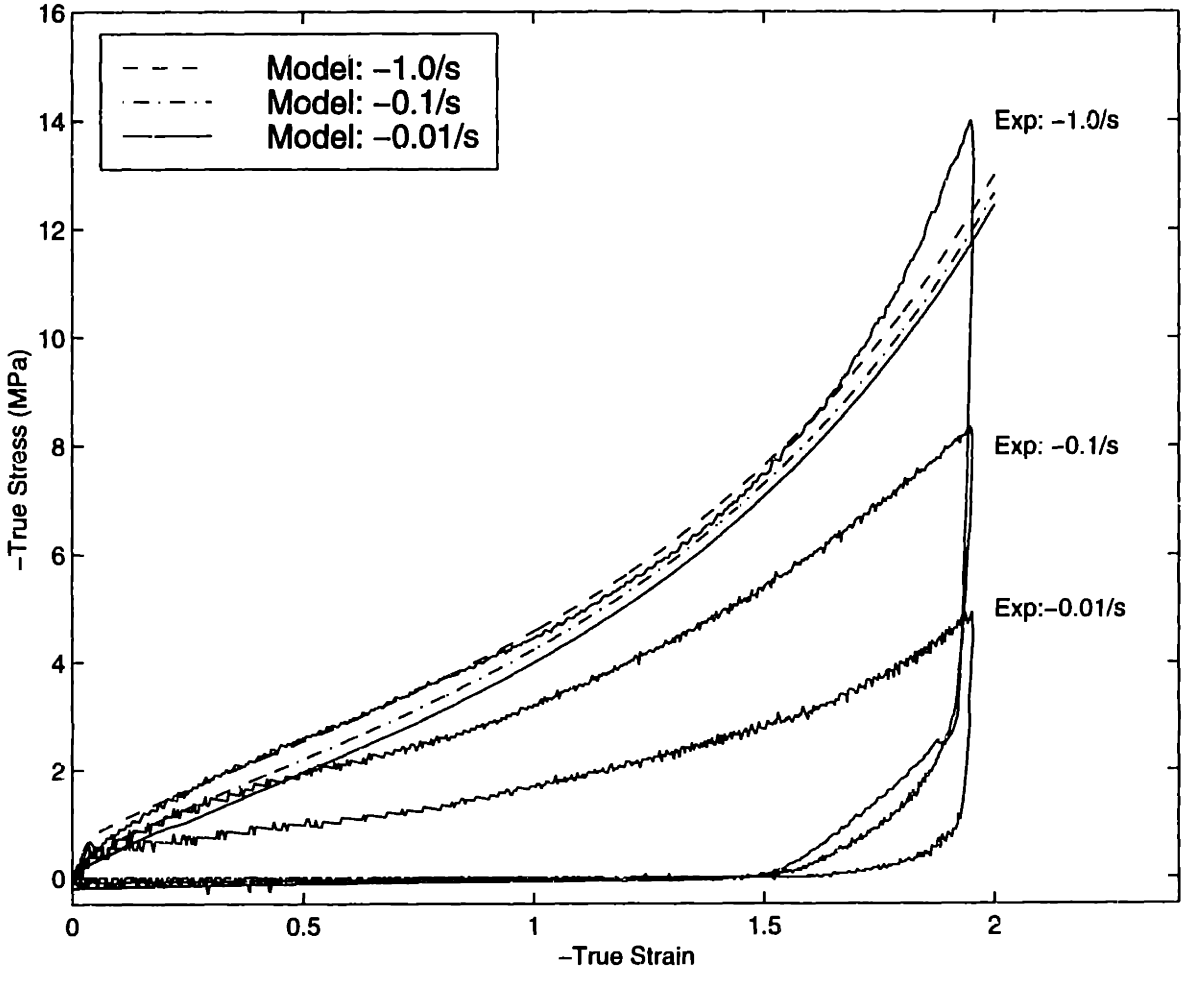

Figure 3.13: Comparison of three-component dual resistance model to experimental data in uniaxial compression at $100°C$

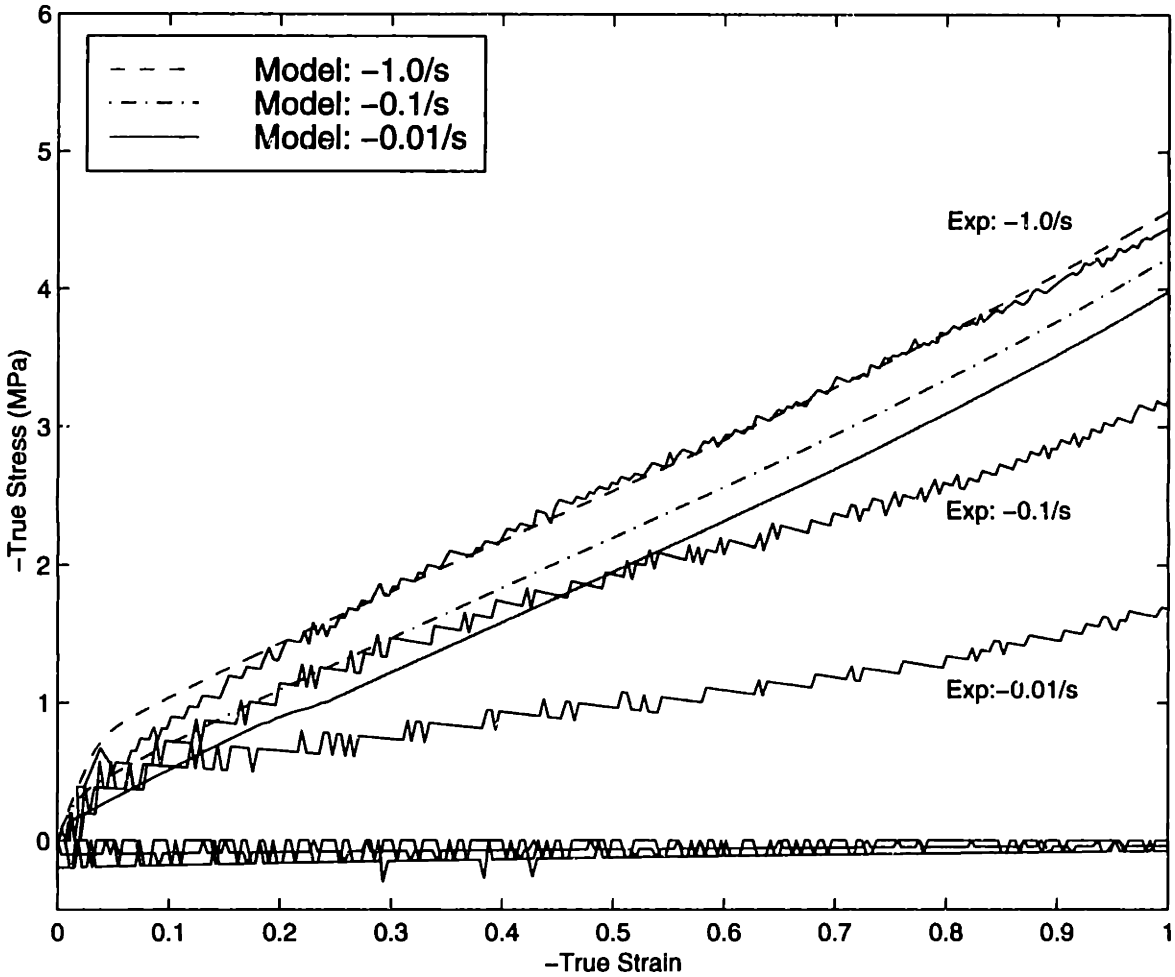

Figure 3.14: Blow up of comparison of dual resistance model to experimental data in uniaxial compression at $100°C$

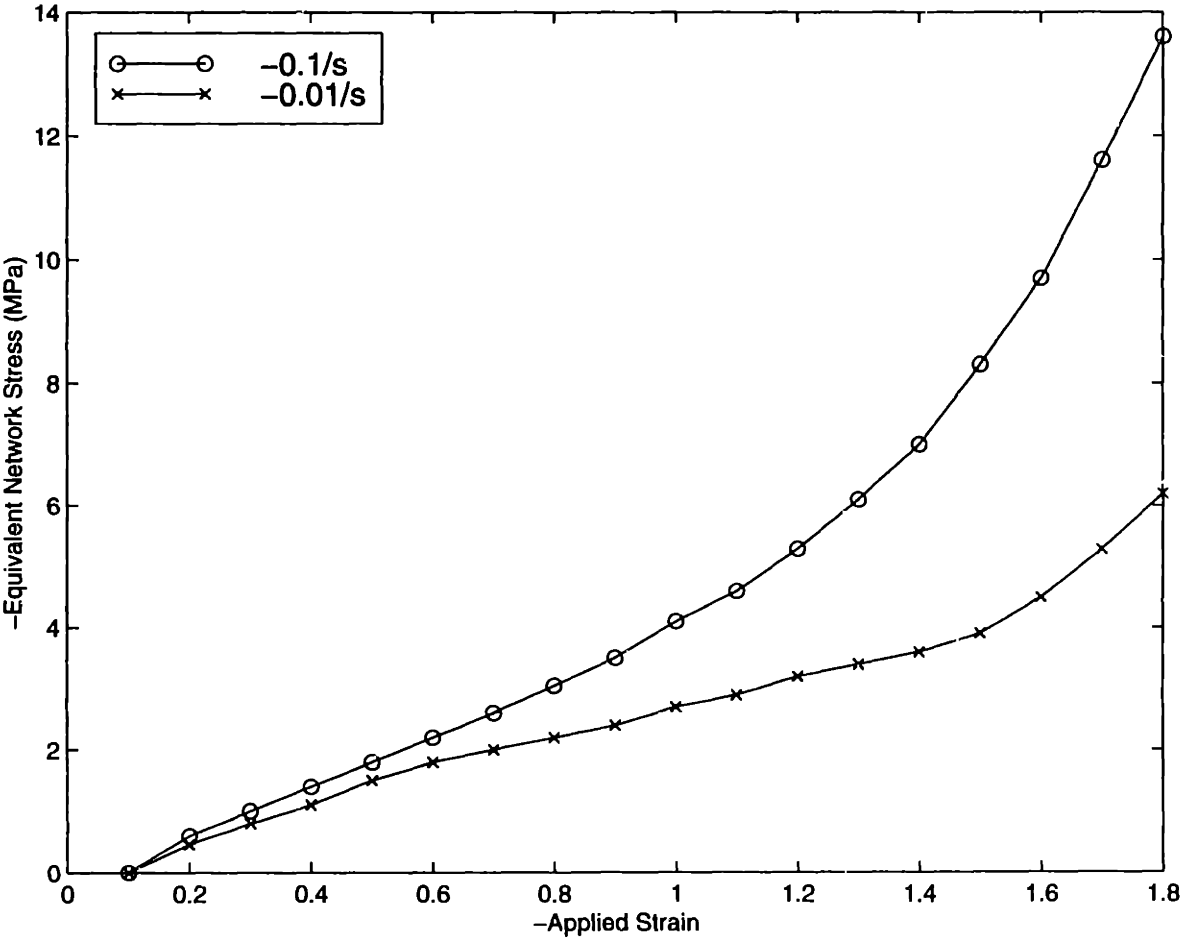

Figure 3.15: Equivalent Network Stress vs. Applied Strain, uniaxial compression at $90°C$

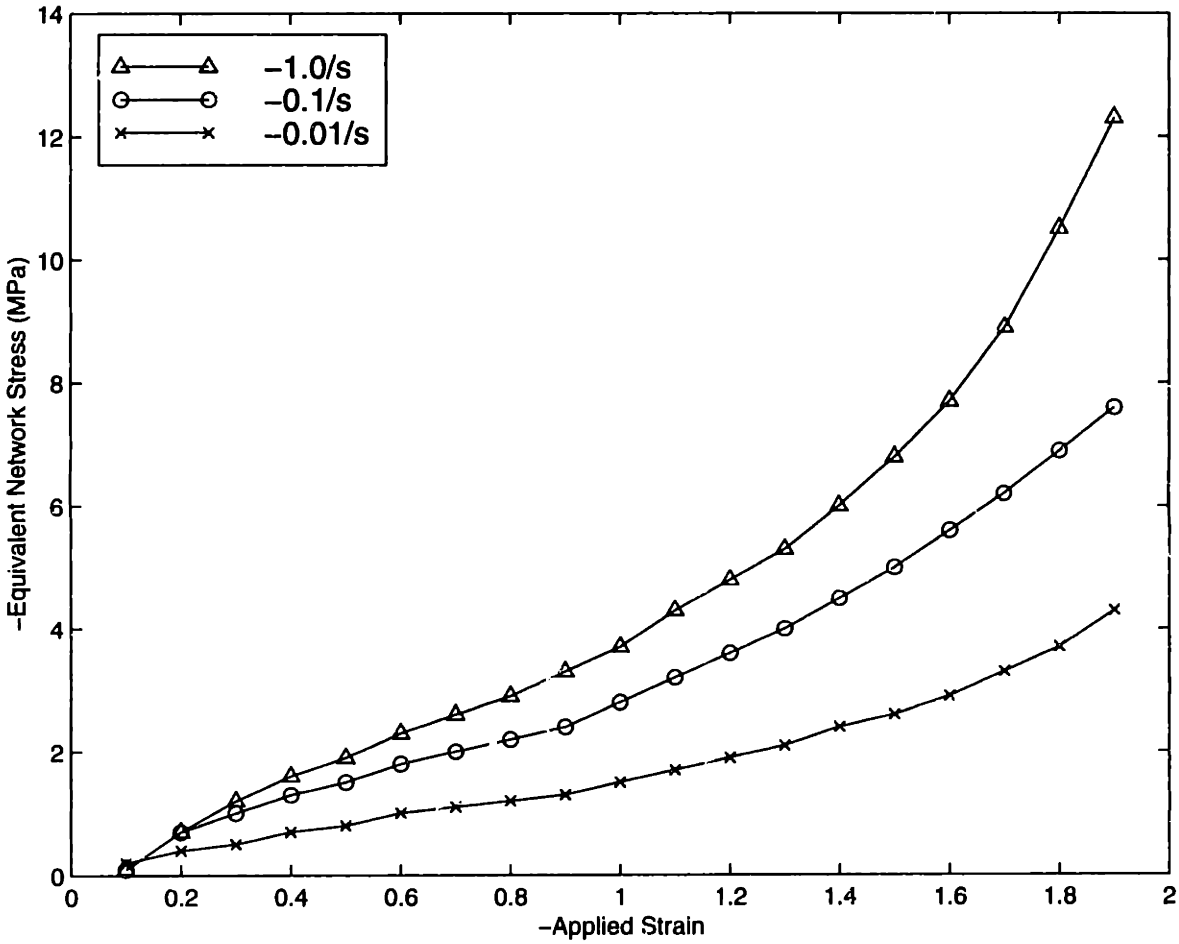

Figure 3.16: Equivalent Network Stress vs. Applied Strain, uniaxial compression at $100°C$

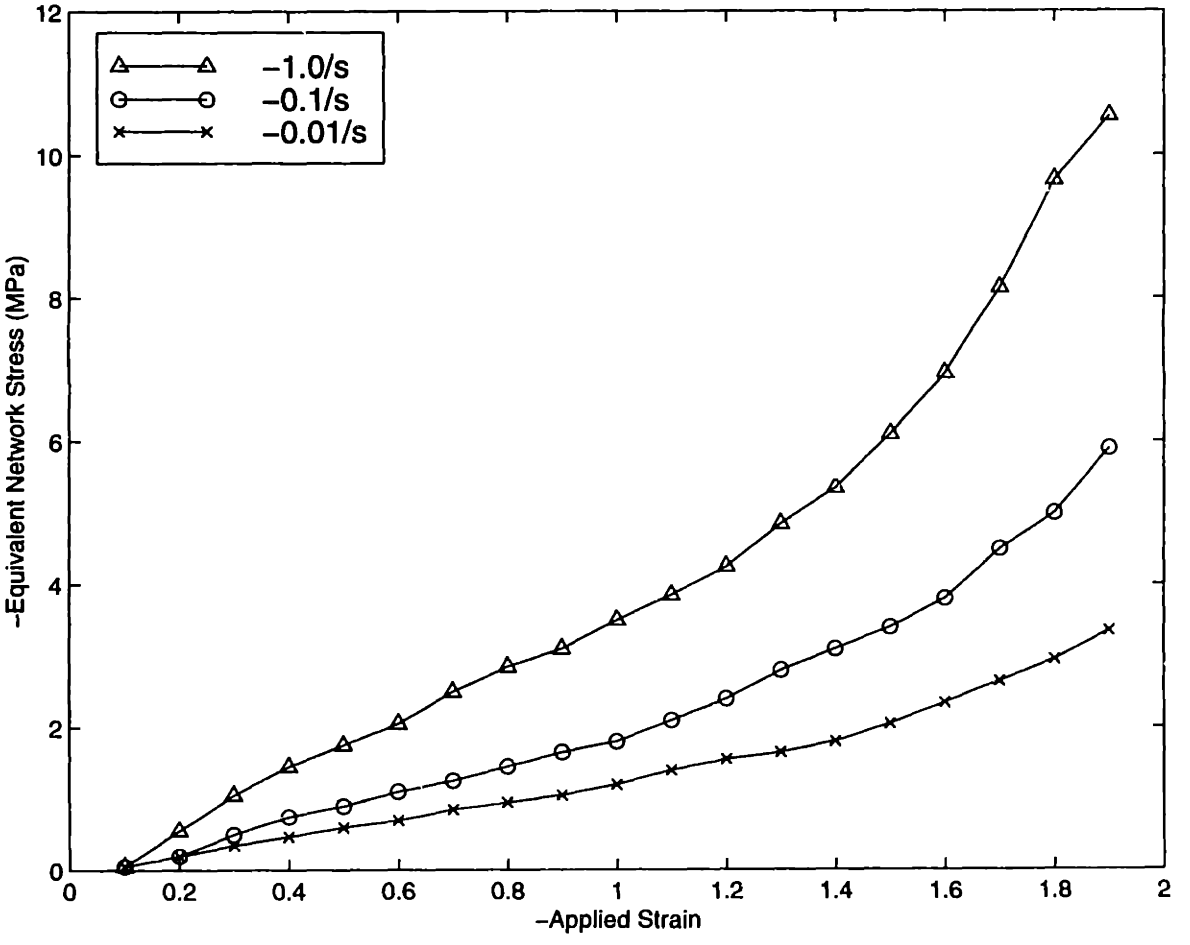

Figure 3.17: Equivalent Network Stress vs. Applied Strain, uniaxial compression at $105°C$

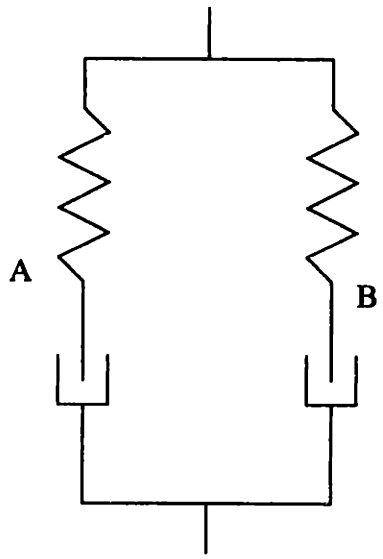

Figure 3.18: Spring and dashpot framework used for the proposed model

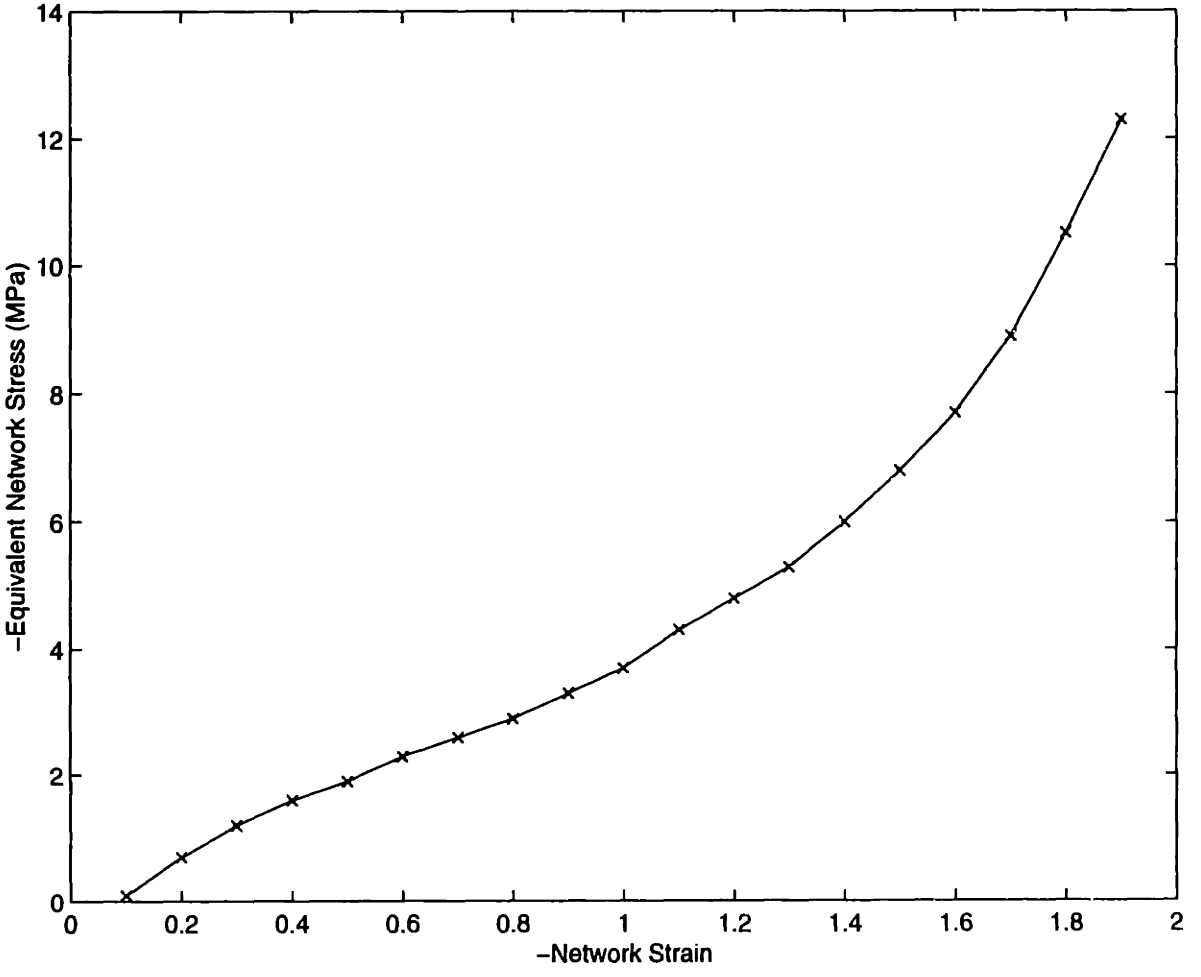

Figure 3.19: Equivalent Network Stress vs. Network Strain, uniaxial compression at $100°C$

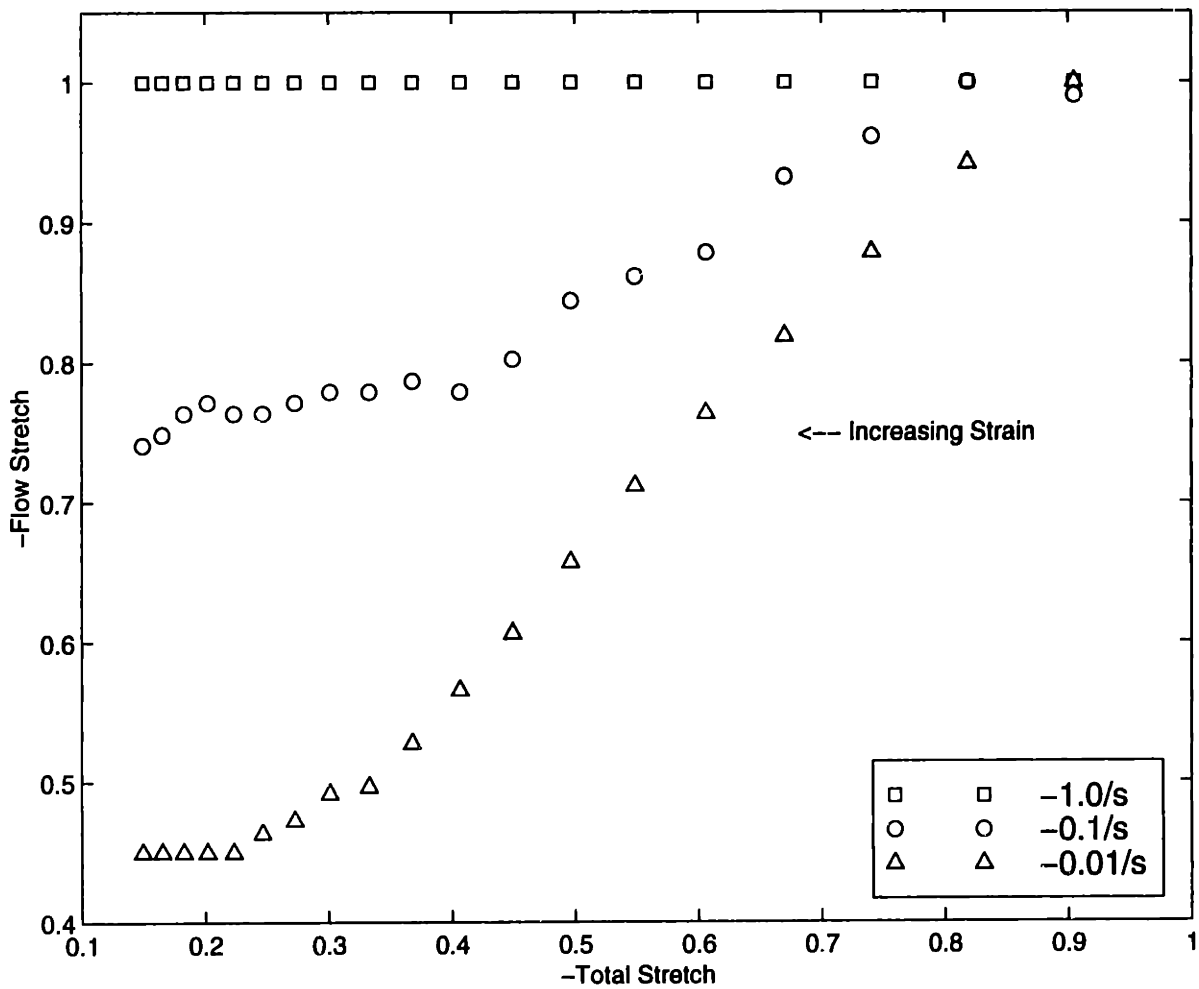

Figure 3.20: Flow Stretch vs. Total Stretch, uniaxial compression at $100°C$

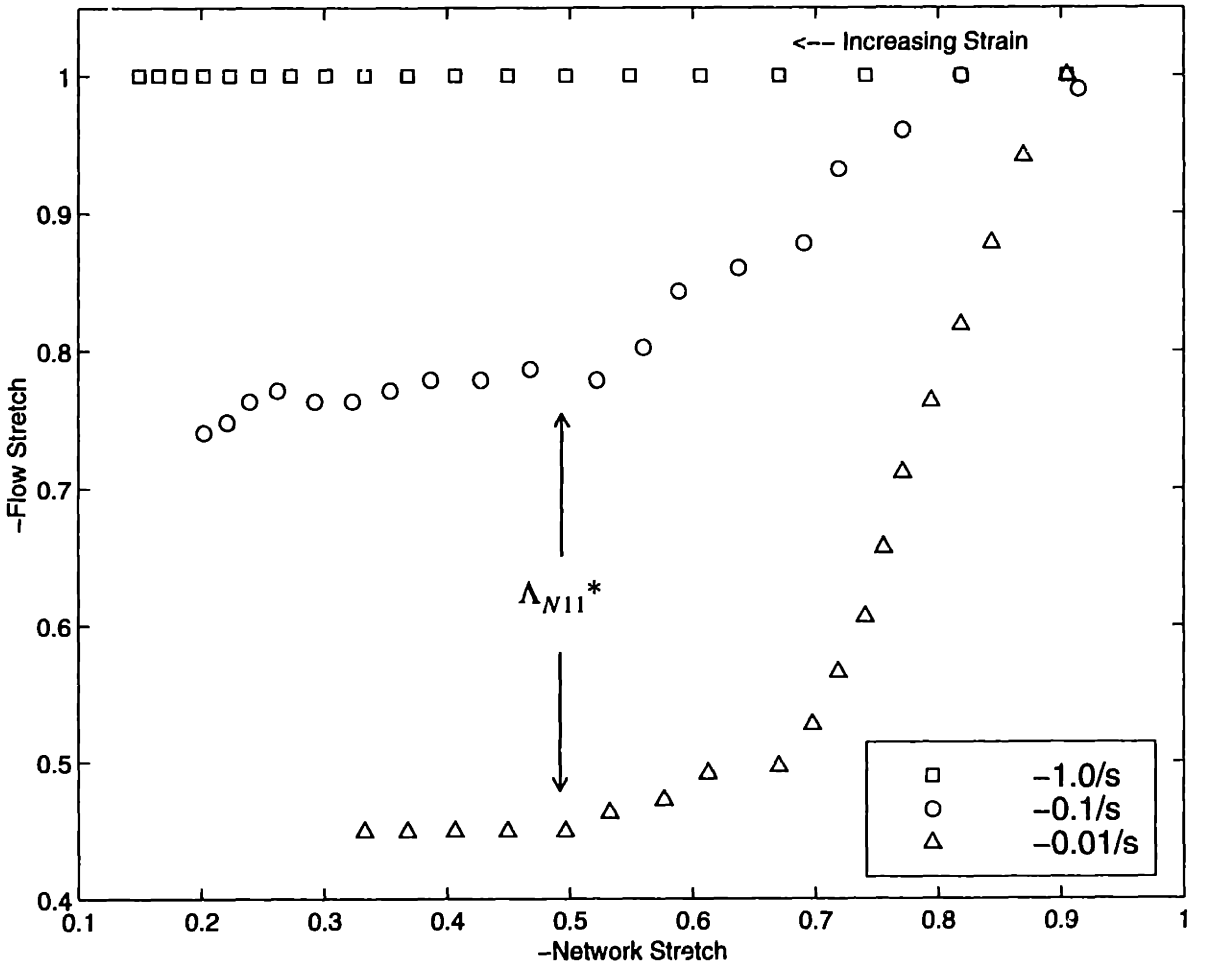

Figure 3.21: Flow Stretch vs. Network Stretch, uniaxial compression at $100°C$

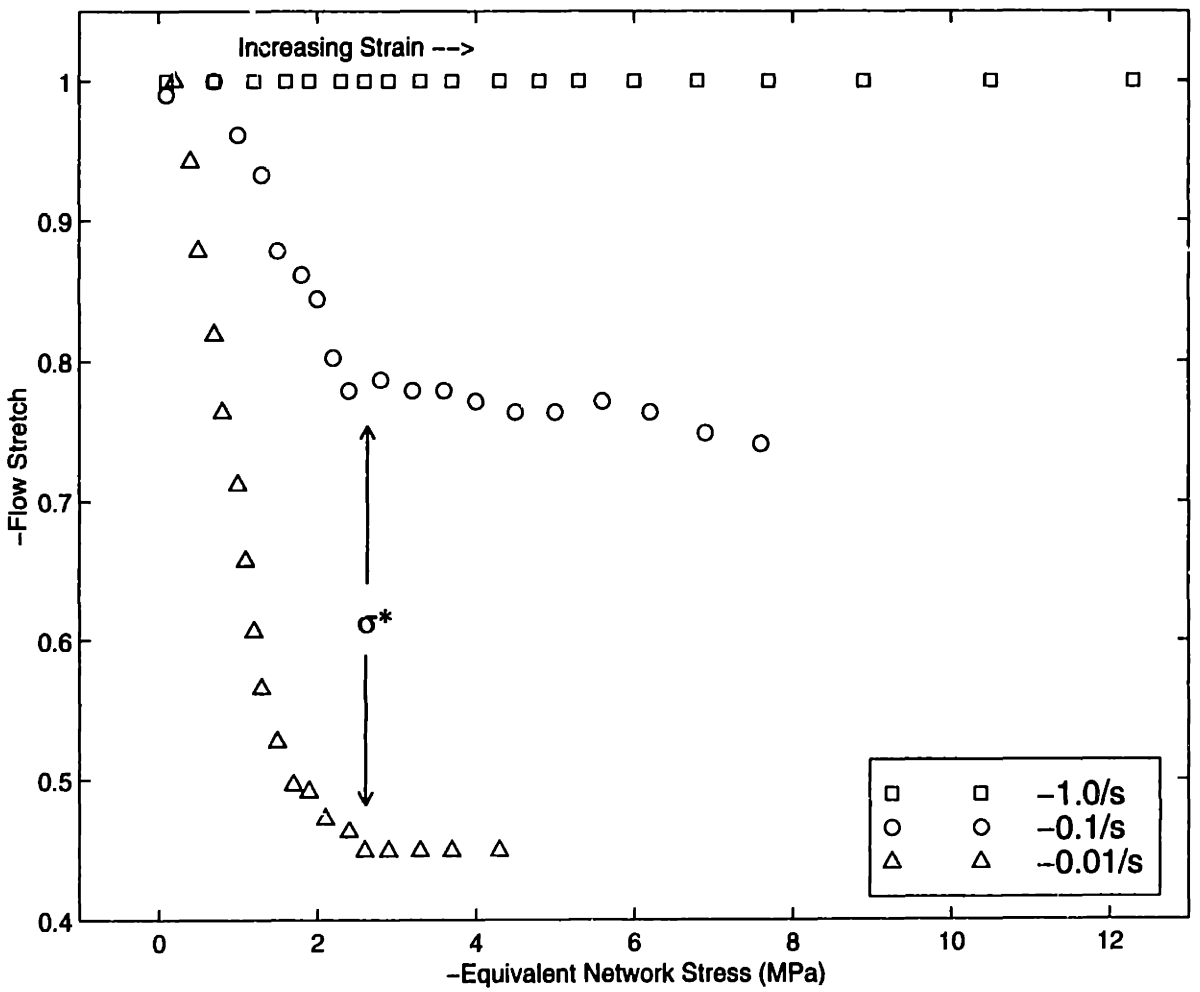

Figure 3.22: Flow Stretch vs. Equivalent Network Stress, uniaxial compression at $100°C$

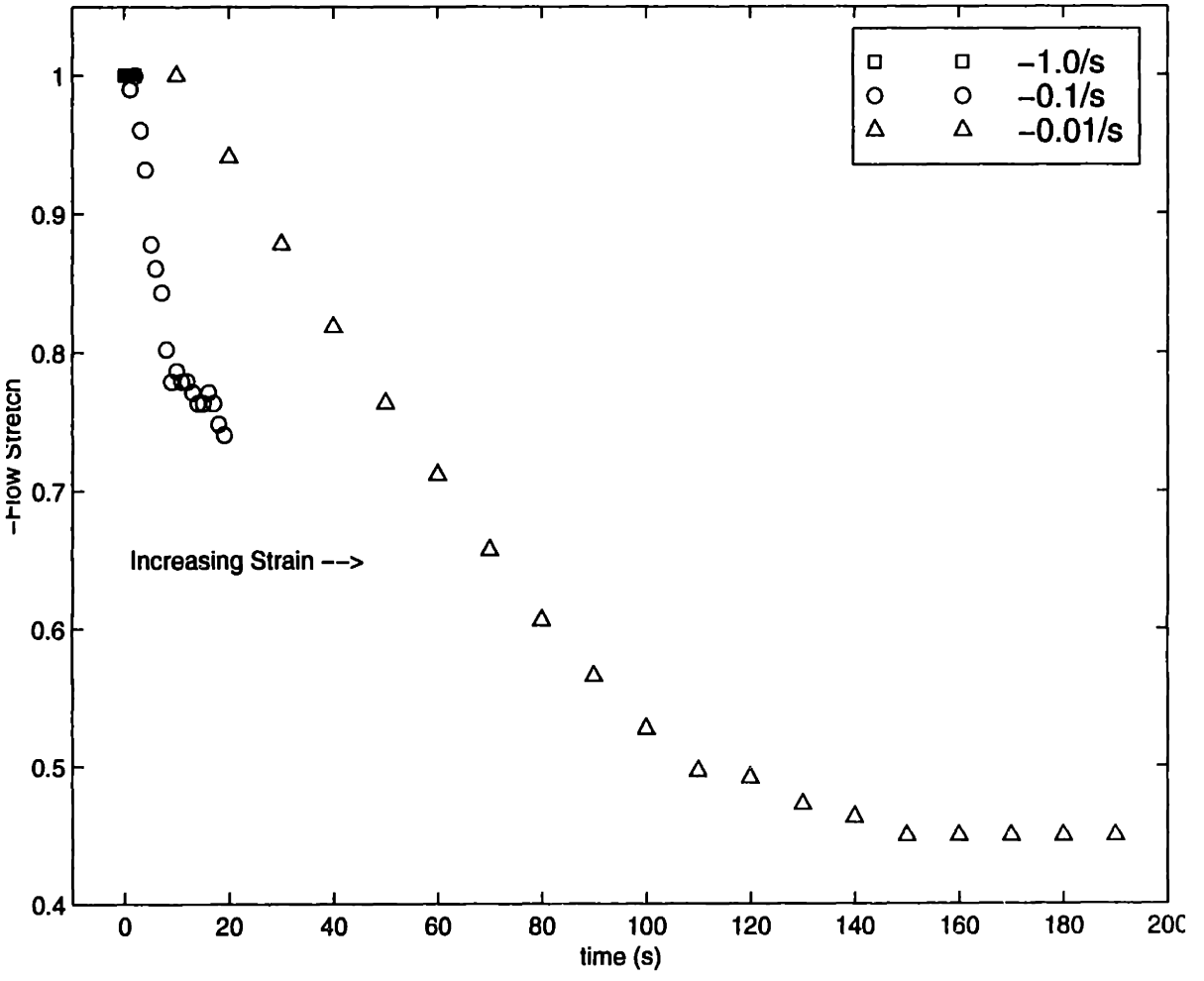

Figure 3.23: Flow Stretch vs. time, uniaxial compression at $100°C$

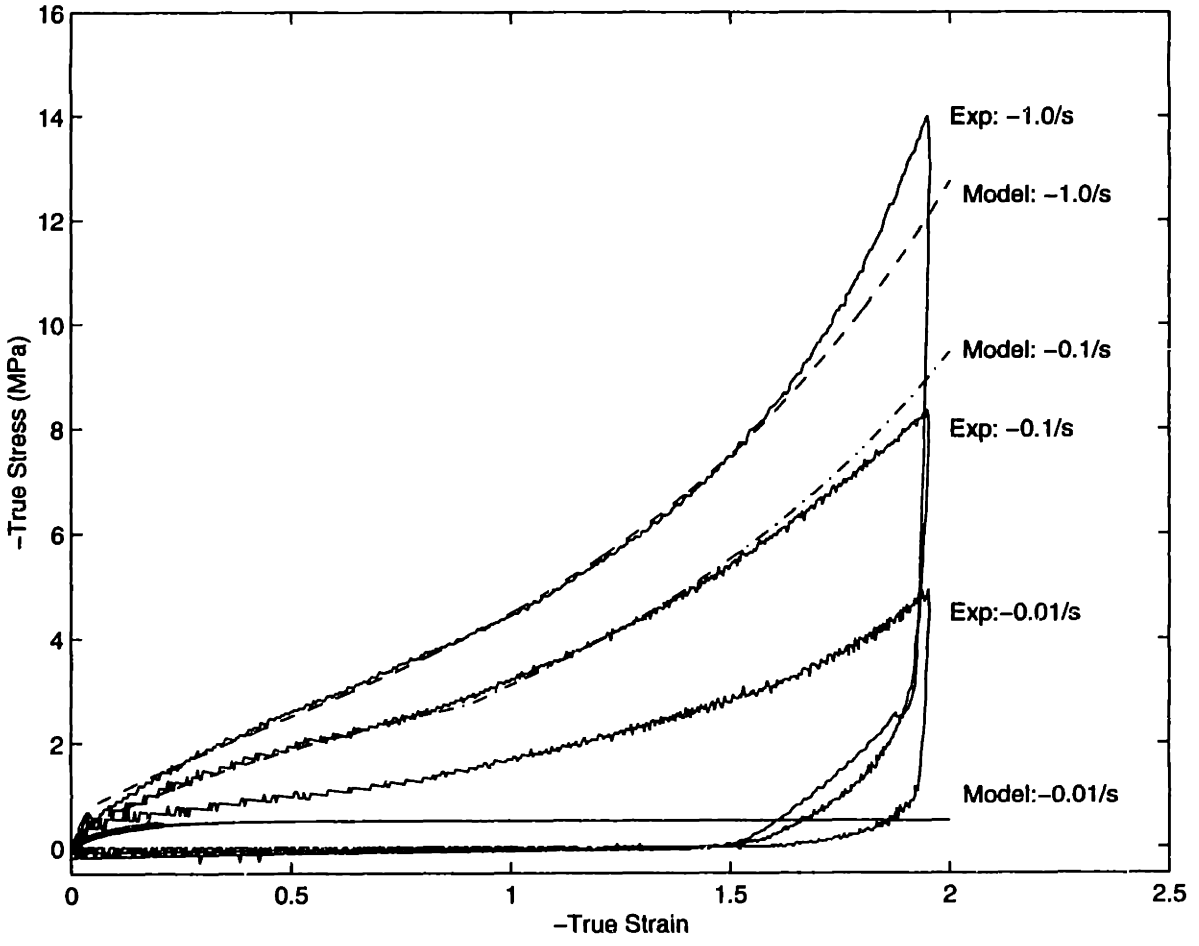

Figure 3.24: Comparison of dual resistance model to experimental data incorporating a linear viscous dashpot in network A, $C = 0.031$

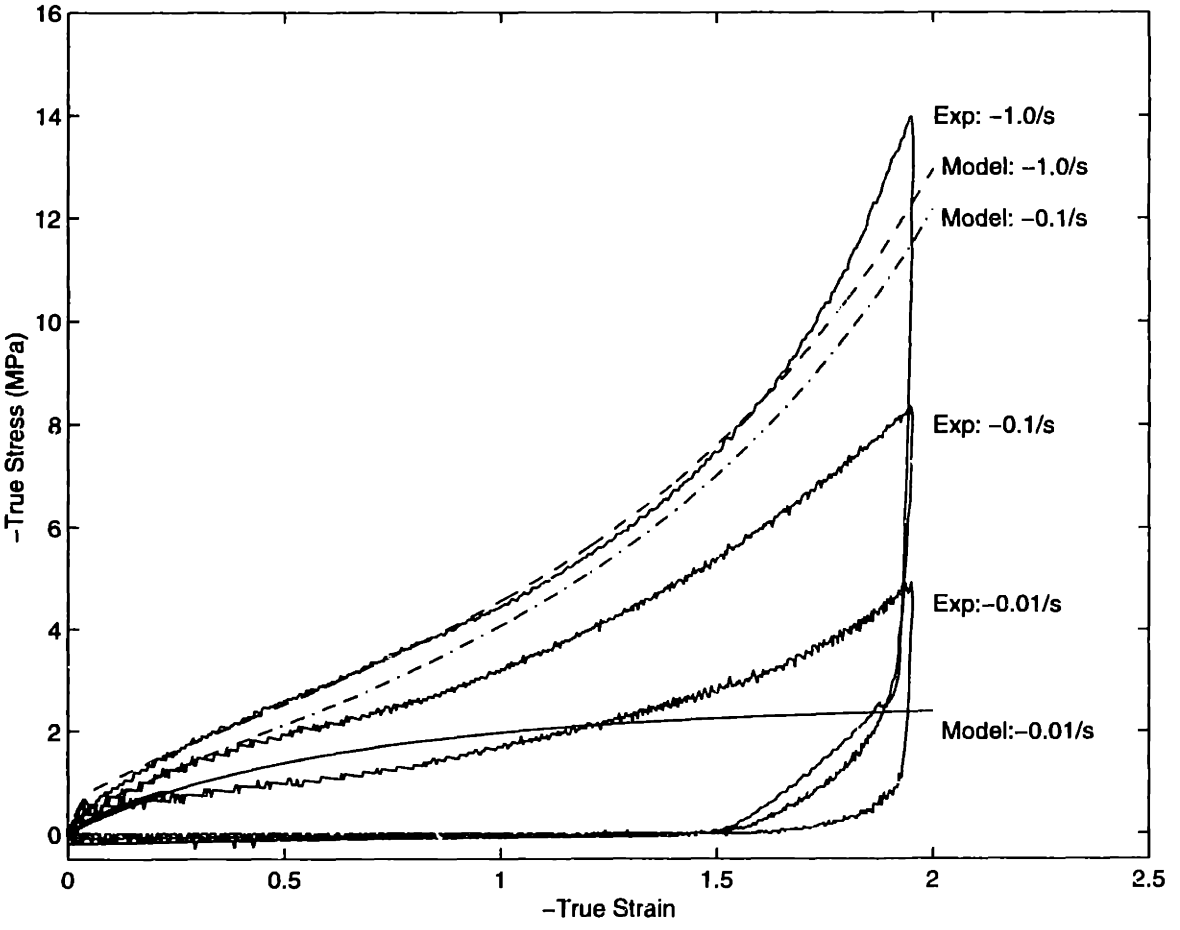

Figure 3.25: Comparison of dual resistance model to experimental data incorporating a linear viscous dashpot in network A, $C = 0.006$

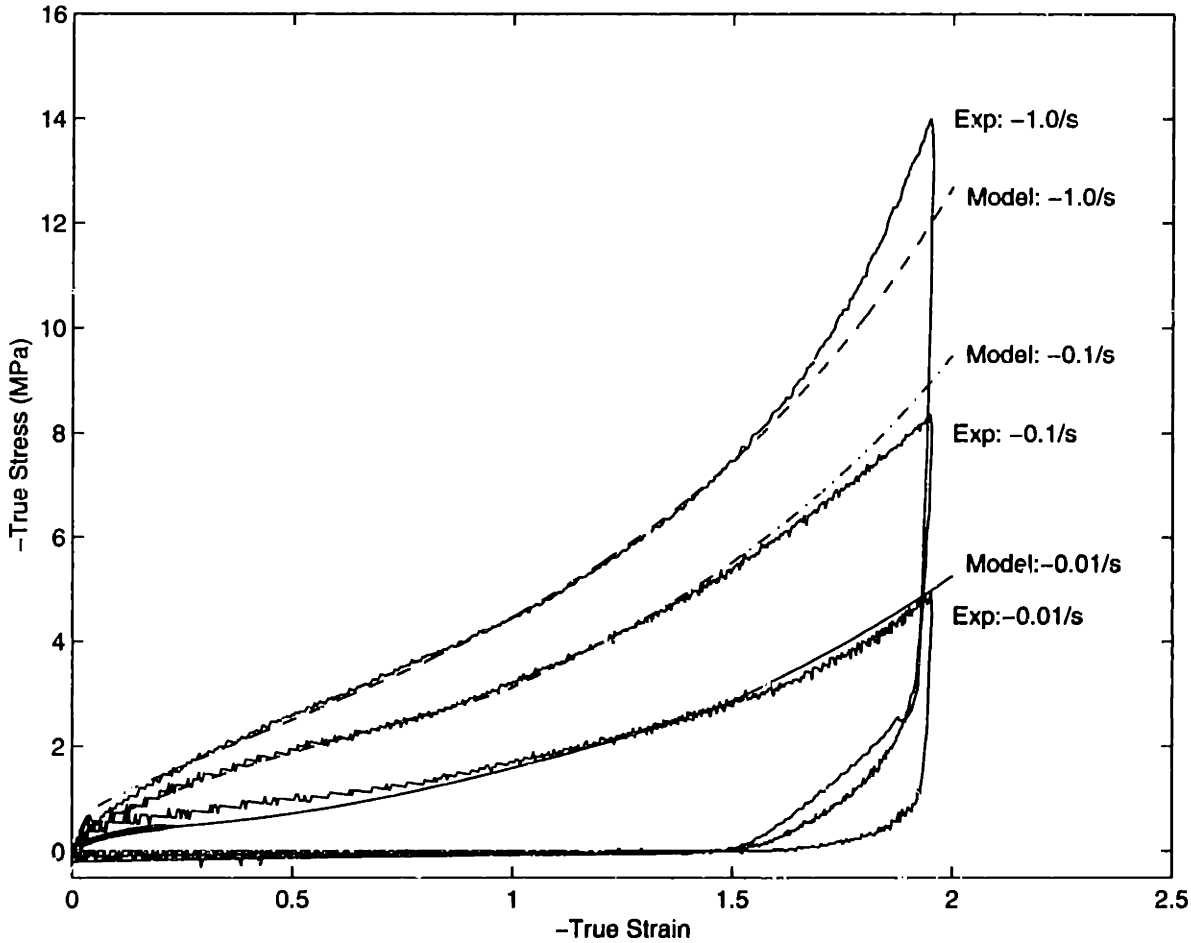

Figure 3.26: Comparison of dual resistance model to experimental data incorporating a nonlinear viscous dashpot in network A, in uniaxial compression at $100°C$

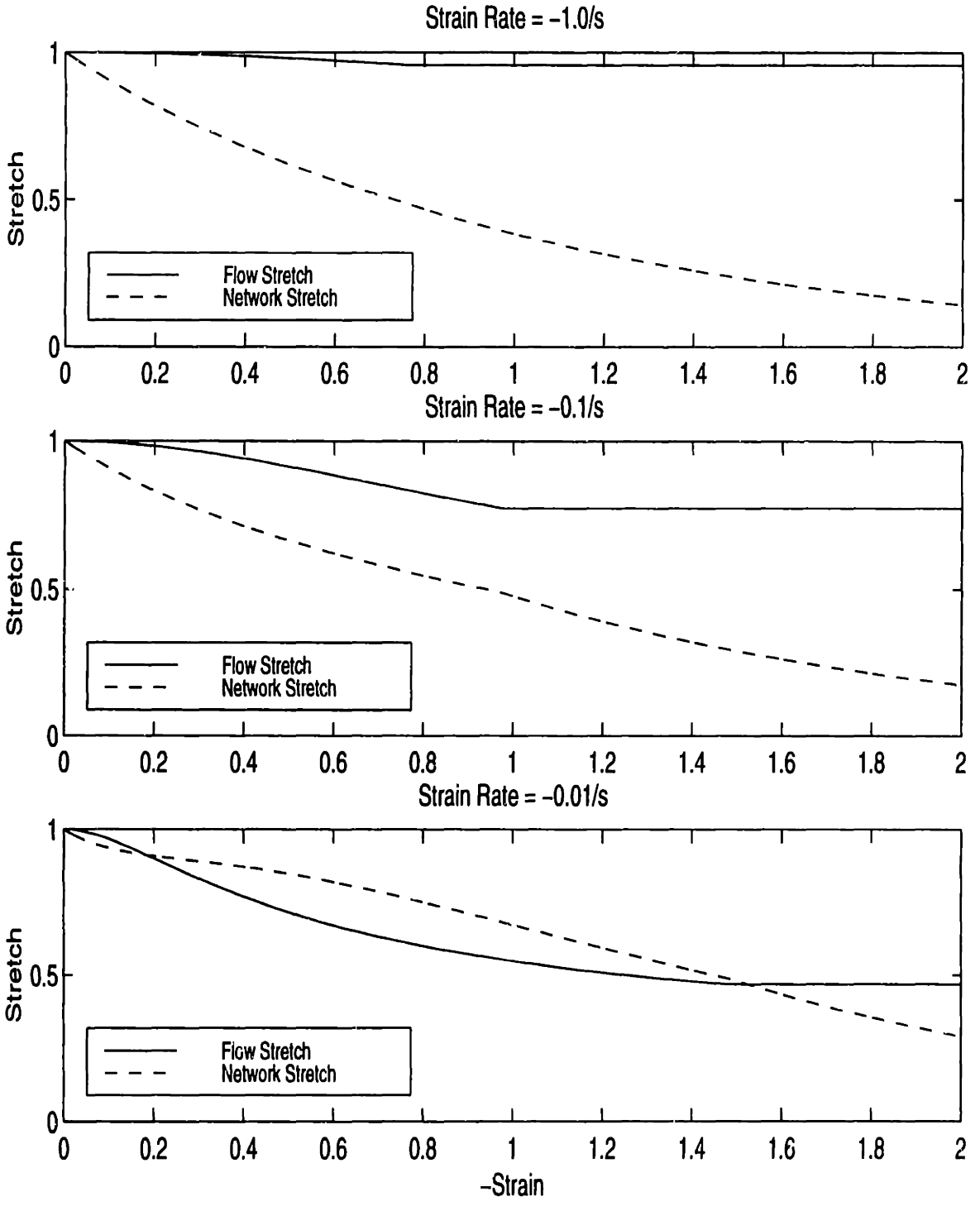

Figure 3.27: Model prediction of evolution of flow stretch and network stretch with increasing strain for the different strain rates in uniaxial compression at $100°C$

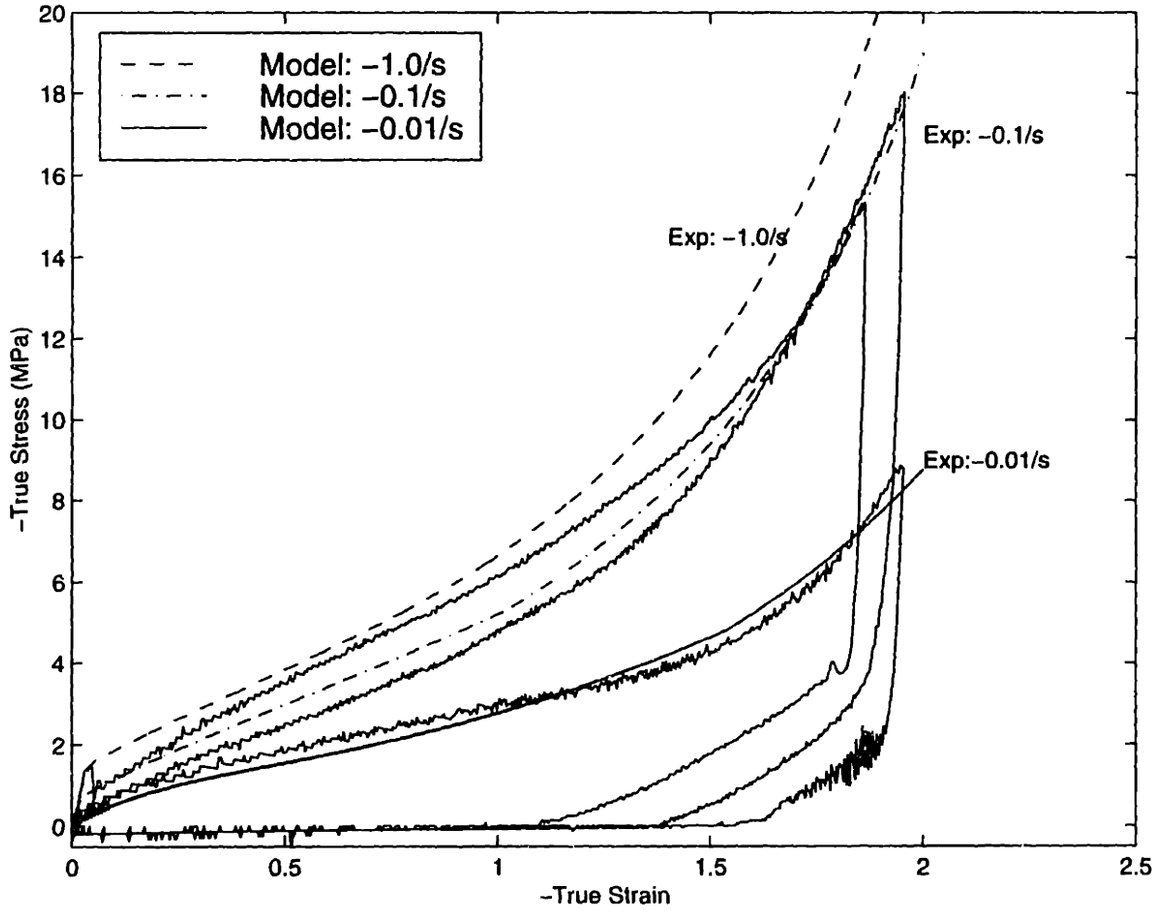

Figure 3.28: Comparison of dual resistance model to experimental data incorporating a nonlinear viscous dashpot in network A, in uniaxial compression at $90°C$

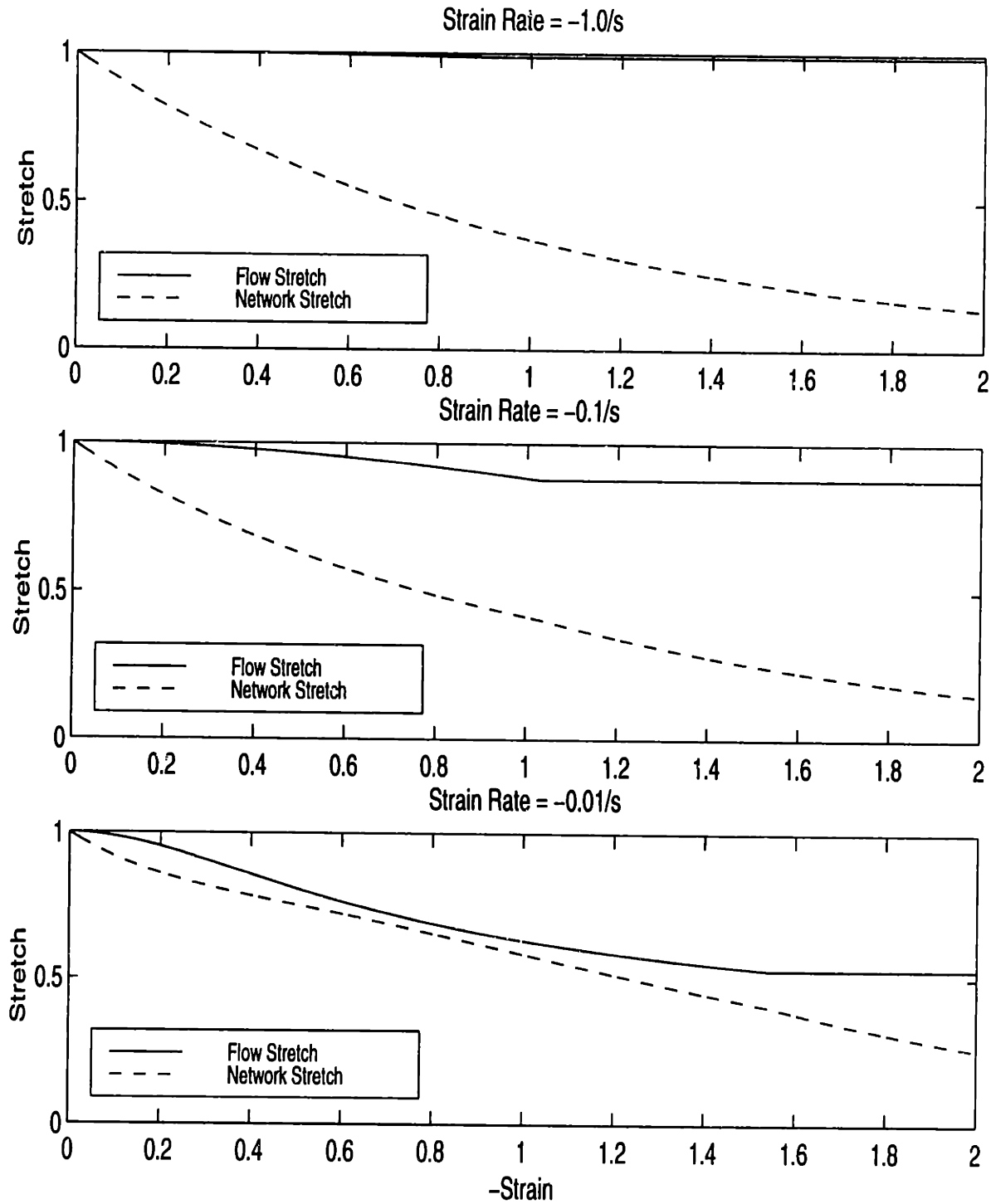

Figure 3.29: Model prediction of evolution of flow stretch and network stretch with increasing strain for the different strain rates in uniaxial compression at $90°C$

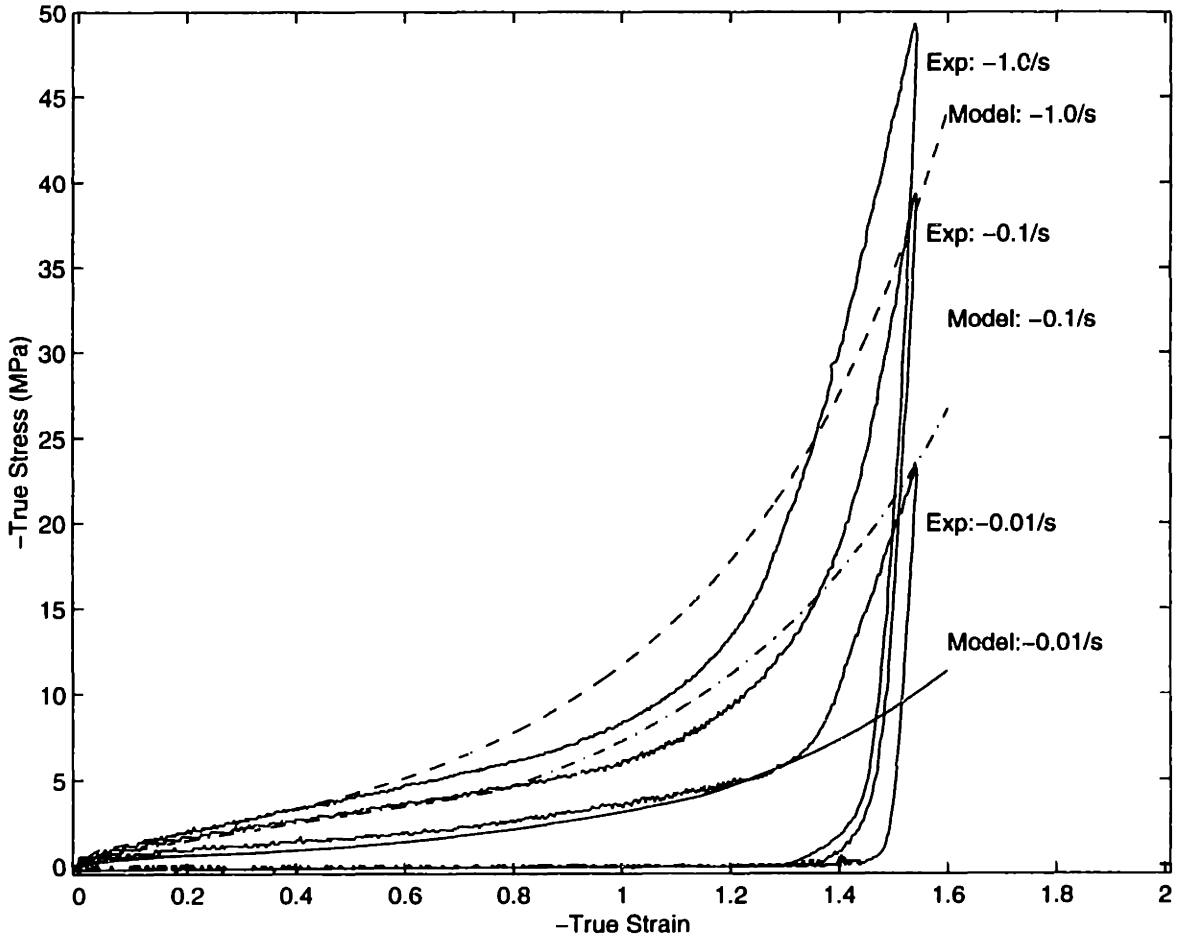

Figure 3.30: Comparison of dual resistance model to experimental data incorporating a nonlinear viscous dashpot in network A, in plane strain compression at $100°C$

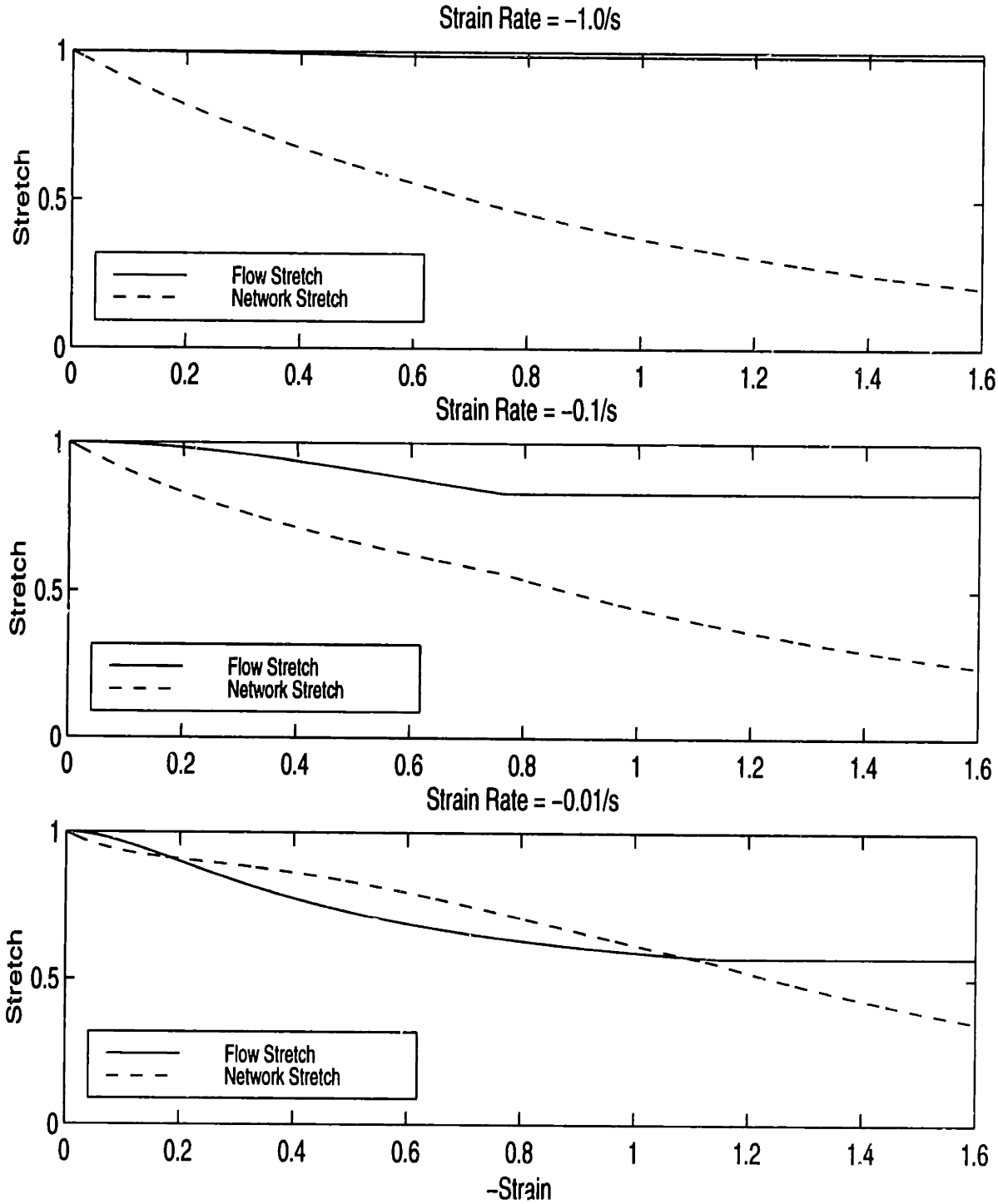

Figure 3.31: Model prediction of evolution of flow stretch and network stretch with increasing strain for the different strain rates in plane strain compression at $100°C$

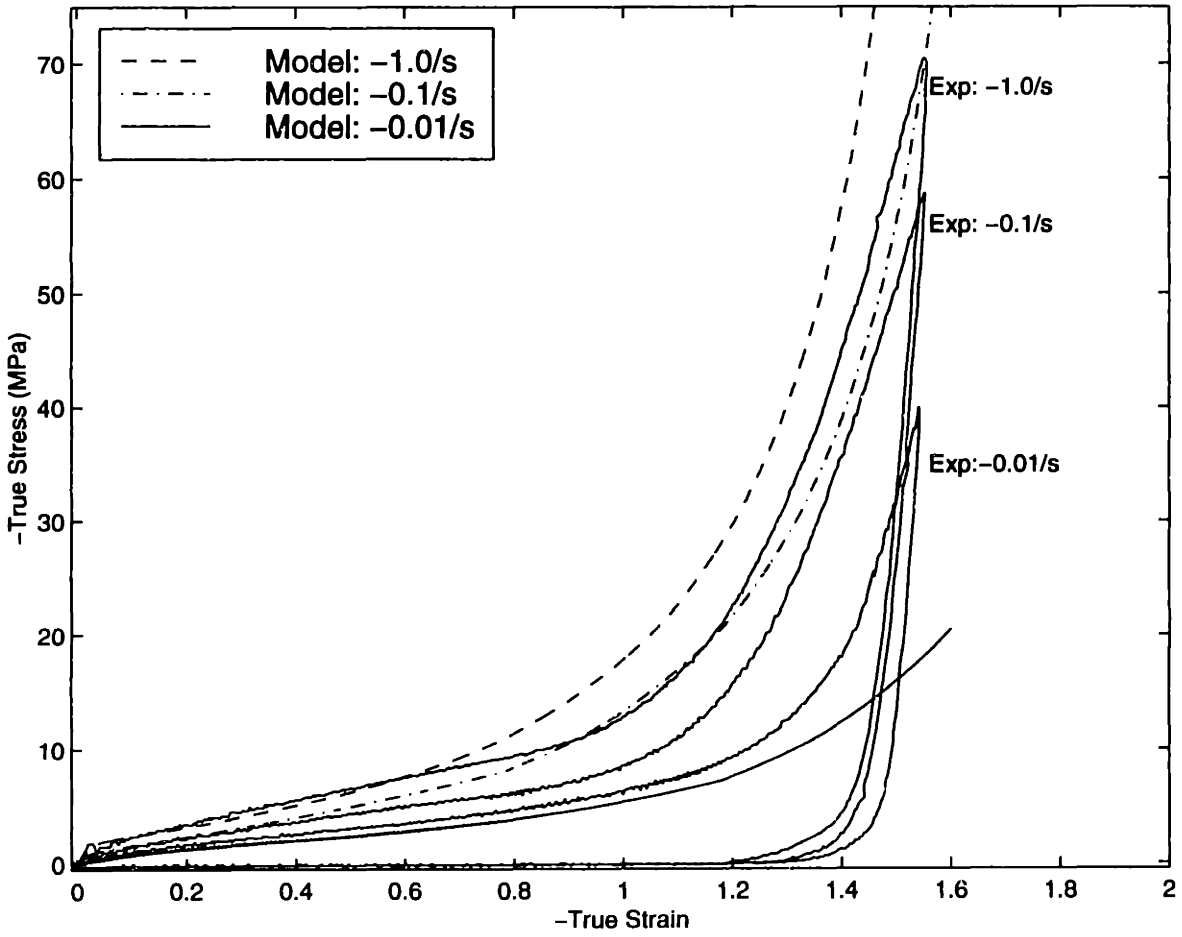

Figure 3.32: Comparison of dual resistance model to experimental data incorporating a nonlinear viscous dashpot in network A, in plane strain compression at $90°C$

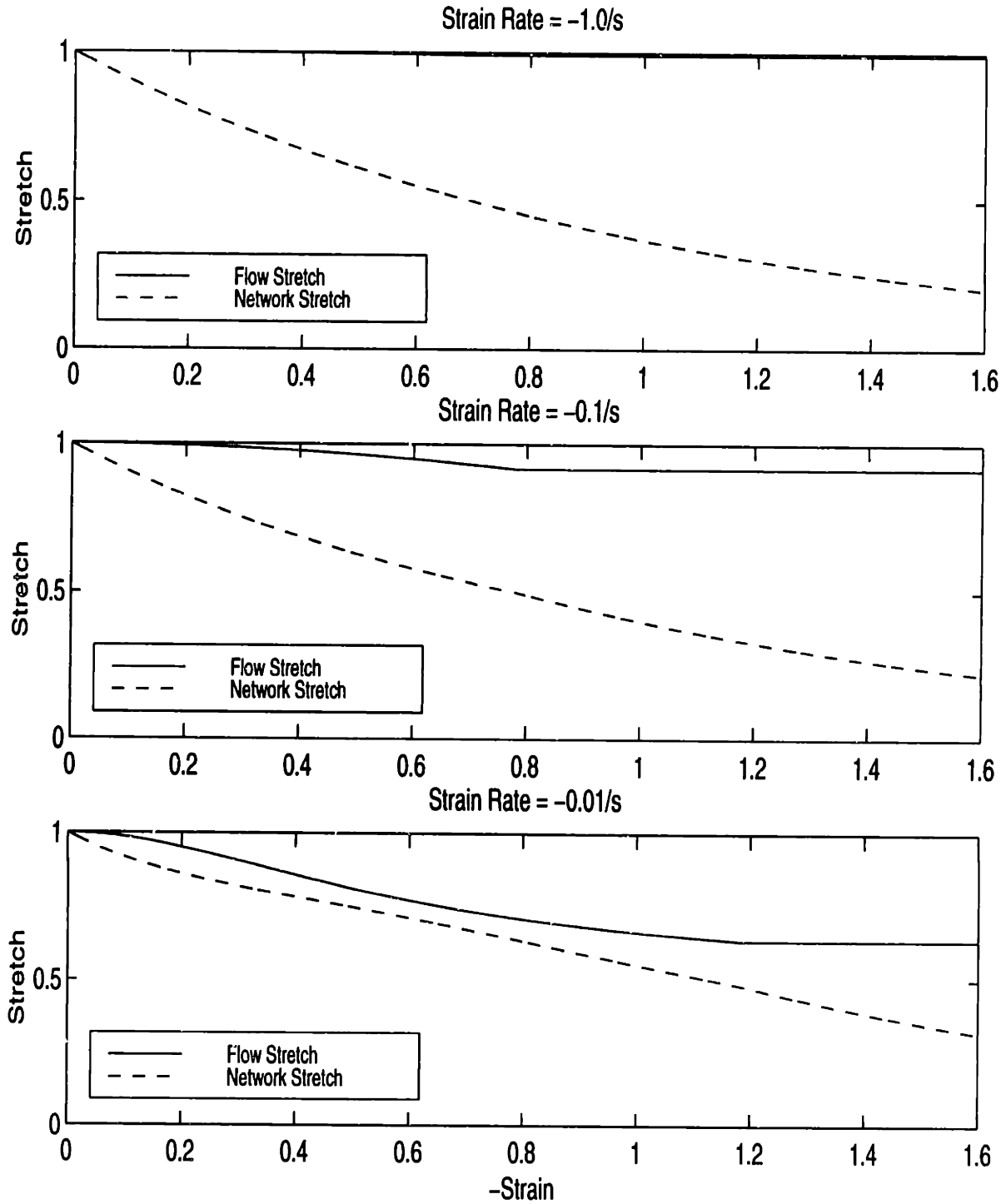

Figure 3.33: Model prediction of evolution of flow stretch and network stretch with increasing strain for the different strain rates in plane strain compression at $90°C$

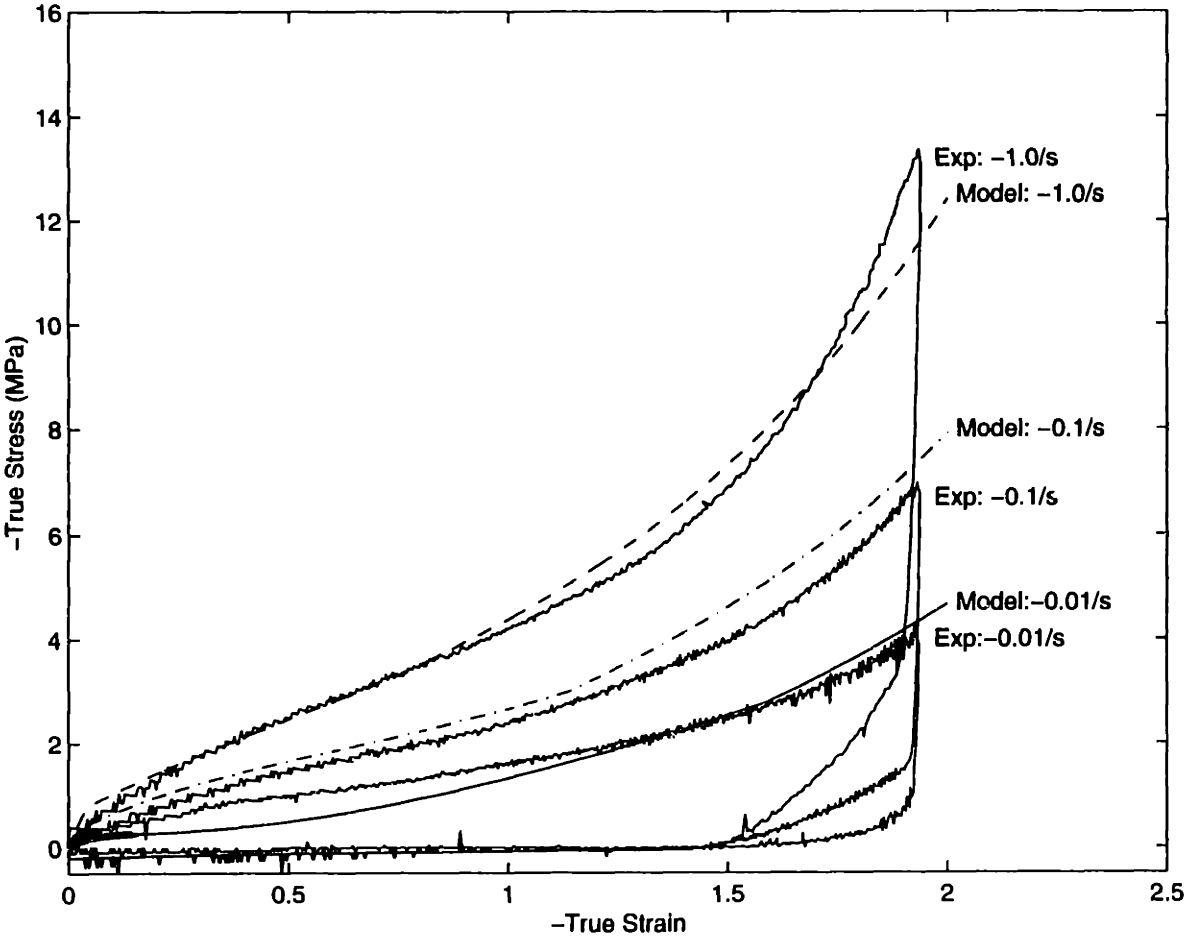

Figure 3.34: Comparison of dual resistance model to experimental data incorporating a nonlinear viscous dashpot with a temperature dependence in network A, in uniaxial compression at $105°C$

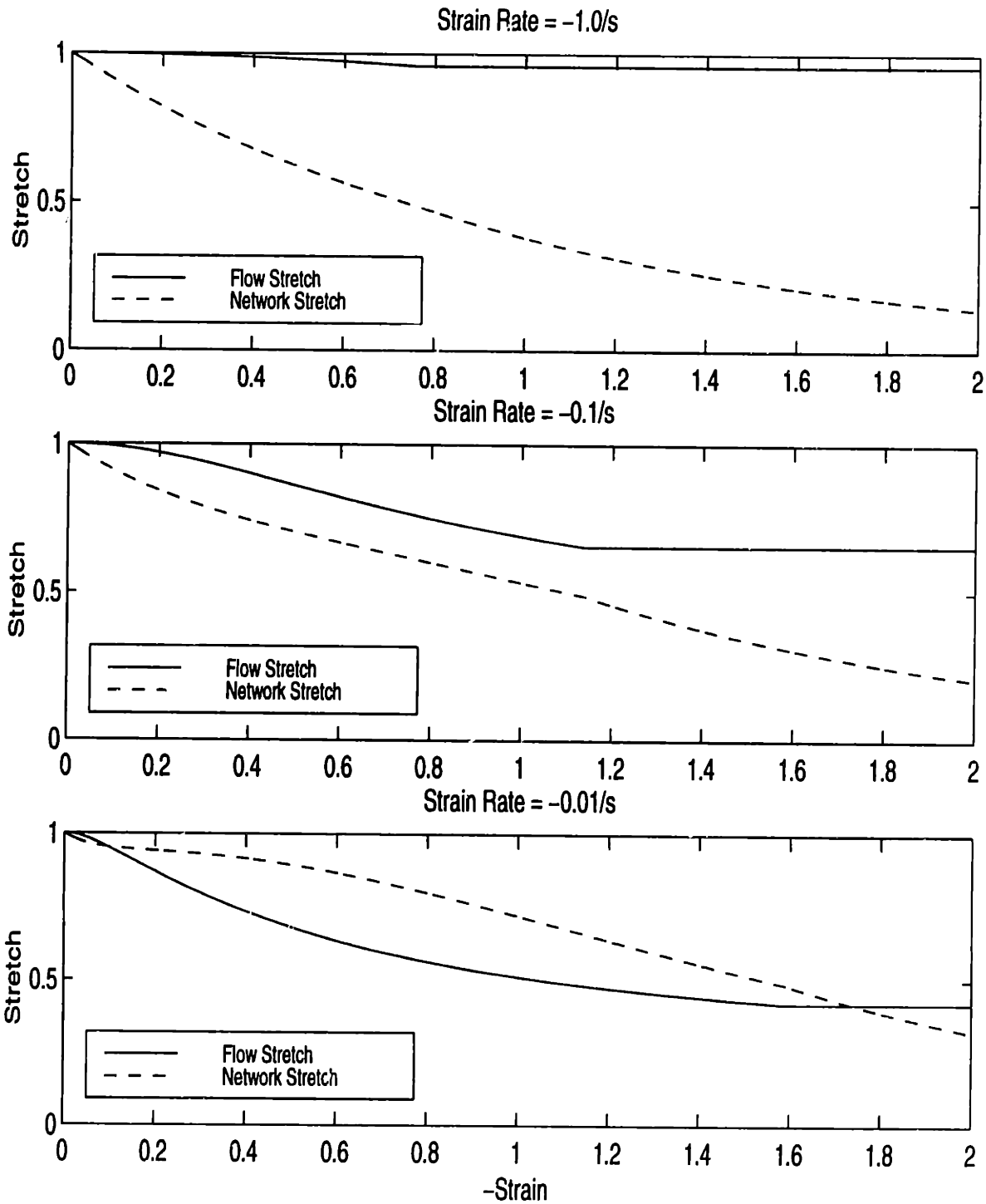

Figure 3.35: Model prediction of evolution of flow stretch and network stretch with increasing strain for the different strain rates in uniaxial compression at $105°C$

Chapter 4

Conclusions and Future Work

The goal of this thesis was to present recent research into the mechanics of strain-induced crystallization of PET. PET exhibits the capability of undergoing crystallization during processing. The result of strain-induced crystallization is increased stiffness and hardness as well as better dimensional stability or resistance to recovery. Experiments were presented which sampled the mechanical behavior of PET under different states of large strain, over a wide range of strain rates, and over a wide range of temperatures spanning the glassy and the rubbery regimes. Differential Scanning Calorimetry (DSC) measurements were utilized to determine the crystallinity content as a function of mechanical loading (strain state, strain rate, final strain, temperature). Wide Angle X-ray Scattering (WAXS) was then used to determine the nature of this crystallinity and the evolution of crystallinity with strain rate, final strain and deformation temperature. A constitutive model of the mechanical behavior for the finite deformation of PET above its glass transition temperature was developed that captures the strain rate, strain state and temperature dependence of the material. The model utilizes a kinematic framework to model the two resistances observed in the mechanical behavior of PET. The model was found to predict the experimental data reasonably well.

4.1 Summary of Conclusions

At fixed deformation temperatures below the glass transition, DSC scans show that strain-induced crystallization does not occur in uniaxial compression in specimens deformed at these glassy temperatures, even at rapid strain rates and large final strains. However, the DSC scans of the specimens deformed in plane strain compression at $25°C$ exhibit an increase in crystallinity only at the fastest strain rate signifying either a locking phenome-

non with respect to molecular orientation and/or the occurrence of strain-induced crystallization at room temperature at very rapid strain rates. However, the stress-strain curve at this temperature and strain rate did not exhibit an increase in strain hardening.

At a deformation temperature of $80°C$, which is in the leathery region, the deformation is very strain rate dependent. In both uniaxial and plane strain compression, the stress-strain curves at the rapid strain rates exhibit the behavior of a polymer deforming below T_g in the leathery region, with an apparent yield phenomenon, whereas the stress-strain curves at slow strain rates exhibit the behavior of a polymer deforming above T_g in the leathery region, with no yield stress at all. The strain hardening slopes increase as strain rate is increased, but then decrease at faster strain rates due to the adiabatic heating effect. DSC scans show that an increase in crystallinity content does occur in uniaxial compression at $80°C$ but only after a strain of -1.4. However, WAXD scans do not show that any crystallization has occurred in uniaxial compression at this deformation temperature and strain level. Two possible explanations were given to explain this discrepancy, however, it is clear that molecular orientation and packing does occur at this deformation temperature and strain level. DSC and WAXD scans of specimens deformed at $80°C$ in plane strain compression, however, both exhibit marked increases in crystallinity content. The DSC and WAXD scans also show that there is a very slight increase in crystallinity with strain rate.

The most interesting results were obtained in the rubbery region at deformation temperatures of $90°C$ and above. The uniaxial and plane strain stress-strain curves exhibit increasing strain hardening slopes with increasing strain rate until adiabatic heating causes the strain hardening slopes to decrease at the higher strain rates. Due to more severe chain orientation, the plane strain compression curves exhibit much more strain hardening than the uniaxial compression curves. DSC scans of the uniaxial specimens showed that an

increase in crystallinity content does occur at these deformation temperatures, but they also showed that at the same strain rates and final strains, the crystallinities at $90°C$ were about the same regardless of strain rate, whereas at $100°C$ and $105°C$ the crystallinities were an increasing function of strain rate. This makes sense when the stress-strain curves for these specimens are reviewed to find that this correlates with the amount of strain hardening that has occurred at these deformation temperatures and strain rates. The crystallinity at each strain rate at $90°C$ was about the same, correlating to the fact that they had all undergone some strain hardening, but at $100°C$ and $105°C$ at the slower strain rates there is very little strain hardening correlating to very little crystallinity. The DSC scans of the plane strain specimens exhibited not only a large increase in crystallinity content, but that this crystallinity content increased only slightly with increasing strain rate. The WAXD scans exhibited much more strain rate dependence in the crystalline peaks. Mechanical tests, DSC scans and WAXD scans also showed that, in plane strain, the increase in crystallinity occurs before a final strain of -1.0 at $90°C$ and that the percent crystallinity increases with increasing final strain.

The WAXD scans showed that there is a marked difference in the resulting crystallographic textures between uniaxial compression and plane strain compression. In plane strain compression, the crystals lie in all three directions in the same orientation, whereas, in uniaxial compression, the crystals lie in only one direction in the same orientation, the load direction, and lie randomly in the other two directions. It was also postulated that the texture that would develop in a specimen that undergoes crystallinity by plane strain compression and then is subjected to stretching in the previously constrained direction, would be very similar to the texture in the uniaxial compression specimens. The orientation of the (100) planes would not change, but the orientation of the (010) and the $(\bar{1}05)$ planes would become randomized, resembling the texture of a uniaxial compression specimen.

A constitutive model for the deformation of initially amorphous, unoriented PET above its glass transition was developed. The essence of the model is its ability to capture the two distinct resistances exhibited by the experimental data present in PET deforming above its glass transition. The two distinct resistances are: (1) a resistance to initial flow, and (2) an evolving resistance to continued flow (exhibited by strain hardening). Both of these resistances are observed to depend on strain rate and deformation temperature. The model incorporates four constitutive models within a kinematic framework to act together to predict the mechanical behavior of the material. The first two components capture the resistance to initial flow: the first component of the model utilizes the Neo-Hookean law to dictate the initial stiffness of the material that is independent of strain rate, and the second component is a thermal activation law for the temperature and strain rate dependence of the initial flow stress. The last two components capture the evolving resistance to continued flow, as exhibited by strain hardening: the third component is the Arruda-Boyce 8-chain model for the strain hardening behavior of the material, which is based on the idea of a network of chains acting cooperatively during deformation until reaching a limiting chain extensibility, and the fourth component is a viscosity model that governs the strain rate and temperature dependence of the strain hardening behavior, which takes into account the entanglement drift and relaxation of molecules that occurs at lower strain rates in the material, but also provides for a critical network stretch where this entanglement drift/relaxation ceases. The constitutive model was found to predict the experimental data reasonably well, with greater agreement with the uniaxial compression data than plane strain compression data, and with greater agreement at slower strain rates. These minor discrepancies are understandable since the model did not take adiabatic heating effects or crystallization effects into account. It is important to note that, since the constitutive model did not specifically incorporate the effects of strain-induced crystallization, it is thus a net-

work stretch model. The introduction of strain-induced crystallization effects in the model might be able to predict the mechanical behavior in plane strain compression more accurately.

4.2 Future Work

The research presented in this thesis is by no means complete. Further research needs to be conducted in the form of more experimental tests structured to solve the ambiguity of exactly when crystallization occurs, whether it is occurring during deformation, or afterwards as an annealing effect. Simultaneous deformation and WAXD scans utilizing synchrotron radiation would be very helpful in probing the evolution and development of the crystallinity with time under different conditions of strain rate, strain state and deformation temperature. Another method of studying the evolution and development of the crystallinity with time would be simultaneous deformation of PET and nuclear magnetic resonance spectroscopy (NMR). Once this aspect of the strain-induced crystallization is better understood, a more robust and complete constitutive model for the large strain deformation of PET can be formulated that captures the strong strain rate, strain state and temperature dependencies of the material. This model would be instrumentally useful in the design of the industrial processing of PET. By being able to predict the behavior of the material over a wide range of strain rates, strain states and temperatures, a substantial reduction of cost and waste of material can be achieved as well as improvements on the design of products made with PET.

Appendix A

DSC Thermogram Repeatability

There is a considerable slant in the DSC thermograms shown in Figures 2.35 to 2.39, and Figure 2.41. However, the crystallinities calculated from these thermograms were very repeatable. For each mechanical test specimen, two DSC scans were needed in order to obtain the correct DSC thermogram for that specimen. A baseline scan had to be conducted, which is a scan performed with two empty pans, that was then subtracted from the raw data of the scan performed with a small piece of the specimen in one of the pans. Figure A.1 shows the scans performed for the mechanical specimen deformed in plane strain compression at $90°C$ to a final strain of -1.6 at a strain rate of $-0.1/s$. The three curves are: (1) the raw data DSC scan of the specimen, (2) the baseline DSC scan of empty pans, and (3) the reduced data calculated by subtracting the baseline from the raw data. In order to determine the repeatability of the DSC scans, two sets of scans were conducted to obtain two reduced data sets for each specimen. However, in order to further test the repeatability of the data, a third scan was performed for the same specimen over a week later. These three scans are shown in Figure A.2. As can be seen in the Figure A.2, the scans performed on the same day are slightly more similar to each other than the scan performed on a different day, but the percent crystallinity calculated from each scan is the same. Figure A.3 shows the scans performed on the later date. Upon examination of Figures A.1 and A.3, one can see why the reduced data thermograms are slanted due to the nonrepeatability of the baselines. The more slanted the baseline, the more slanted the reduced data. However, it is important to note that the crystallinities calculated from the slanted reduced data thermograms are still very repeatable.

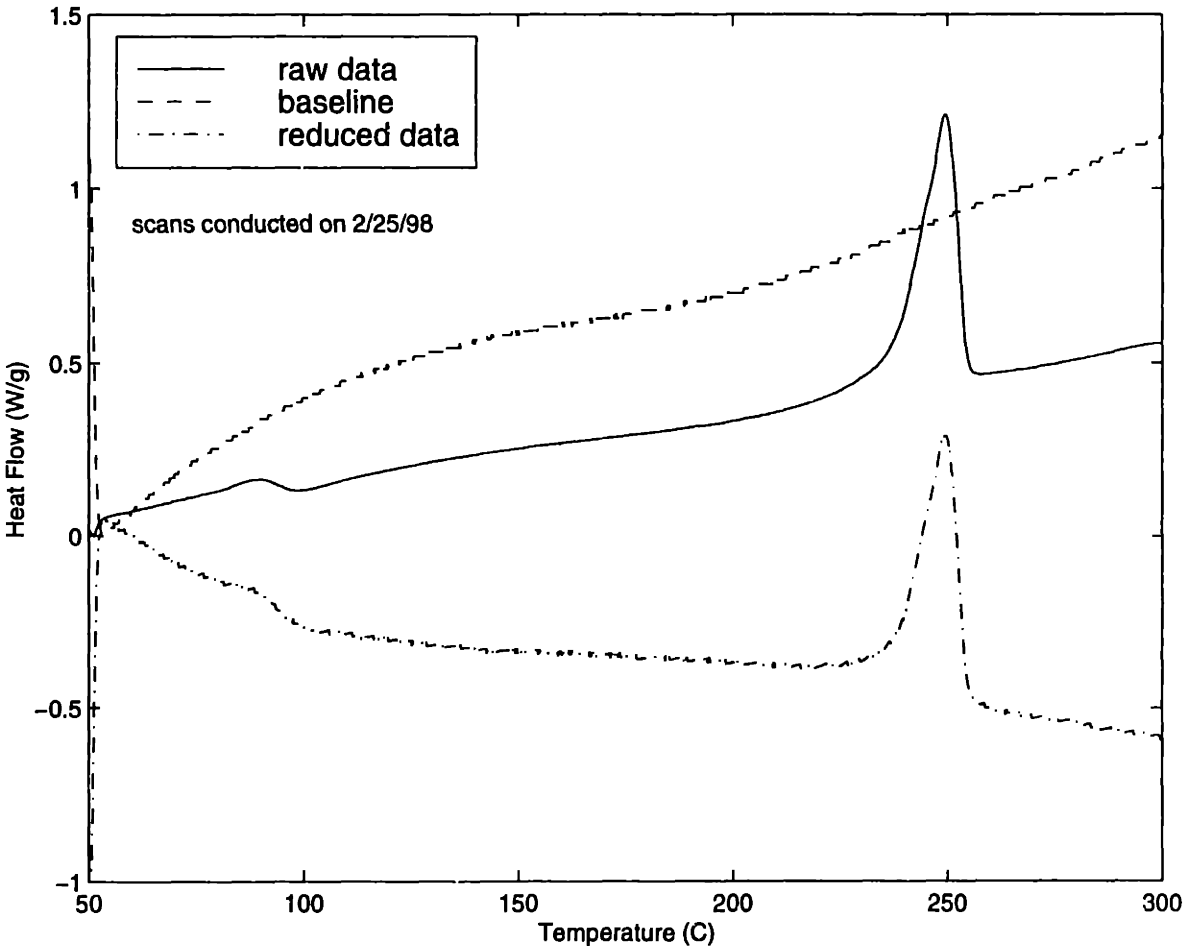

Figure A.1: Data obtained from DSC scans performed on specimen deformed in plane strain compression at $90°C$ to a final strain of -1.6 at a strain rate of -0.1/*s*, with date of scans as indicated

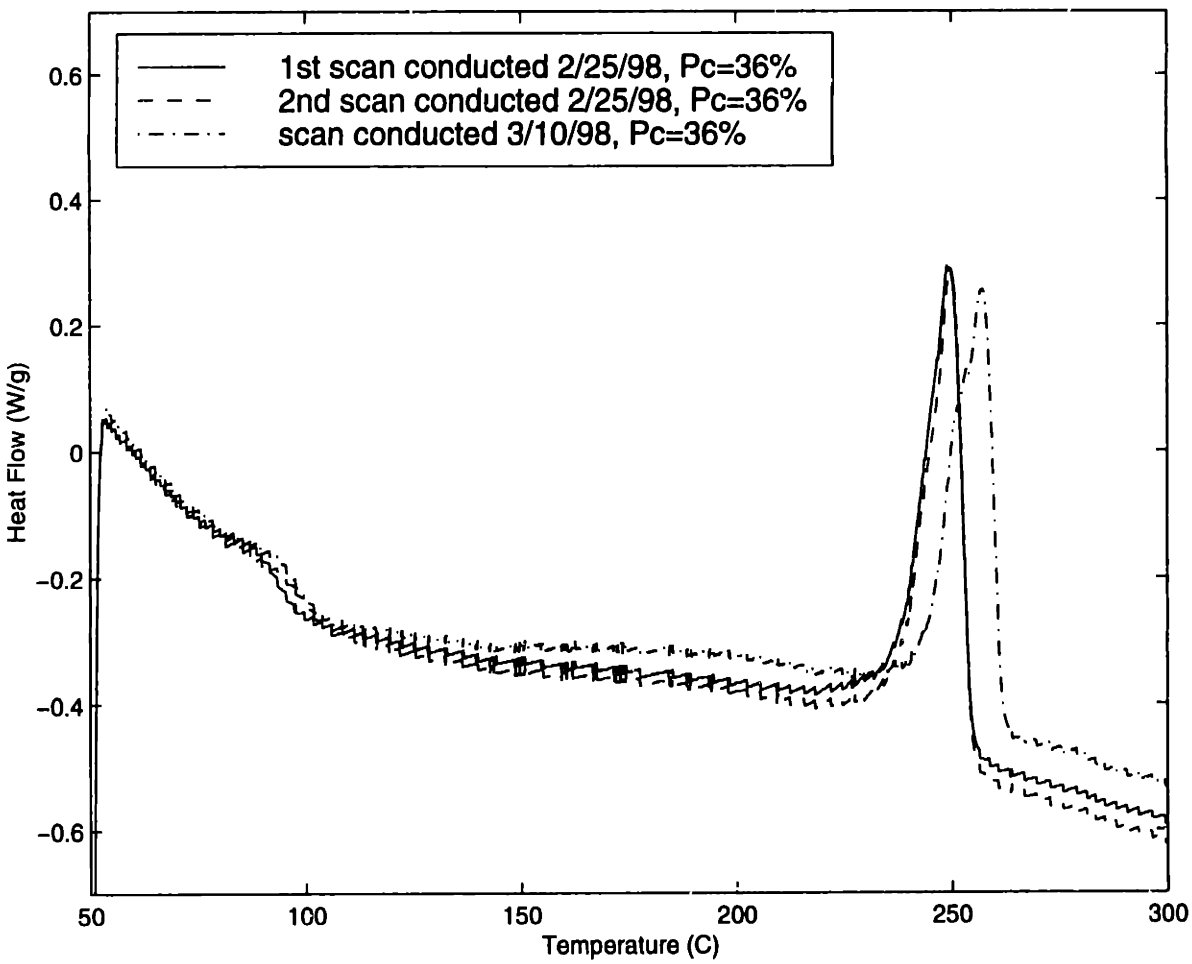

Figure A.2: Reduced data obtained from DSC thermograms performed three times on the same specimen on two different dates

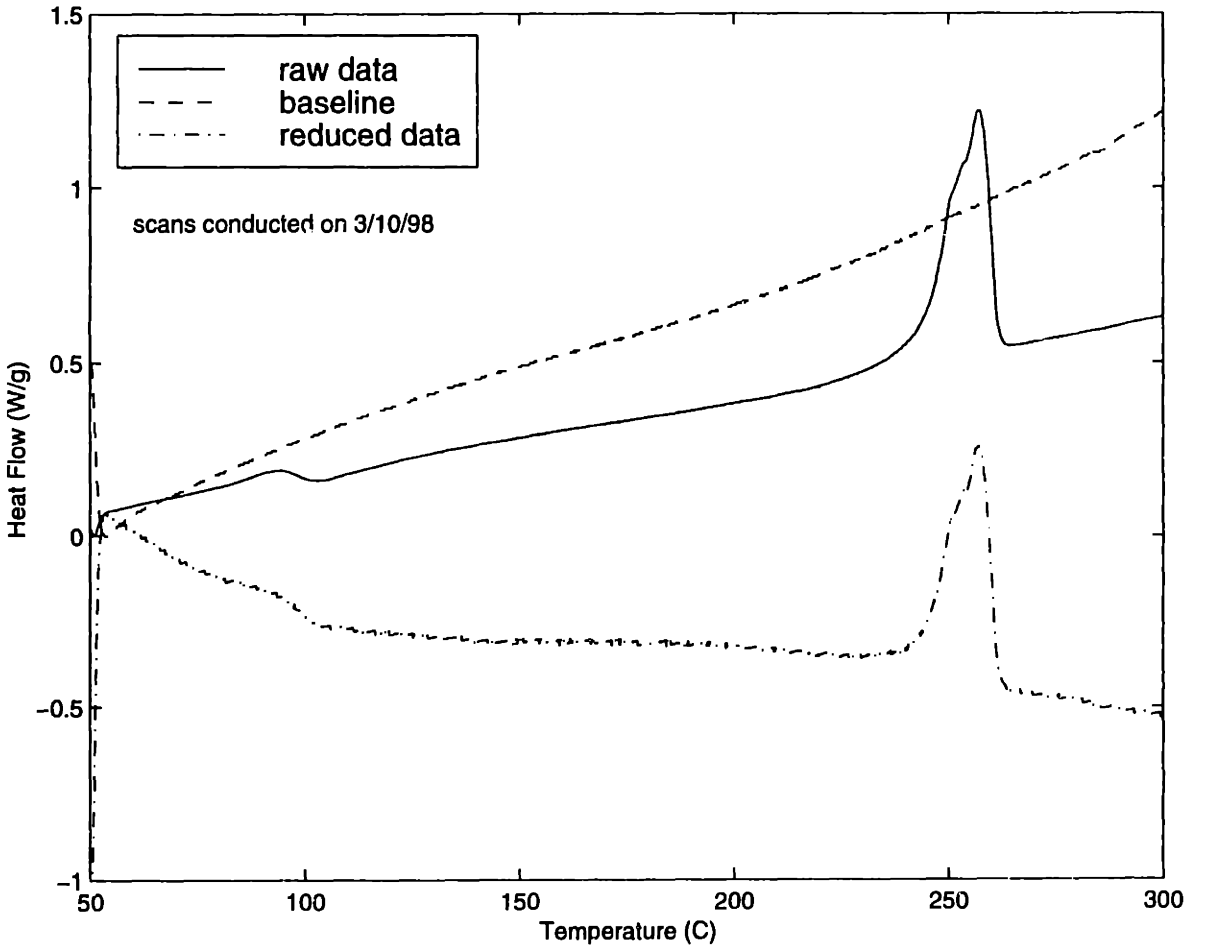

Figure A.3: Data obtained from DSC scans performed on specimen deformed in plane strain compression at $90°C$ to a final strain of -1.6 at a strain rate of $-0.1/s$, with date of scans as indicated

Appendix B

Repeatability of Mechanical Tests

The following figures give the stress strain curves of the repeatability tests. Several tests were conducted in order to verify the repeatability of the mechanical test data. The figures are in the following order:

Figures B.1 to B.8: Uniaxial Compression Tests, $25°C$

Figures B.9 to B.13: Uniaxial Compression Tests, $70°C$

Figures B.14 to B.20: Uniaxial Compression Tests, $80°C$

Figures B.21 to B.26: Uniaxial Compression Tests, $90°C$

Figures B.27 to B.32: Uniaxial Compression Tests, $100°C$

Figures B.33 to B.38: Uniaxial Compression Tests, $105°C$

Figures B.39 to B.45: Plane Strain Compression Tests, $25°C$

Figures B.46 to B.49: Plane Strain Compression Tests, $80°C$

Figures B.50 to B.53: Plane Strain Compression Tests, $90°C$

Figures B.54 to B.57: Plane Strain Compression Tests, $100°C$

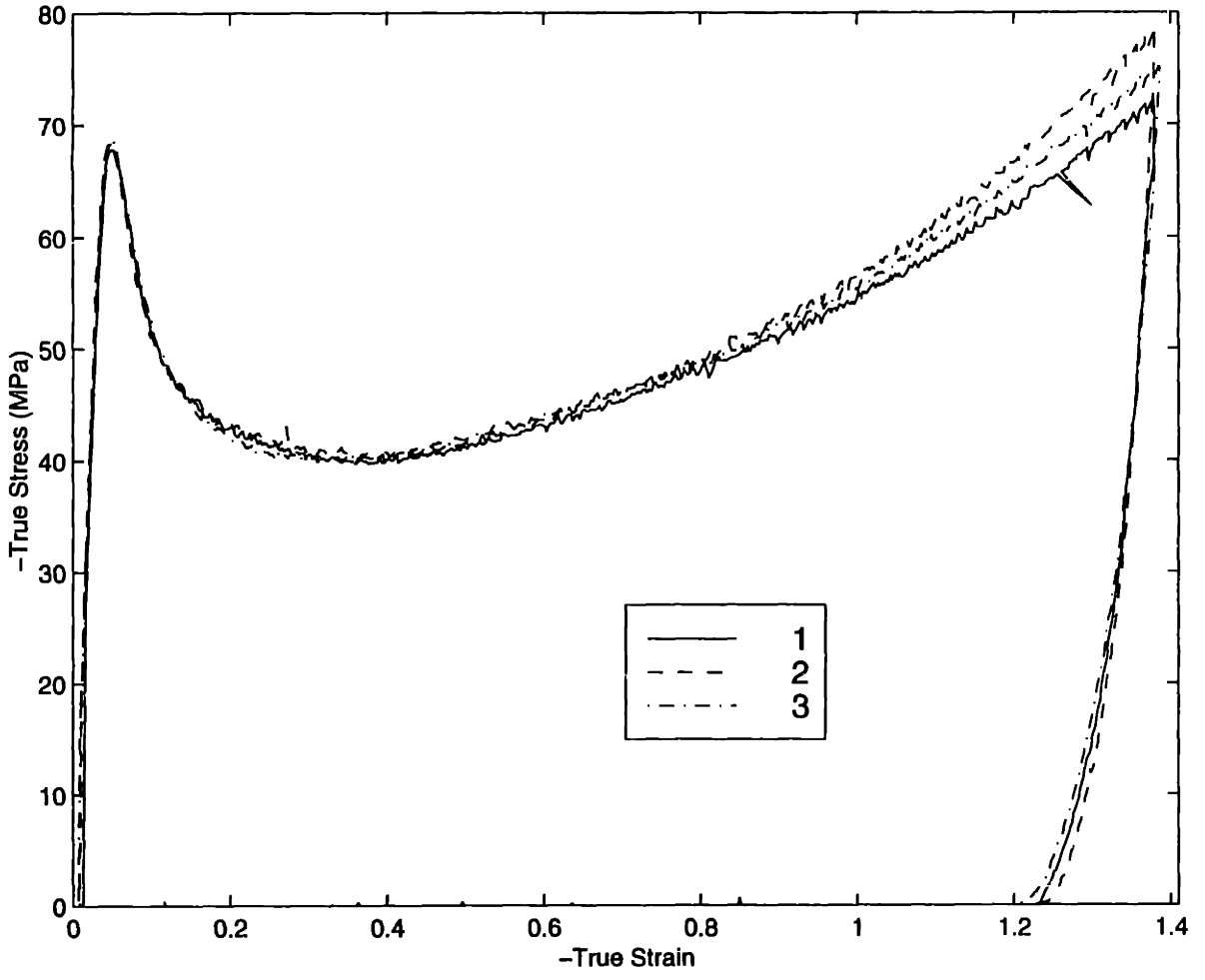

Figure B.1: Uniaxial Compression Tests, $25°C$, $\dot{\varepsilon} = -0.005/s$

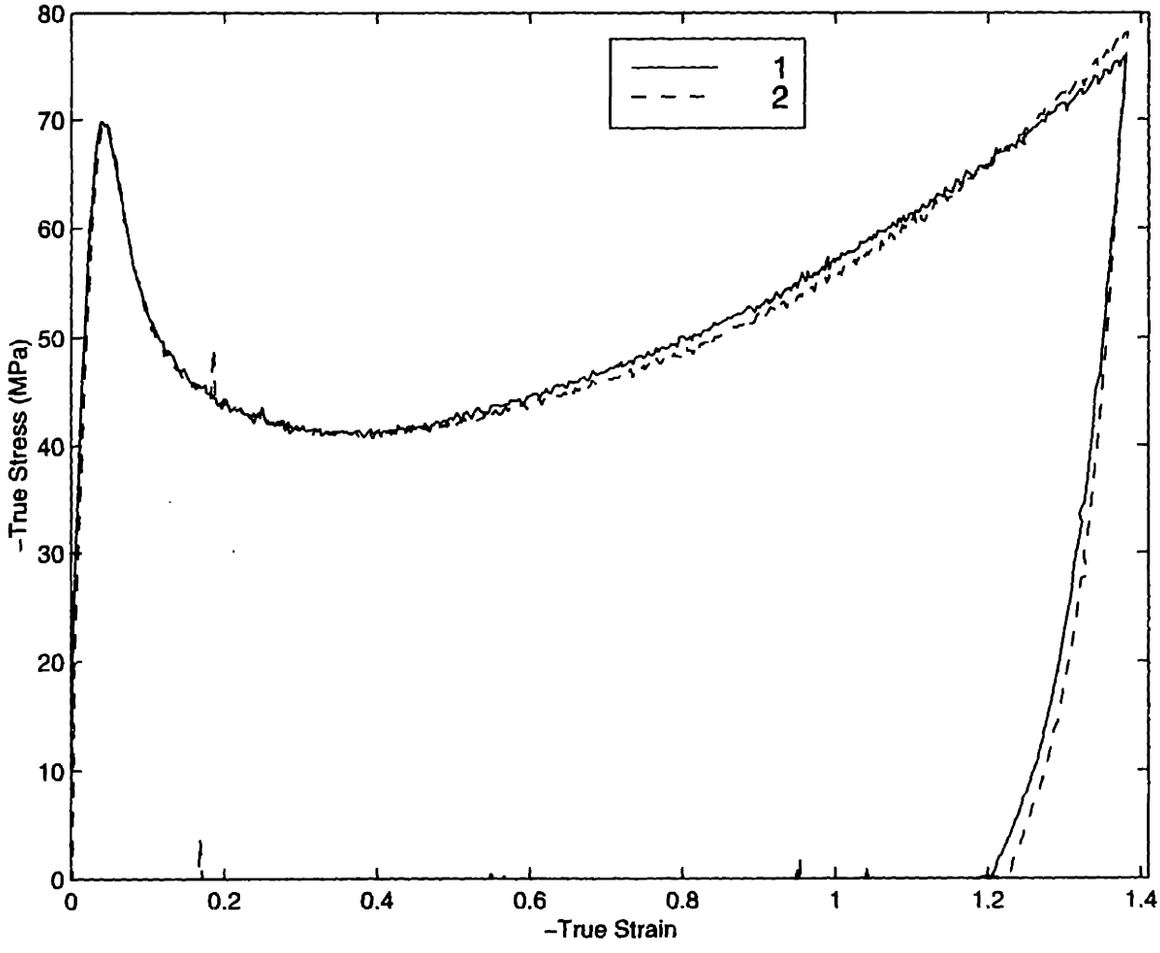

Figure B.2: Uniaxial Compression Tests, $25°C$, $\dot{\varepsilon} = -0.01/s$

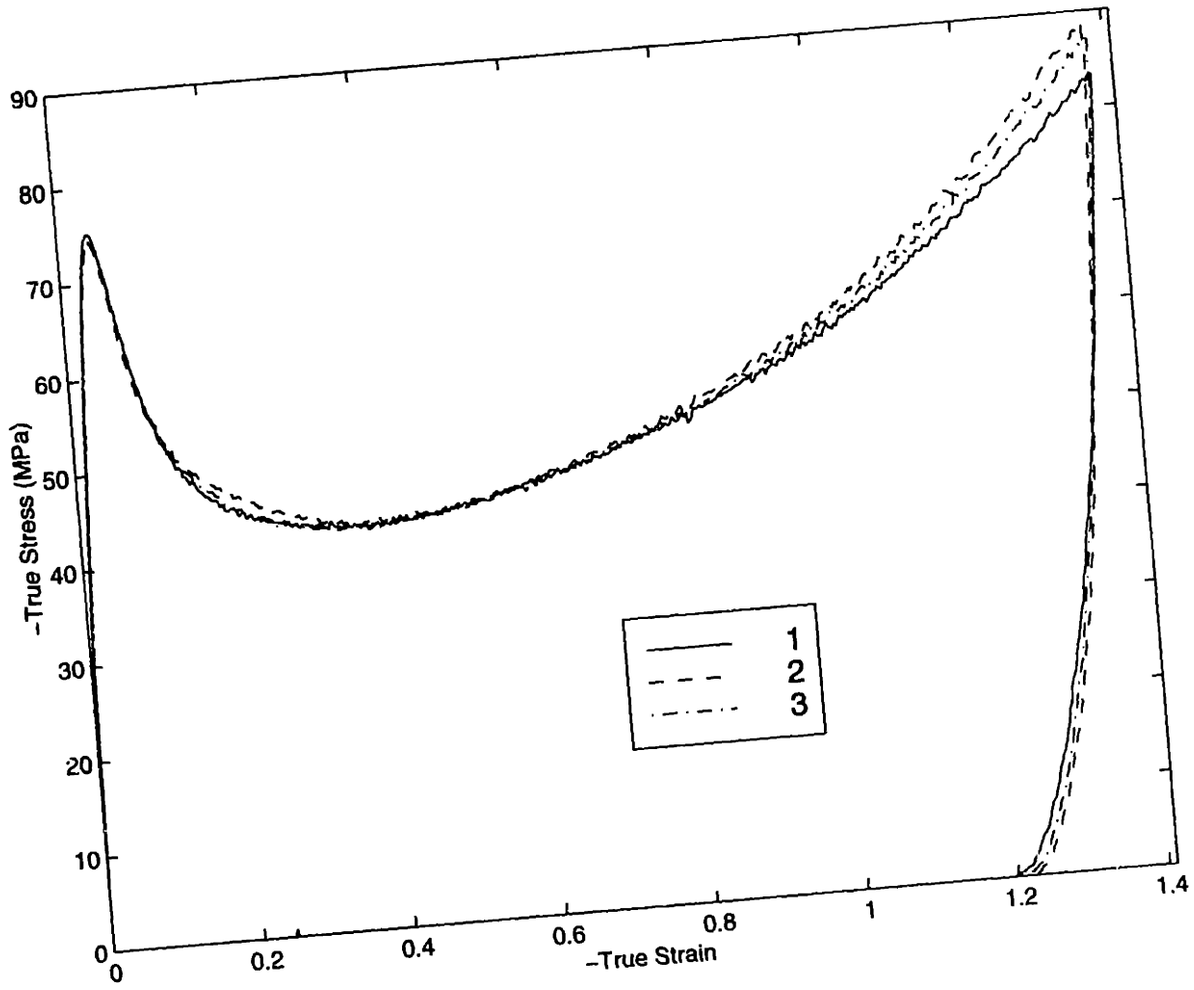

Figure B.3: Uniaxial Compression Tests, $25°C$, $\dot{\epsilon} = -0.05/s$

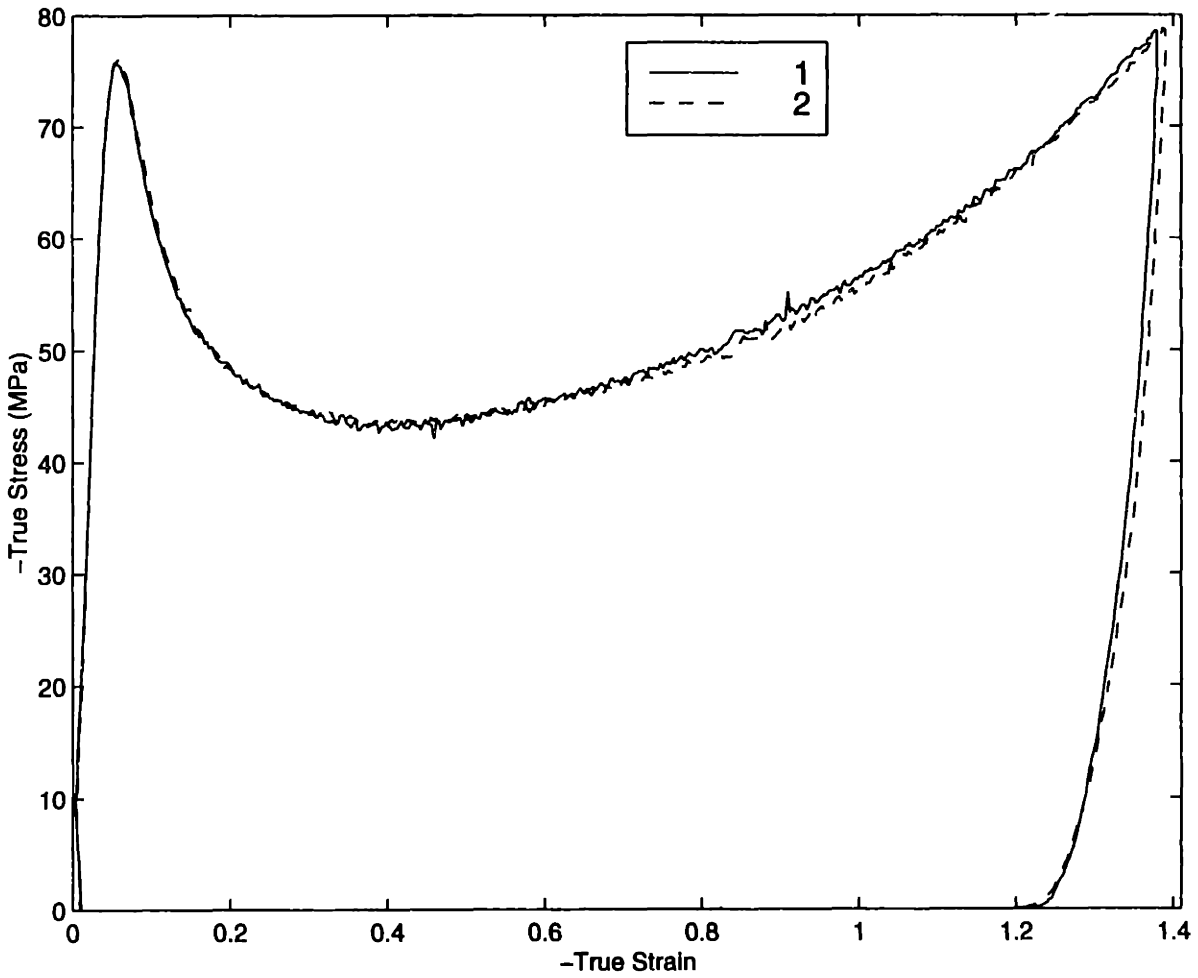

Figure B.4: Uniaxial Compression Tests, $25°C$, $\dot{\epsilon} = -0.1/s$

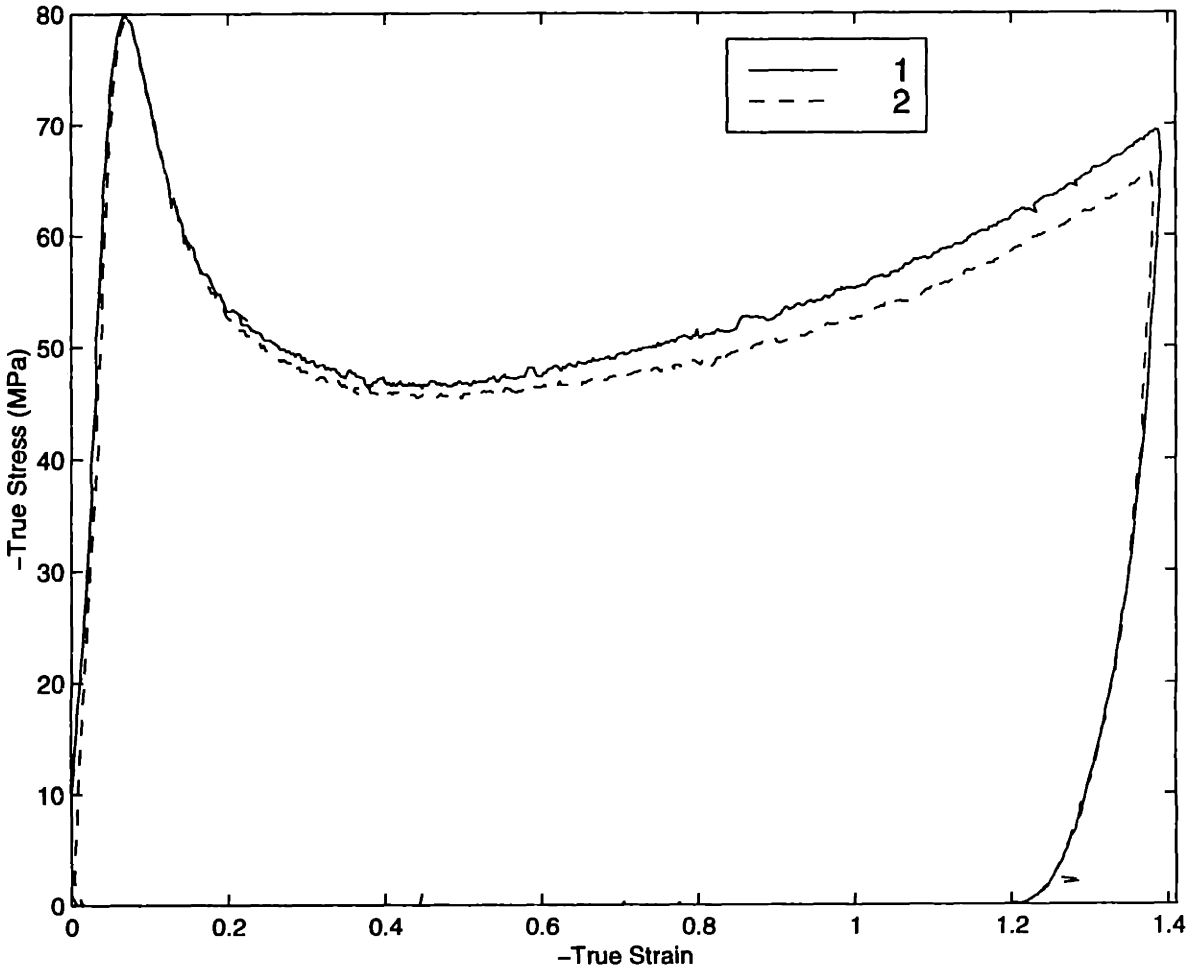

Figure B.5: Uniaxial Compression Tests, $25°C$, $\dot{\varepsilon} = -0.5/s$

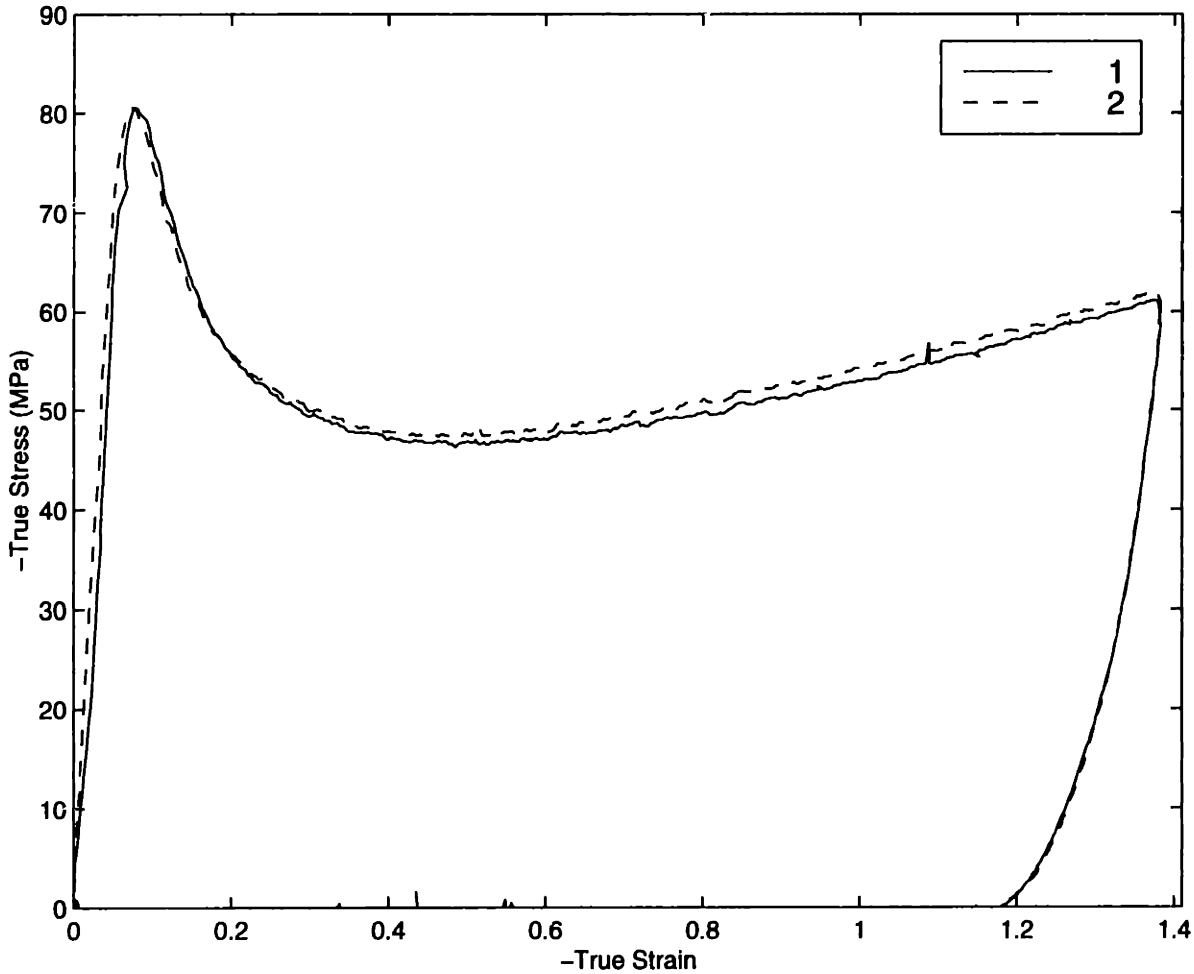

Figure B.6: Uniaxial Compression Tests, $25°C$, $\dot{\epsilon} = -1.0/s$

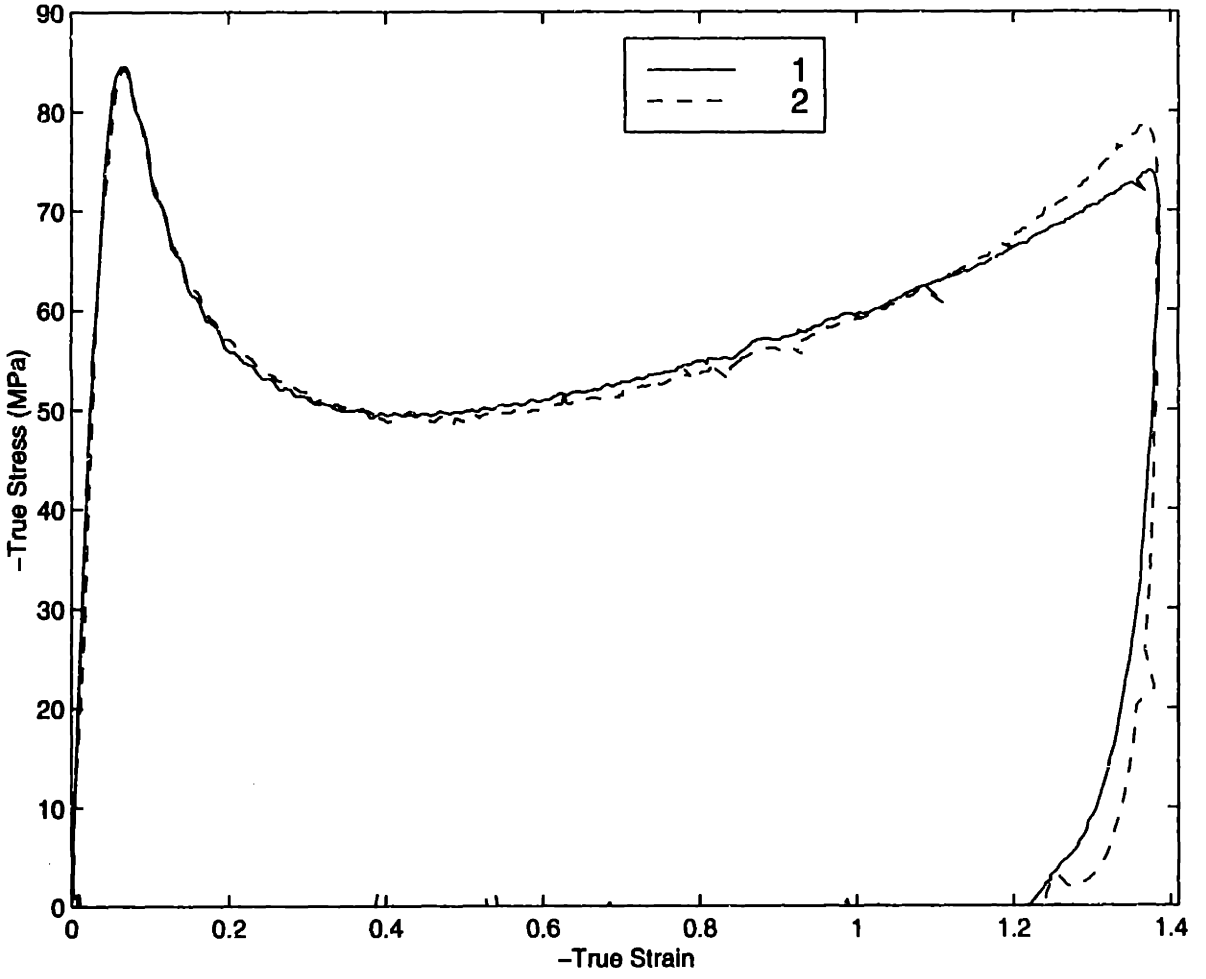

Figure B.7: Uniaxial Compression Tests, $25°C$, $\dot{\epsilon} = -1.5/s$

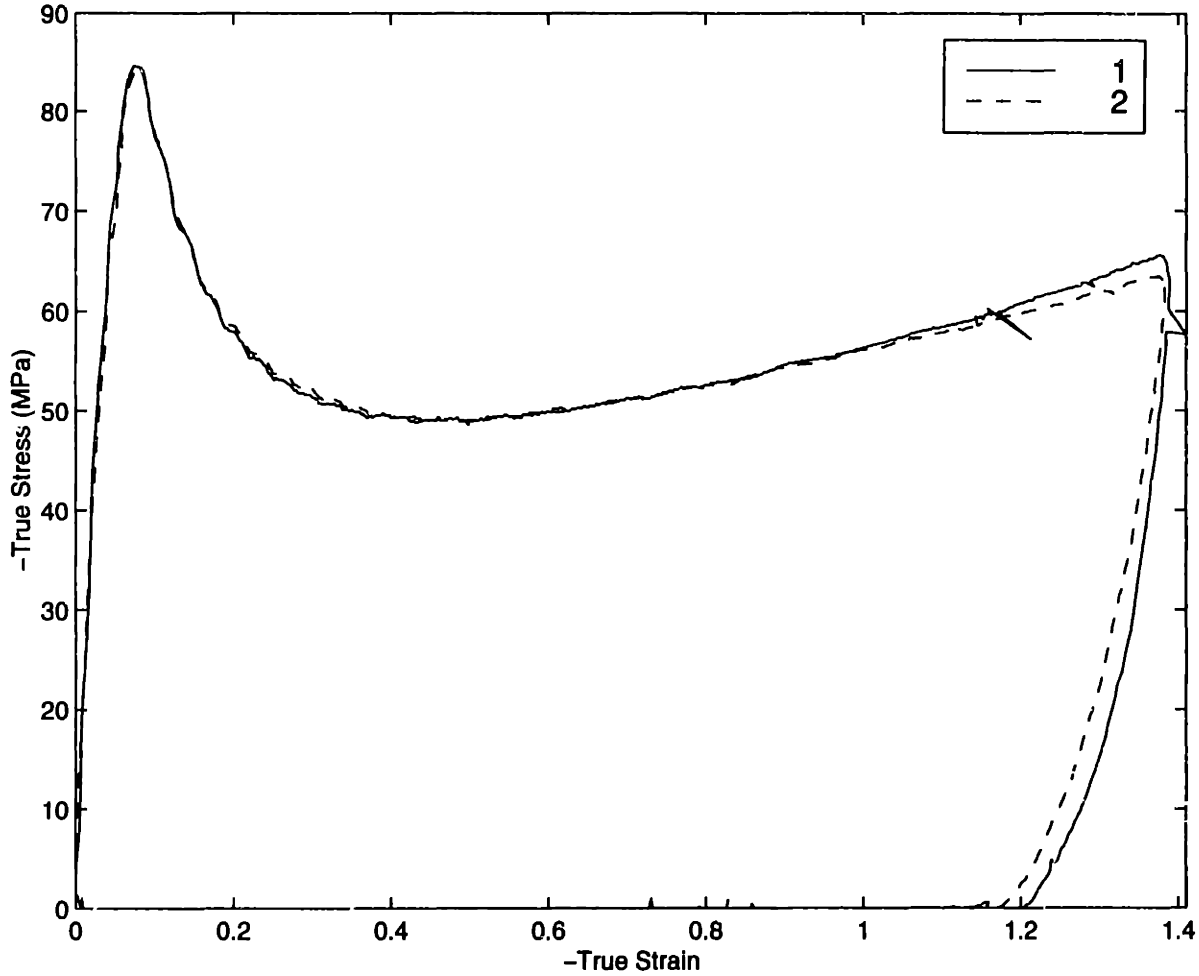

Figure B.8: Uniaxial Compression Tests, $25°C$, $\dot{\epsilon} = -2.0/s$

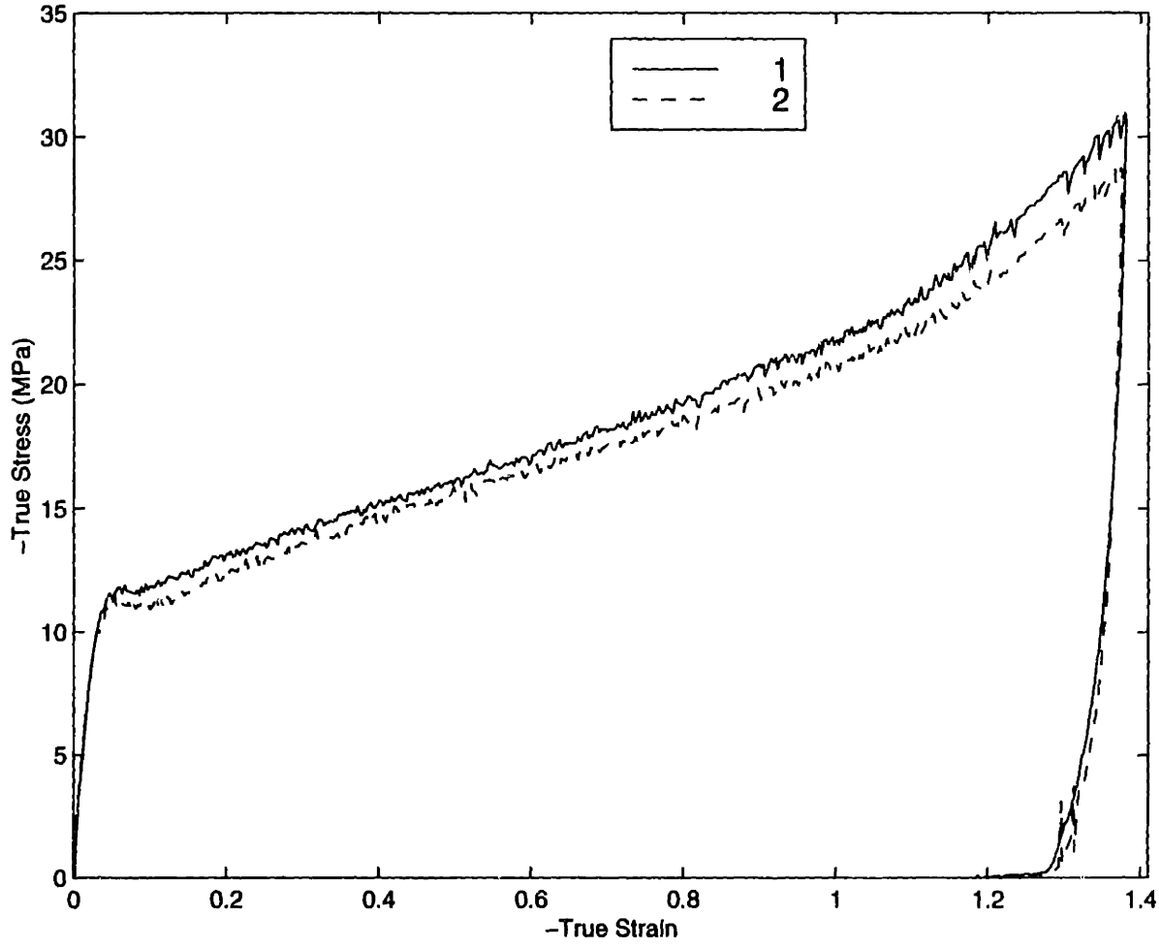

Figure B.9: Uniaxial Compression Tests, $70°C$, $\dot{\epsilon} = -0.005/s$

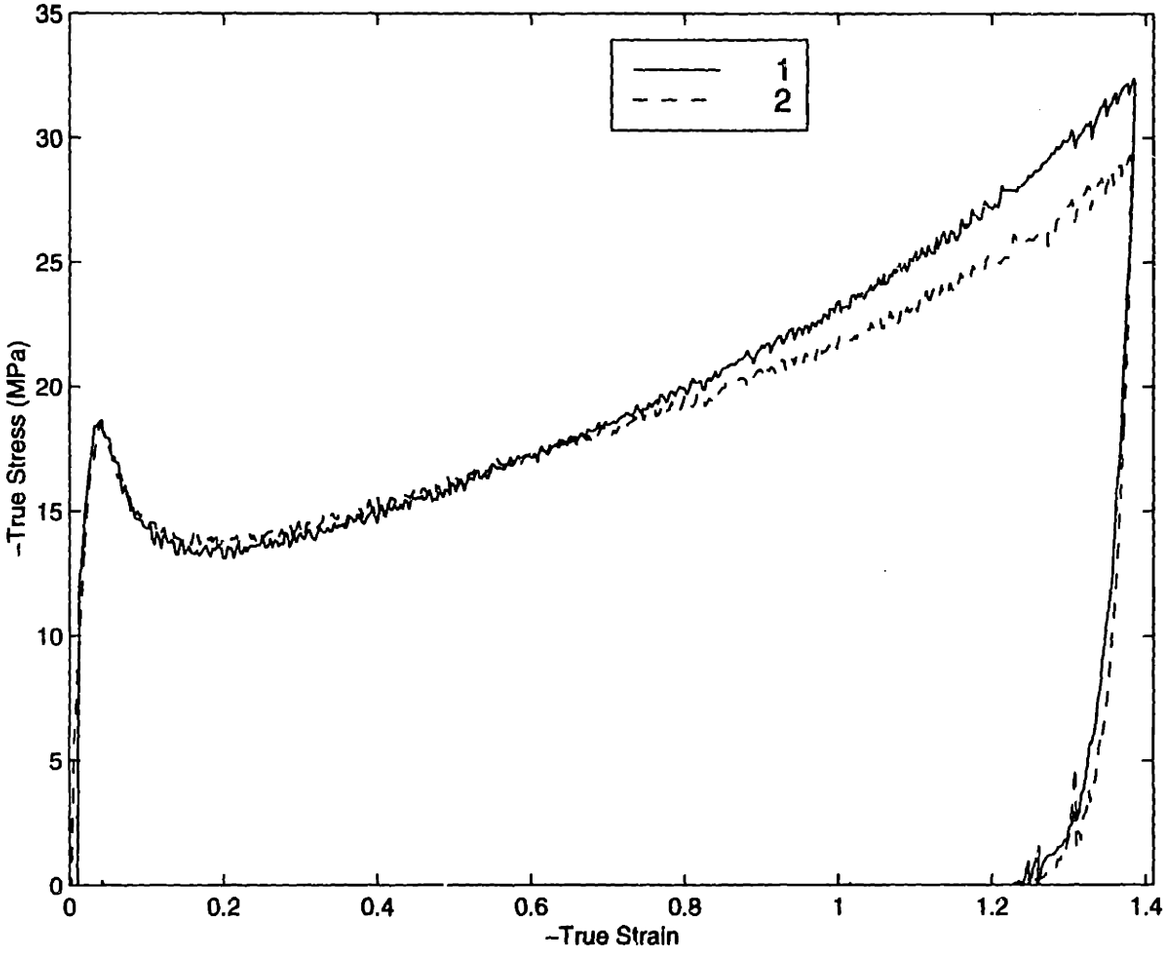

Figure B.10: Uniaxial Compression Tests, $70°C$, $\dot{\epsilon} = -0.01/s$

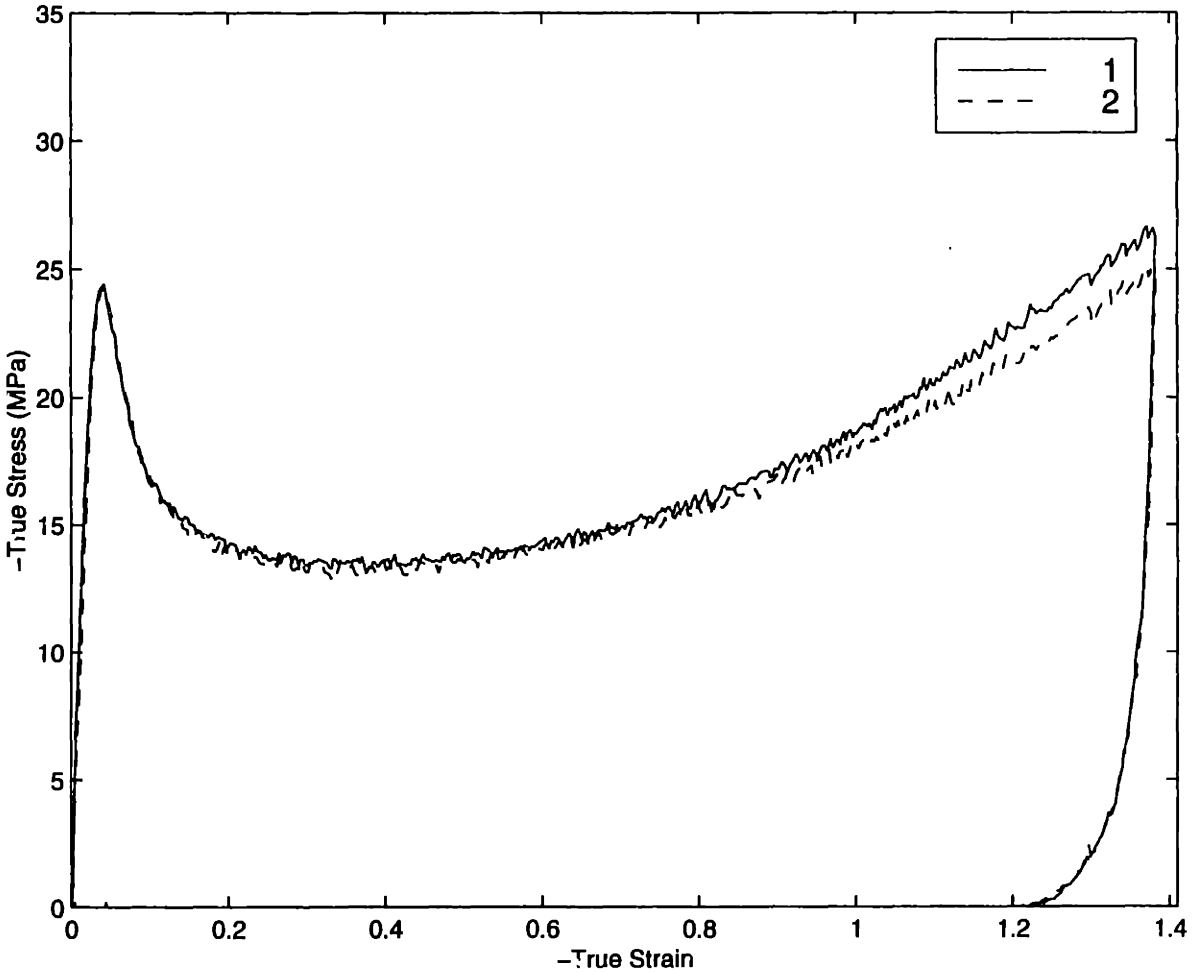

Figure B.11: Uniaxial Compression Tests, $70°C$, $\dot{\varepsilon} = -0.05/s$

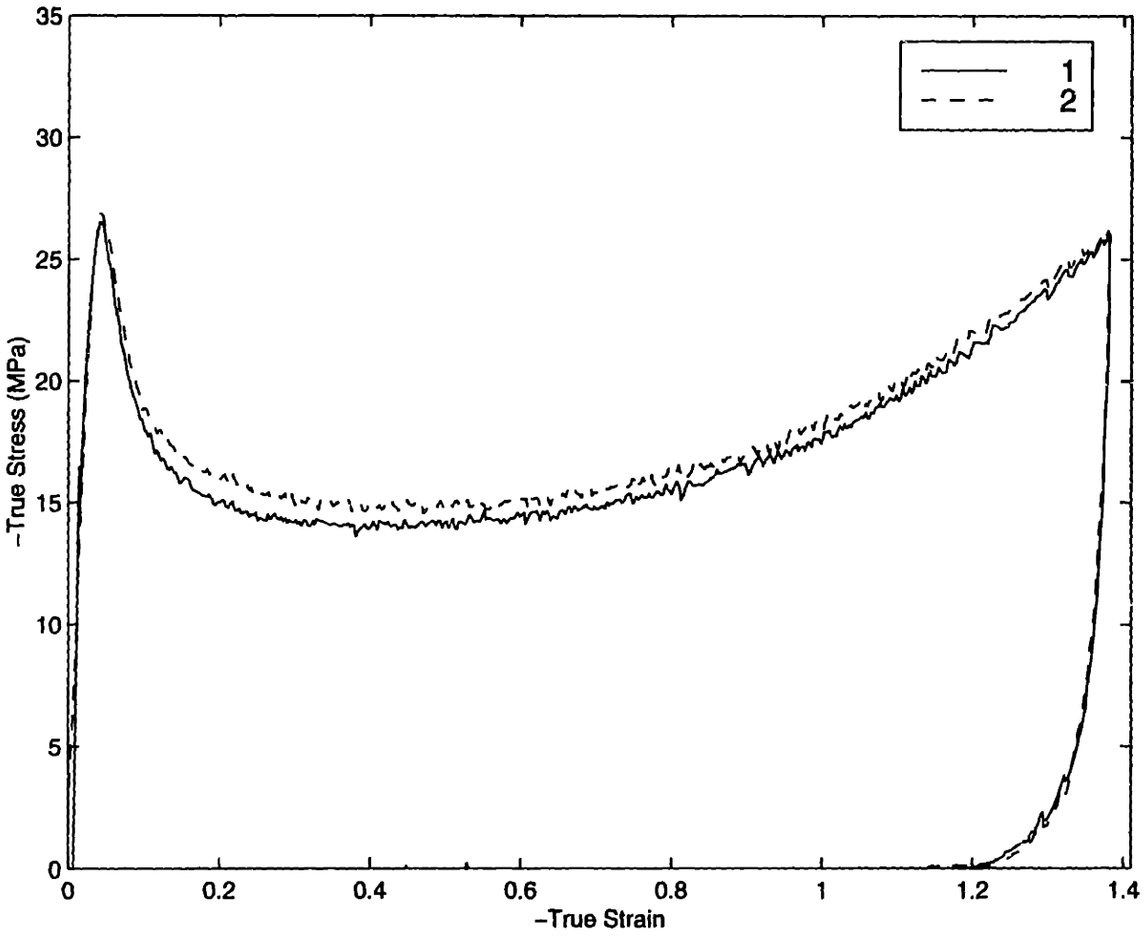

Figure B.12: Uniaxial Compression Tests, $70°C$, $\dot{\varepsilon} = -0.1/s$

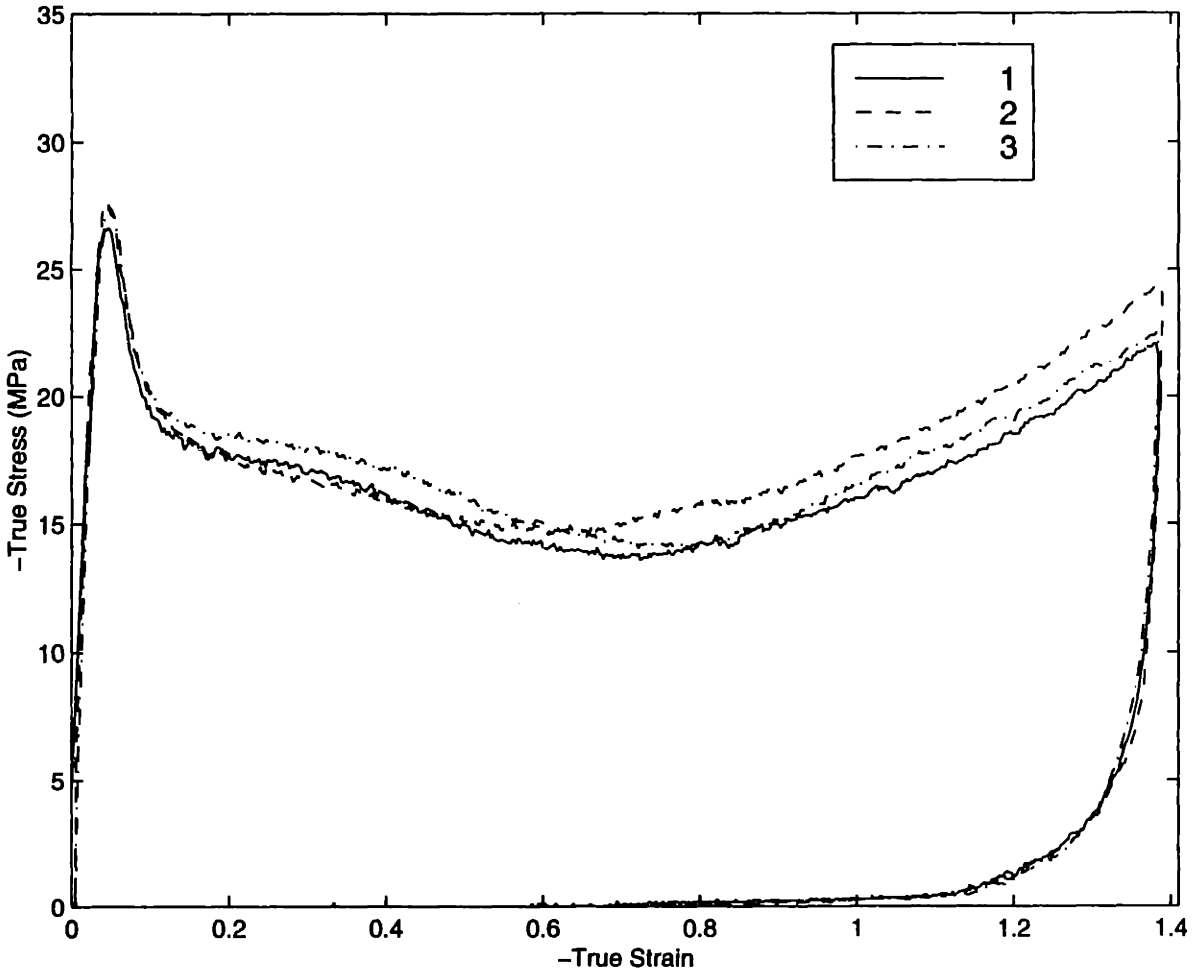

Figure B.13: Uniaxial Compression Tests, $70°C$, $\dot{\varepsilon} = -0.5/s$

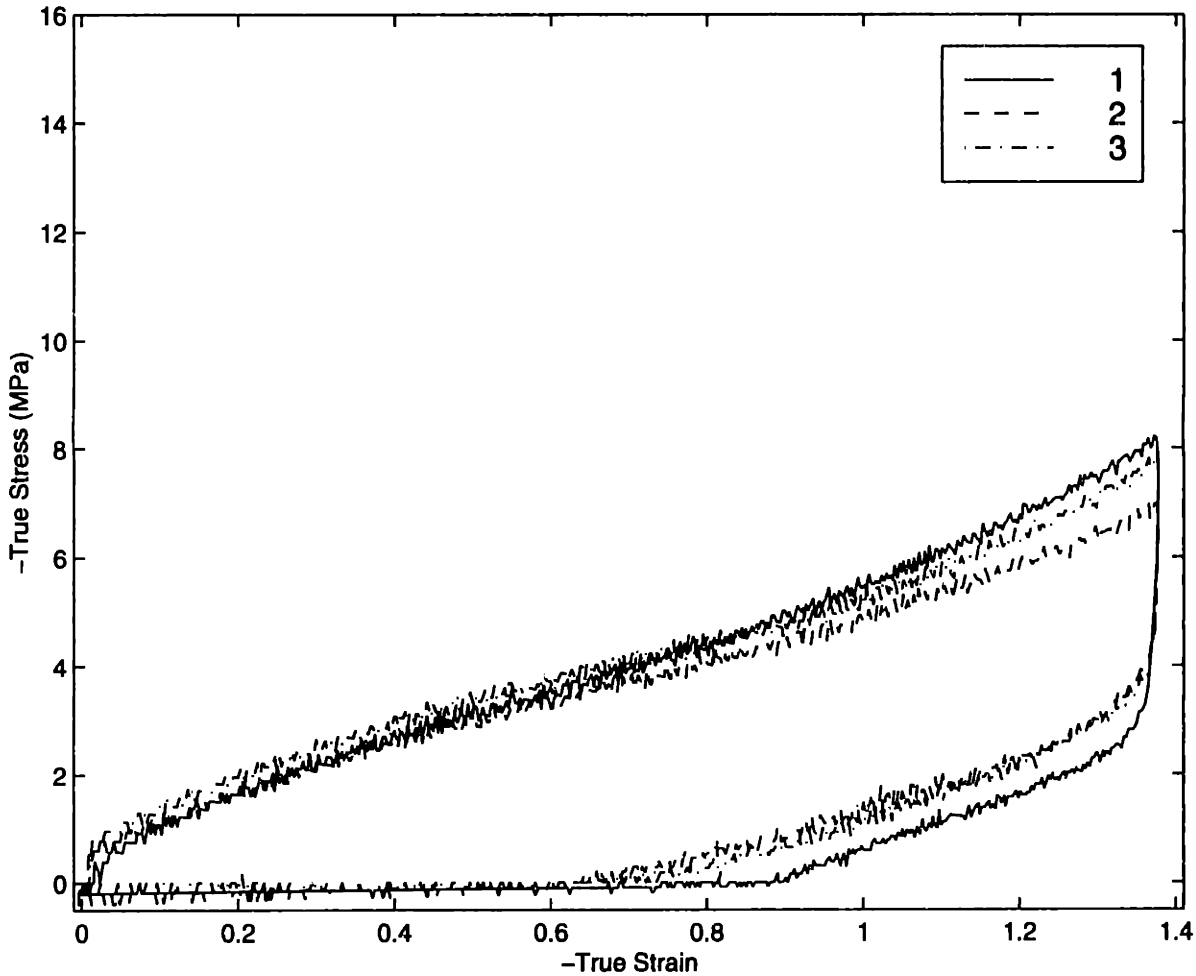

Figure B.14: Uniaxial Compression Tests, $80°C$, $\dot{\epsilon} = -0.005/s$

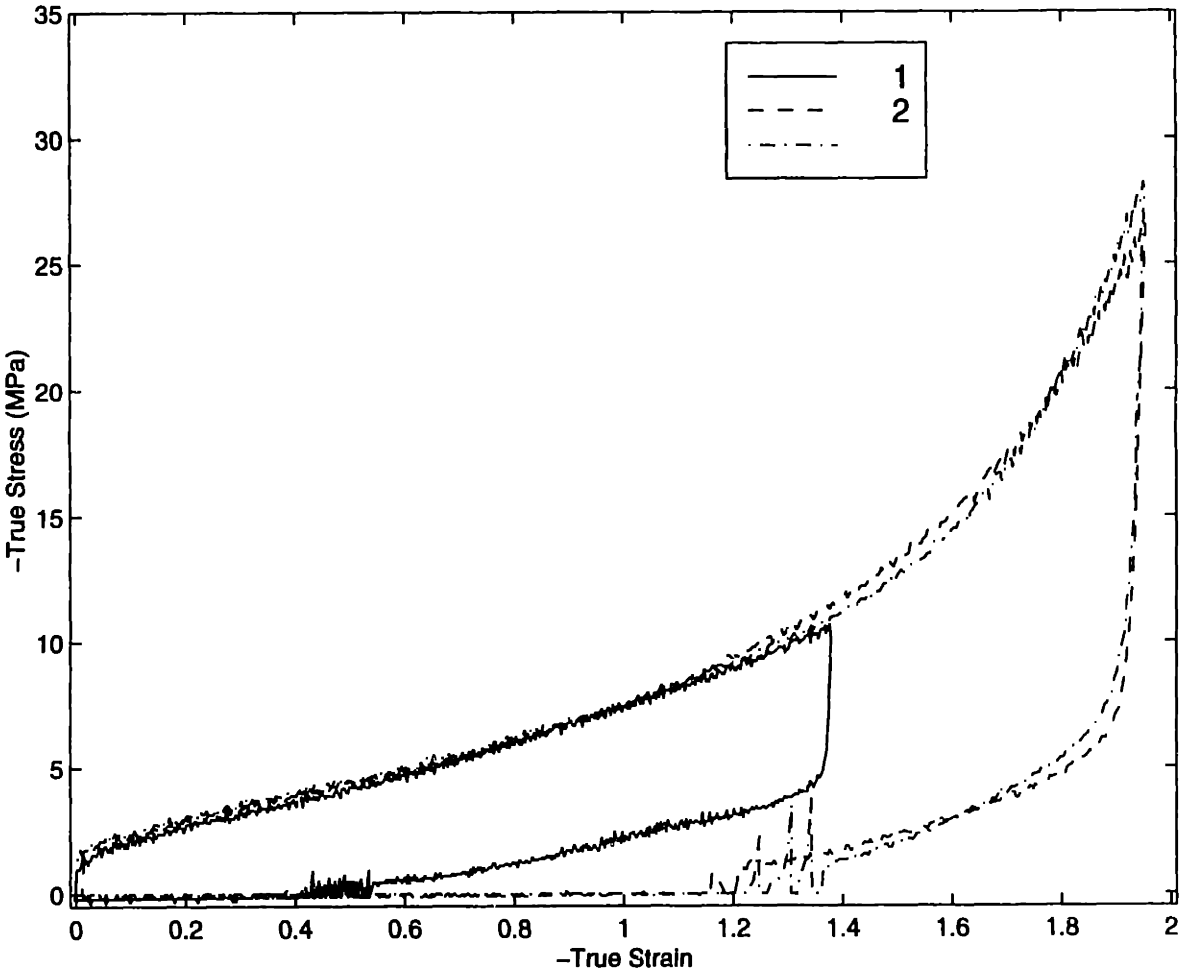

Figure B.15: Uniaxial Compression Tests, $80°C$, $\dot{\varepsilon} = -0.01/s$

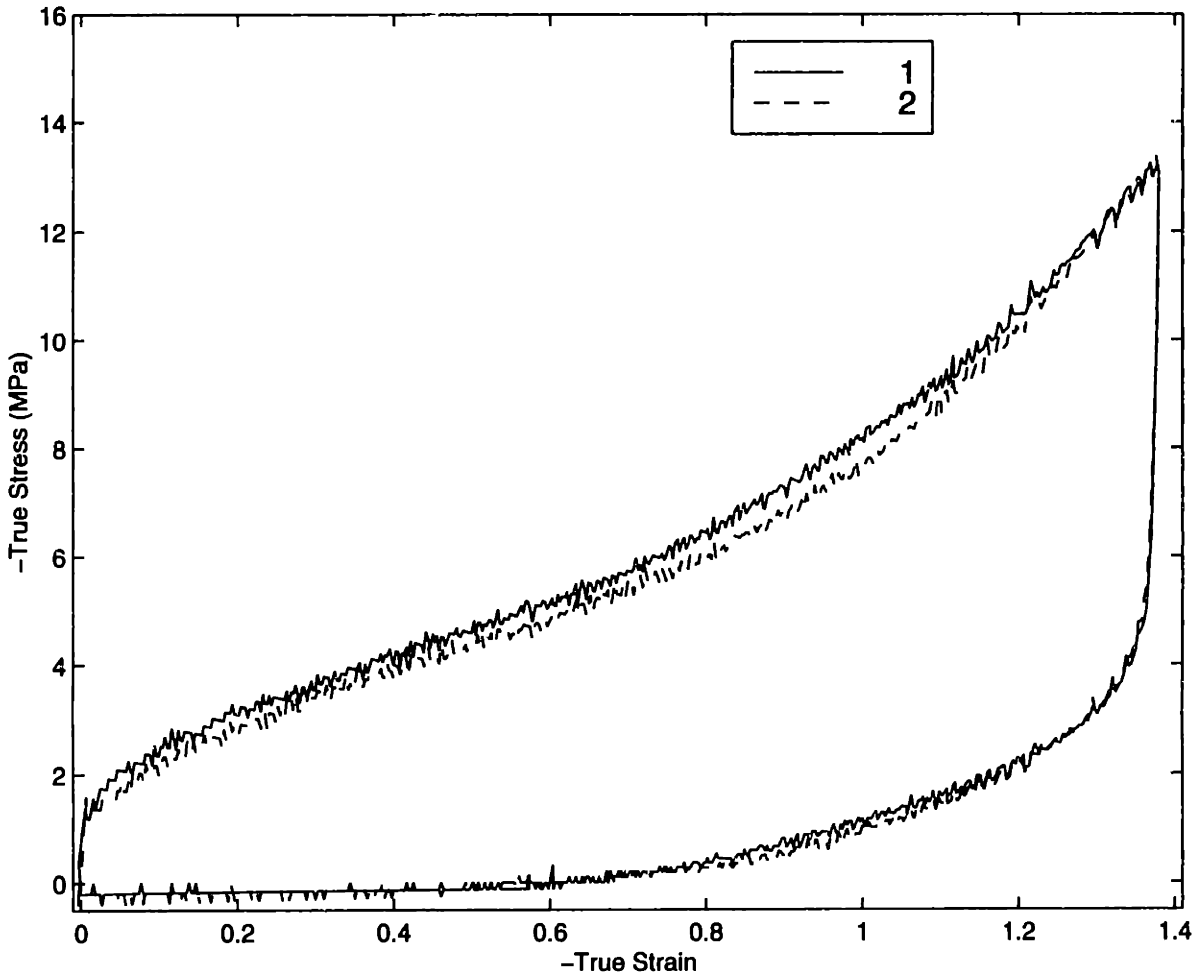

Figure B.16: Uniaxial Compression Tests, $80°C$, $\dot{\epsilon} = -0.05/s$

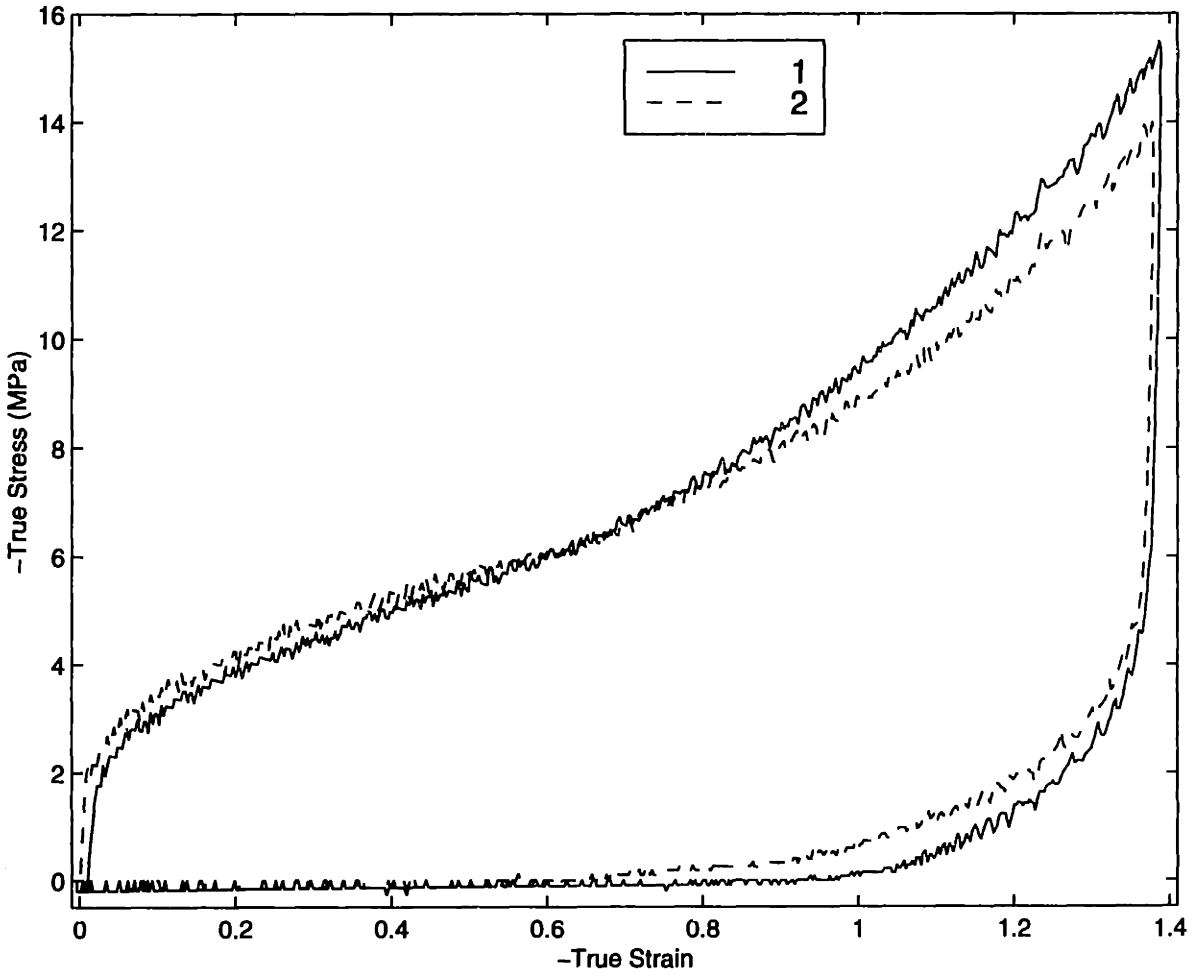

Figure B.17: Uniaxial Compression Tests, $80°C$, $\dot{\epsilon} = -0.1/s$

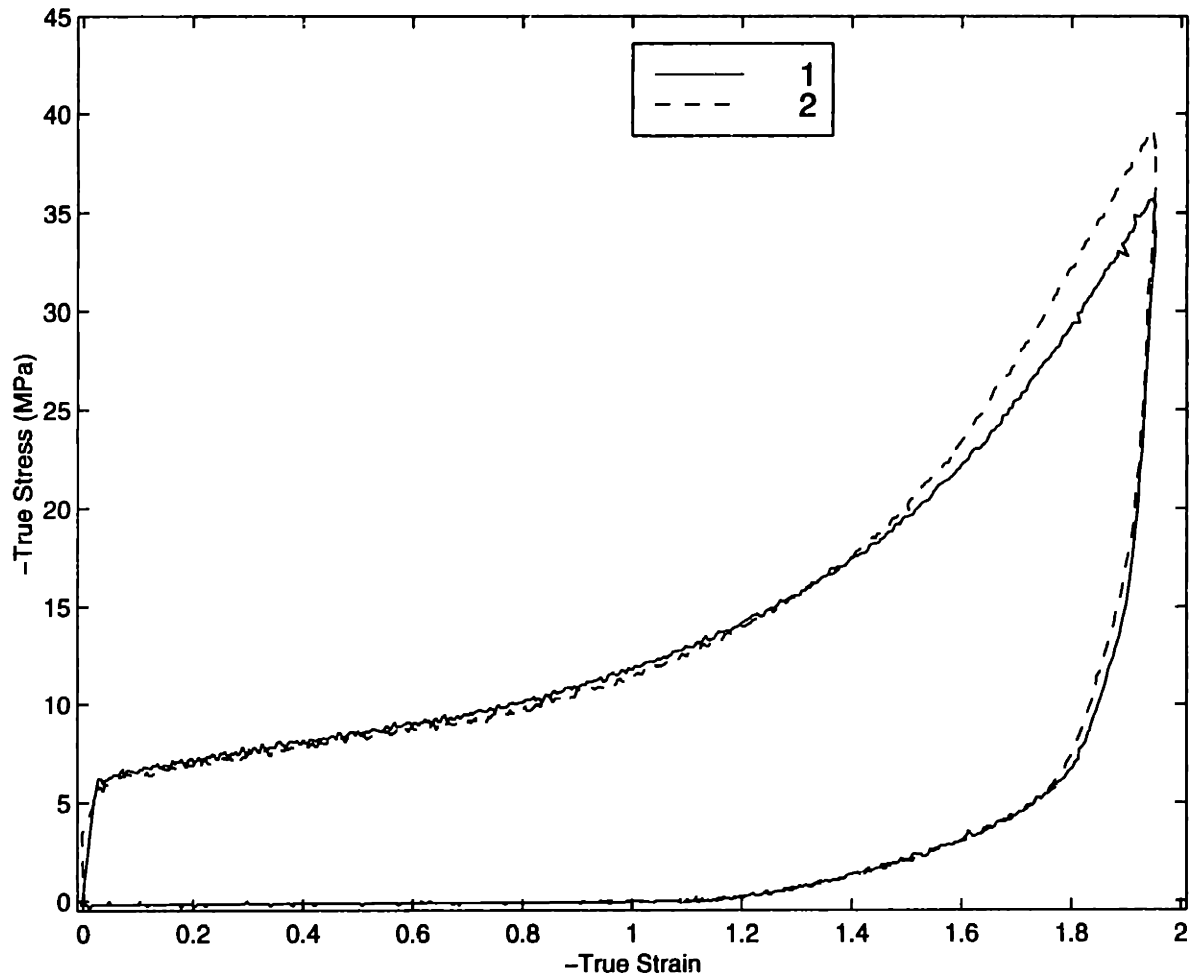

Figure B.18: Uniaxial Compression Tests, $80°C$, $\dot{\varepsilon} = -0.5/s$

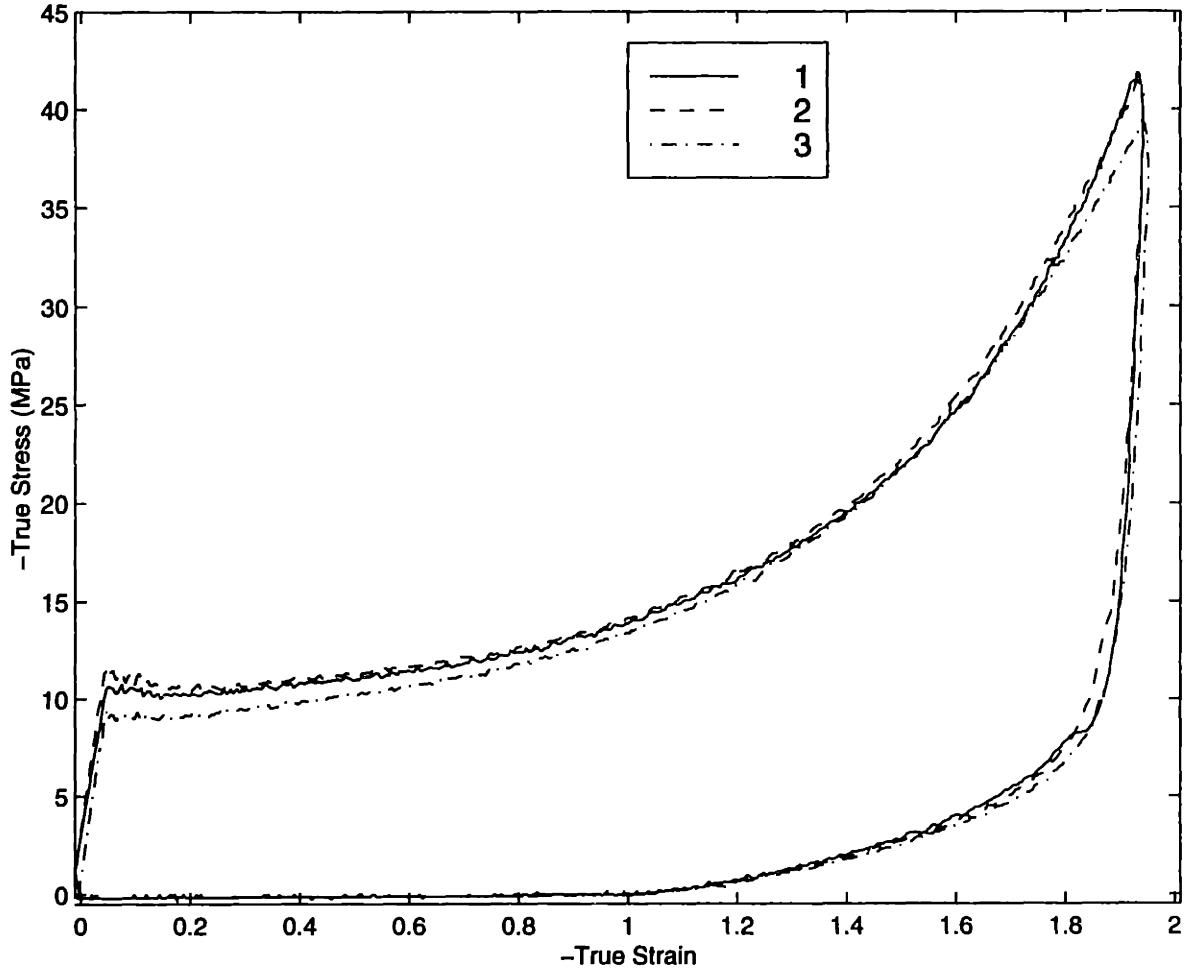

Figure B.19: Uniaxial Compression Tests, $80°C$, $\dot{\epsilon} = -1.0/s$

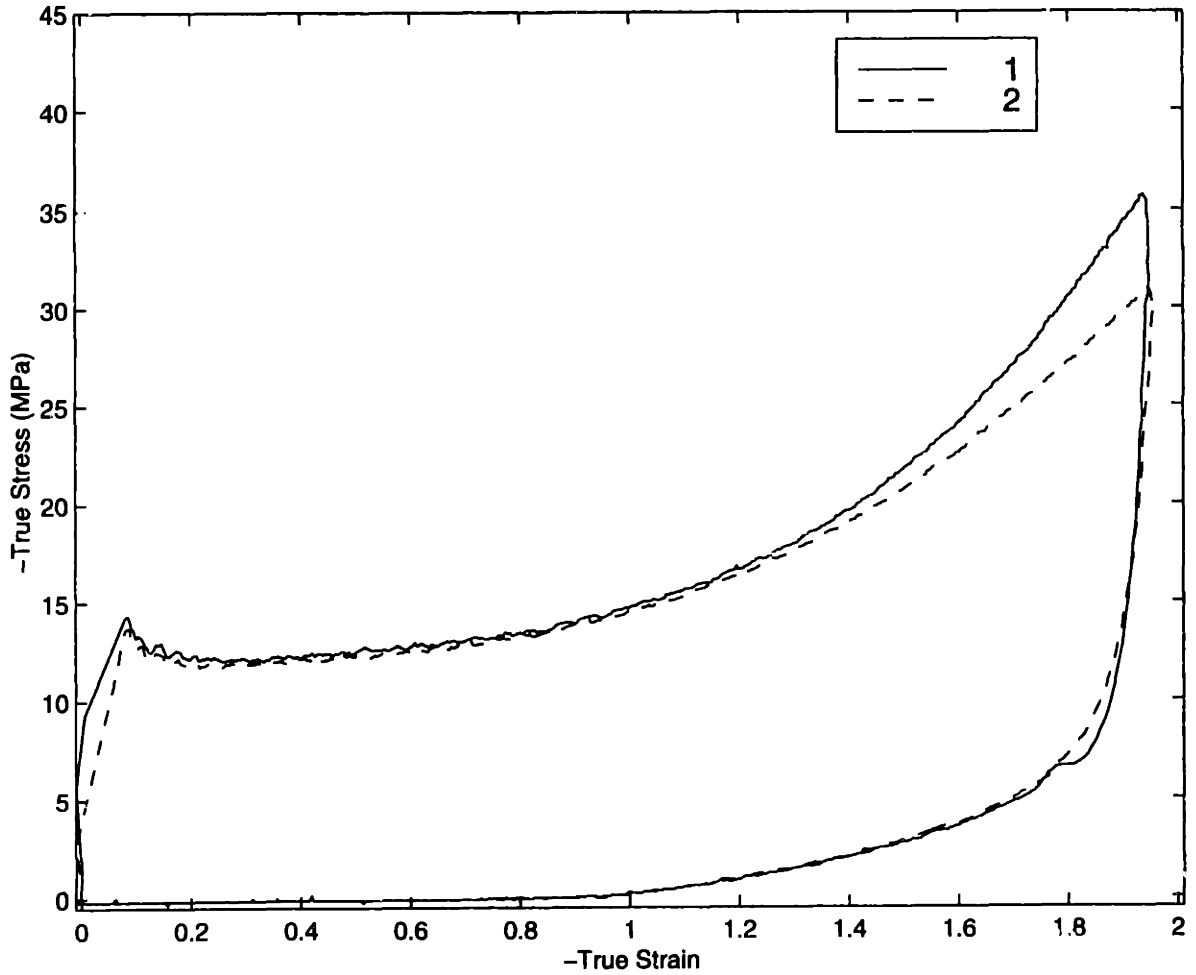

Figure B.20: Uniaxial Compression Tests, $80°C$, $\dot{\varepsilon} = -2.0/s$

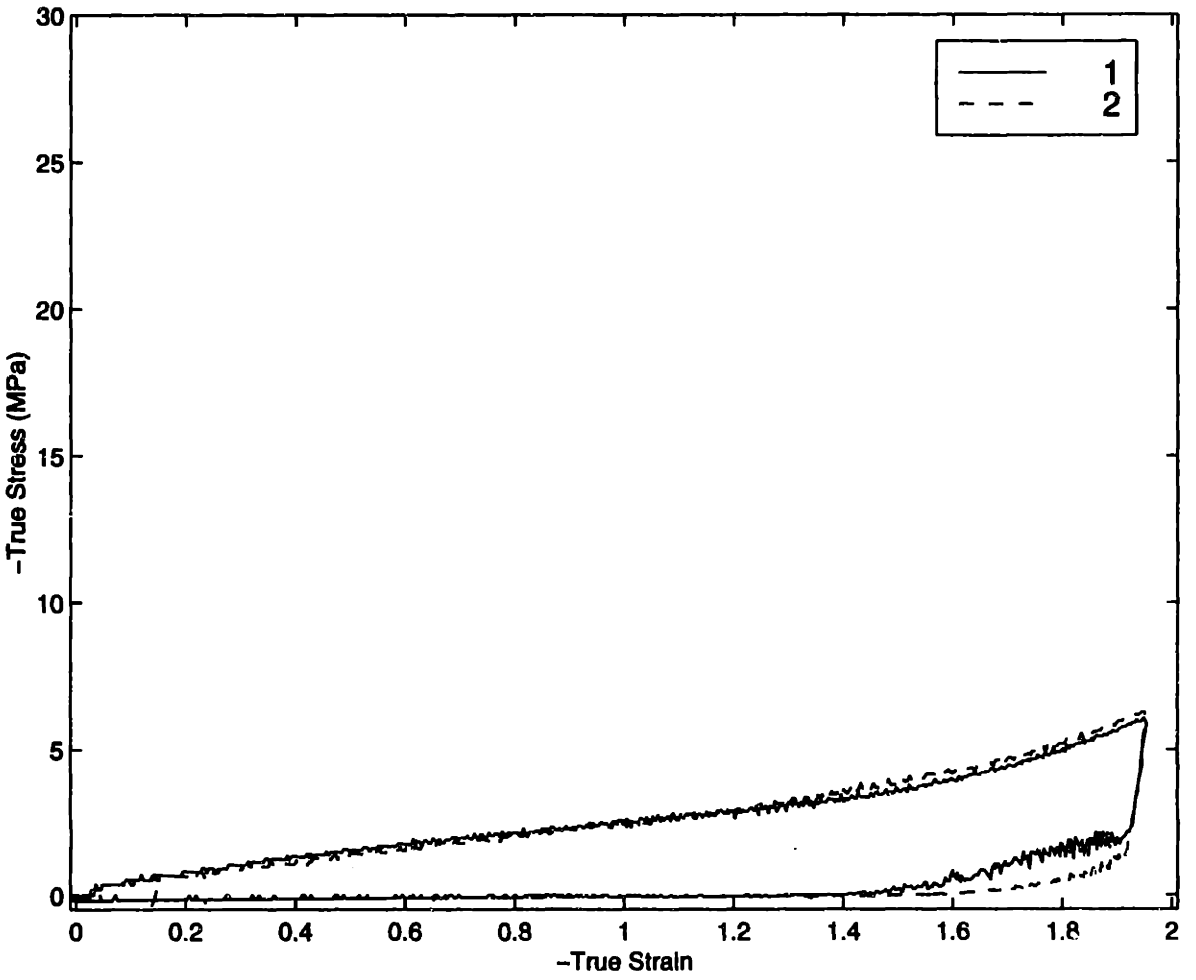

Figure B.21: Uniaxial Compression Tests, $90°C$, $\dot{\varepsilon} = -0.005/s$

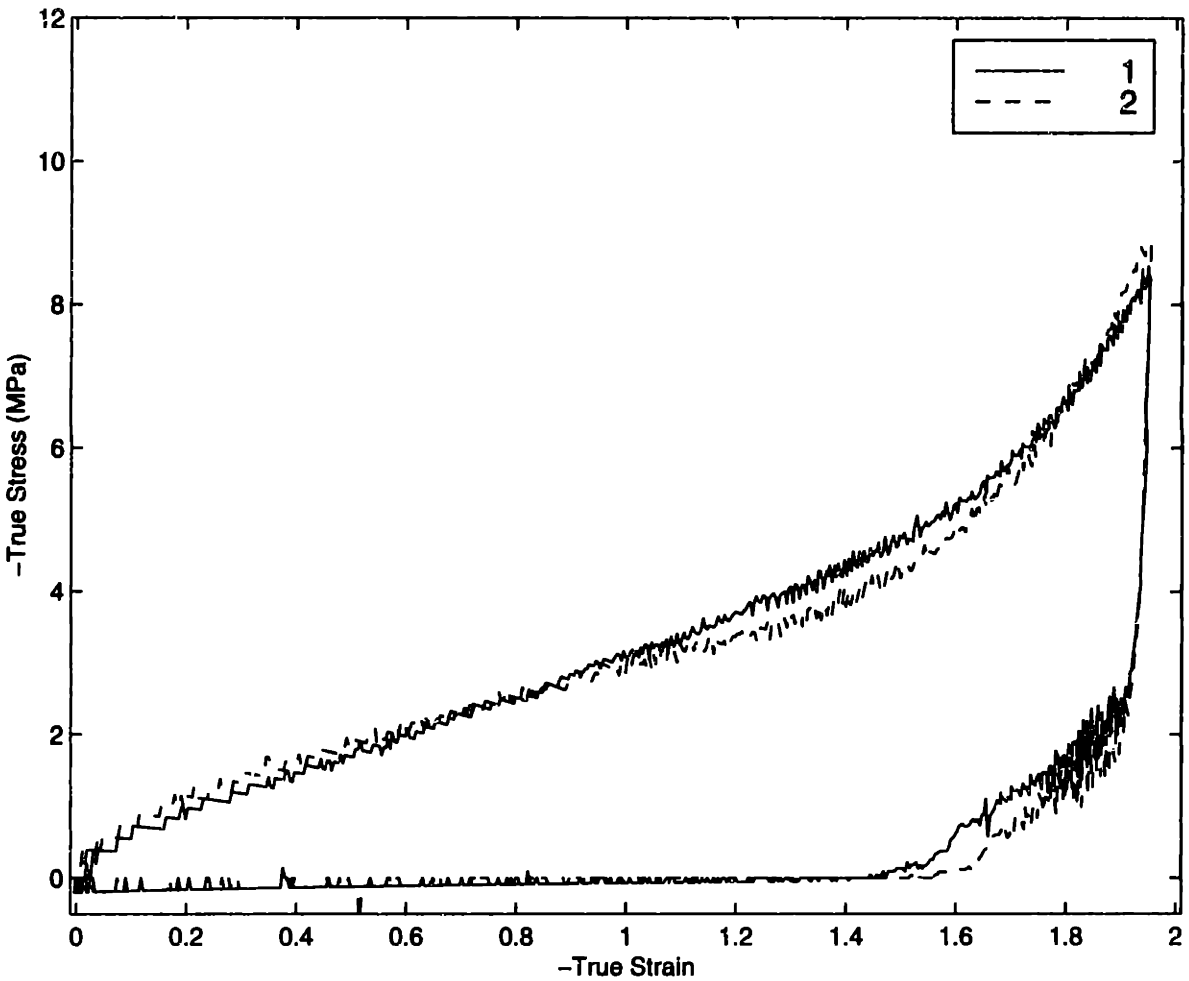

Figure B.22: Uniaxial Compression Tests, $90°C$, $\dot{\varepsilon} = -0.01/s$

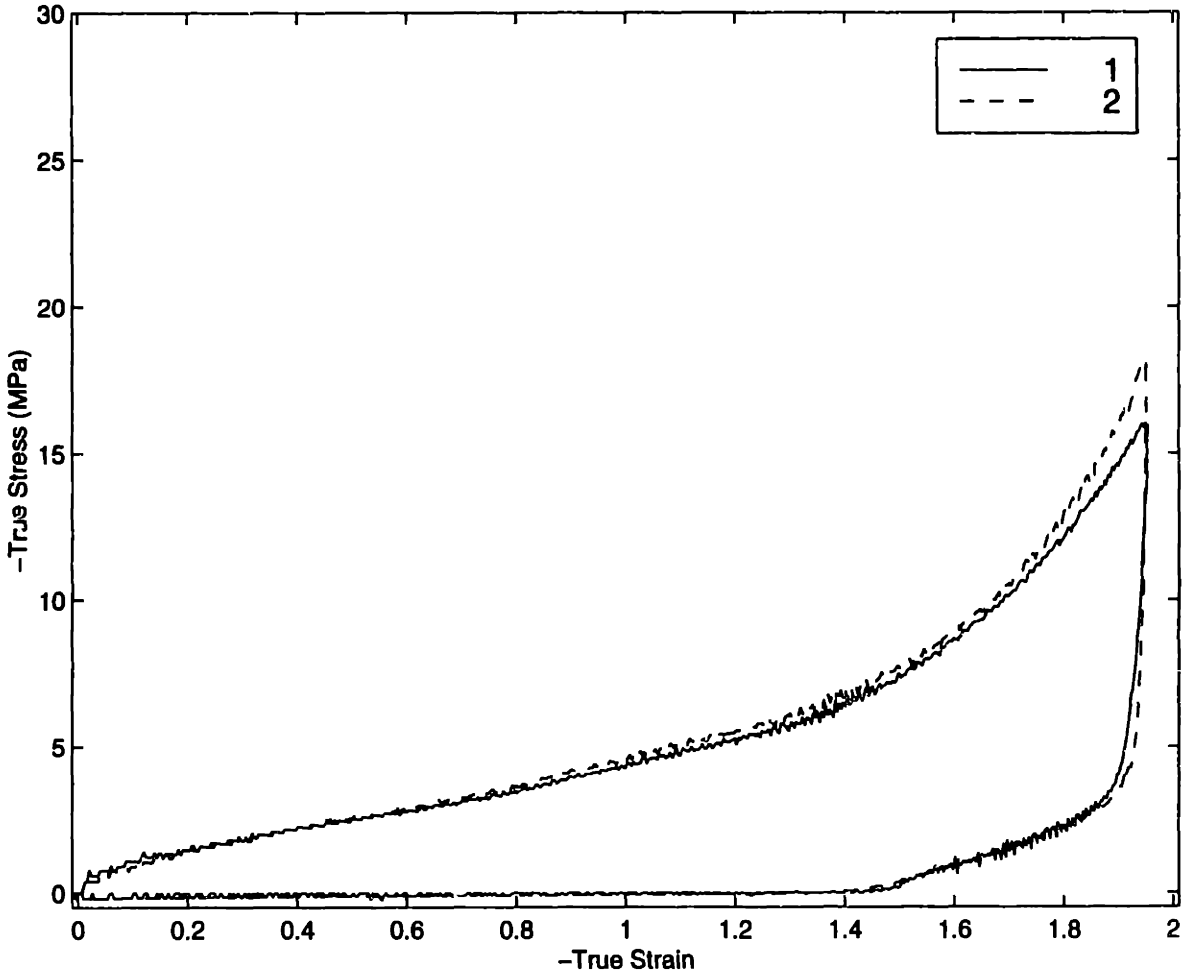

Figure B.23: Uniaxial Compression Tests, $90°C$, $\dot{\varepsilon} = -0.05/s$

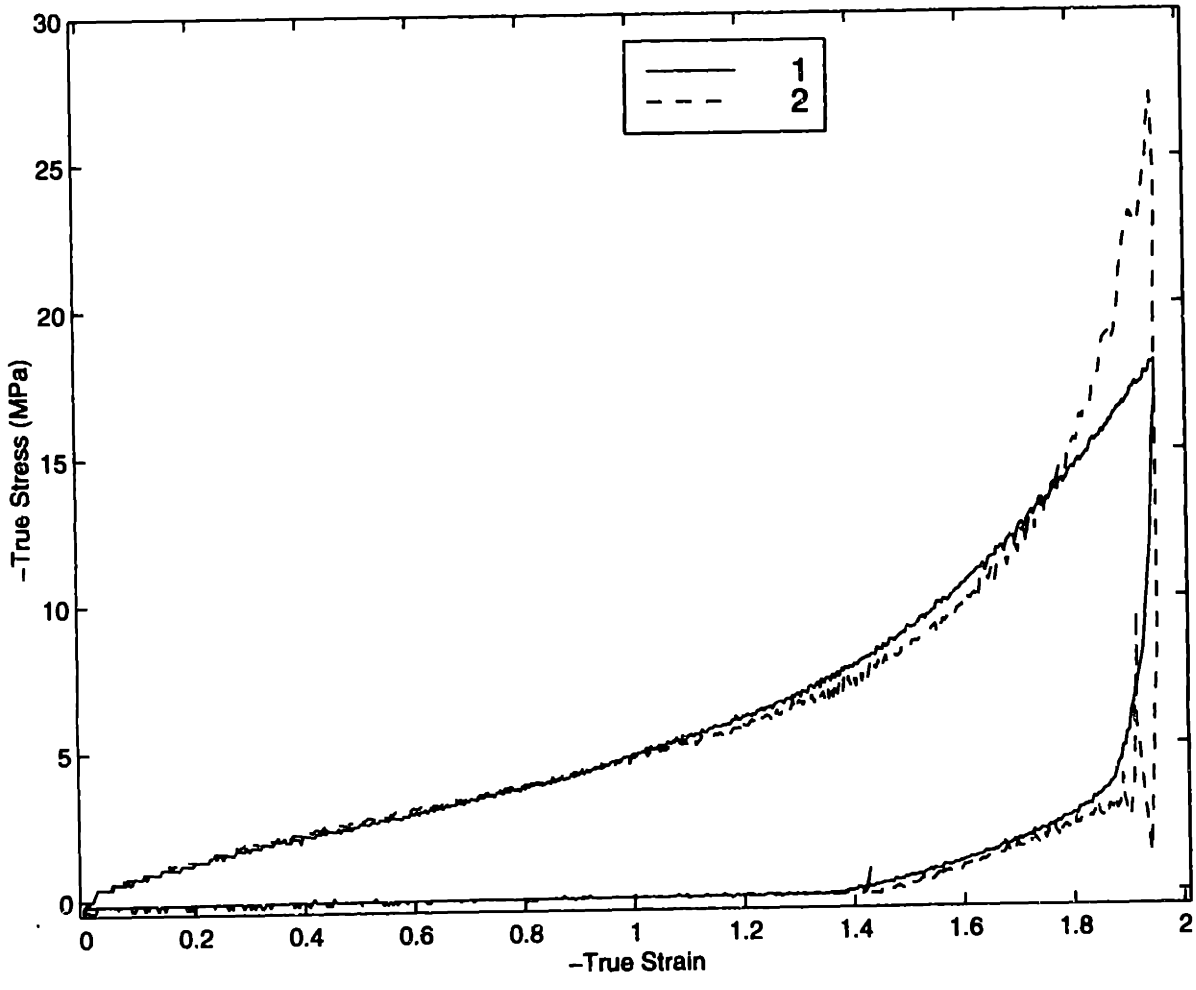

Figure B.24: Uniaxial Compression Tests, $90°C$, $\dot{\epsilon} = -0.1/s$

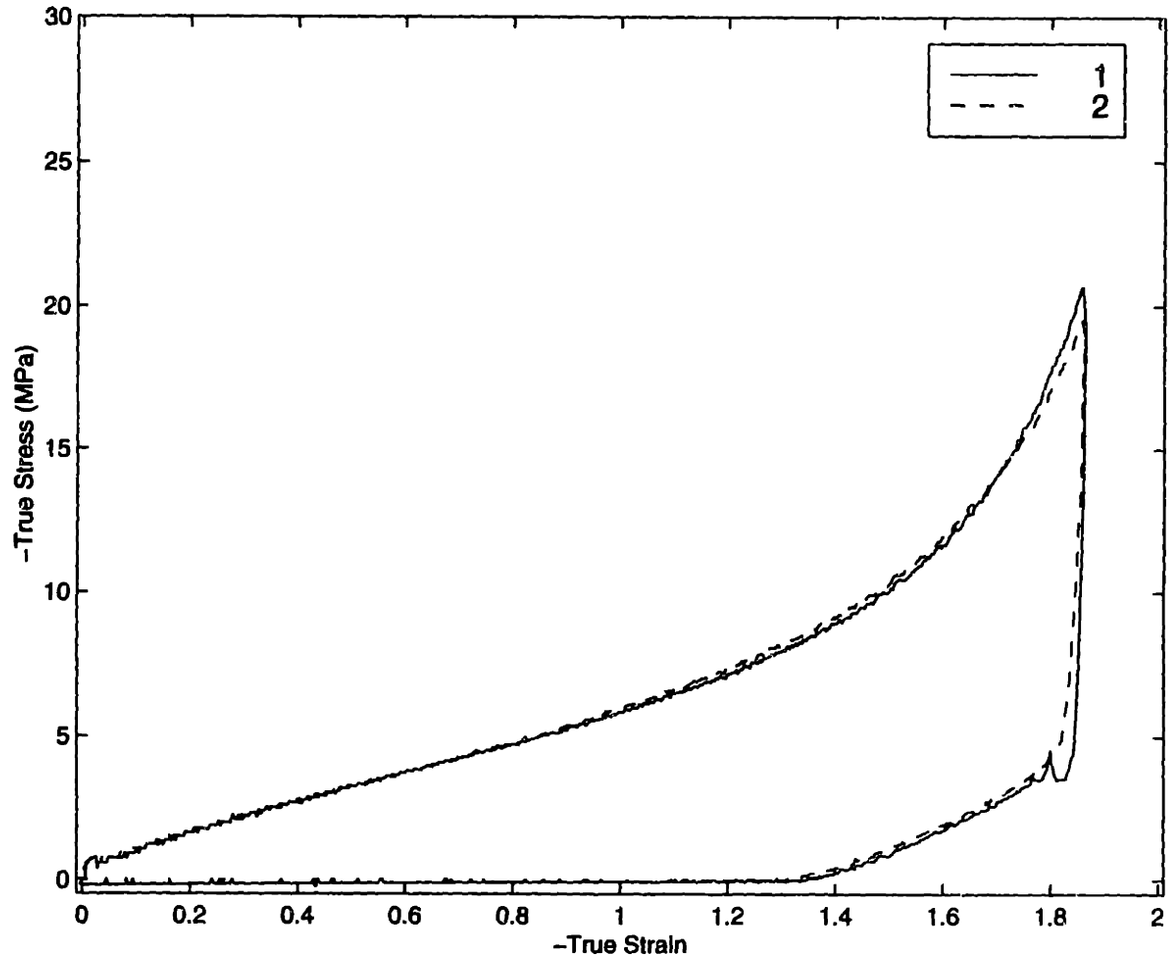

Figure B.25: Uniaxial Compression Tests, $90°C$, $\dot{\varepsilon} = -0.5/s$

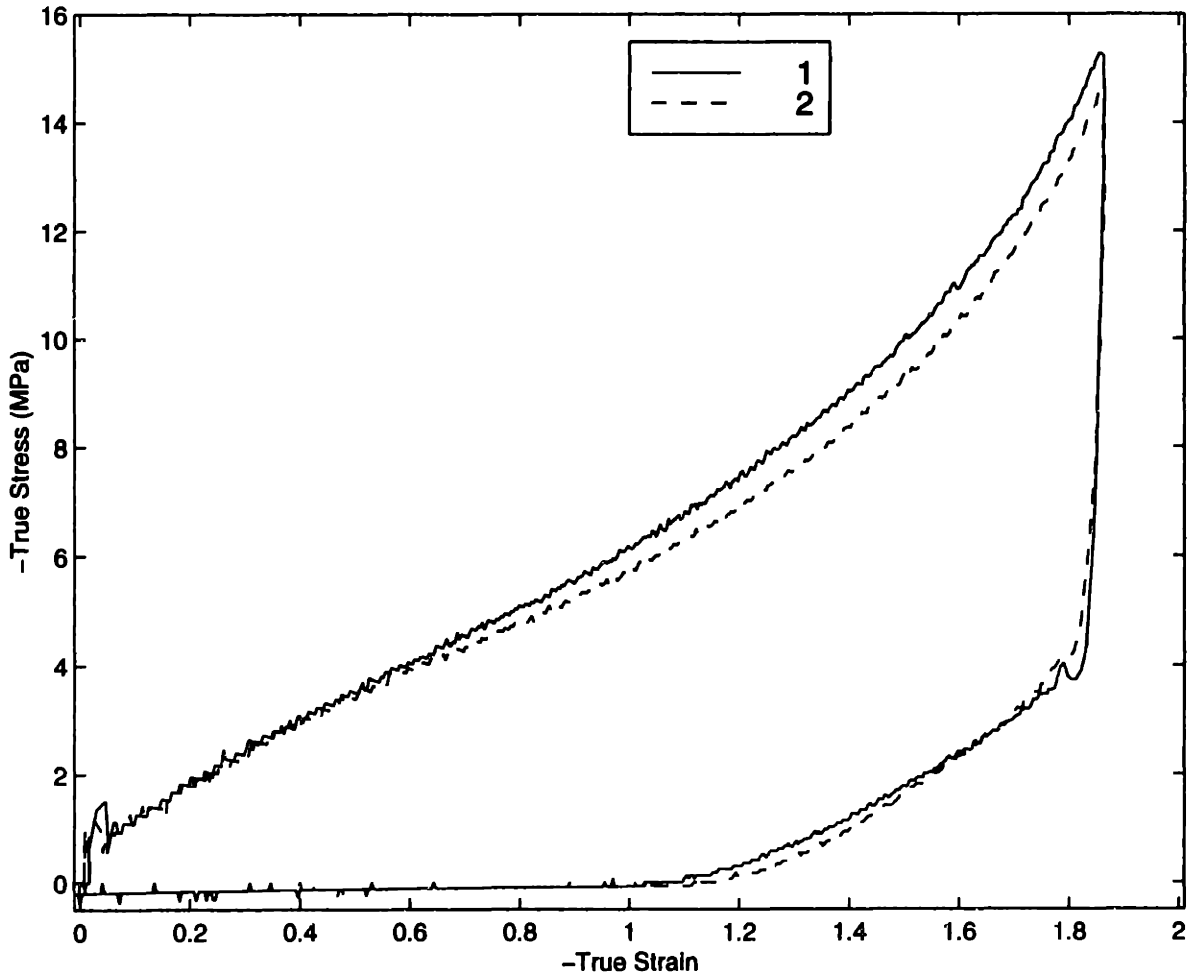

Figure B.26: Uniaxial Compression Tests, $90°C$, $\dot{\epsilon} = -1.0/s$

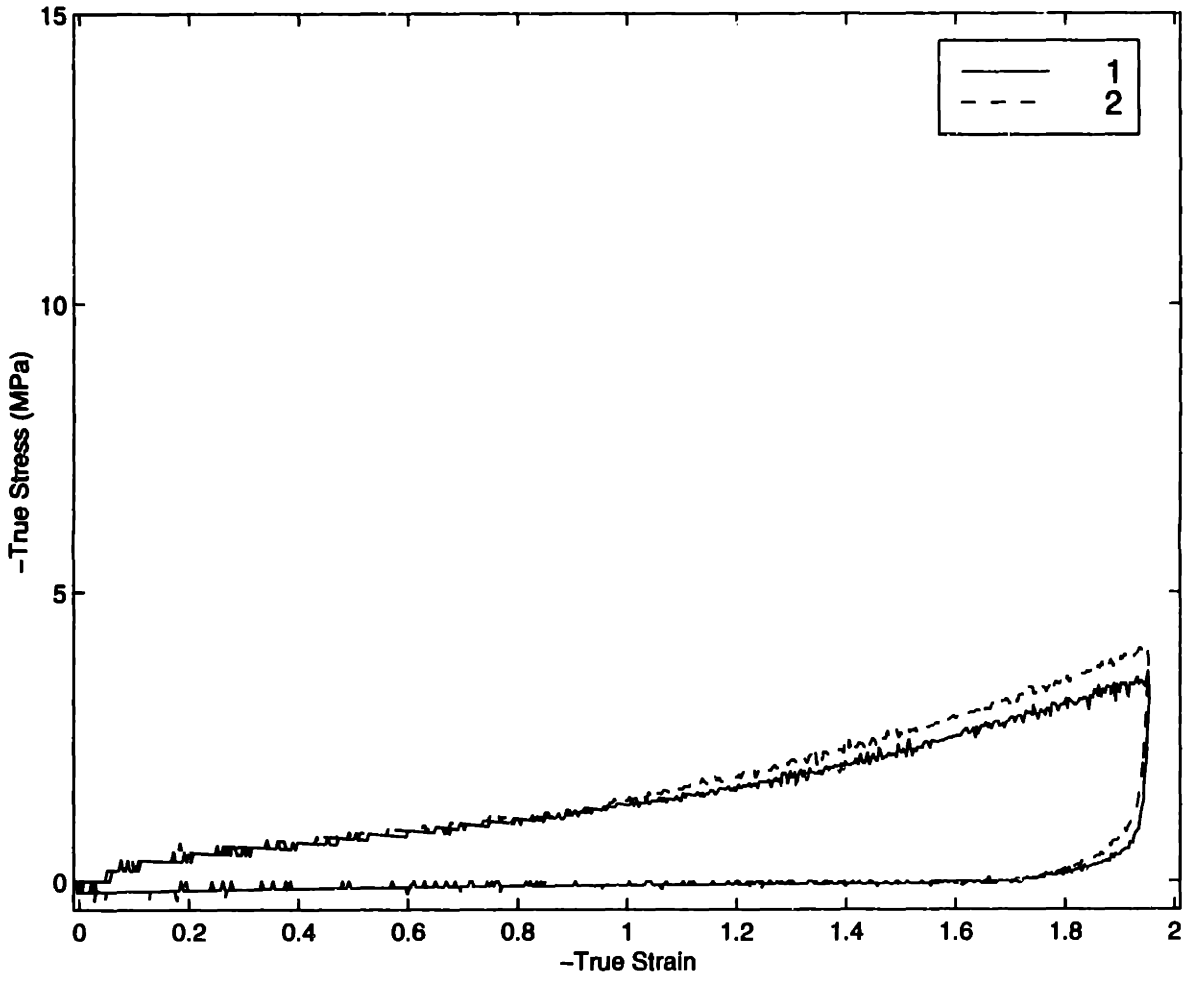

Figure B.27: Uniaxial Compression Tests, $100°C$, $\dot{\varepsilon} = -0.005/s$

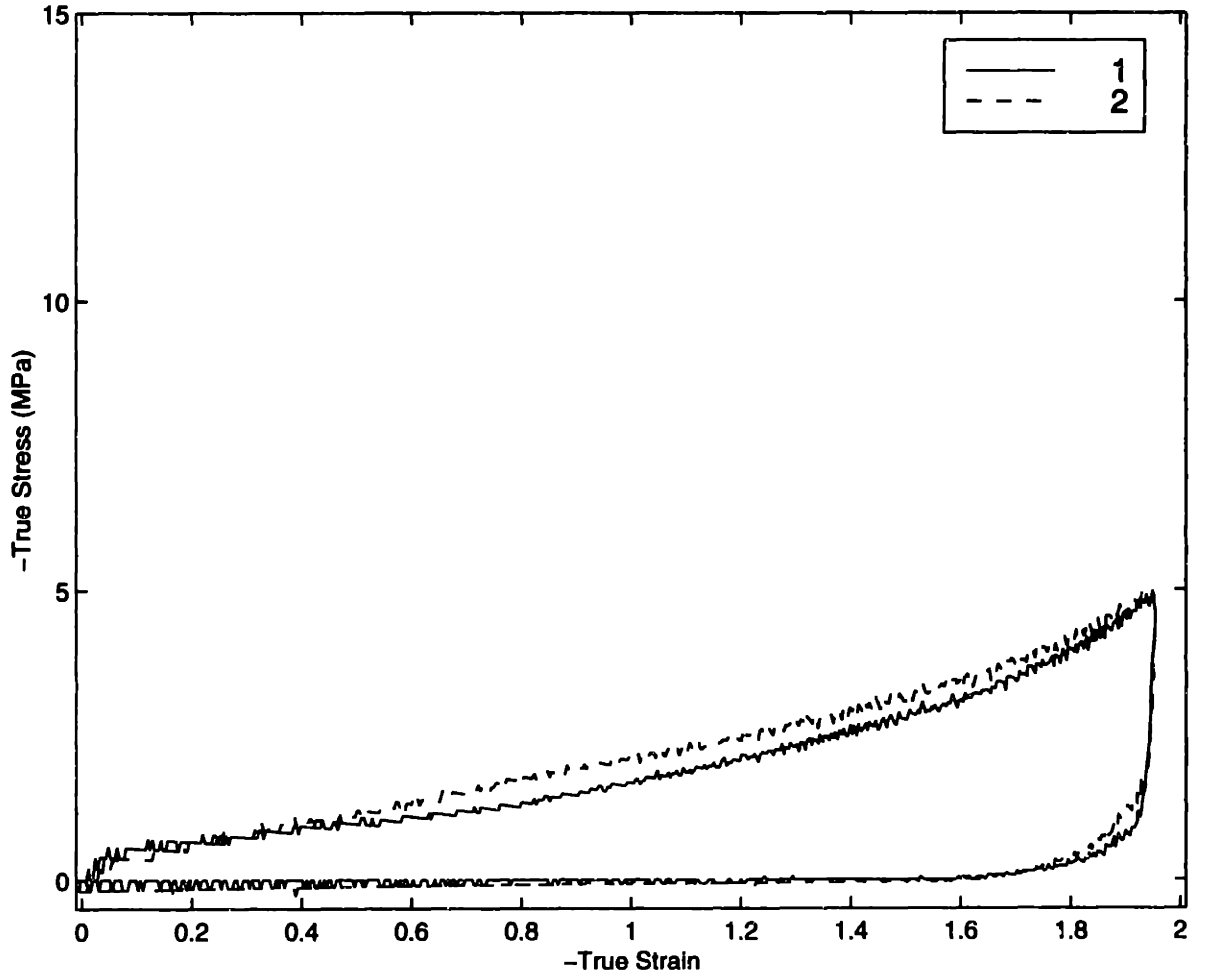

Figure B.28: Uniaxial Compression Tests, $100°C$, $\dot{\epsilon} = -0.01/s$

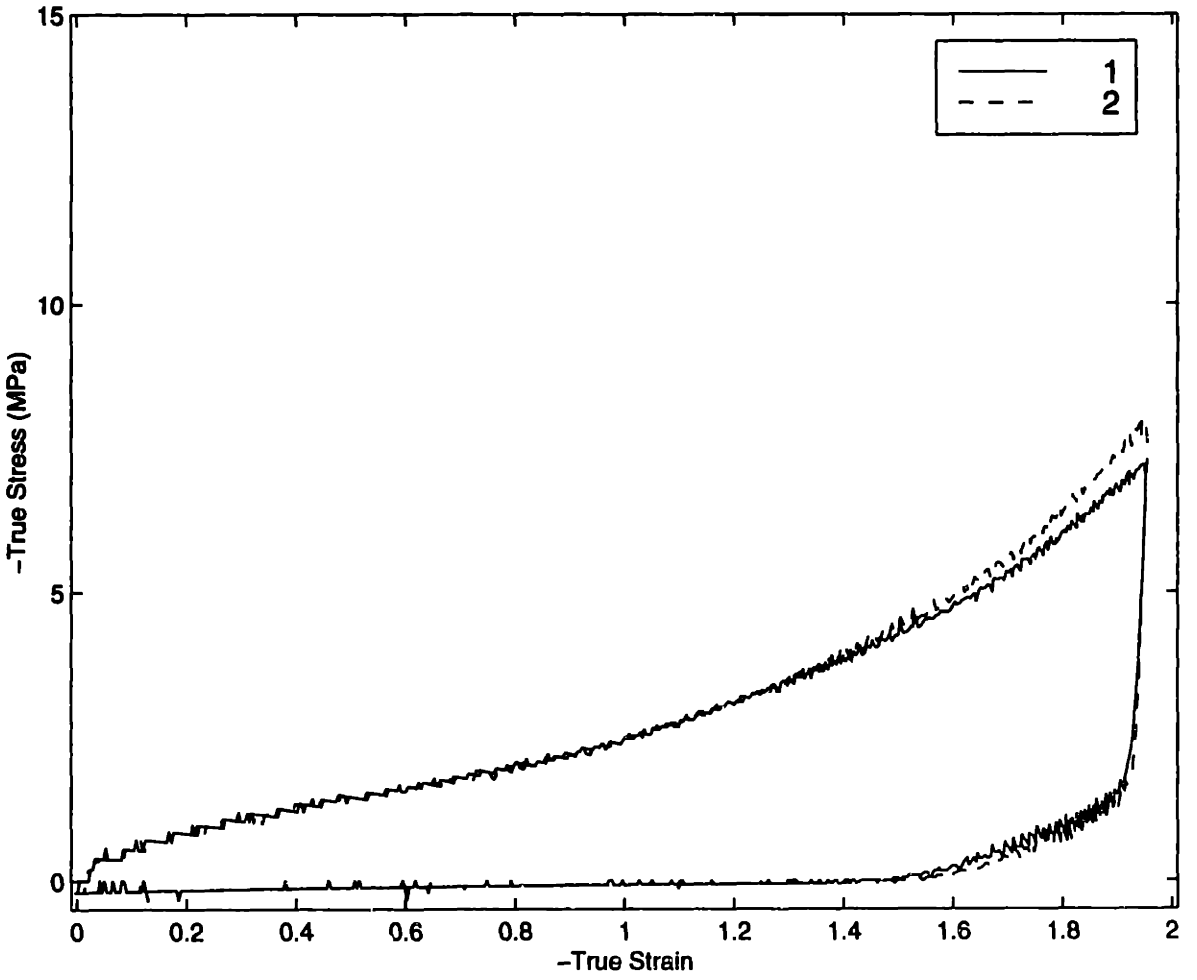

Figure B.29: Uniaxial Compression Tests, $100°C$, $\dot{\epsilon} = -0.05/s$

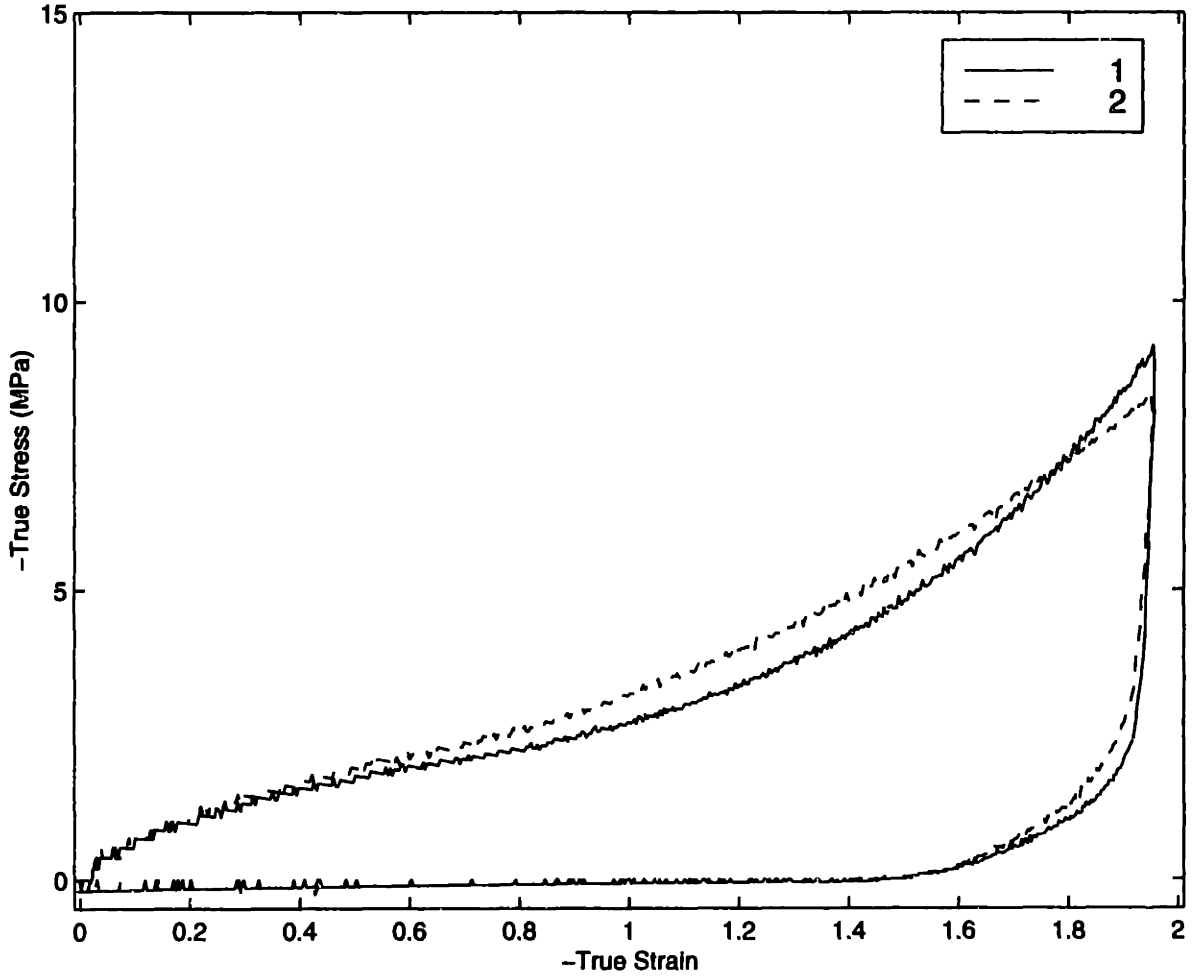

Figure B.30: Uniaxial Compression Tests, $100°C$, $\dot{\varepsilon} = -0.1/s$

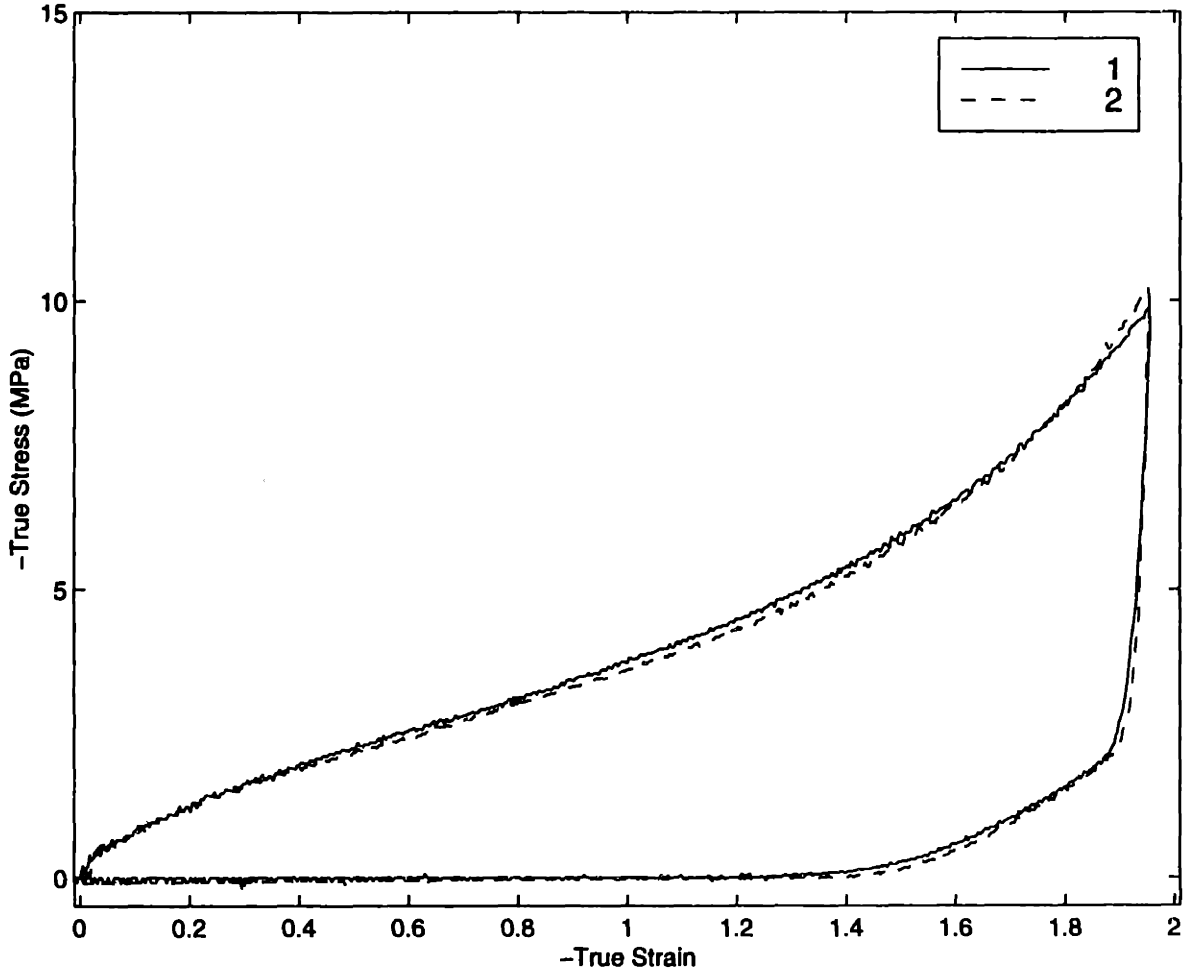

Figure B.31: Uniaxial Compression Tests, $100°C$, $\dot{\varepsilon} = -0.5/s$

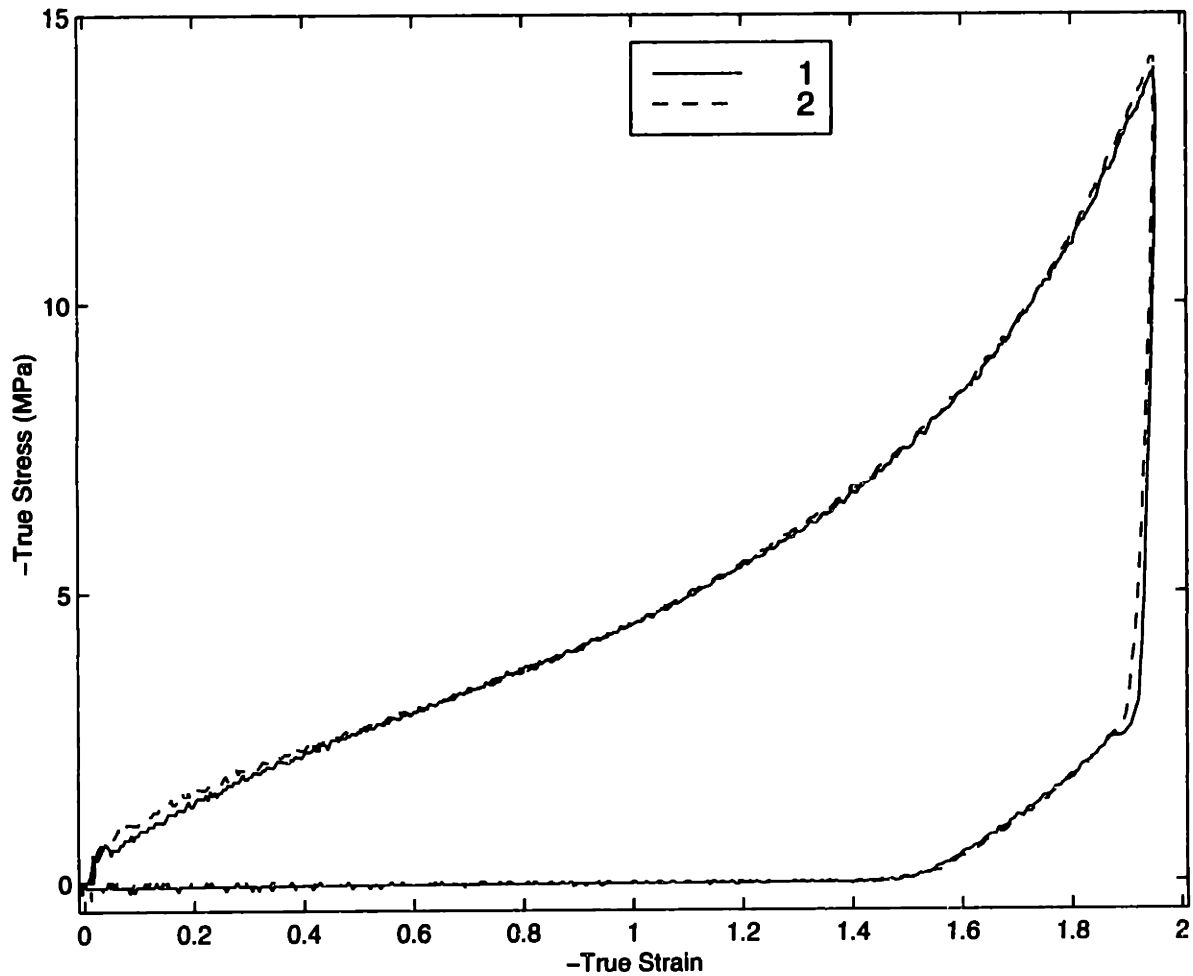

Figure B.32: Uniaxial Compression Tests, $100°C$, $\dot{\varepsilon} = -1.0/s$

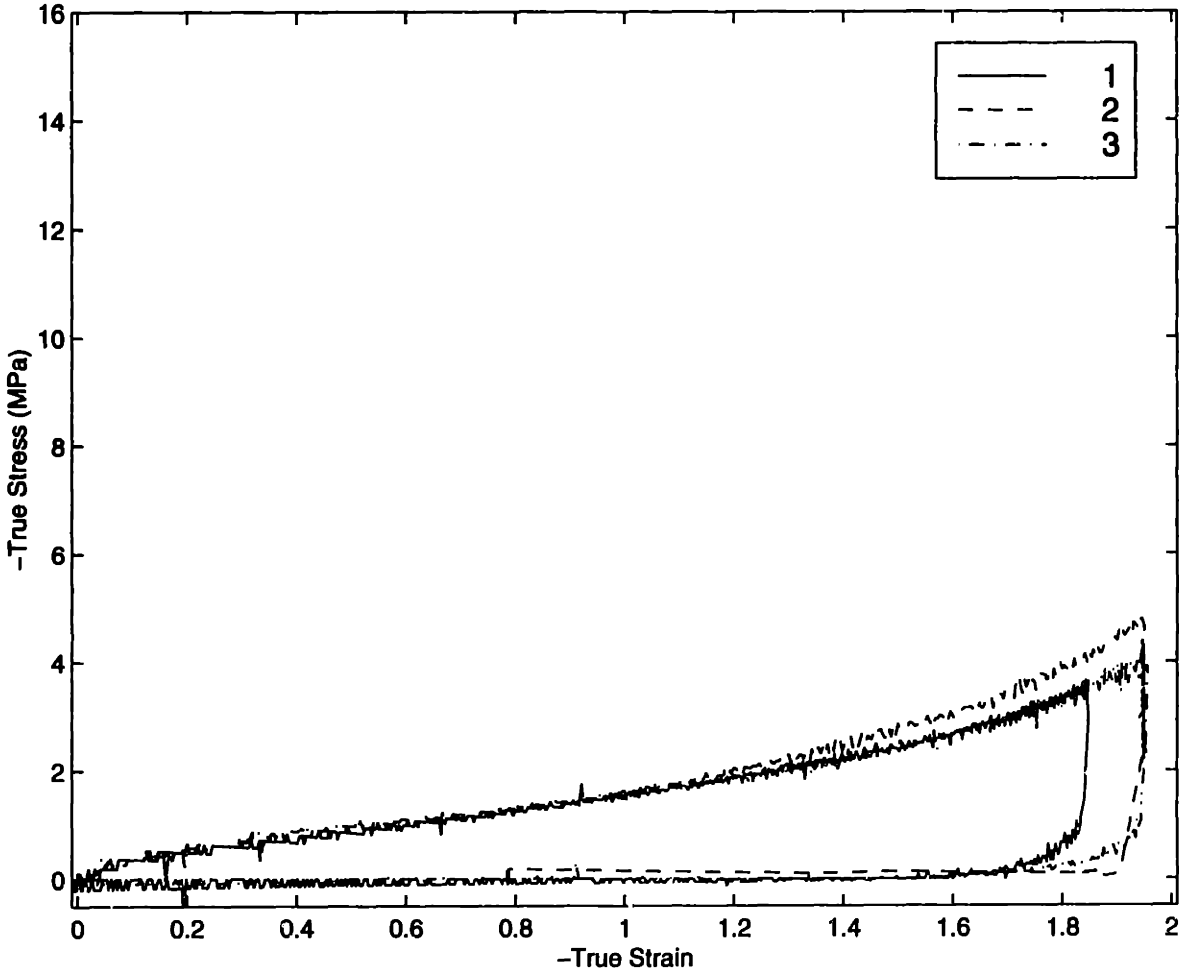

Figure B.33: Uniaxial Compression Tests, $105°C$, $\dot{\epsilon} = -0.01/s$

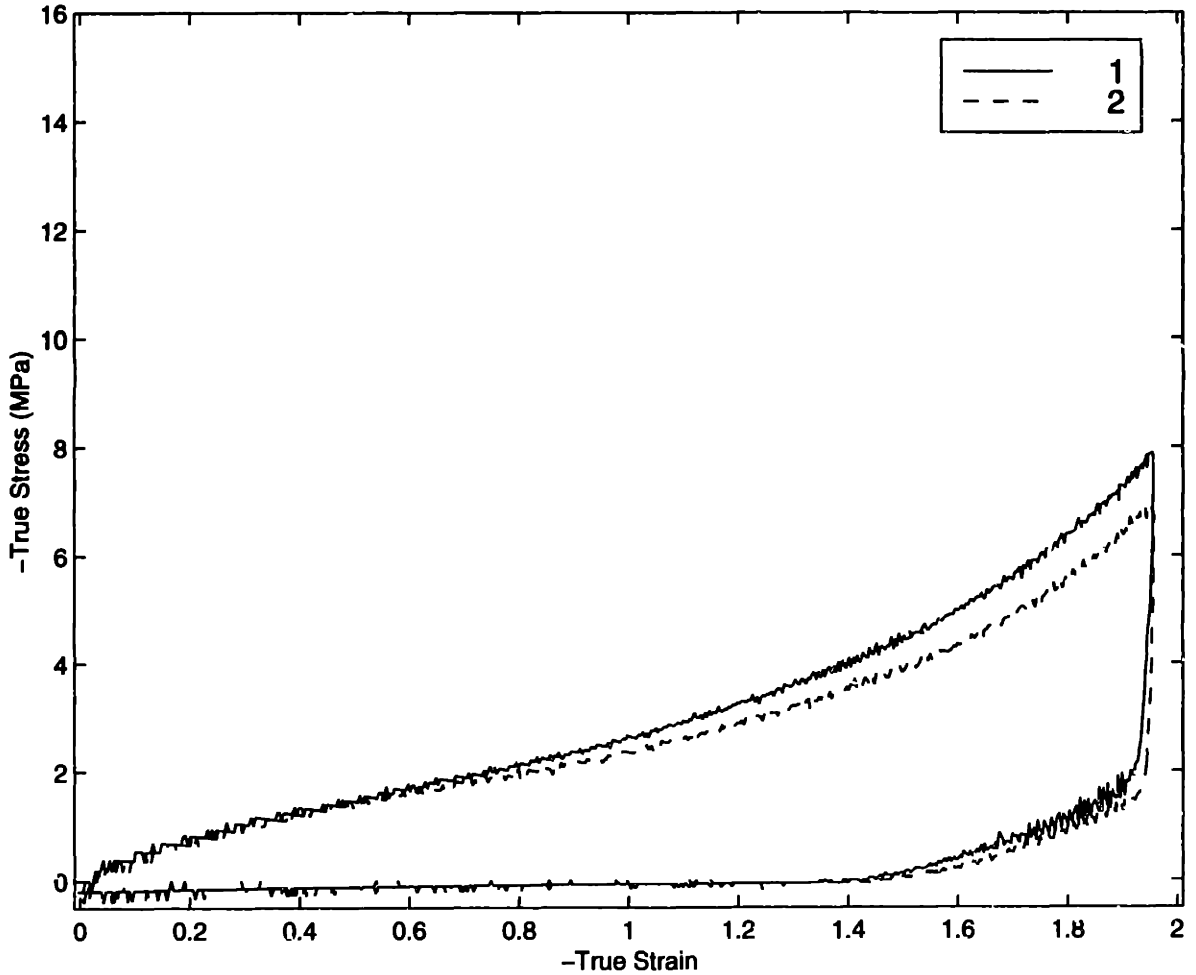

Figure B.34: Uniaxial Compression Tests, $105°C$, $\dot{\varepsilon} = -0.1/s$

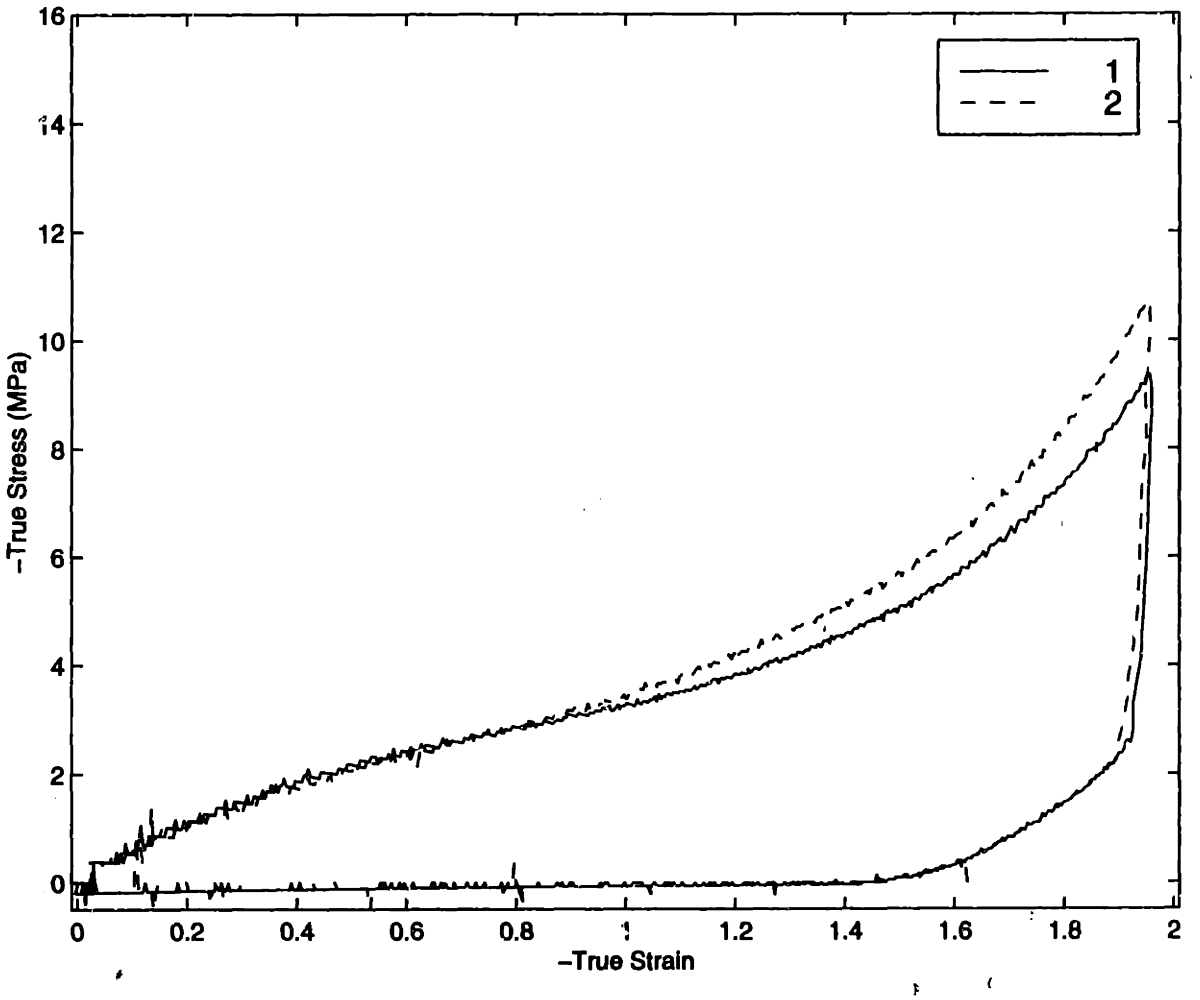

Figure B.35: Uniaxial Compression Tests, $105°C$, $\dot{\epsilon} = -0.5/s$

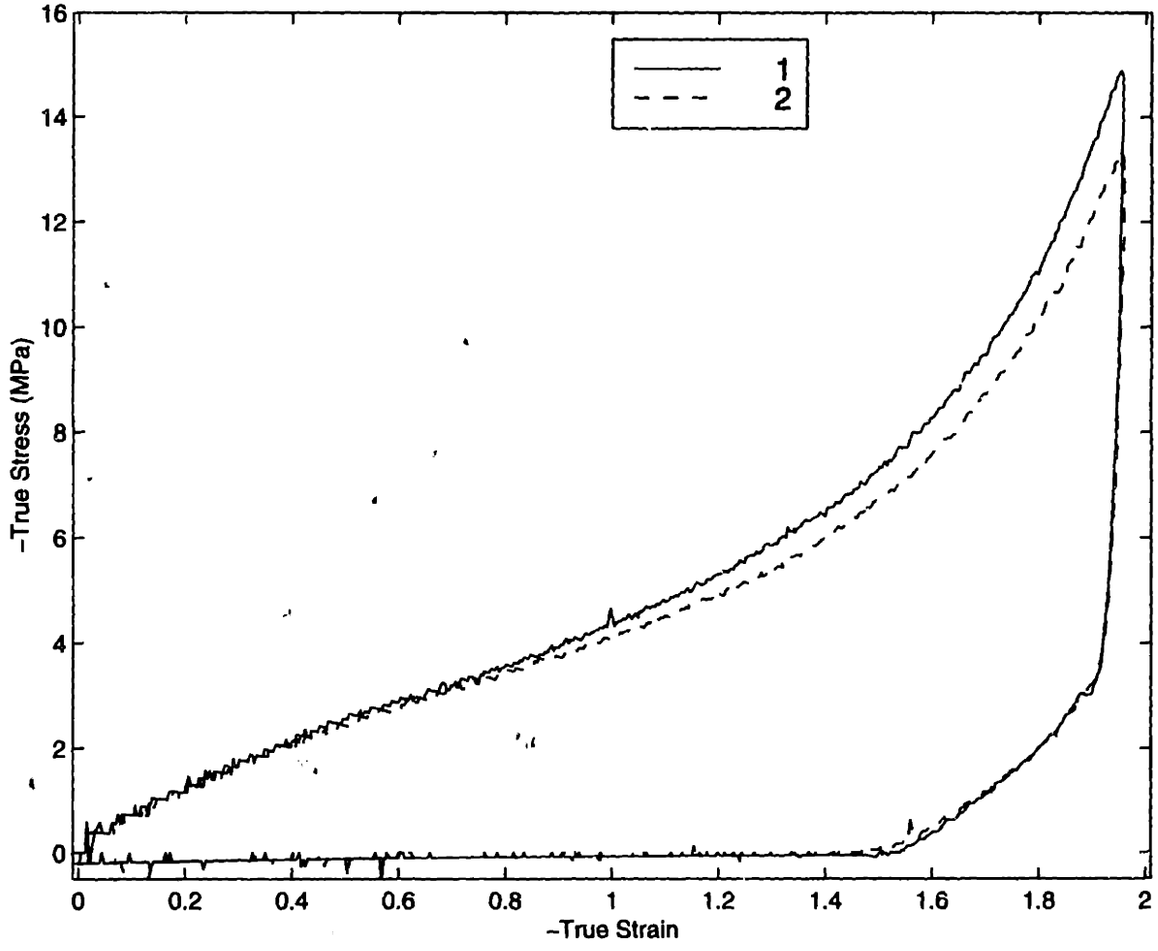

Figure B.36: Uniaxial Compression Tests, $105°C$, $\dot{\varepsilon} = -1.0/s$

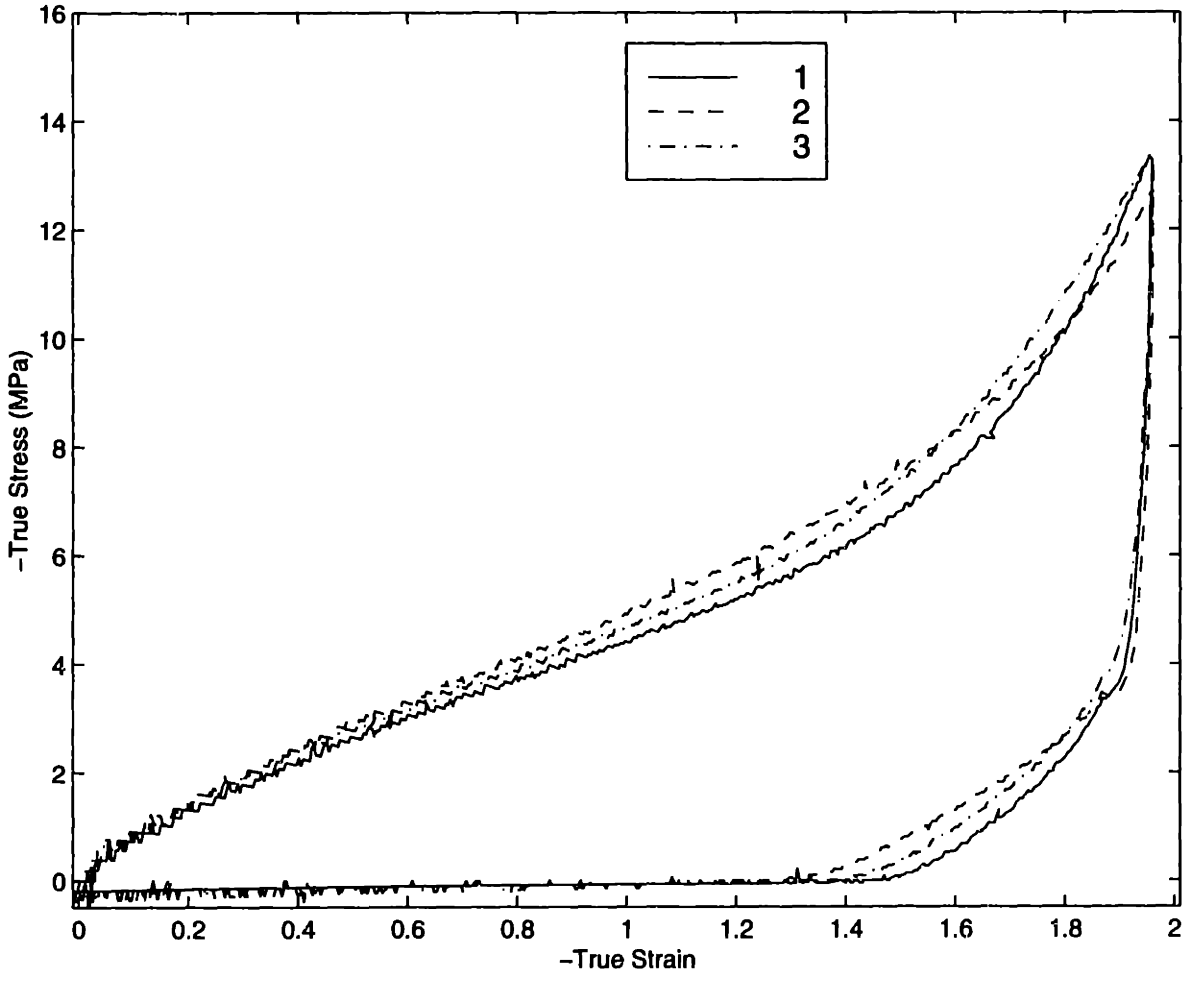

Figure B.37: Uniaxial Compression Tests, $105°C$, $\dot{\epsilon} = -1.5/s$

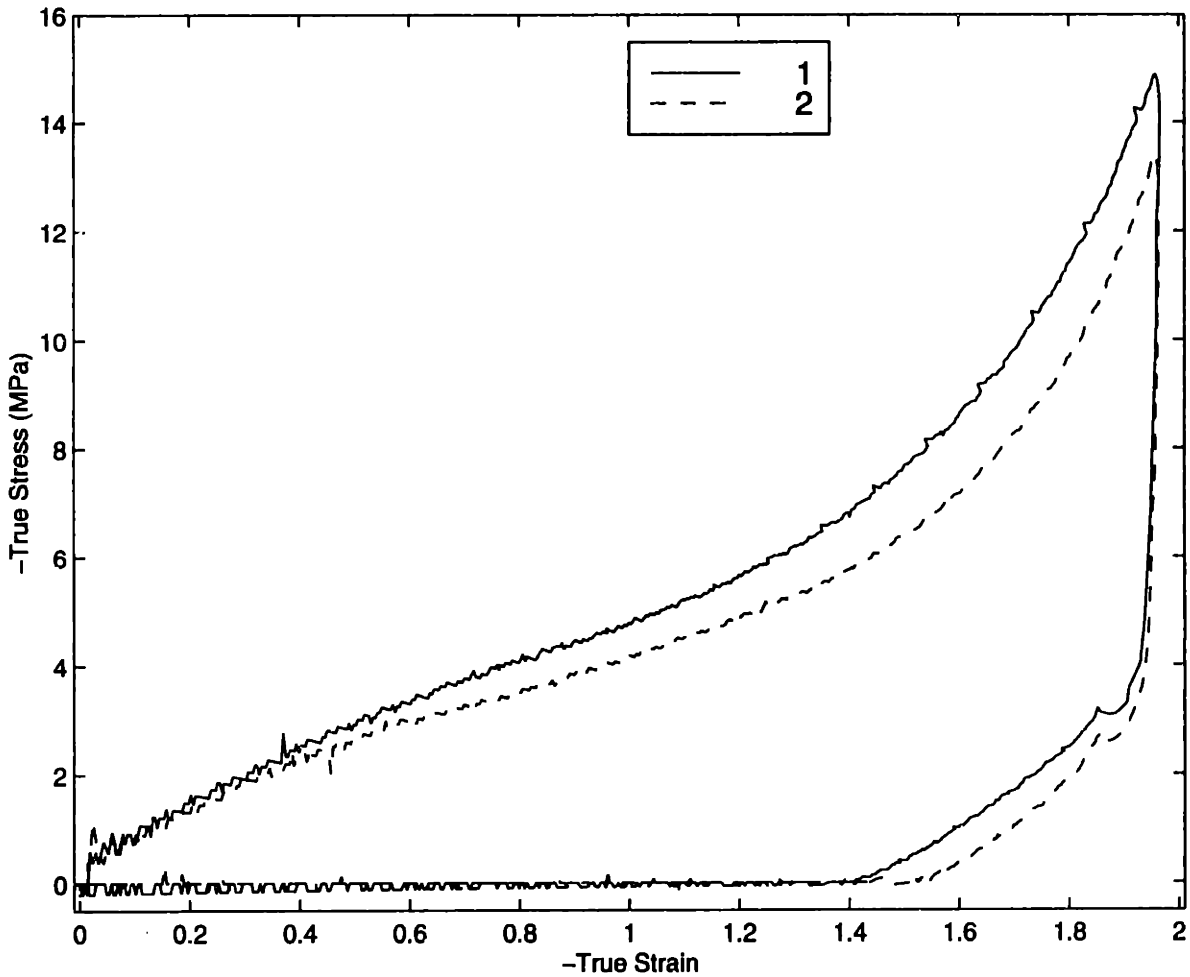

Figure B.38: Uniaxial Compression Tests, $105°C$, $\dot{\varepsilon} = -2.0/s$

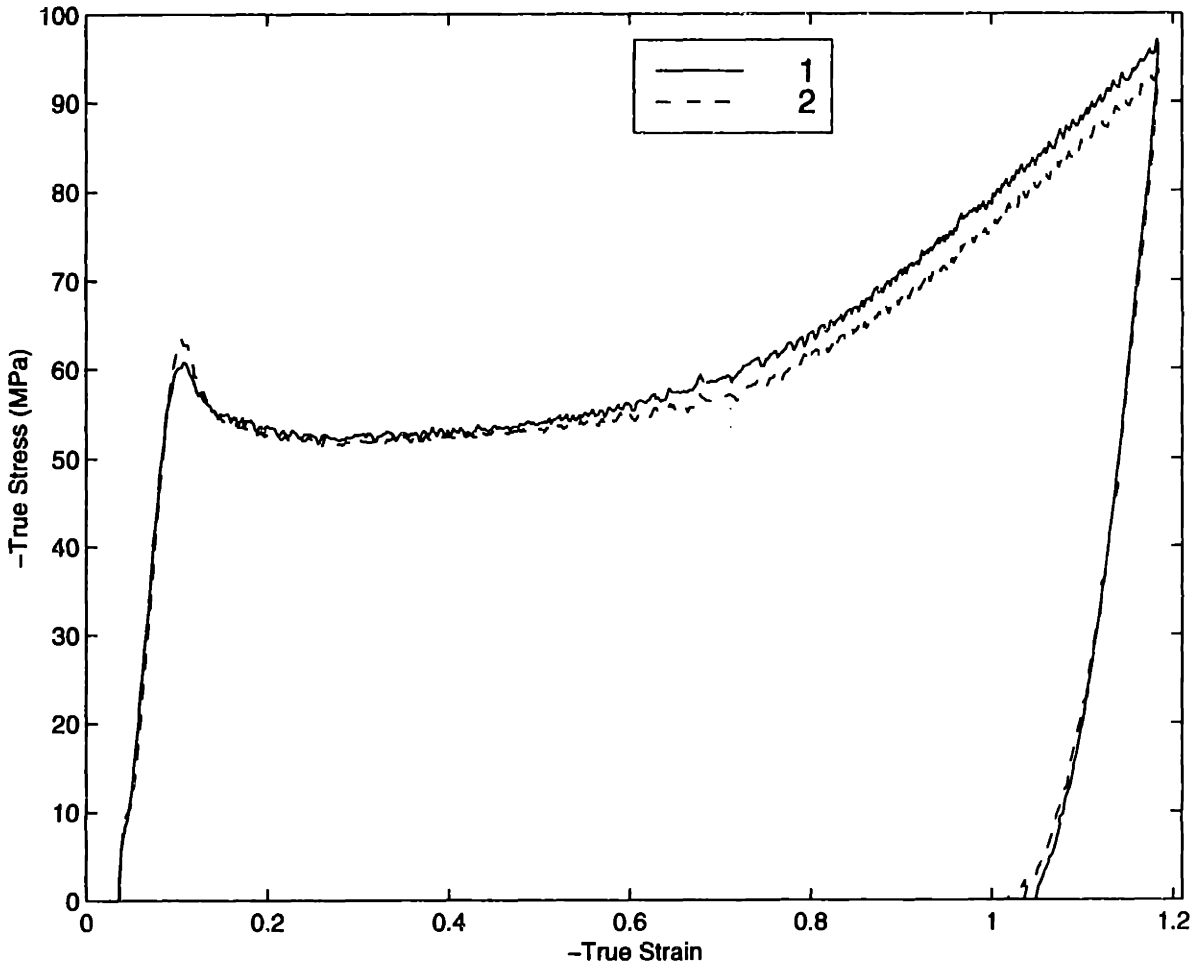

Figure B.39: Plane Strain Compression Tests, $25°C$, $\dot{\varepsilon} = -0.005/s$

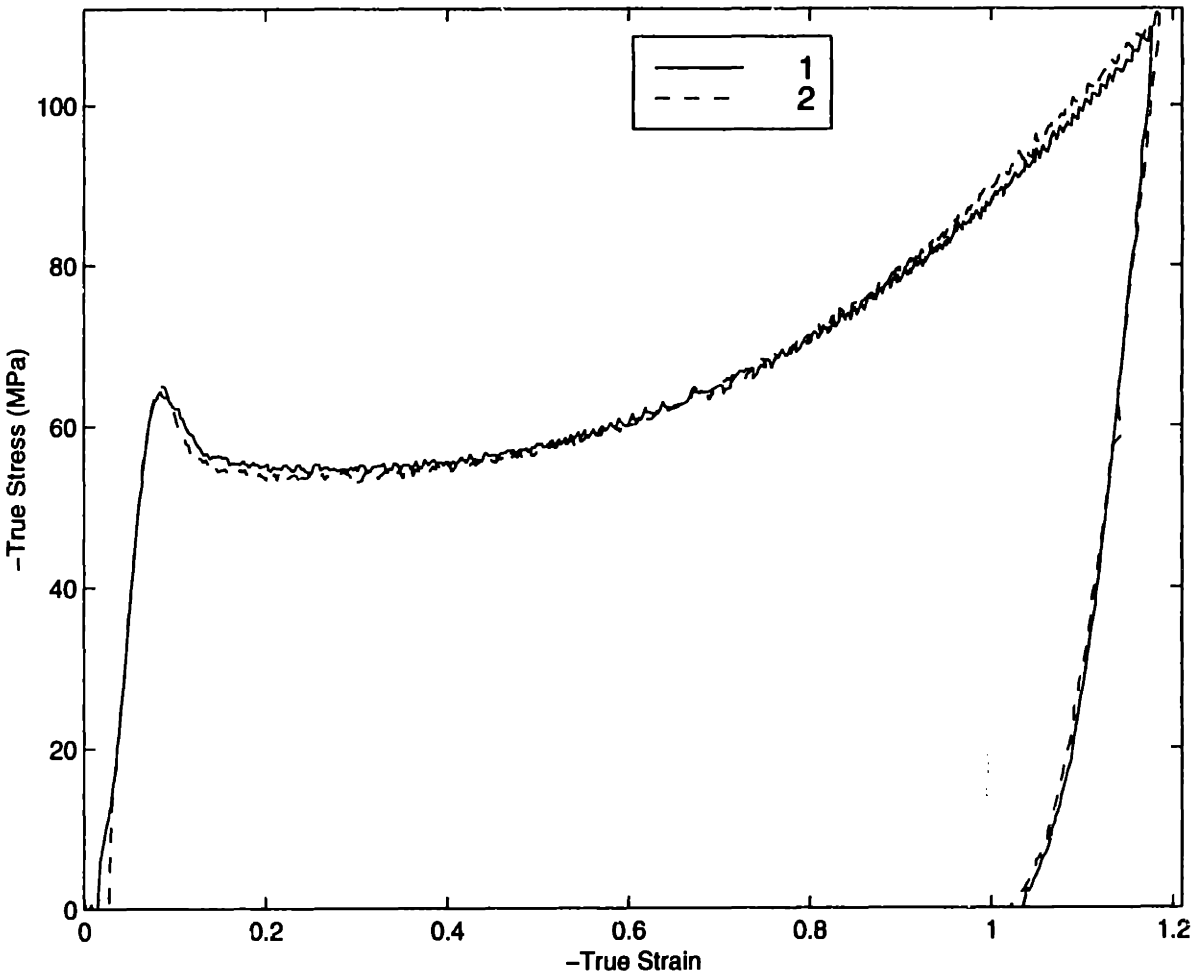

Figure B.40: Plane Strain Compression Tests, $25°C$, $\dot{\epsilon} = -0.01/s$

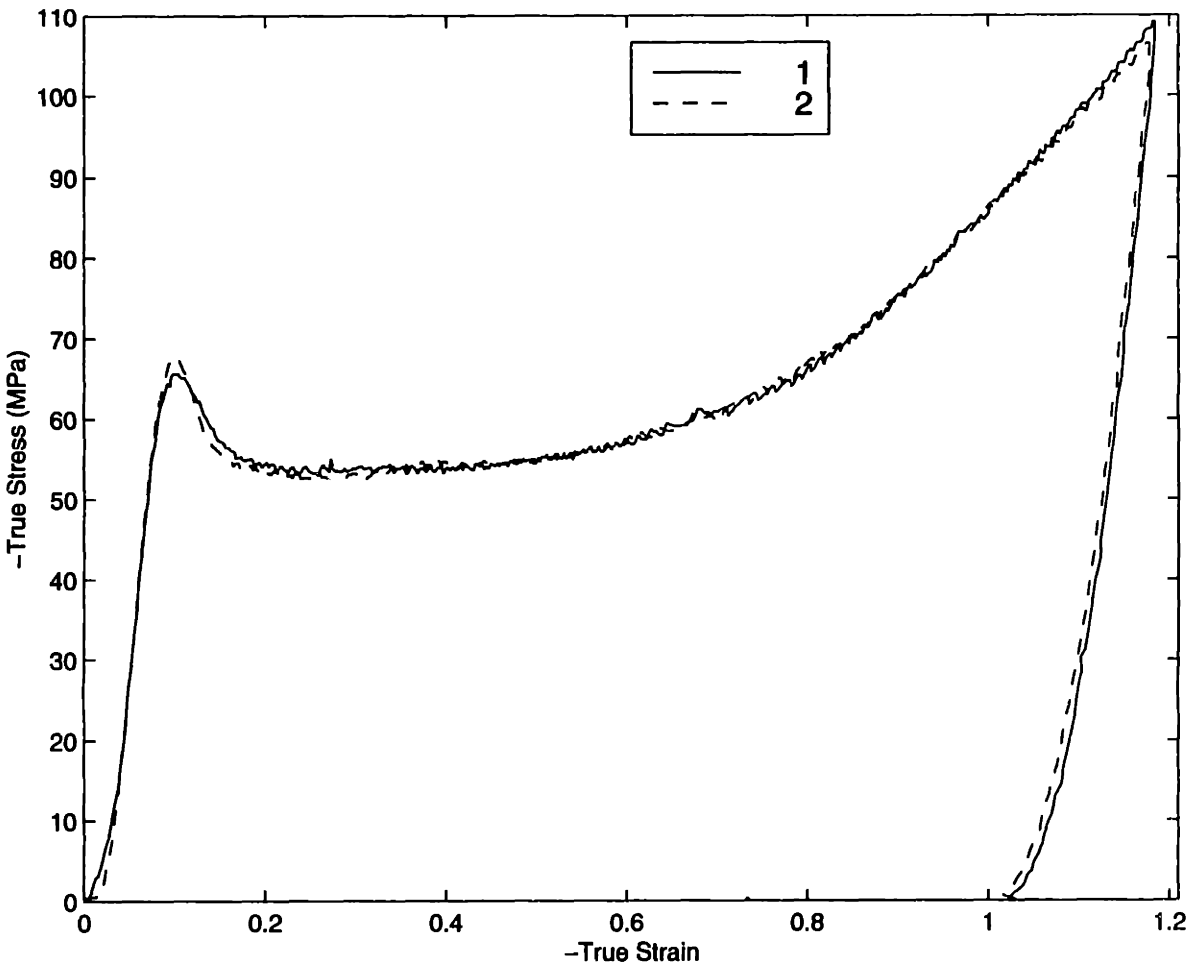

Figure B.41: Plane Strain Compression Tests, $25°C$, $\dot{\varepsilon} = -0.05/s$

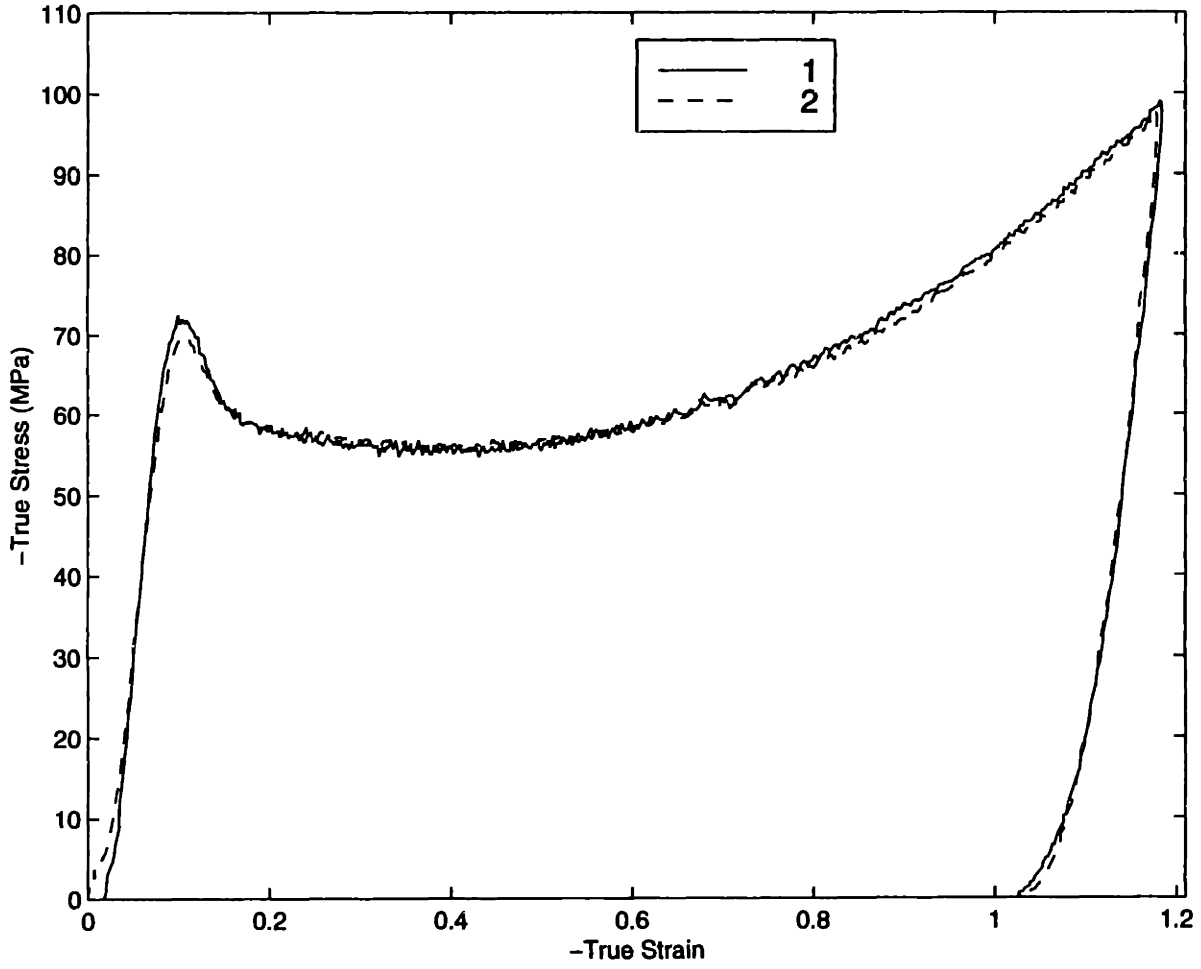

Figure B.42: Plane Strain Compression Tests, $25°C$, $\dot{\varepsilon} = -0.1/s$

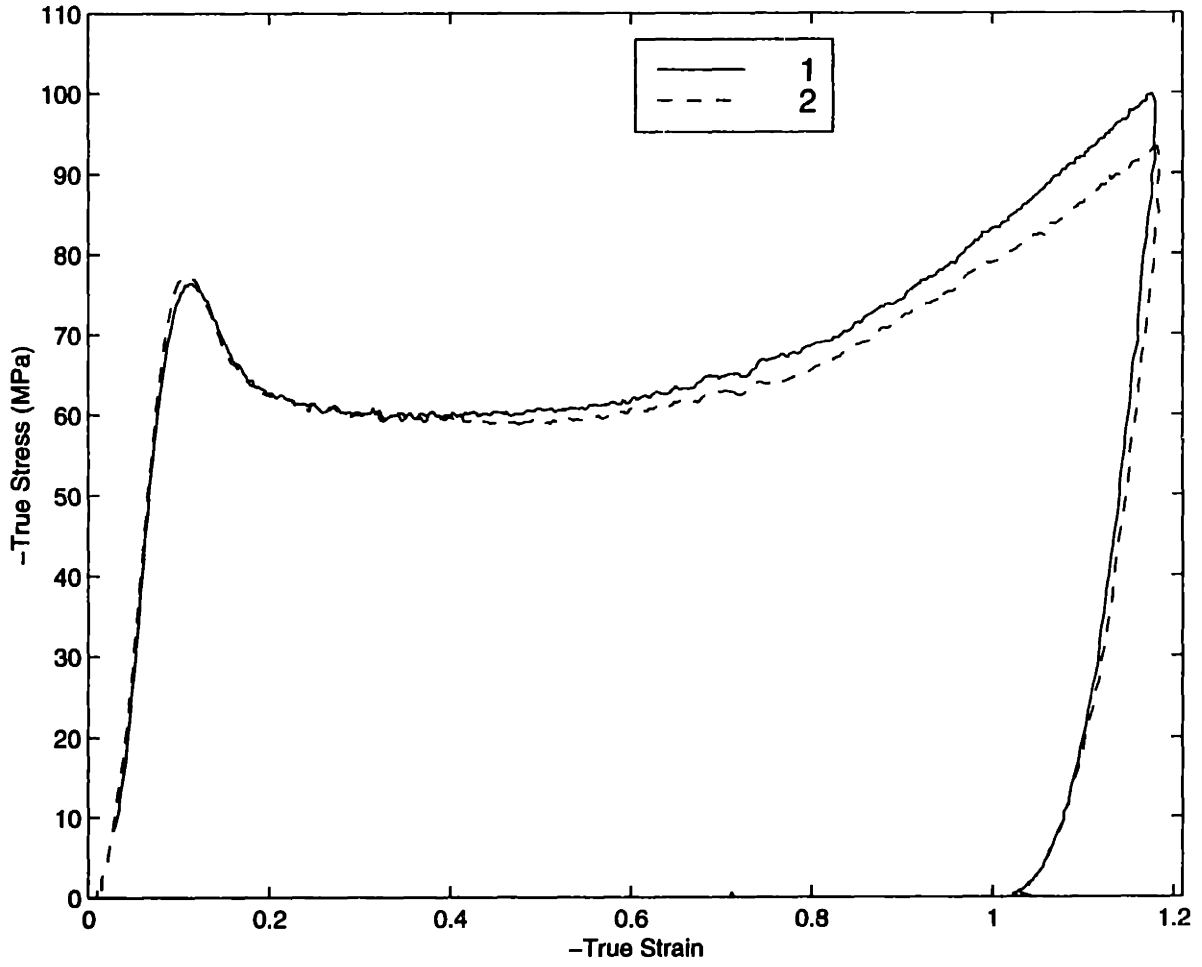

Figure B.43: Plane Strain Compression Tests, $25°C$, $\dot{\epsilon} = -0.5/s$

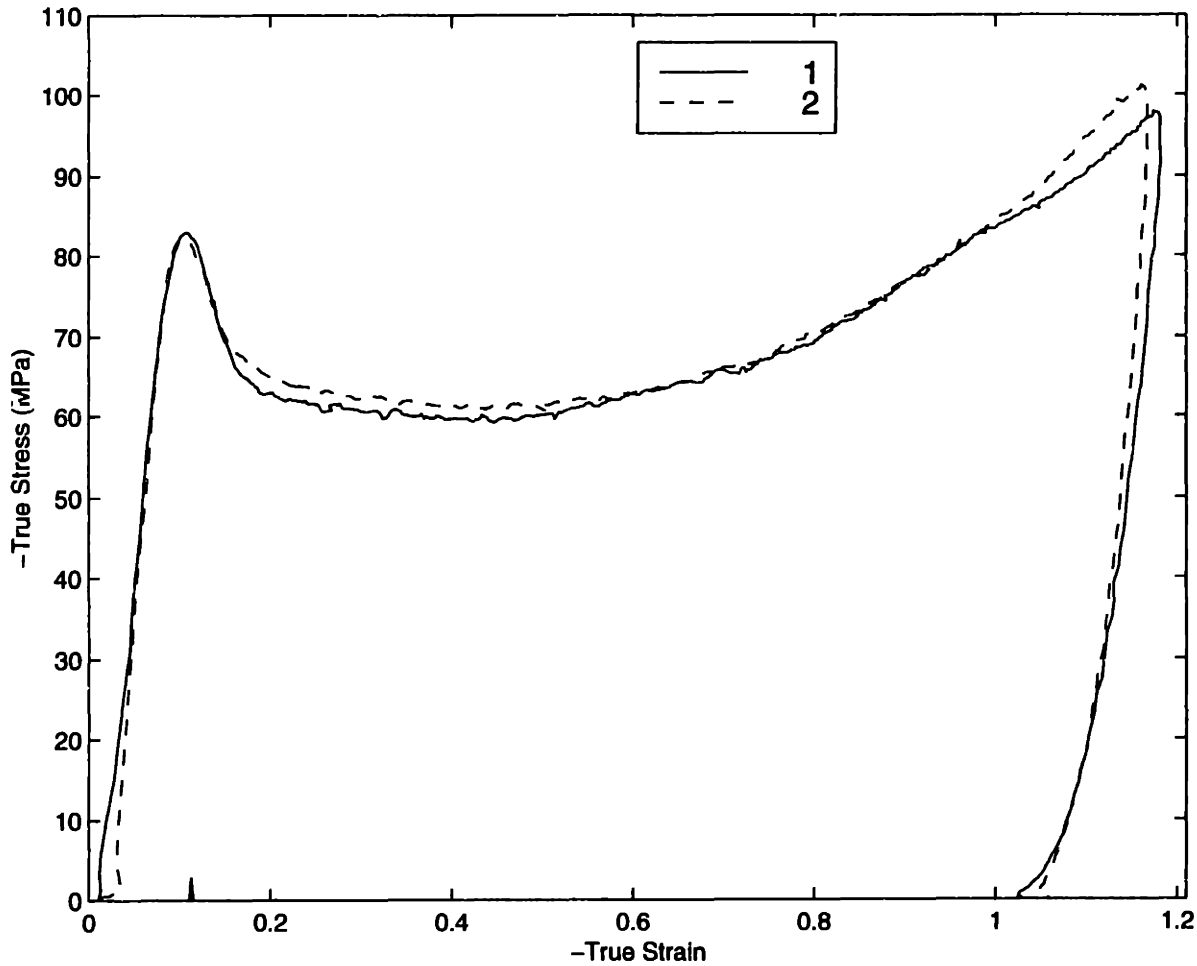

Figure B.44: Plane Strain Compression Tests, $25°C$, $\dot{\epsilon} = -1.0/s$

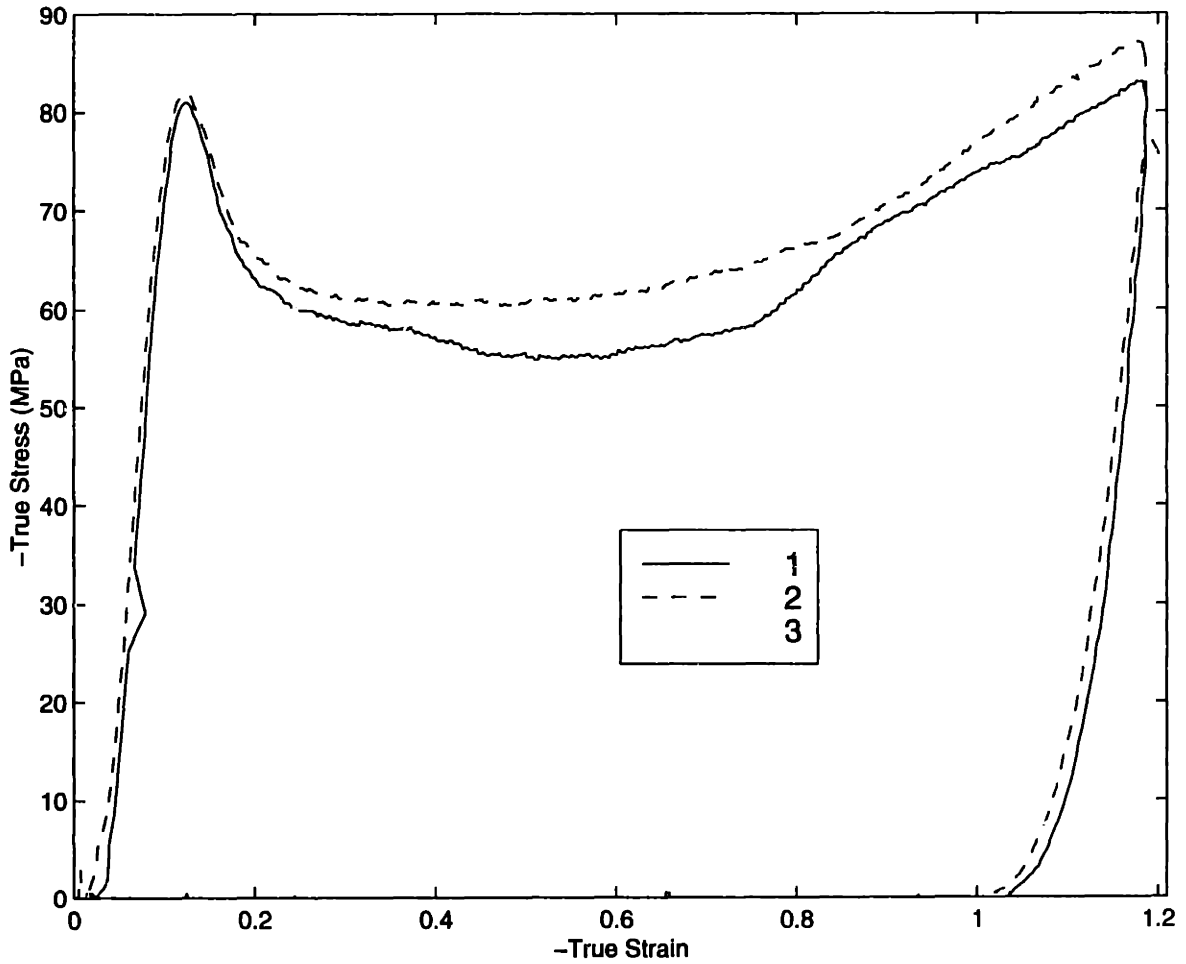

Figure B.45: Plane Strain Compression Tests, $25°C$, $\dot{\varepsilon} = -1.5/s$

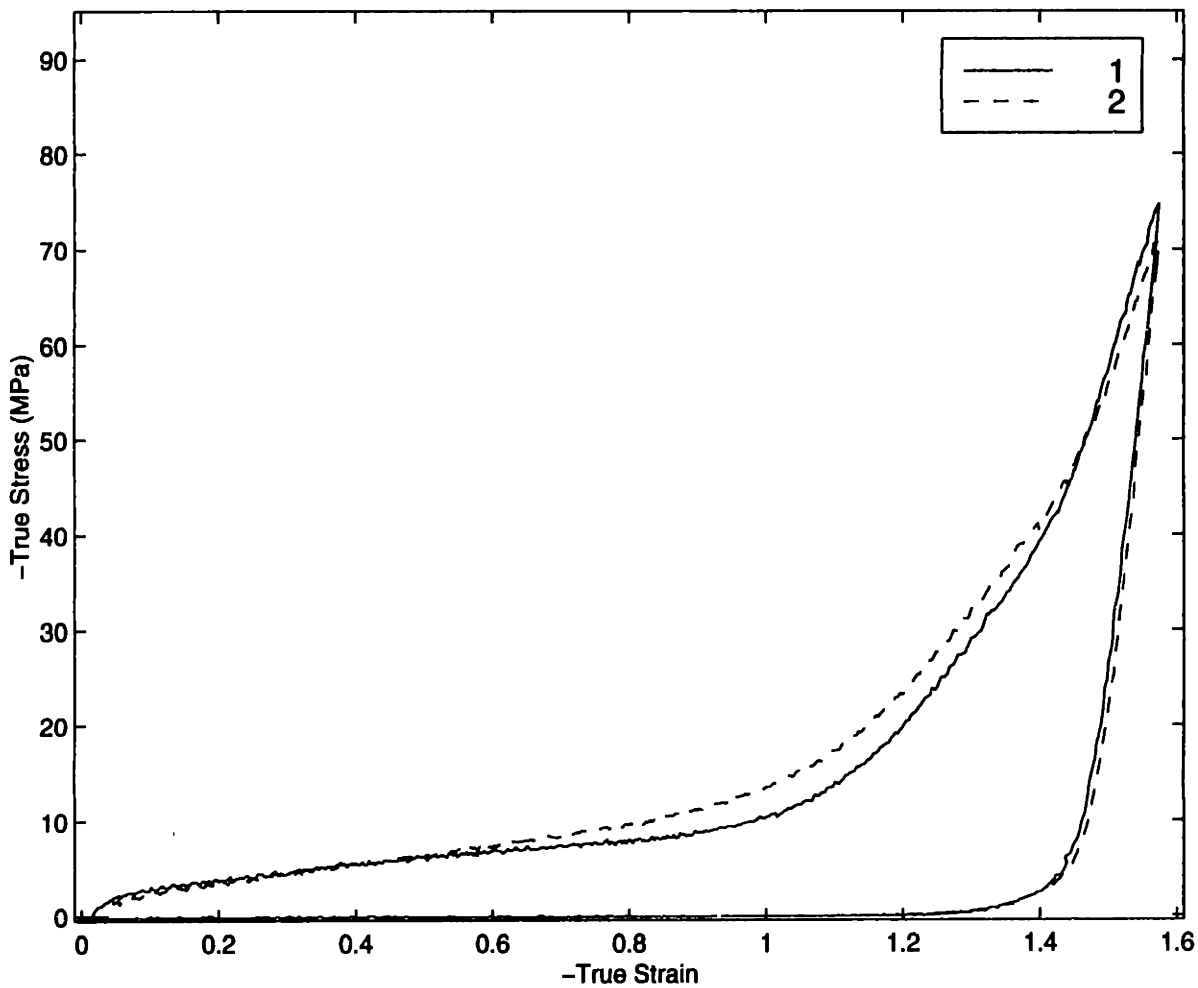

Figure B.46: Plane Strain Compression Tests, $80°C$, $\dot{\varepsilon} = -0.01/s$

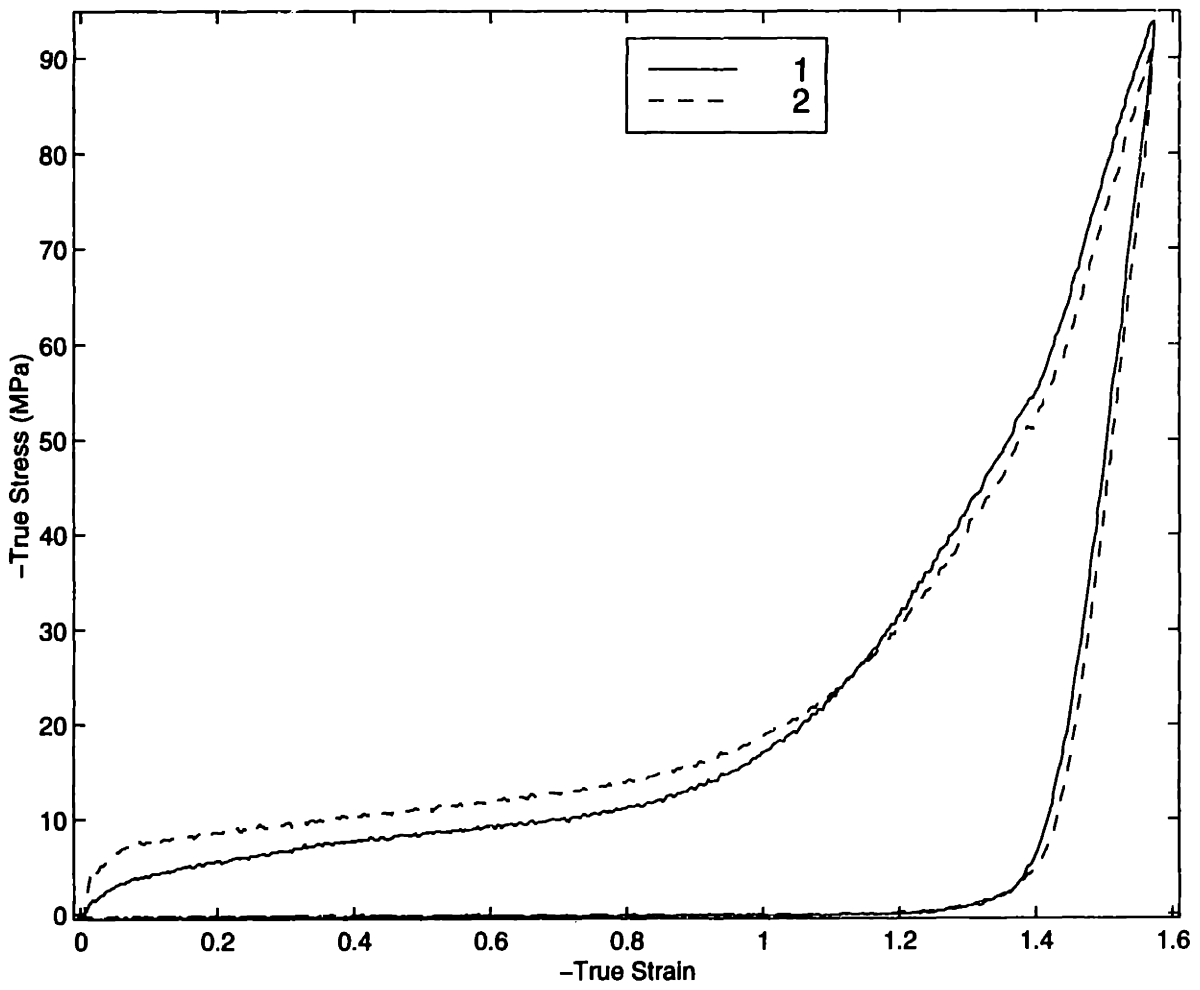

Figure B.47: Plane Strain Compression Tests, $80°C$, $\dot{\varepsilon} = -0.1/s$

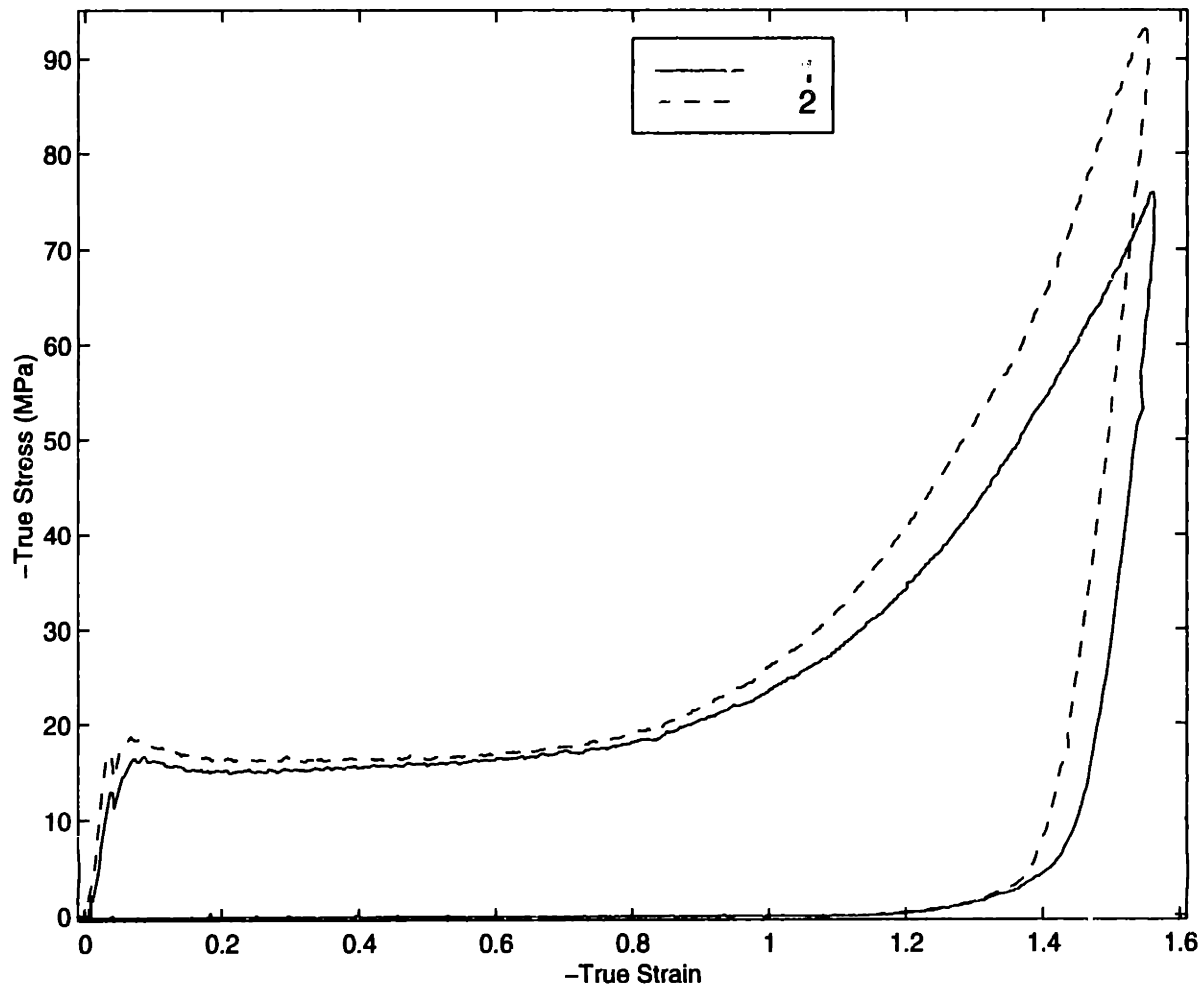

Figure B.48: Plane Strain Compression Tests, $80°C$, $\dot{\epsilon} = -1.0/s$

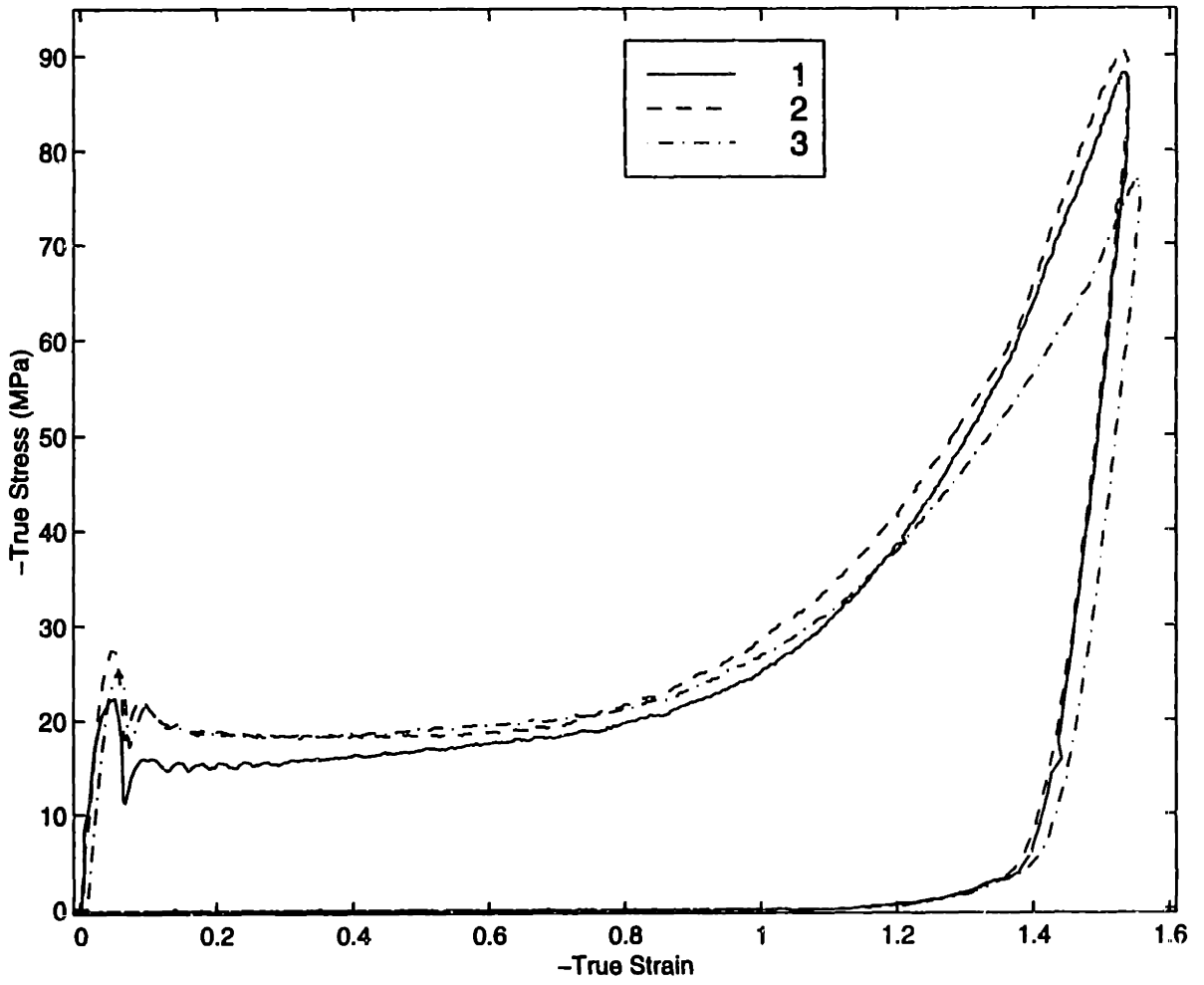

Figure B.49: Plane Strain Compression Tests, $80°C$, $\dot{\epsilon} = -2.0/s$

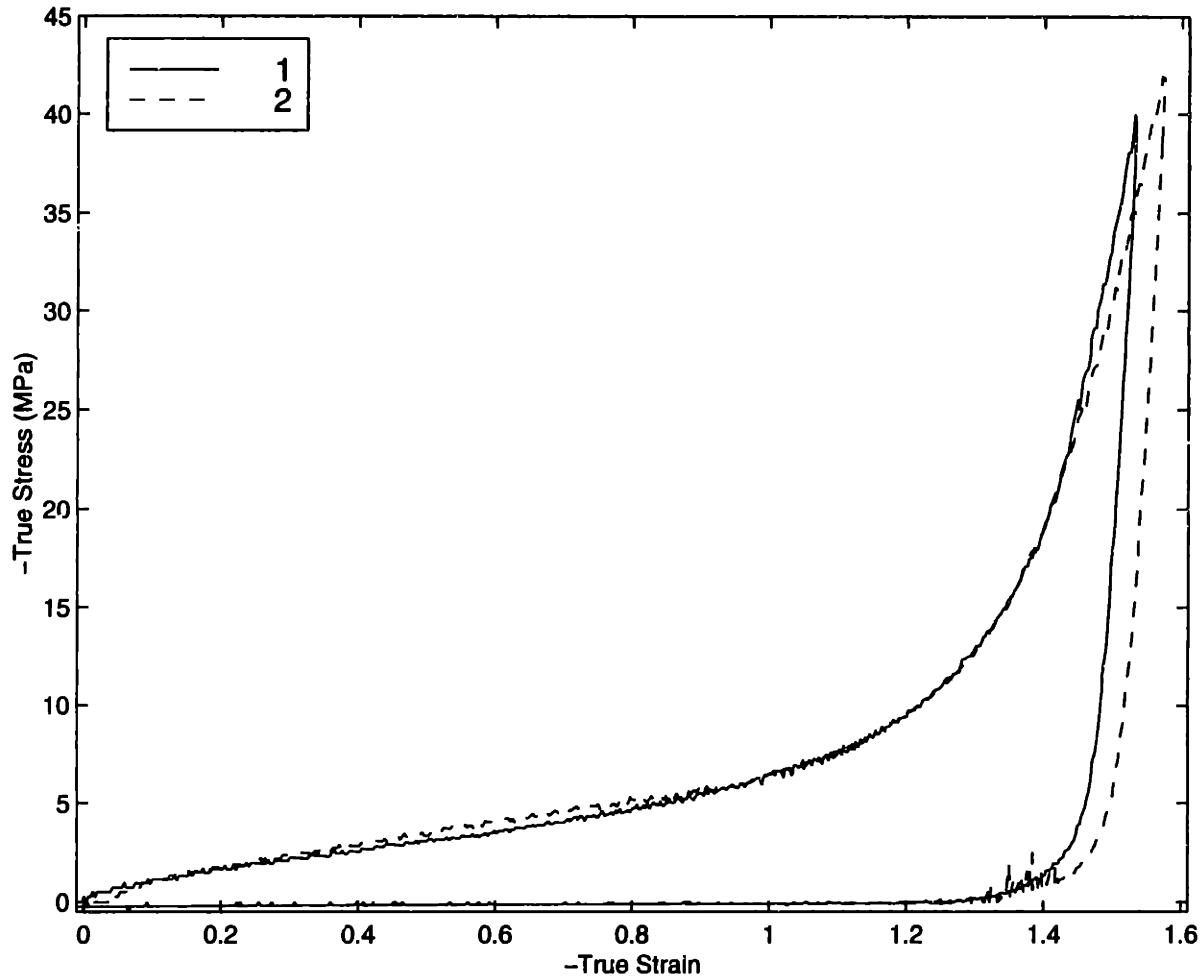

Figure B.50: Plane Strain Compression Tests, $90°C$, $\dot{\varepsilon} = -0.01/s$

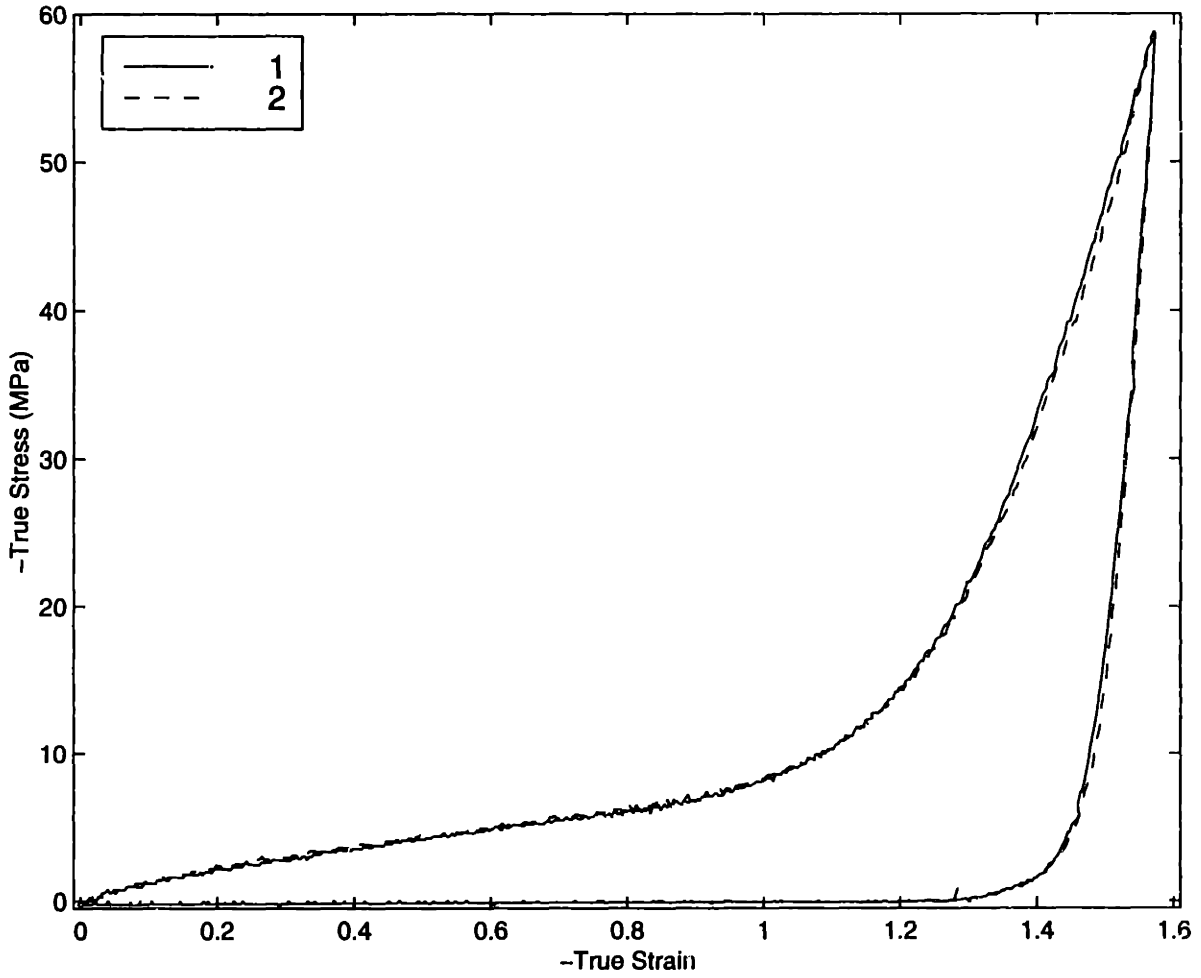

Figure B.51: Plane Strain Compression Tests, $90°C$, $\dot{\epsilon} = -0.1/s$

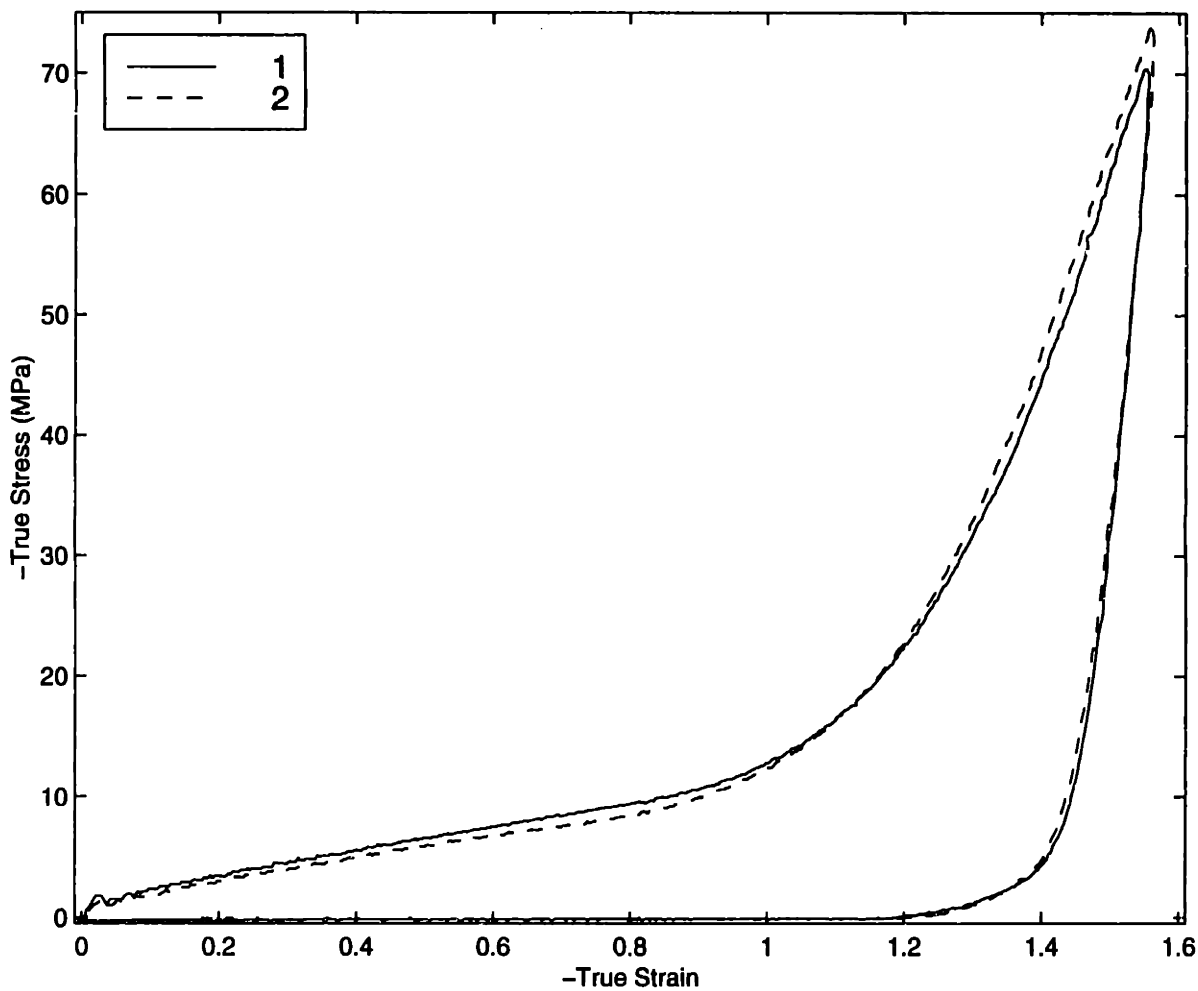

Figure B.52: Plane Strain Compression Tests, $90°C$, $\dot{\varepsilon} = -1.0/s$

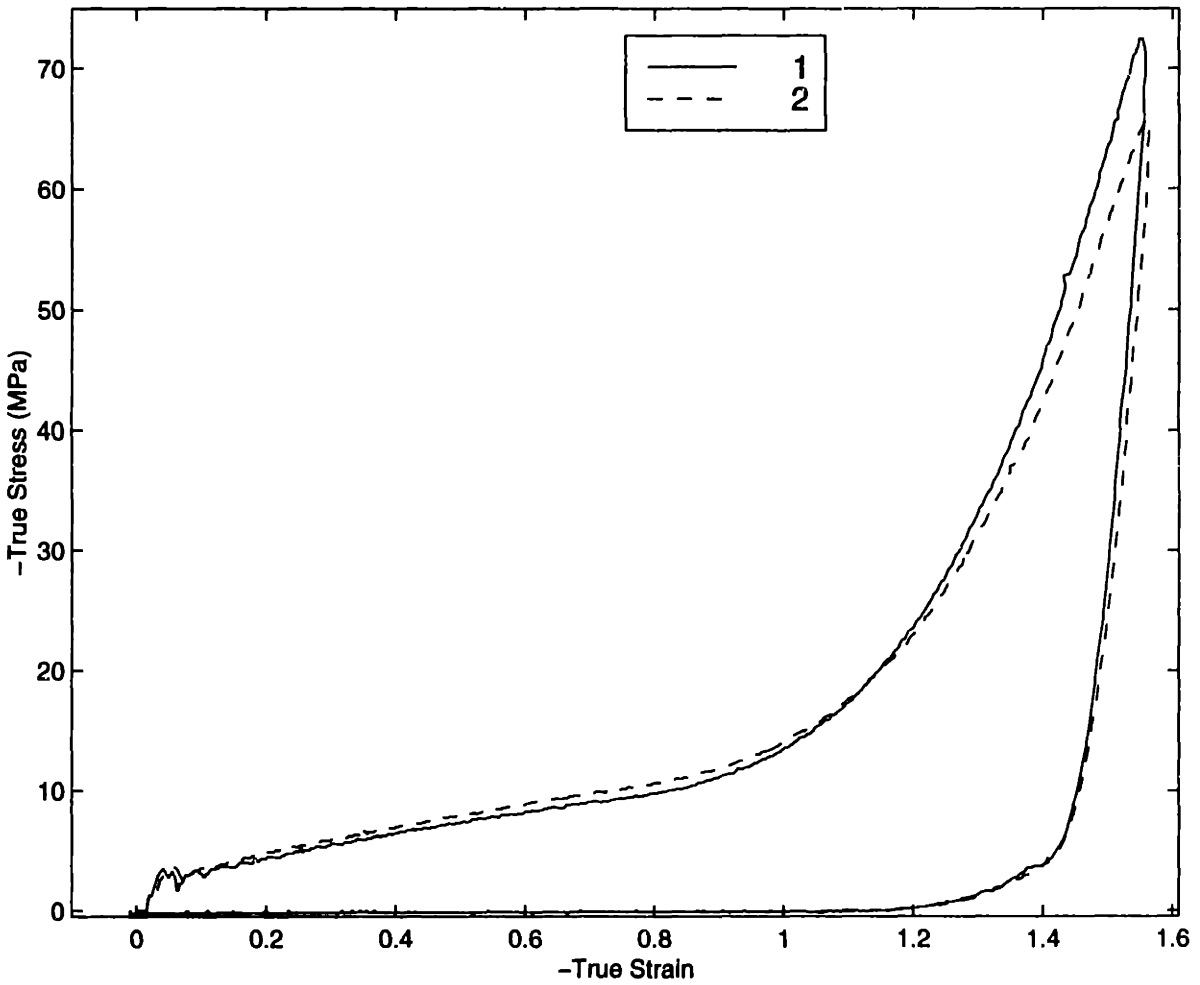

Figure B.53: Plane Strain Compression Tests, $90°C$, $\dot{\varepsilon} = -2.0/s$

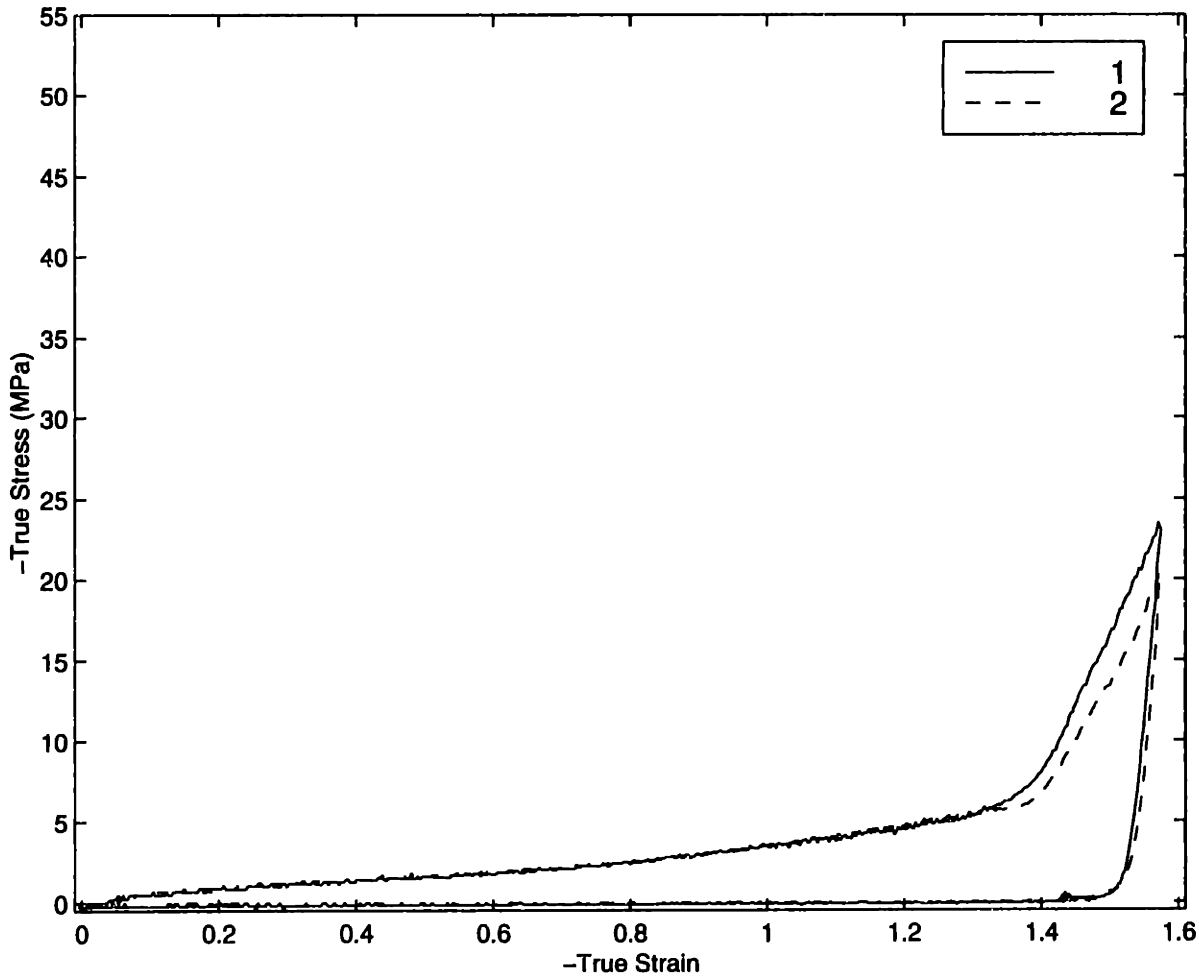

Figure B.54: Plane Strain Compression Tests, $100°C$, $\dot{\epsilon} = -0.01/s$

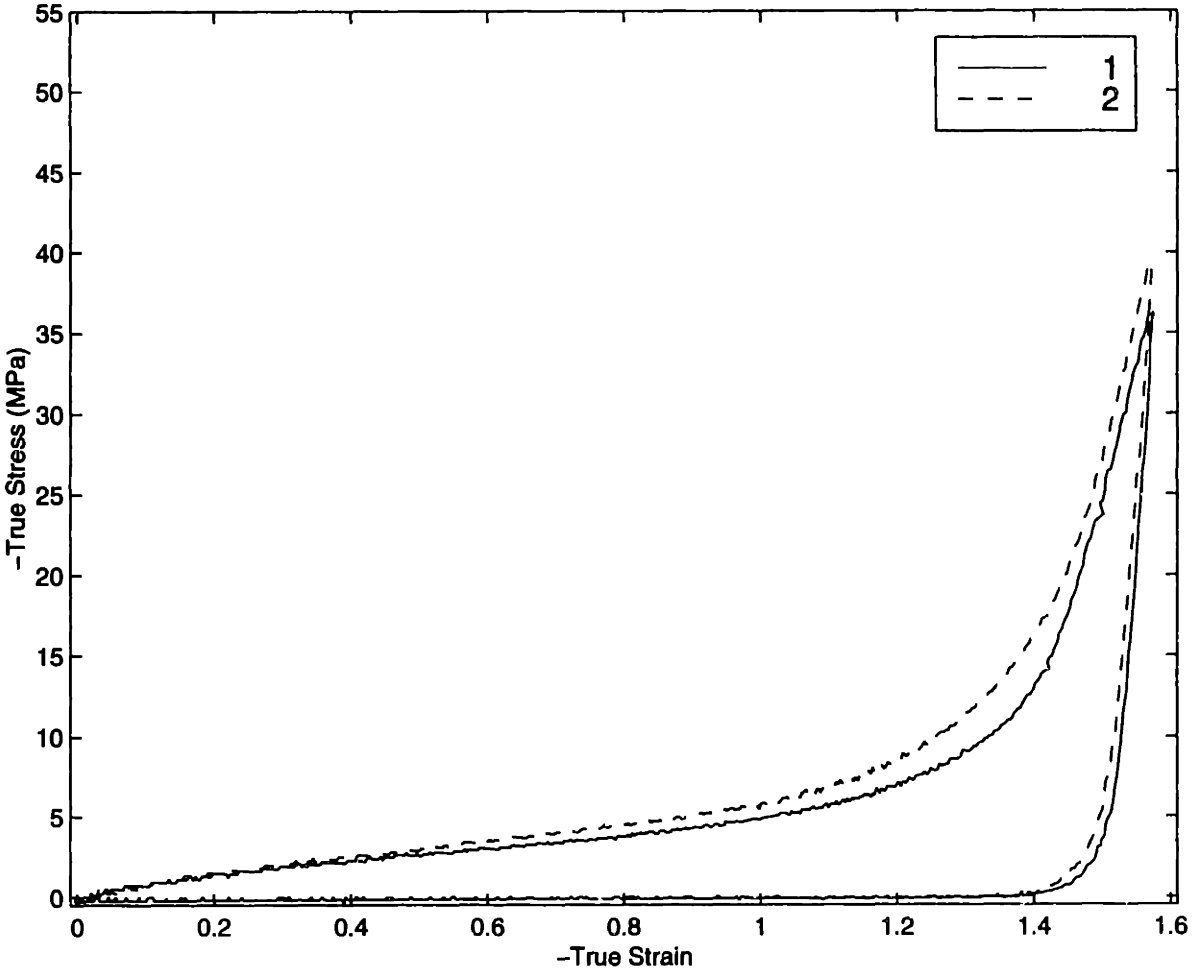

Figure B.55: Plane Strain Compression Tests, $100°C$, $\dot{\varepsilon} = -0.1/s$

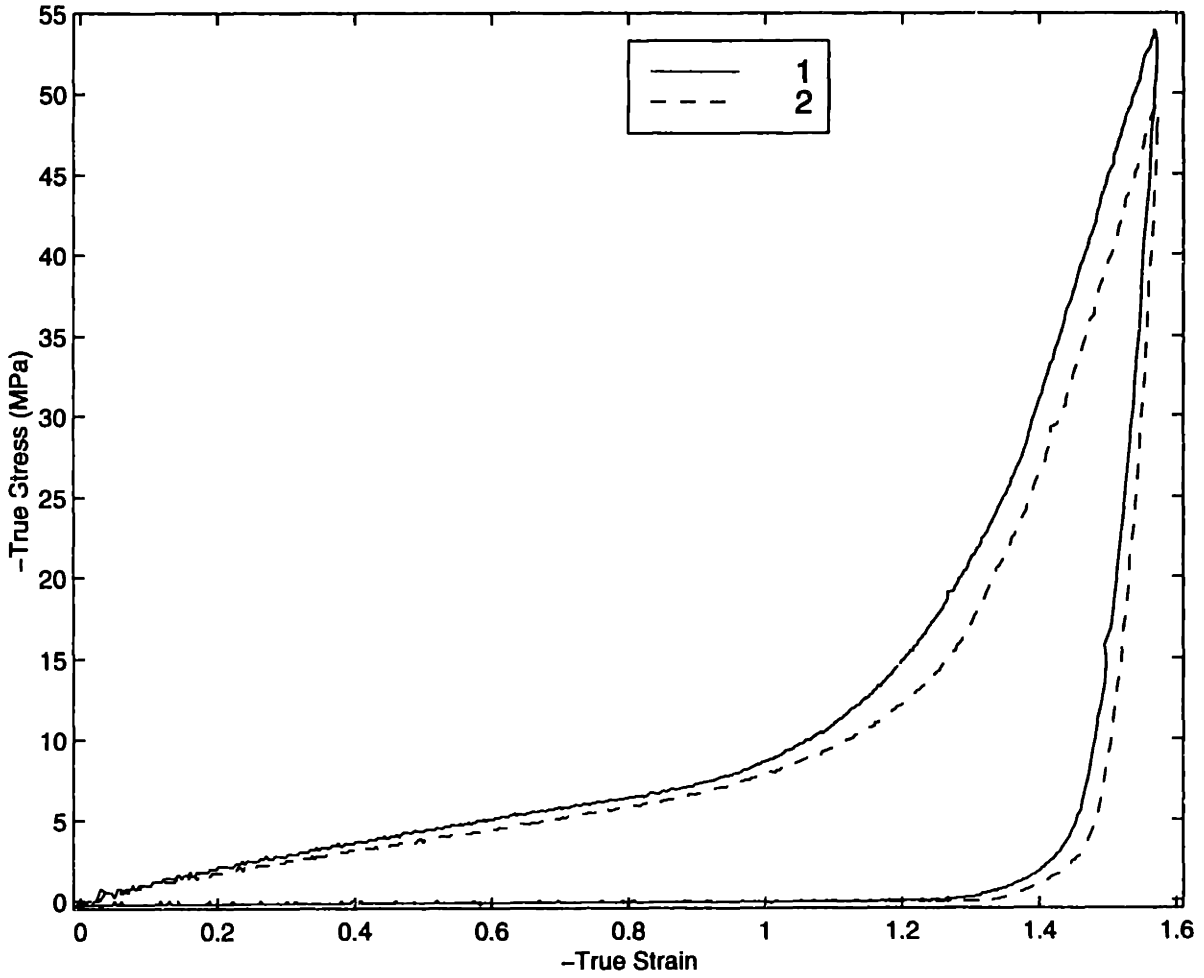

Figure B.56: Plane Strain Compression Tests, $100°C$, $\dot{\varepsilon} = -1.0/s$

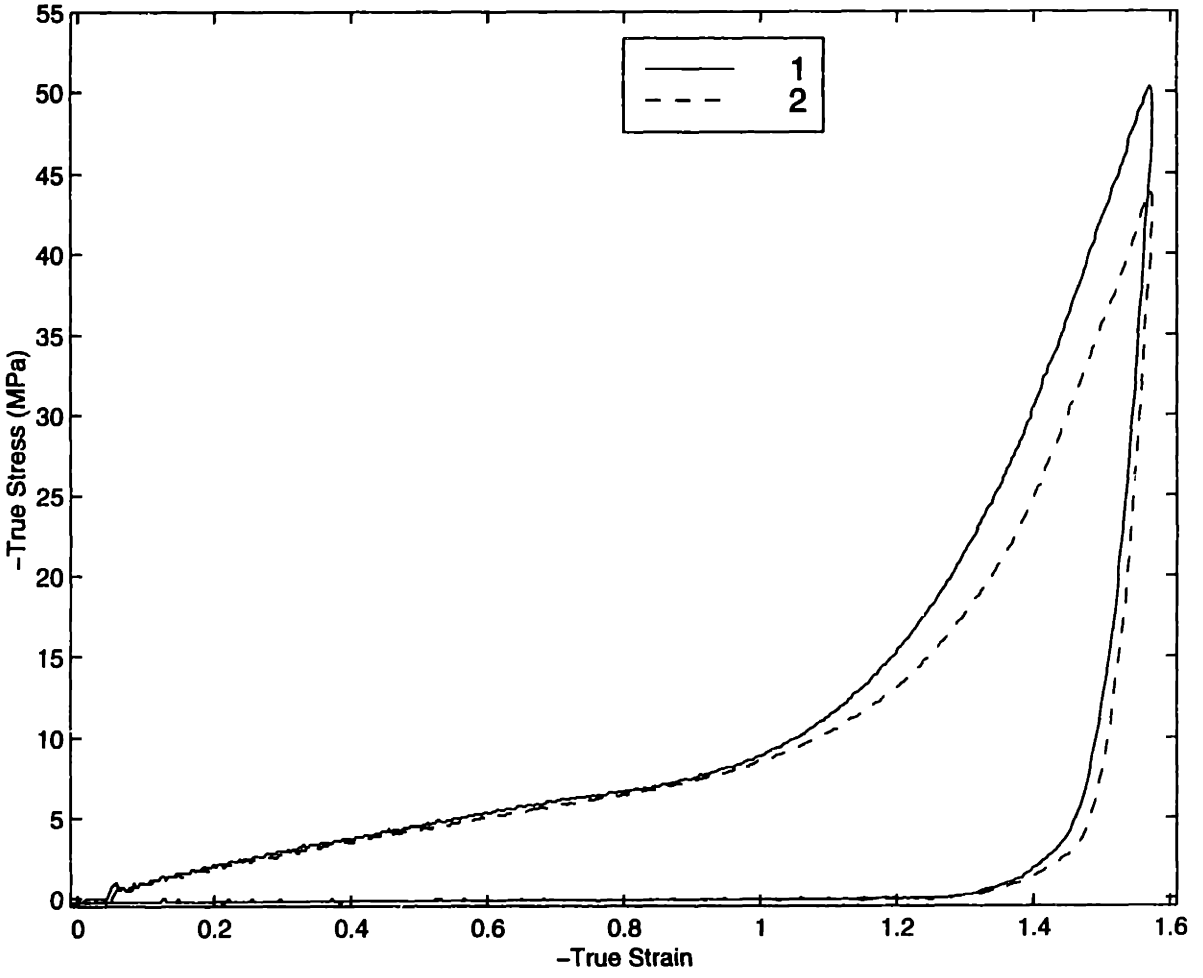

Figure B.57: Plane Strain Compression Tests, $100°C$, $\dot{\varepsilon} = -2.0/s$

Appendix C

WAXD Data

This appendix contains all of the WAXD scans performed on the specimens. The figures show WAXD scans conducted in three different directions. For the uniaxial compression specimens, the scans were conducted in: (1) the through direction (TD), which was in the direction of the load, (2) the edge direction (ED1), which was in the direction of the flow, and (3) the second edge direction (ED2), which was also in the direction of the flow, but 90° from the direction of ED1. In the WAXD scans for the specimens deformed in uniaxial compression, it can be seen that the scans for ED1 and ED2 are identical in shape although different in absolute intensity. This is as expected since the specimens are deformed in uniaxial compression and therefore the structure in all directions perpendicular to the load direction should be the same, resulting in WAXD scans in these directions that are identical in shape. The reason that the absolute intensities are different is due to the slight difference in thickness of the specimen at the locations where the WAXD scans were taken as a result of the buckling of the specimens after unloading.

For the plane strain compression specimens, the scans were conducted in: (1) the constrained direction (CD), which was in the direction of the constrained dimension in the channel die, (2) the flow direction (FD), which was in the direction of the flow, and (3) the load direction (LD), which was in the direction of the load.

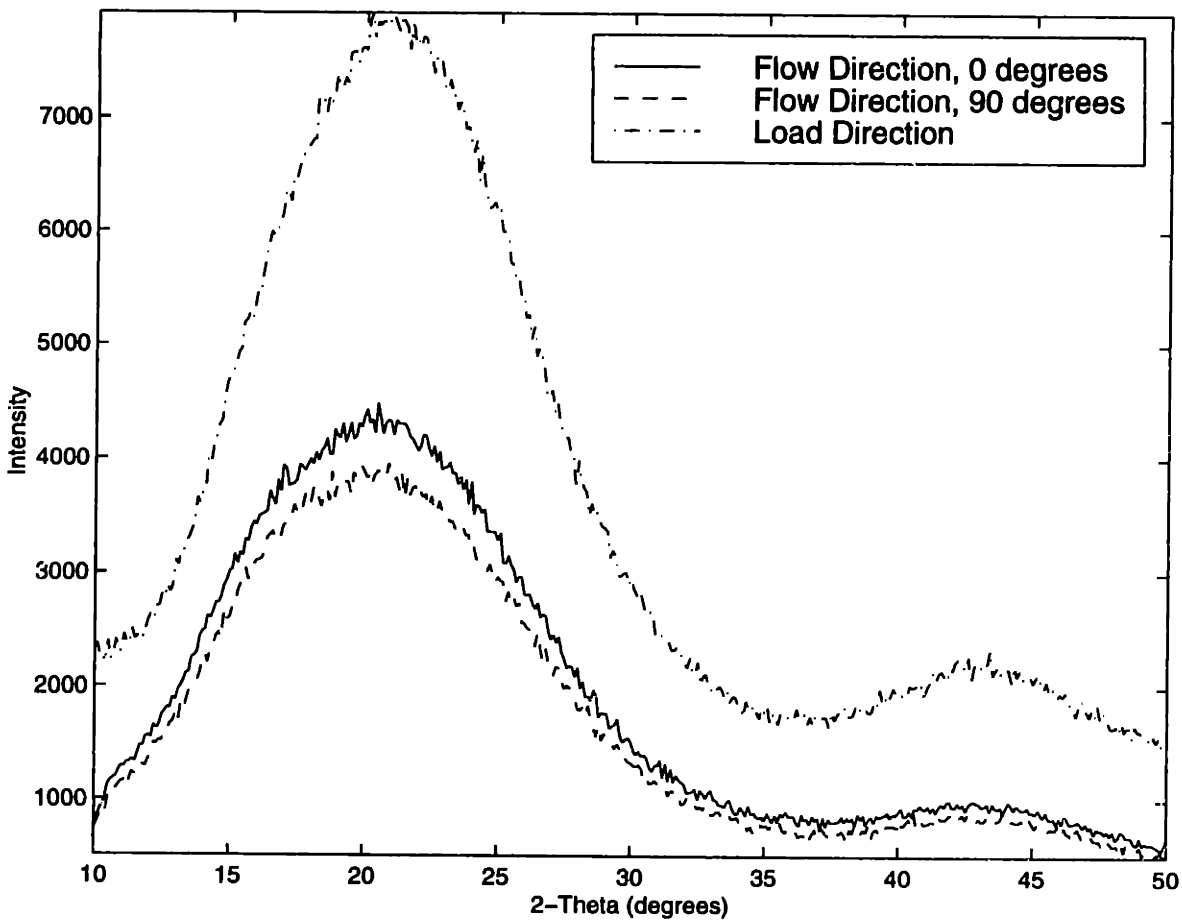

Figure C.1: WAXD scans on as-received material

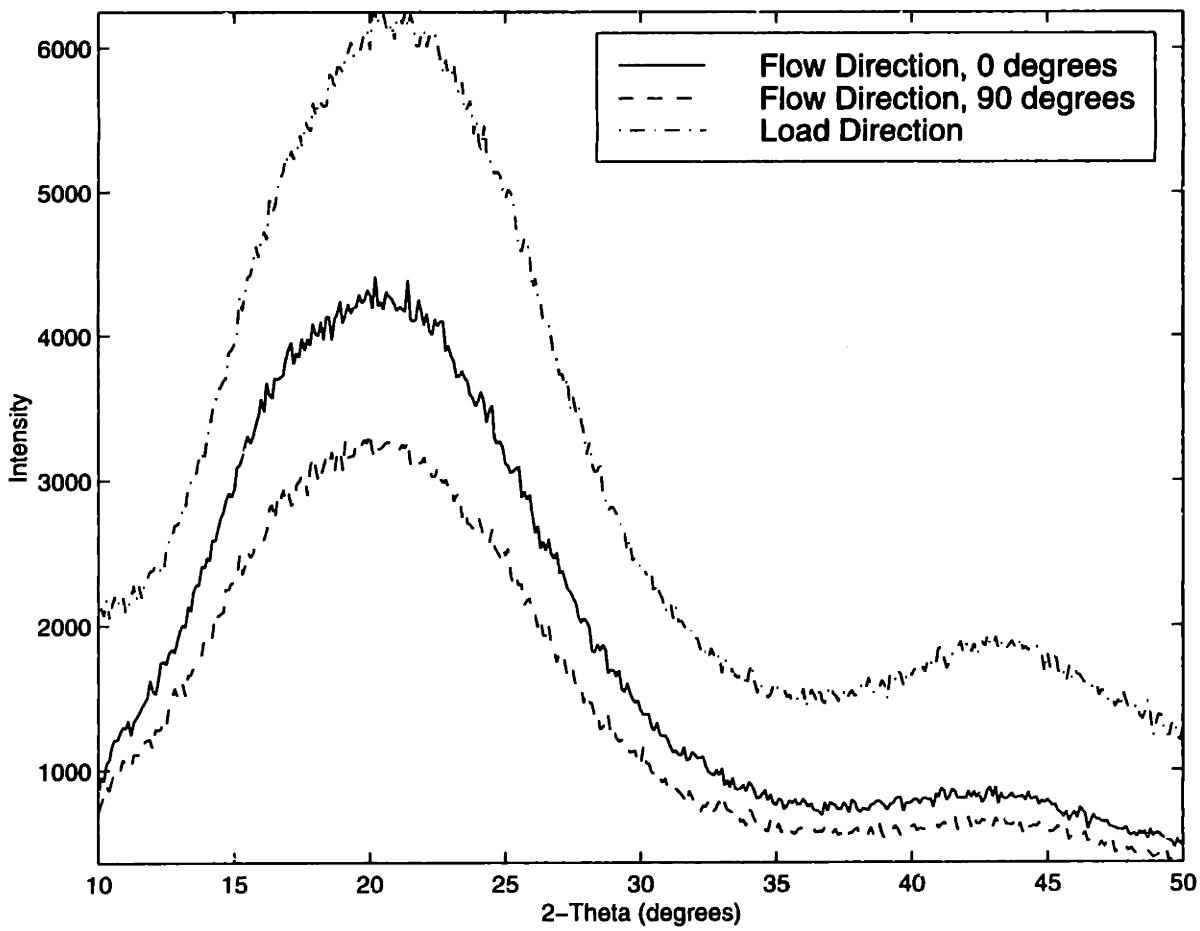

Figure C.2: WAXD scans of specimen deformed in uniaxial compression at $80°C$ to a final strain of -1.4 at a strain rate of $-0.01/s$

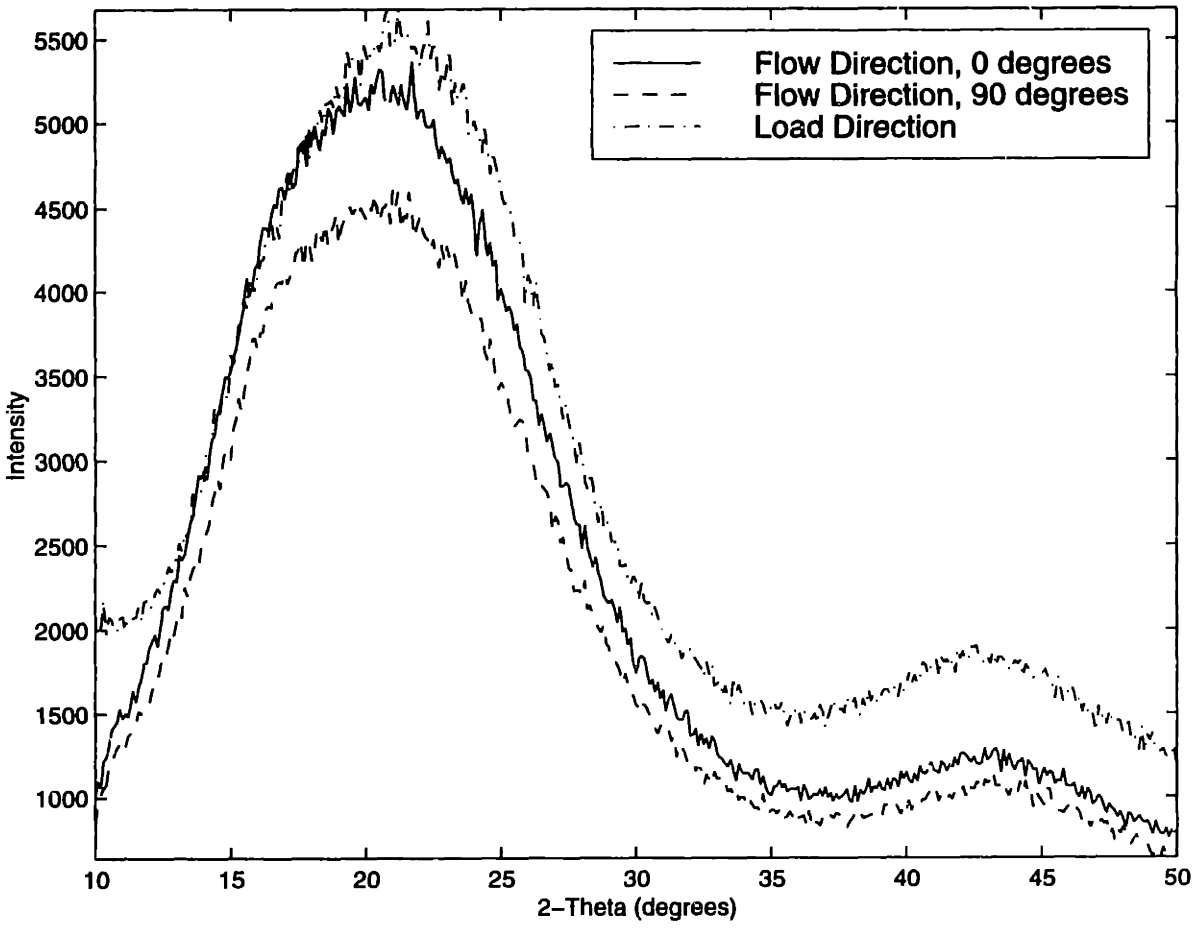

Figure C.3: WAXD scans of specimen deformed in uniaxial compression at $80°C$ to a final strain of -2.0 at a strain rate of -0.01/*s*

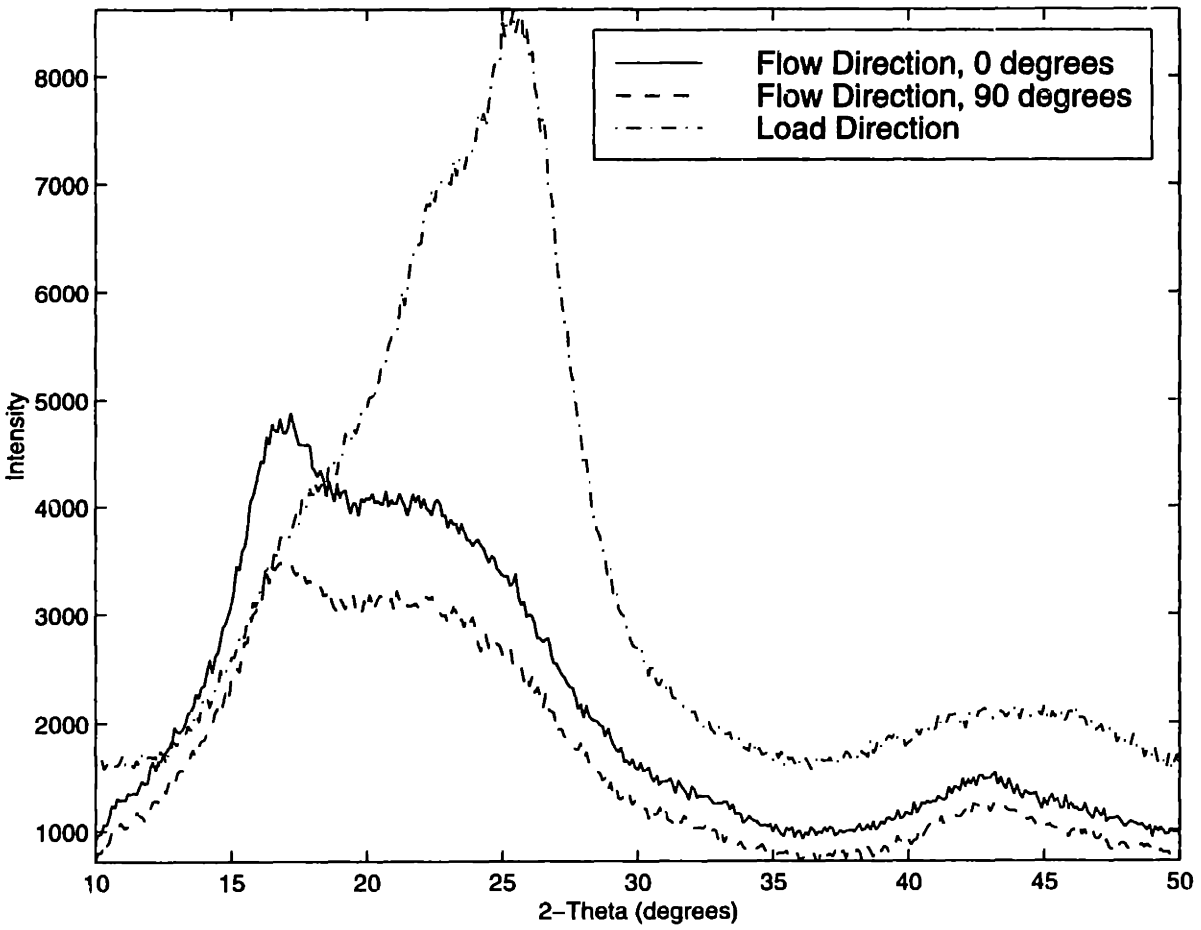

Figure C.4: WAXD scans of specimen deformed in uniaxial compression at $90°C$ to a final strain of -2.0 at a strain rate of -0.1/*s*

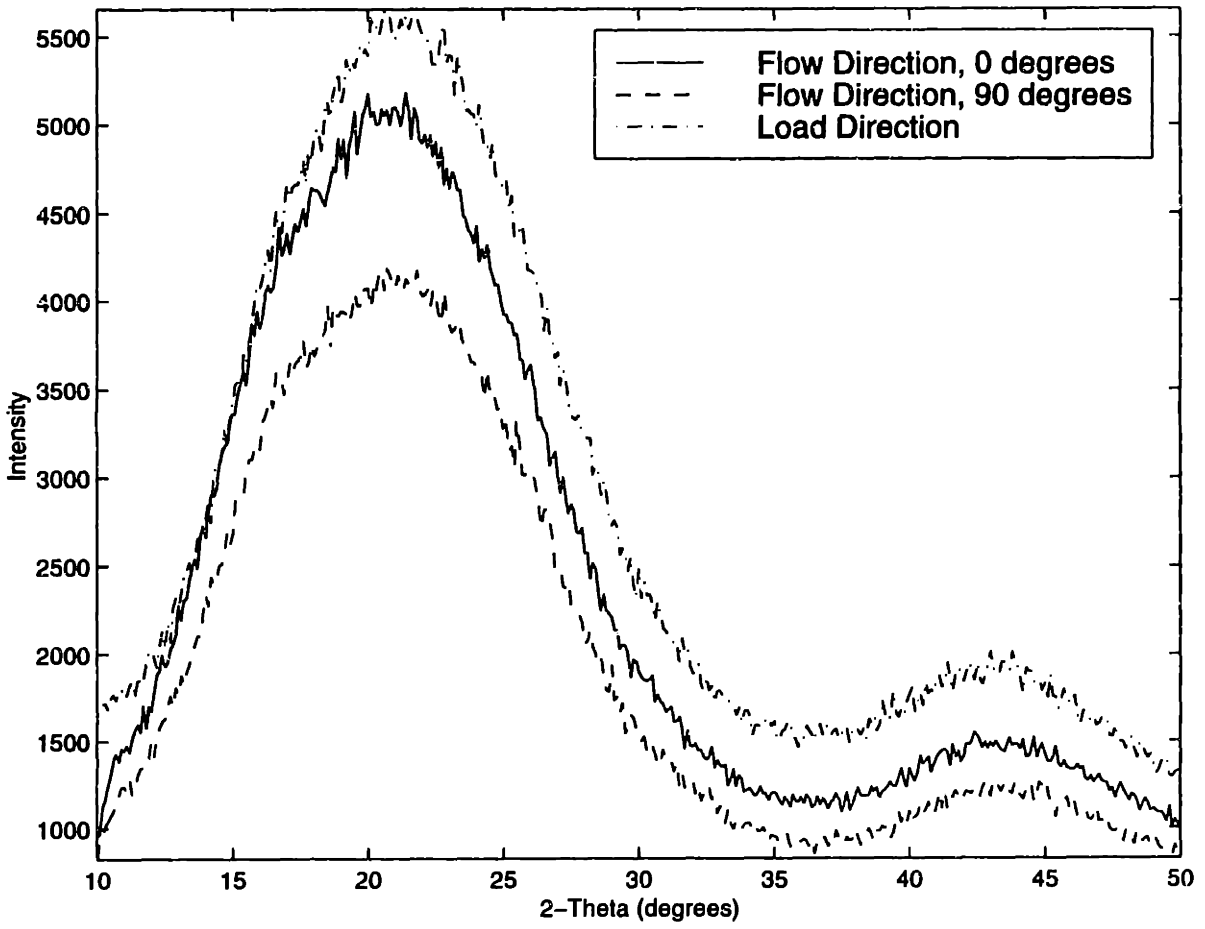

Figure C.5: WAXD scans of specimen deformed in uniaxial compression at $100°C$ to a final strain of -2.0 at a strain rate of -0.005/*s*

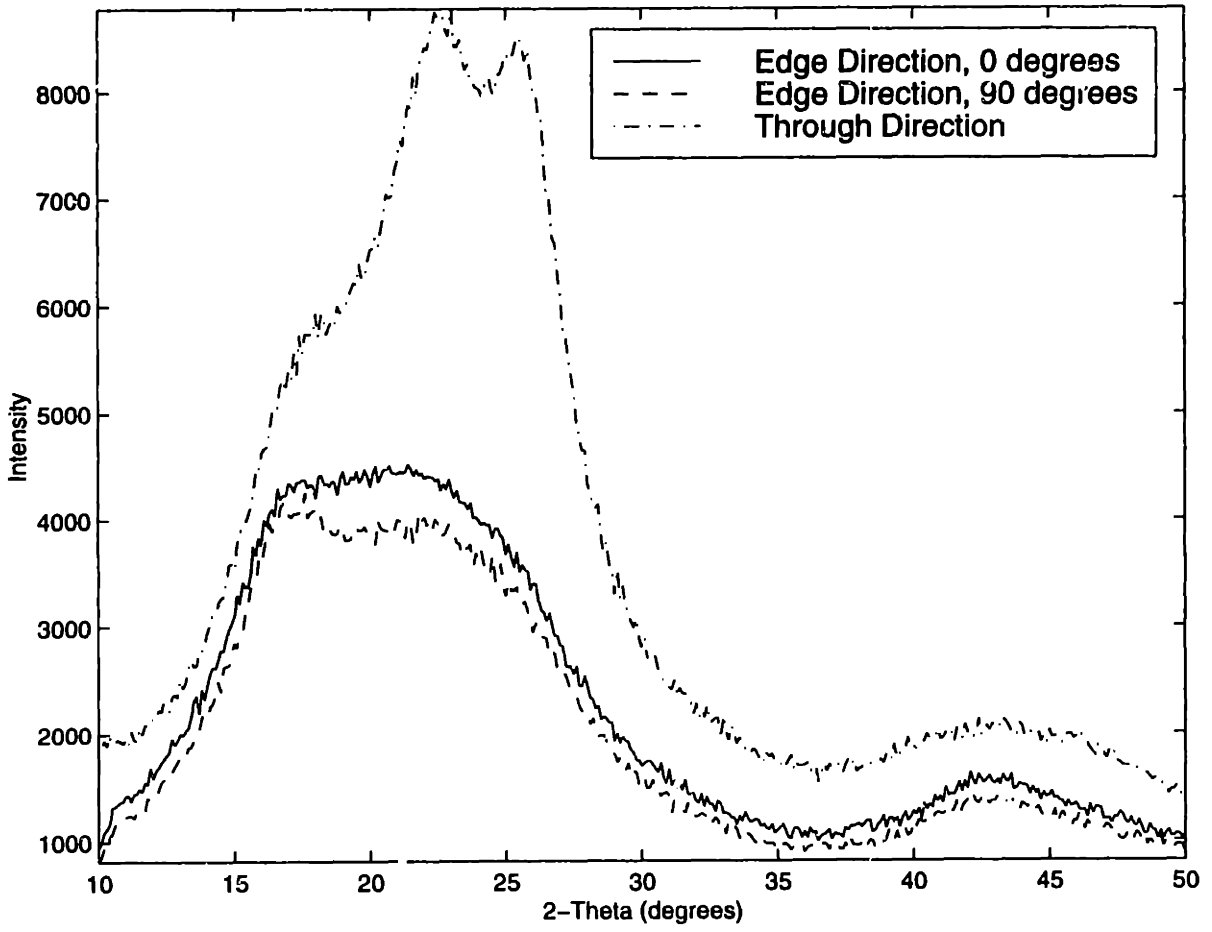

Figure C.6: WAXD scans of specimen deformed in uniaxial compression at $100°C$ to a final strain of -2.0 at a strain rate of $-0.1/s$

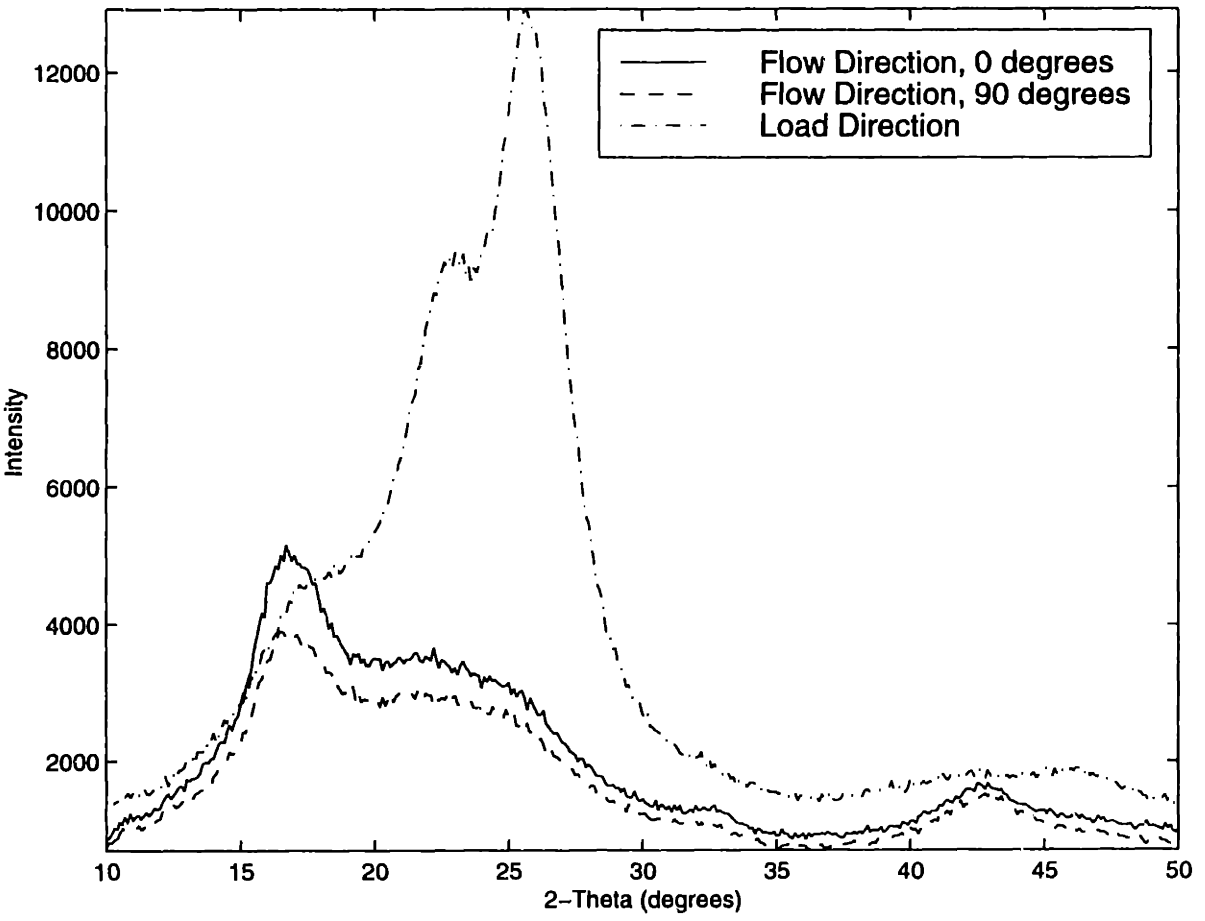

Figure C.7: WAXD scans of specimen deformed in uniaxial compression at $100°C$ to a final strain of -2.0 at a strain rate of $-1.0/s$

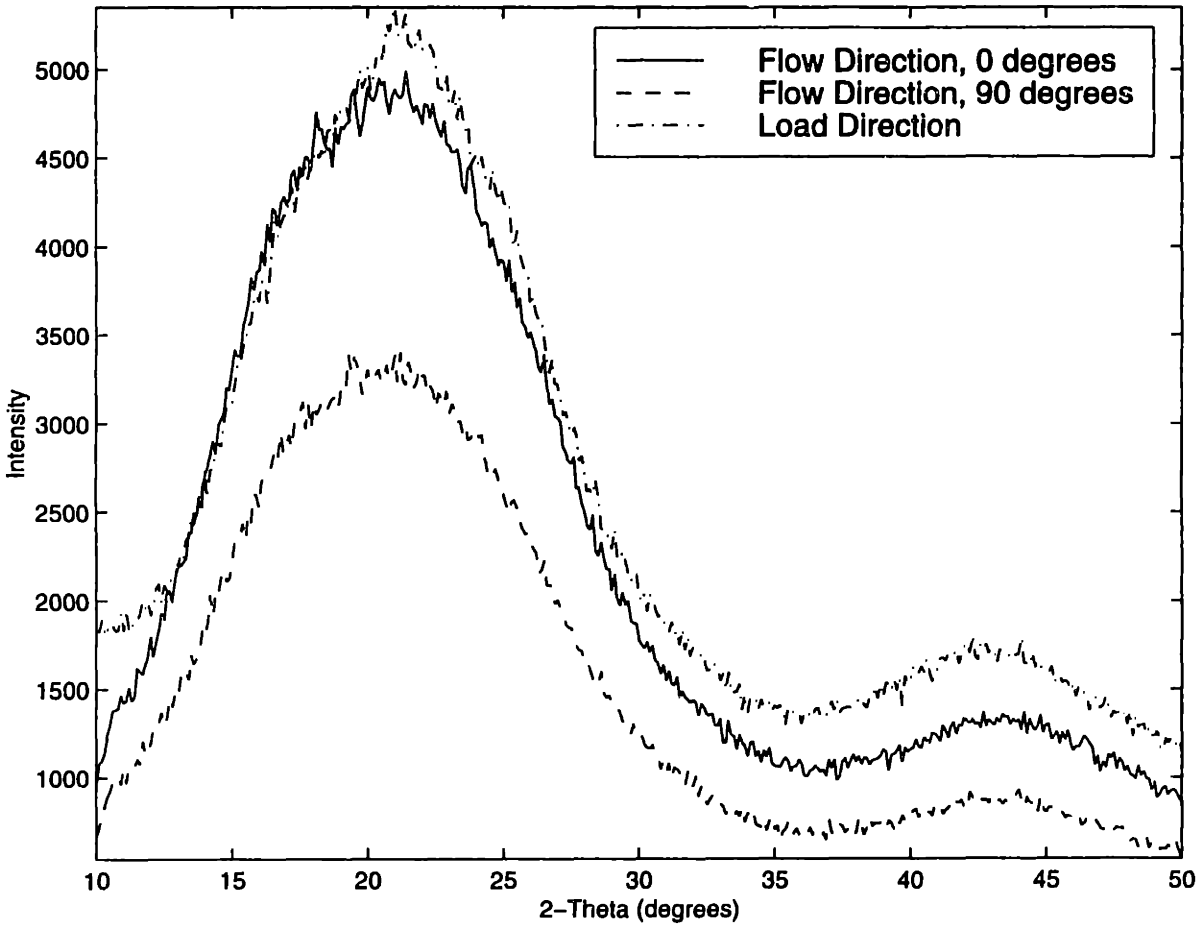

Figure C.8: WAXD scans of specimen deformed in uniaxial compression at $105°C$ to a final strain of -2.0 at a strain rate of $-0.01/s$

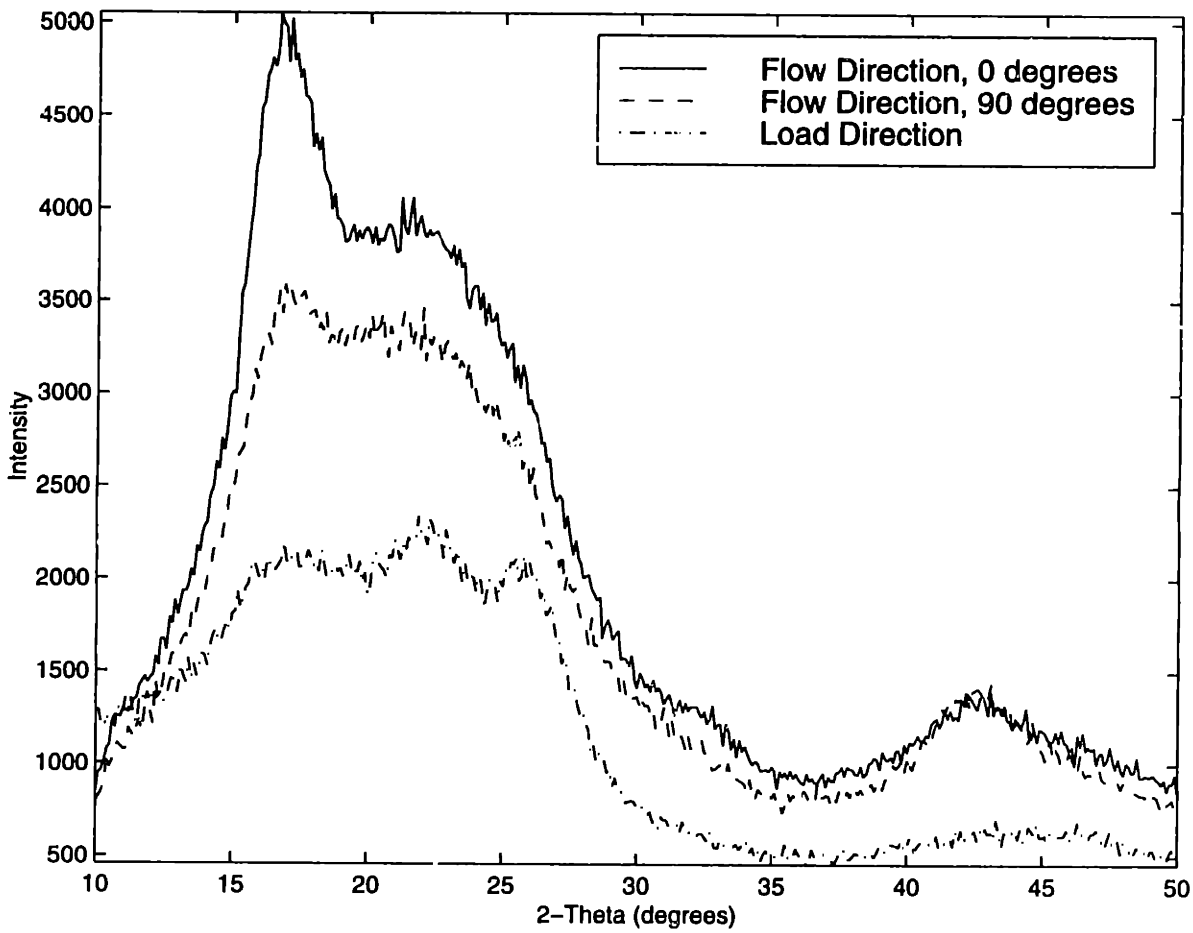

Figure C.9: WAXD scans of specimen deformed in uniaxial compression at $105°C$ to a final strain of -2.0 at a strain rate of $-0.1/s$

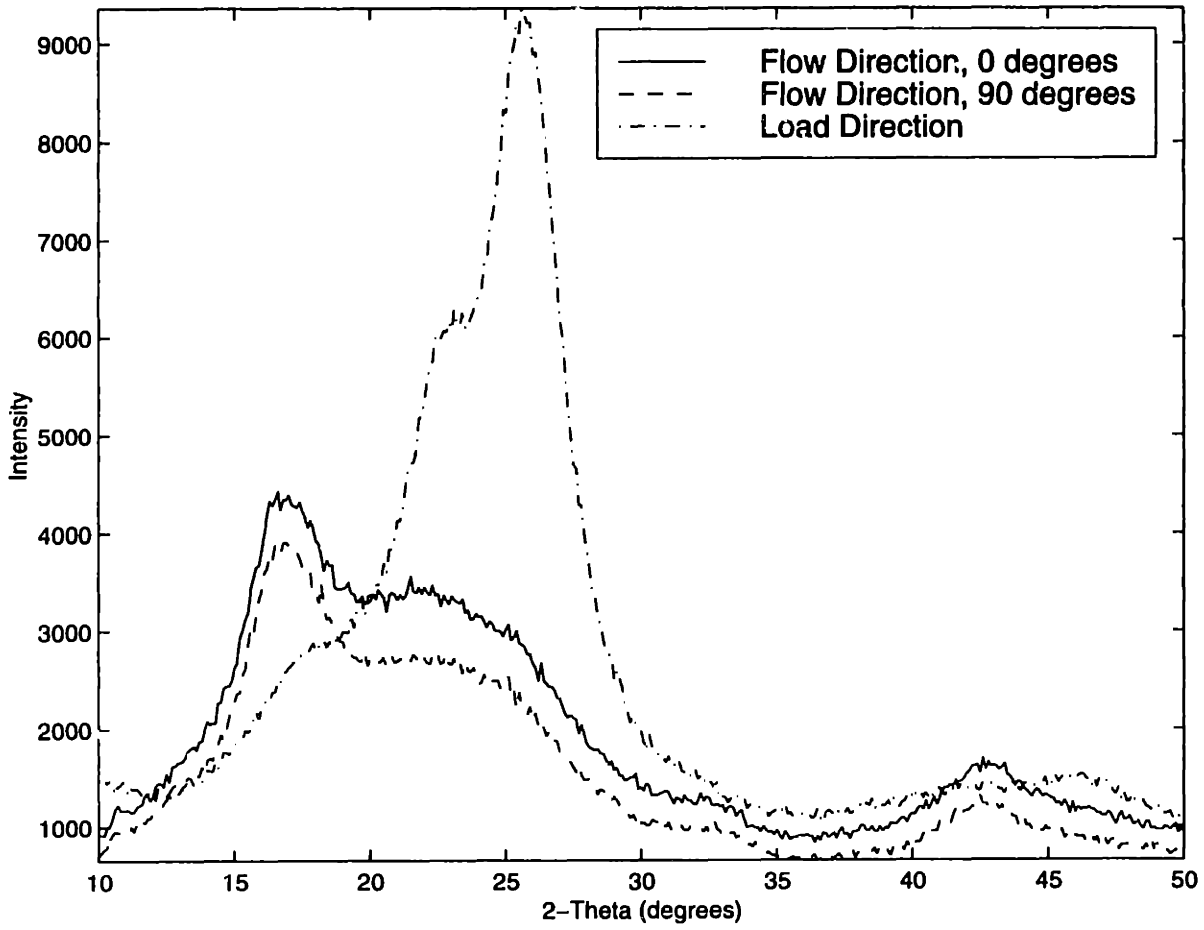

Figure C.10: WAXD scans of specimen deformed in uniaxial compression at $105°C$ to a final strain of -2.0 at a strain rate of $-1.0/s$

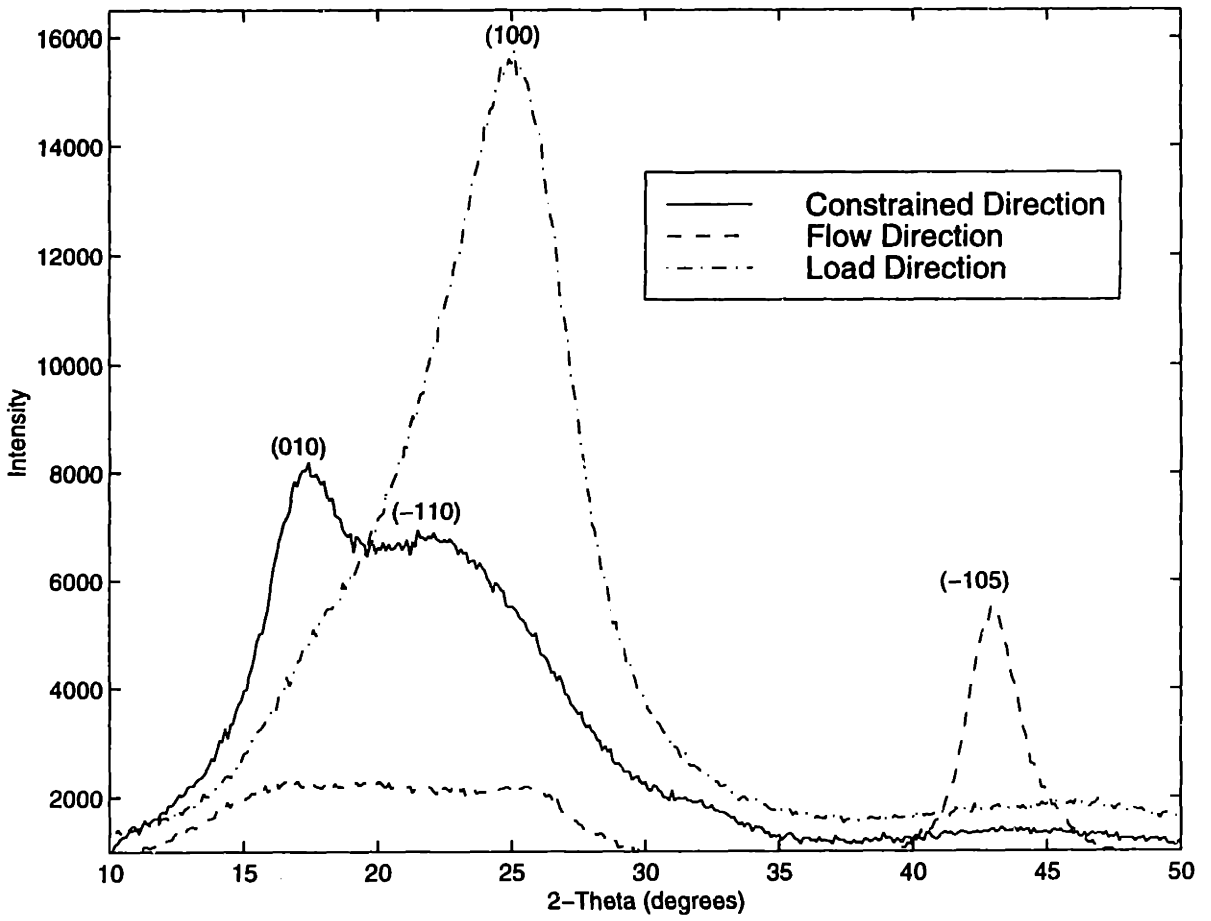

Figure C.11: WAXD scans of specimen deformed in plane strain compression at $80°C$ to a final strain of -1.6 at a strain rate of $-0.1/s$

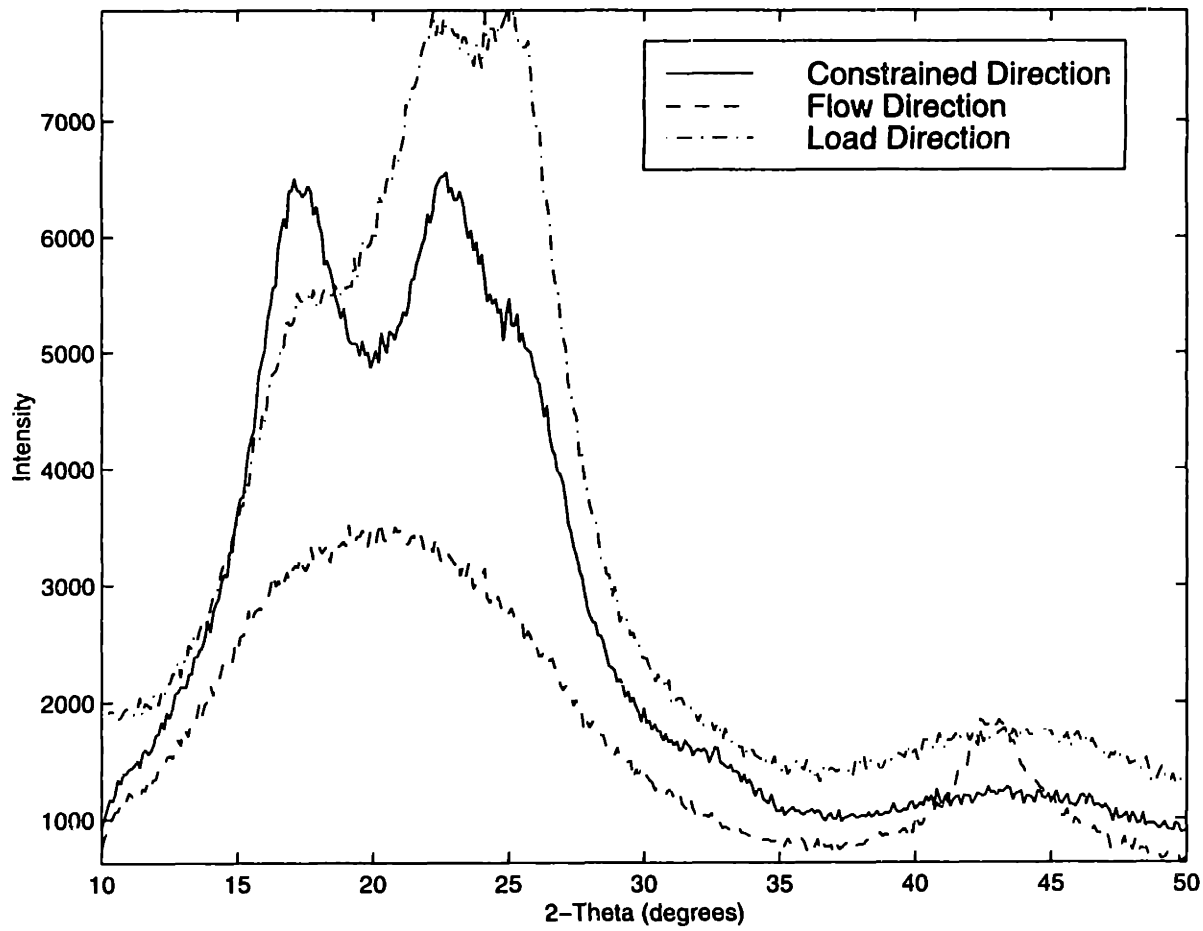

Figure C.12: WAXD scans of specimen deformed in plane strain compression at $90°C$ to a final strain of -1.0 at a strain rate of $-0.1/s$

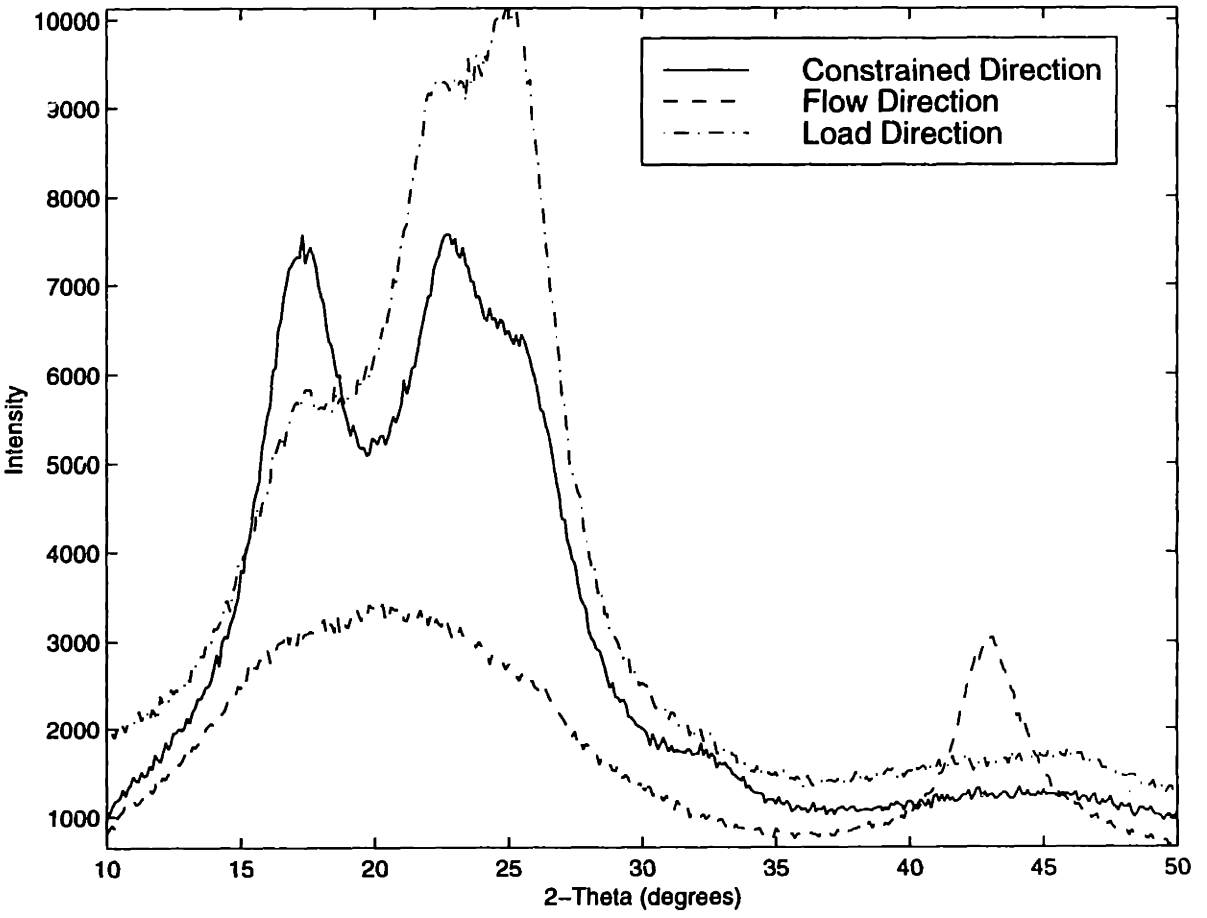

Figure C.13: WAXD scans of specimen deformed in plane strain compression at $90°C$ to a final strain of -1.2 at a strain rate of $-0.1/s$

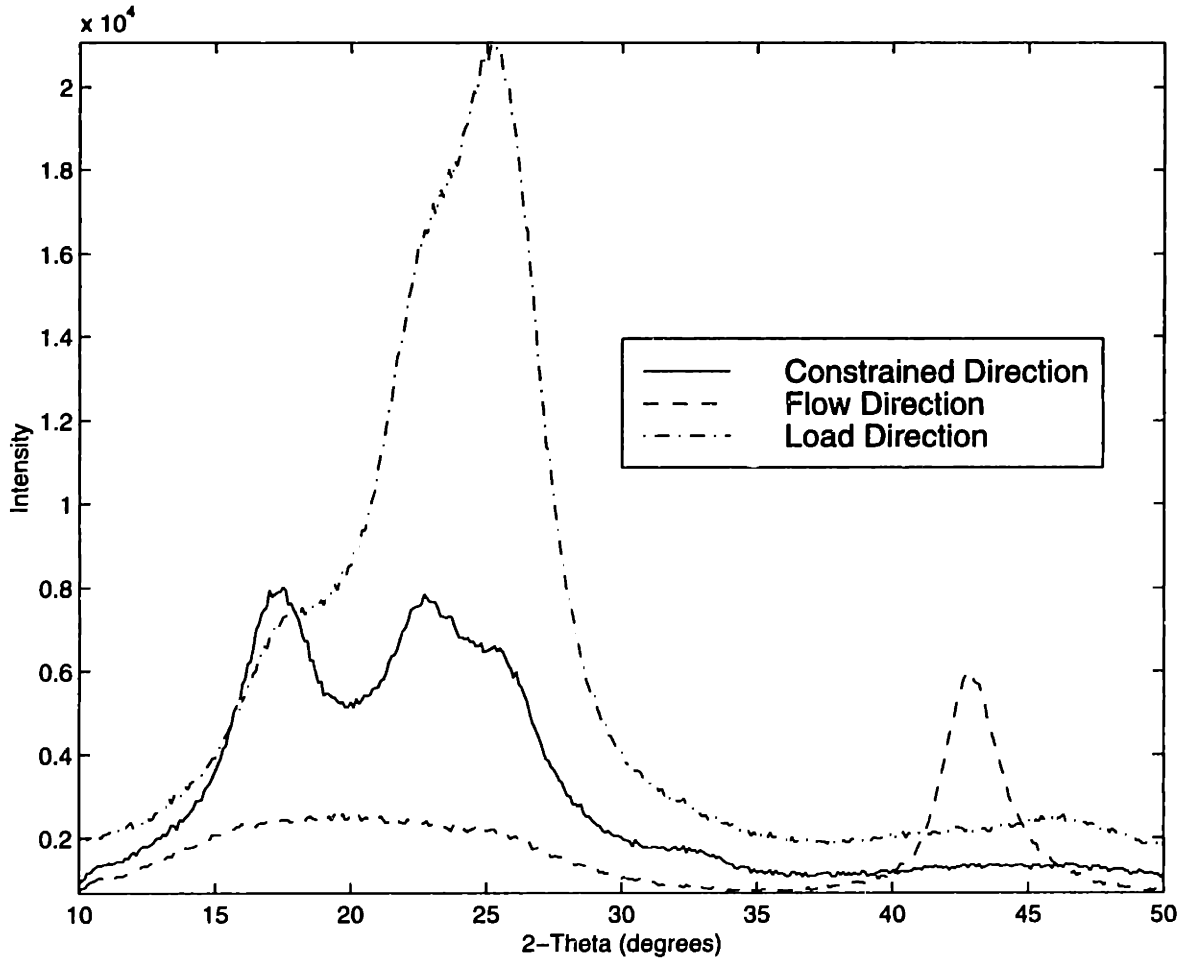

Figure C.14: WAXD scans of specimen deformed in plane strain compression at $90°C$ to a final strain of -1.4 at a strain rate of $-0.1/s$

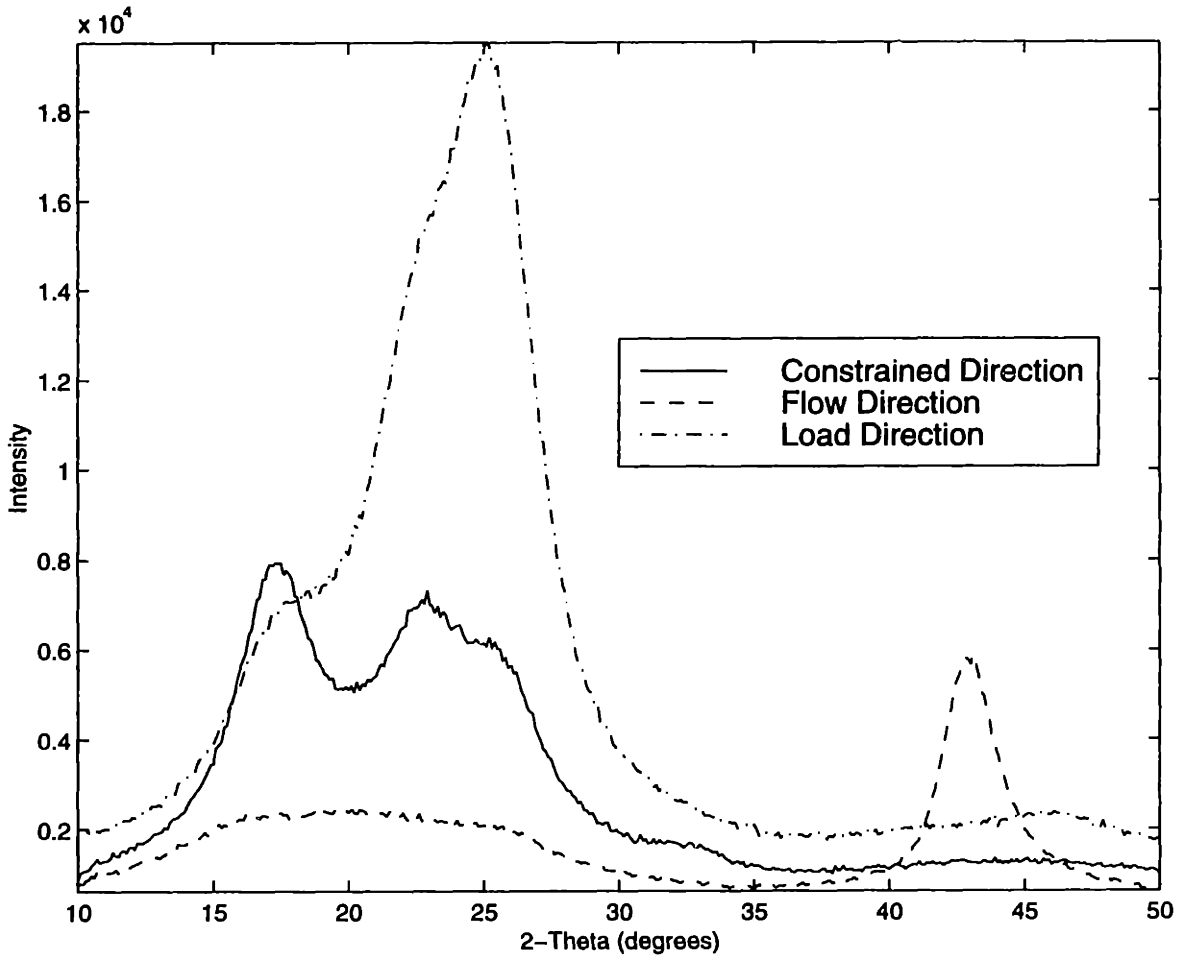

Figure C.15: WAXD scans of specimen deformed in plane strain compression at $90°C$ to a final strain of -1.6 at a strain rate of -0.1/*s*

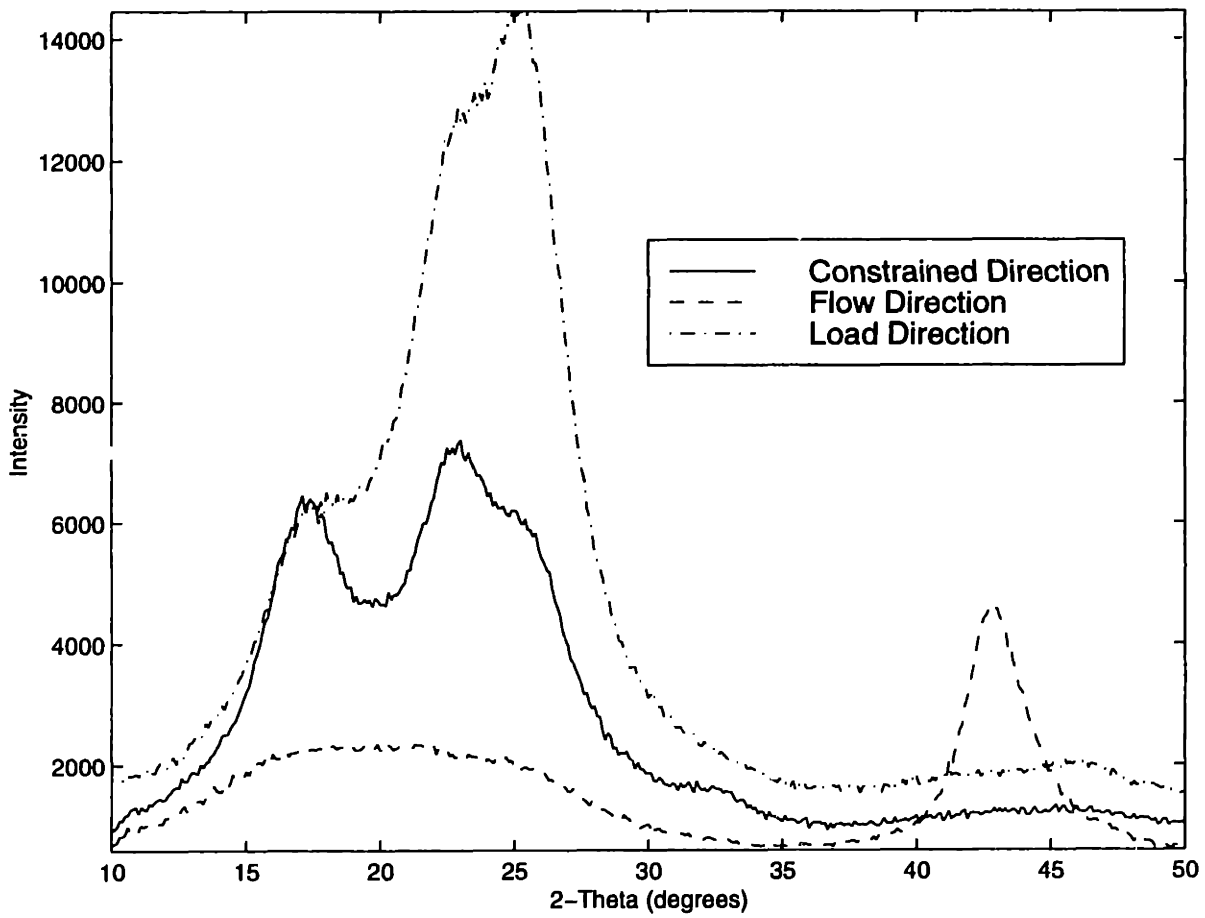

Figure C.16: WAXD scans of specimen deformed in plane strain compression at $90°C$ to a final strain of -1.6 at a strain rate of -0.01/*s*

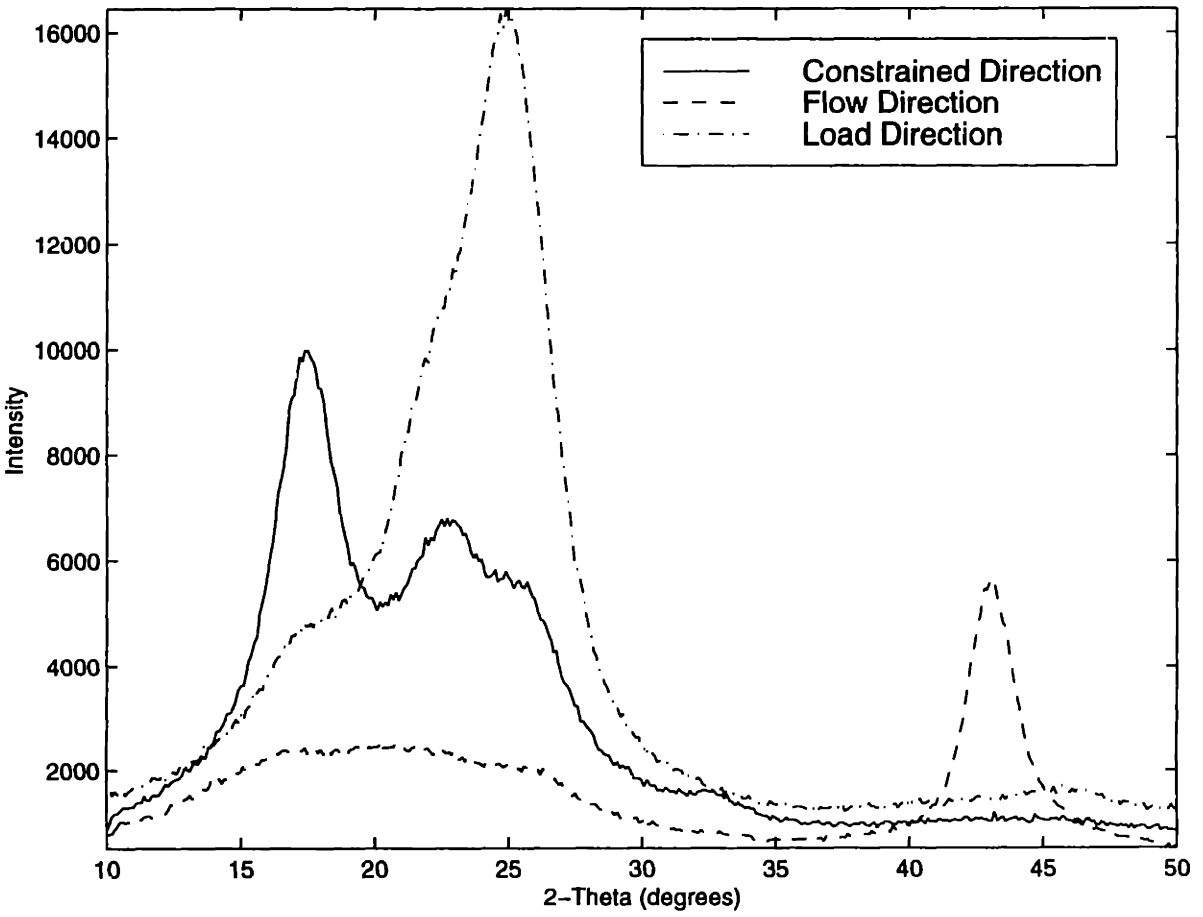

Figure C.17: WAXD scans of specimen deformed in plane strain compression at $90°C$ to a final strain of -1.6 at a strain rate of -1.0/*s*

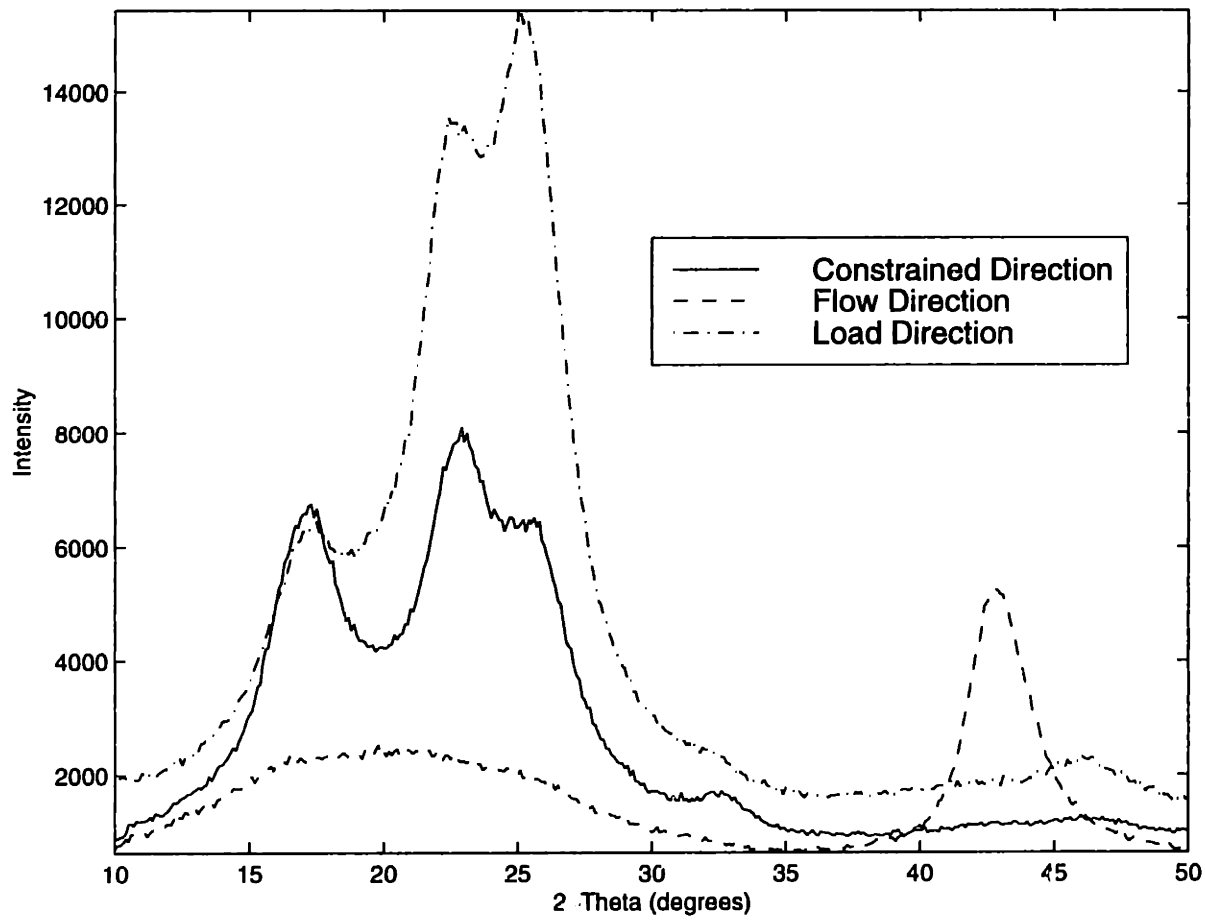

Figure C.18: WAXD scans of specimen deformed in plane strain compression at $100°C$ to a final strain of -1.6 at a strain rate of $-0.1/s$

References

[1] I. Marshall and A. B. Thompson. The Drawing of Terylene. *Journal of Applied Chemistry*, **4**:145-153, 1954.

[2] E. M. Arruda, M. C. Boyce and R. Jayachandran. Effects of Strain Rate, Temperature and Thermo-Mechanicial Coupling on the Finite Strain Deformation of Glassy Polymers. *Mechanics of Materials*, **19**:193-212, 1995.

[3] A. B. Thompson. Strain-Induced Crystallization of Polyethylene Terephthalate. *Journal of Polymer Science*, **34**:741-759, 1959.

[4] I. M. Ward. The Mechanical Behavior of Poly(ethylene terephthalate). *Journal of Macromolecular Science*, **4**:667-694, 1967.

[5] R. A. Duckett, S. Rabinowitz and I. M. Ward. The Strain-rate, Temperature and Pressure Dependence of yield of Isotropic Poly(methylmethacrylate) and Poly(ethylene terephthalate). *Journal of Materials Science*, **5**:909-915, 1970.

[6] A. Misra and R. S. Stein. Stress-Induced Crystallization of Poly(ethylene terephthalate). *Journal of Polymer Science: Polymer Physics Edition*, **17**:235-257, 1979.

[7] A. M. Ghanem and R. S. Porter. Cold Crystallization and Thermal Shrinkage of Uniaxially Drawn Poly(ethylene2,6-naphthalate) by Solid-state Coextrusion. *Journal of Polymer Science: Part B: Polymer Physics*, **27**:2587-2603, 1989.

[8] J. Y. Guan, L. Wang and R. S. Porter. Planar Deformation of Amorphous Poly(ethylene Terephthalate) by Stretching and Forging. *Journal of Polymer Science: Part B: Polymer Physics*, **30**:687-691, 1992.

[9] T. Sun, J. Pereira and R. S. Porter. Crystallization Kinetics for Poly(ethylene Terephthalate) Oriented by Solid-State Coextrusion. *Journal of Polymer Science: Polymer Physics Edition*, **22**:1163-1171, 1984.

[10] S. A. Jabarin. Strain-Induced Crystallization of Poly(ethylene Terephthalate). *Polymer Engineering and Science*, **32**:1341-1349, 1992.

[11] P. Chandran and S. Jabarin. Biaxial Orientationof Poly(ethylene Terephthalate). Part I: Nature of the Stress-Strain Curves. *Advances in Polymer Technology*, **12**:119-132, 1993.

[12] C. P. Buckley, D. C. Jones and D. P. Jones. Hot-drawing of poly(ethylene terephthalate) under biaxial stress: application of a three-dimensional glass-fubber constitutive model. *Polymer*, **37**:2403-2414, 1996.

[13] J. S. Zaroulis and M. C. Boyce. Temperature, strain rate, and strain state dependence of the evolution in mechanical behaviour and structure of poly(ethylene terephthalate) with finite strain deformation. *Polymer*, **38**:1303-1315, 1997.

[14] D. J. Blundell, D. H. MacKerron, W. Fuller, A. Mahendrasingam, C. Martin, R. J. Oldman, R. J. Rule and C. Riekel. Characterization of strain-induced crystallization of (poly ethylene terephthalate) at fast draw rates using synchrotron radiation. *Polymer*, **37**:3303-3311, 1996.

[15] A. Mahendrasingam, C. Martin, W. Fuller, A. M. Adams, C. P. Buckley, D. J. Blundell, D. P. Jones and D. H. MacKerron. Structural Changes and Stress Relaxation Following Drawing of PET. *Tenth International Conference on Deformation, Yield and Fracture of Polymers*, Churchill College, Cambridge, UK, 45-48, 1997.

[16] *Polymer Handbook*, 3rd Edition, Wiley, New York, 1989.

[17] O. A. Hasan and M. C. Boyce. Energy storage during inelastic deformation of glassy polymers. *Polymer*, **34**:5085-5092, 1993.

[18] E. M. Arruda and M. C. Boyce. An Experimental and Analytical Investigation of the Large Strain Compressive and Tensile Response of Glassy Polymers. *Polymer Engineering and Science*, **30**:1288-1298, 1990.

[19] O. A. Hasan, M. C. Boyce, X. S. Li and S. Berko. An Investigation of the Yield and Postyield Behavior and Corresponding Structure of Poly(methyl methacrylate). *Journal of Polymer Science: Part B: Polymer Physics*, **31**:185-197, 1993.

[20] R. J. Young and P. A. Lovell. *Introduction to Polymers*, 2nd Edition, Chapman & Hall, London, 1991.

[21] *Encyclopedia of Polymer Science & Engineering*(fill this in later!)

[22] D. J. Blundell, D. R. Beckett and P. H. Willcocks. Routine crystallinity measurements of polymers by d.s.c., *Polymer*, **22**:704-707, 1981.

[23] S. Kavesh and J. M. Schultz. Meaning and Measurement of Crystallinity in Polymers: A Review, *Polymer Engineering and Science*, **9**:452-460, 1969.

[24] B. C. Cullity. *Elements of X-ray Diffraction*, 2nd Edition, Addison-Wesley, Massachusetts, 1978.

[25] D. R. Salem. Development of crystalline order during hot-drawing of poly(ethylene terephthalate) film: influence of strain rate, *Polymer*, **33**:3182-3188, 1992.

[26] P. N. Peszkin and J. M. Schultz. Kinetics of Fiber Heat Treatment. II. Poly(ethylene terephthalate) Fibers, *Journal of Polymer Science: Part B: Polymer Physics*, **24**:2591-2616, 1986.

[27] A. Bellare, R. E. Cohen and A. S. Argon. Development of texture in poly(ethylene terephthalate) by plane-strain compression, *Polymer*, **34**:1393-1403, 1993.

[28] S. G. Charati, A. Y. Houde, S. S. Kulkarni, and M. G. Kulkarni. Transport of Gases in Aromatic Polyesters: Correlation with WAXD Studies, *Journal of Polymer Science: Part B: Polymer Physics*, **29**:921-931, 1991.

[29] R. E. Robertson. On the Cold-Drawing of Plastics, *Journal of Applied Polymer Science*, **7**:443-450, 1963.

[30] R. E. Robertson. Theory for the Plasticity of Glassy Polymers, *The Journal of Chemical Physics*, **44**:3950-3956, 1966.

[31] A. S. Argon. A theory for the low-temperature plastic deformation of glassy polymers, *Philosophical Magazine*, **28**:839-865, 1973.

[32] A. S. Argon and M. I. Bessonov. Plastic deformation in polyimides, with new implications on the theory of plastic deformation of glasys polymers, *Philosophical Magazine*, **35**:917-933, 1977.

[33] U. F. Kocks, A. S. Argon and M. F. Ashby. *Progress in Materials Science*, **19**, 1975.

[34] A. S. Argon, P. H. Mott and U. W. Suter. Simulations of Plastic Deformation in a Flexible Chain Glassy Polymer, *Phys. Stat. Sol. (b)*, **172**:193-204, 1992.

[35] P. H. Mott, A. S. Argon and U. W. Suter. Atomistic modeling of plastic deformation of glassy polymers, *Philosophical Magazine A*, **67**: 931-978, 1993.

[36] D. N. Theodorou and U. W. Suter. Local Structure and the Mechanism of Response to Elastic Deformation in a Glassy Polymer, *Macrmolecules*, **19**:379-387, 1986.

[37] L. R. G. Treloar. *The Physics of Rubber Elasticity*, Oxford University Press, Oxford, 1975.

[38] L. R. G. Treloar. The mechanics of rubber elasticity, *Proceedings of the Royal Society of London*, **A351**:301-330, 1976.

[39] R. S. Rivlin. Large Elastic Deformations of Isotropic Materials, IV. Further Developments of the General Theory, *Philosophical Transactions of the Royal Society of London A*, **241**:379-397, 1948.

[40] K. C. Valanis and R. F. Landel. The Strain-Energy Function of a Hyperelastic Material in Terms of the Extension Ratios, *Journal of Applied Physics*, **38**:2997-3002, 1967.

[41] R. W. Ogden. Large deformation isotropic elasticity - on the correlation of theory and experiment for incompressible rubberlike solids, *Proceeding of the Royal Society of London*, **A326**:565-584, 1972.

[42] P. J. Flory and J. Rehner, Jr. Statistical Mechanics of Cross-Linked Polymer Networks, *Journal of Chemical Physics*, **11**:512-520, 1943.

[43] S. F. Edwards and T. Vilgis. The Effect of Entanglements in Rubber Elasticity, *Polymer*, **27**:483-492, 1986.

[44] M. C. Wang and E. Guth. Statistical Theory of Networks of Non-Gaussian Flexible Chains, *The Journal of Chemical Physics*, **20**:1144-1157, 1952.

[45] E. M. Arruda and M. C. Boyce. A Three-Dimensional Constitutive Model for the Large Stretch Behavior of Rubber Elastic Materials, *Journal of Mechanics and Physics of Solids*, **41**:389-412, 1993.

[46] M. C. Boyce, D. M. Parks and A. S. Argon. Large Inelastic Deformation of Glassy Polymers. Part I: Rate Dependent Constitutive Model, *Mechanics of Materials*, **7**:15-33, 1988.

[47] C. P. Buckley and D. C. Jones. Glass-rubber constitutive model for amorphous polymers near the glass transition, *Polymer*, **36**:3301-3312, 1995.

[48] J. S. Bergstrom and M. C. Boyce. Constitutive Modeling of the Large Strain Time-Dependent Behavior of Elastomers. Accepted for publication in *Journal of Mechanics and Physics of Solids.*

[49] M. C. Boyce, G. G. Weber and D. M. Parks. On the Kinematics of Finite Strain Plasticity, *Journal of Mechanics and Physics of Solids*, **37**:647-665, 1989.